

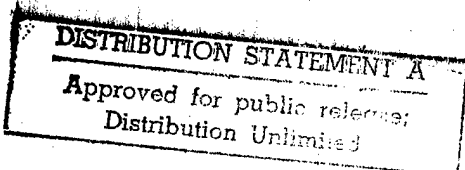

REPORT DOCUMENTATION PAGE,

AFRL-SR-BL-TR-98-

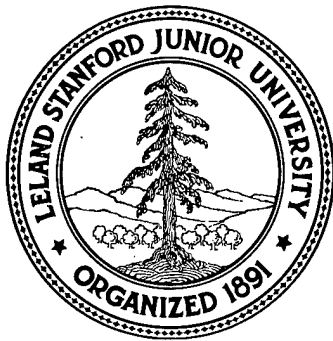
0376

s, gathering  
collection of  
hway, Suite

Public reporting burden for this collection of information is estimated to average 1 hour per response, includ and maintaining the data needed, and completing and reviewing the collection of information. Send corr information, including suggestions for reducing this burden, to Washington Headquarters Services, Director 1204, Arlington, VA 22202-4302, and to the Office of management and Budget, Paperwork Reduction Projec

1. AGENCY USE ONLY (Leave Blank)		2. REPORT DATE September 1995	3. REI Final
4. TITLE AND SUBTITLE Ion-Assisted Nucleation of Diamond			5. FUNDING NUMBERS
6. AUTHORS Sean P. McGinnis			
7. PERFORMING ORGANIZATION NAME(S) AND ADDRESS(ES) Stanford University			8. PERFORMING ORGANIZATION REPORT NUMBER
9. SPONSORING/MONITORING AGENCY NAME(S) AND ADDRESS(ES) AFOSR/NI 110 Duncan Avenue, Room B-115 Bolling Air Force Base, DC 20332-8080			10. SPONSORING/MONITORING AGENCY REPORT NUMBER
11. SUPPLEMENTARY NOTES			
12a. DISTRIBUTION AVAILABILITY STATEMENT Approved for Public Release			12b. DISTRIBUTION CODE
13. ABSTRACT (Maximum 200 words) See attached.			
			
			
14. SUBJECT TERMS			15. NUMBER OF PAGES
			16. PRICE CODE
17. SECURITY CLASSIFICATION OF REPORT Unclassified	18. SECURITY CLASSIFICATION OF THIS PAGE Unclassified	19. SECURITY CLASSIFICATION OF ABSTRACT Unclassified	20. LIMITATION OF ABSTRACT UL

0376



## ION-ASSISTED NUCLEATION OF DIAMOND

A DISSERTATION SUBMITTED TO THE  
DEPARTMENT OF MATERIALS SCIENCE  
AND ENGINEERING AND THE COMMITTEE ON  
GRADUATE STUDIES OF STANFORD UNIVERSITY  
IN PARTIAL FULFILLMENT OF THE REQUIREMENTS  
FOR THE DEGREE OF DOCTOR OF PHILOSOPHY

Sean P. McGinnis  
September 1995

19980505 133

Department of MATERIALS SCIENCE AND ENGINEERING

STANFORD UNIVERSITY

# **ION-ASSISTED NUCLEATION OF DIAMOND**

**A DISSERTATION SUBMITTED TO THE  
DEPARTMENT OF MATERIALS SCIENCE  
AND ENGINEERING AND THE COMMITTEE ON  
GRADUATE STUDIES OF STANFORD UNIVERSITY  
IN PARTIAL FULFILLMENT OF THE REQUIREMENTS  
FOR THE DEGREE OF DOCTOR OF PHILOSOPHY**

*Sean P. McGinnis*

Sean P. McGinnis

September 1995

© Copyright by Sean P. McGinnis 1995  
All Rights Reserved

I certify that I have read this dissertation and that in my opinion it is fully adequate, in scope and quality, as a dissertation for the degree of Doctor of Philosophy.



---

Professor Stig B. Hagström (Principal Advisor)

I certify that I have read this dissertation and that in my opinion it is fully adequate, in scope and quality, as a dissertation for the degree of Doctor of Philosophy.



---

Professor Michael A. Kelly

I certify that I have read this dissertation and that in my opinion it is fully adequate, in scope and quality, as a dissertation for the degree of Doctor of Philosophy.



---

Professor Piero Pianetta

Approved for the University Committee on Graduate Studies:

---

## ABSTRACT:

Diamond thin films are envisioned for a wide variety of applications due to the unique chemical, mechanical, electrical, and optical properties of this material. However, deposition limitations currently prevent the realization of many of these applications. The nucleation of diamond is one critical limitation which severely restricts the use of diamond films for emerging technologies. The nucleation process dictates the structure and morphology of the diamond thin films; therefore, nucleation ultimately affects a wide range of film properties including adhesion, strength, thermal and electrical conductivity, and optical transmissivity. Without specific pretreatments to overcome nucleation problems, heterogeneous diamond nucleation is inadequate for use in most applications. Therefore, several techniques for improving diamond nucleation were investigated in this thesis to improve the understanding of this critical aspect of diamond technology.

Thin carbon films with varied structure proved ineffective for nucleation enhancement. Scratching/abrasion of substrates with diamond powder significantly enhanced nucleation, however, associated with this technique are a number of disadvantages. Ion-assisted nucleation, also called bias-enhanced nucleation, is a promising *in-situ* technique for diamond nucleation densities in excess of  $10^{10}$  cm<sup>-2</sup>. In this process a negative bias is applied to the substrate in a microwave plasma chemical vapor deposition (MPCVD) system. The bombardment of the substrate by energetic carbon ions during the bias pretreatment controls the nucleation. A critical bias voltage is required for significant nucleation enhancement and the process is relatively independent of temperature and carbon concentration over specific ranges. Characterization of the bias-deposited material by scanning and transmission electron microscopy, raman spectroscopy, x-ray photoelectron spectroscopy, and x-ray and electron diffraction confirms the presence of small diamond nuclei in a non-diamond carbon matrix. Monte Carlo computer simulations of the ion energy distribution at the substrate agree with experimental ion energy distributions measured with a retarding field probe. These ion energies are significantly less than the applied bias voltage due to ion-neutral collisions in the sheath. Bias current measurements suggest that hydrogen species dominate carbon species in the ion flux. Increases in bias current with time during the ion-assisted nucleation process are attributed to ion-induced electron emission at the surface. Several nucleation mechanisms are discussed and carbon subplantation accounts for the experimental observations better than either preferential sputtering or thermal spike models.

## ACKNOWLEDGEMENTS:

Although a doctoral thesis is typically regarded as the product of a individual graduate student, this is rarely true and is not the case here. I am indebted to many people for their help along the long path which has brought me to this point. It is impossible to acknowledge everyone who has contributed to this thesis; nonetheless, I would like to mention some of the people who have helped to make this thesis possible.

First, I would like to thank my parents, Robert and Jaclyn McGinnis, for their constant support and encouragement in all my endeavors, especially academic. They continually showed interest in my research and studies without a true sense of my research and graduate life at Stanford. Second, I have benefitted from interaction with many teachers and professors over the years who significantly influenced the path I have followed in academics. I would like to thank them all and mention Robert Claxton (Chemistry teacher - Brainerd Senior High School) and John Weaver (Professor of Materials Science - University of Minnesota) as pivotal figures in my interest and pursuit of science and engineering; they did not simply teach, but rather instilled in me a scientific curiosity and drive which led to my interest in materials science.

In terms of the project represented by this thesis and its genesis, I owe thanks to Professor Stig Hagström who was instrumental in my early interest in diamond thin film deposition. Even though he moved on to other opportunities in Sweden during my tenure at Stanford, his passion for science, thought-provoking philosophies, and pleasant nature and support were important in my graduate work. Although I did not initially realize or appreciate its significance, I now also thank him for allowing me to choose my own research path. In Stig's absence as a scientific collaborator, I must single out Professor Mike Kelly as the person most influential in the scope, content, and quality of this thesis. It was a privilege and incredible learning opportunity to work with Mike in the laboratory. Mike helped me address difficult scientific problems from alternative perspectives and challenged me to ask the correct (or at least better) questions when I was unsure of my research path. I am a better person and scientist as a result of interaction with Mike Kelly. I thank him for his scientific insights, his personal philosophies, and his friendship.

I am grateful for all my friends, near and far, who have supported me as I pursued my doctorate. They were, and continue to be, more important to me than they realized. The role of the past and present students of the diamond lab (Ciaran Fox, Brian Holloway, Sanjiv Kapoor, Darin Olson, Ainissa Ramirez, Rochelle Higa, and Hiromu

Shiomi) cannot be fully acknowledged in this limited space. They were rarely too busy to lend a hand or an ear, and their help and insights are an integral part of this thesis. I hope I helped them as much as they helped me. Additional thanks go to Rochelle Higa for continuing the bias-enhanced nucleation work in the HFCVD system - some of which is included in this thesis. Ciaran Fox has been a great friend and constant source of good humor and useful insights since day one (literally) of graduate school. His constant input in research discussions and constructive criticism of presentations, journal articles, and this thesis have been invaluable. We have gone through both good (Hawaii ECS Conference) and bad (quals studying) together. Elliott Horch was a great source of scientific information, a perfect hiking companion, and an intelligent listener and talker throughout a wide variety of discussions. Mike Kautzky has been as great friend as well as my personal computer consultant, devil's advocate, and late-night ping-pong rival. Brian Holloway was a great officemate, work-out partner, and friend. Whenever I needed any help - no matter what, when, or where - Brian was always there. Bill Lewis, Brian Daniels, Tom Marieb, Doug Werner, Grant McFarland, Harvey Fishman, and the Rains IM football team members were all good friends during our time at Stanford together. I will certainly miss all of these people in the future.

Additional thank you's are also necessary: to Turgut Gür, Technical Director of the Center For Materials Research (CMR), for early assistance as I began diamond research and for continued help and advice in scientific and other matters during the past five years; to Professor Bruce Clemens, Todd Hufnagel, Brian Daniels, and the rest of the Clemens' research group for the use of their equipment, time, and x-ray diffraction expertise at the Stanford Synchrotron Radiation Lab (SSRL); to Paul Dennig and his advisor, the late Professor Dave Stevenson, for use of the MPCVD system which Paul designed and built; to visiting scientists Jan-Otto Carlsson (Uppsala University, Sweden) and Louie Schlapbach (Fribourg University, Switzerland) who provided keen insights into diamond deposition, nucleation phenomena, science and technology, and cultural perspective; to Roger Alvis for his time and effort in TEM analysis of several samples; to Joseph Han who provided help in using the *IONTRANS* simulation program; to Captain Pat Emmert (Wright-Patterson Air Force Base) who worked with me during the summer of 1993 to implement the bias into a MPCVD system and also who provided many of the digitized SEM images which appear in this thesis; and to the diamond research group at NC State of Professor Jeff Glass, Scott Wolter, Mike McClure, and especially Brian Stoner who provided me with information, ideas, and insights into biased nucleation which helped focus my early thesis research. I could go on and on . . . . .



I would also like to thank the National Defense Science and Engineering Graduate Fellowship Program (NDSEG) and the Air Force Office of Scientific Research (AFOSR) for the funding of my first three years of graduate school. Finally, I would like to extend my gratitude once again to those who served on my doctoral reading and dissertation committees. I appreciated the time and effort spent to improve the quality of this thesis.

# TABLE OF CONTENTS:

CHAPTER 1 - Introduction.....	1
1.1 Diamond Thin Films - Properties, Synthesis, Applications.....	1
1.2 Nucleation of Diamond.....	4
1.3 Scope and Approach of this Thesis.....	8
1.4 References.....	8
CHAPTER 2 - Experimental Considerations.....	12
2.1 Hot Filament Chemical Vapor Deposition (HFCVD).....	12
2.2 Microwave Plasma Chemical Vapor Deposition (MPCVD).....	15
2.3 Sequential Deposition.....	20
2.4 Temperature and Pressure Issues.....	21
2.5 Substrates and Substrate Preparation.....	25
2.6 References.....	26
CHAPTER 3 - Characterization Techniques.....	28
3.1 Scanning Electron Microscopy (SEM).....	28
3.2 Raman Spectroscopy.....	32
3.3 X-Ray Photoelectron Spectroscopy (XPS).....	35
3.4 X-Ray Diffraction (XRD).....	41
3.5 Transmission Electron Microscopy (TEM).....	44
3.6 References.....	45
CHAPTER 4 - Results and Discussion.....	46
4.1 Diamond Nucleation on Pristine Substrates.....	46
4.2 Carbon Pretreatments and Nucleation Enhancement.....	48
4.3 Nucleation by Diamond Scratching/Abrasion Pretreatments.....	52
4.4 Ion-Assisted Nucleation of Diamond.....	54
4.41 Role of Energetic Species (Ions/Neutrals).....	56
4.42 Role of Substrate Temperature.....	63
4.43 Effect of Carbon Concentration and Plasma Chemistry.....	66
4.44 Sequential Deposition Using Bias.....	71
4.45 Role of Secondary Electron Emission.....	74
4.46 Retarding Field Probe Measurements.....	81
4.47 Characterization of Bias-Deposited Material.....	86
4.5 References.....	108

CHAPTER 5 - Nucleation Mechanisms.....	113
5.1 Nucleation Theory and Diamond Nucleation Considerations.....	114
5.2 Relevant Chemical Species and Fluxes.....	115
5.3 Neutral and Ion Flux Considerations.....	120
5.4 Ion Energy Distribution.....	126
5.5 Ion-Assisted Diamond Nucleation Mechanisms.....	136
5.51 Preferential Sputtering.....	137
5.52 Thermal Spikes.....	139
5.53 Subplantation of Carbon.....	146
5.4 References.....	152
CHAPTER 6 - Summary.....	156
6.1 Experimental Conclusions.....	156
6.2 Modeling Conclusions.....	159
6.3 Directions for Future Work.....	160
6.4 References.....	163
APPENDIX A.....	164
A.1 Related Publications by the Author.....	164
A.2 Chemical Bond Strengths.....	165
A.3 X-Ray Photoelectron Spectroscopy Quantification.....	166
A.4 Structure Factor Calculations for Diamond.....	169
A.5 Sample Preparation Method for Cross-Sectional Transmission Electron Microscopy (TEM).....	170

## LIST OF TABLES:

Table 1.1 - Properties of natural diamond.....	2
Table 2.1 - Typical experimental conditions for HFCVD. ....	14
Table 2.2 - Typical parameters for (a) unbiased MPCVD deposition and (b) ion- assisted MPCVD pretreatments. ....	19
Table 2.3 - Typical parameters for biased sequential deposition. ....	21
Table 3.1 - Typical raman parameters for analysis of diamond films/nuclei. ....	35
Table 3.2 - XPS data for survey scan shown in Figure 3.5. ....	38
Table 3.3 - XPS peak fit data for C(1s) high resolution scan.....	40
Table 3.4 - XPS peak fit data for Si(2p) high resolution scan.....	40
Table 3.5 - Comparison of XPS peak assignments to literature values. ....	40
Table 3.6 - d-spacings and relative integrated intensities for diamond and graphite planes. ....	43
Table 4.1 - Carbon thin film deposition and pretreatment processes prior to HFCVD. ....	49
Table 4.2 - Nucleation Densities for HFCVD of Diamond.....	50
Table 4.3 - Bias voltages, parameters, and nucleation densities for ion-assisted nucleation voltage experiments.....	60
Table 4.4 - Process parameters and nucleation data for ion-assisted nucleation process at various substrate temperature.....	65
Table 4.5 - Nucleation data for studies of the effects of carbon concentration on ion-assisted nucleation. ....	67
Table 4.6 - Deposition conditions and results for sequential deposition with separate carbon and hydrogen applied bias.....	72
Table 4.7 - Deposition conditions and results for sequential deposition with exposure to hydrogen, carbon, and biased He or Ar. ....	74
Table 4.8 - Carbon and silicon work functions. ....	76
Table 4.9 - Calculated overlayer thickness at various angles for a perfectly uniform single overlayer.....	95
Table 4.10 - XPS surface composition data for biased and unbiased MPCVD deposition on silicon. ....	101
Table 4.11 - Experimental X-ray diffraction Bragg angles. ....	103

Table 4.12 - Comparison of experimental TED d-spacings to those expected for diamond and graphite. ....	107
Table 5.1 - Important electron-neutral reactions and threshold values. ....	116
Table 5.2 - Estimates for species flux in biased/unbiased MPCVD. ....	122
Table 5.3 - Surface lifetime as a function of adsorption energy. ....	124
Table 5.4 - Estimated mean free paths for $\text{CH}_4^+$ and $\text{H}_2^+$ as a function of gas temperature. ....	128
Table 5.5 - Input parameters for IONTRANS Monte Carlo simulation. ....	131
Table 5.6 - Nearest neighbor distances for various forms of carbon. ....	145
Table 5.7 - Comparison of nucleation models for ion-assisted diamond nucleation process. ....	151
Table A.1 - Chemical bond strengths. ....	165

## LIST OF FIGURES:

Figure 1.1 - Nucleation density vs. particle size for a single layer film composed of cubic nuclei.....	5
Figure 2.1 - HFCVD diamond reactor schematic. ....	13
Figure 2.2 - Schematic of MPCVD system used in this thesis.....	16
Figure 2.4 - Schematic of sequential deposition reactor for diamond deposition.....	20
Figure 2.5 - Temperature calibration data for the MPCVD system. ....	24
Figure 3.1 - SEM images indicating variations in carbon thin film surface morphologies observed by this technique.....	30
Figure 3.1 - Raman spectra for diamond and polycrystalline graphite. ....	33
Figure 3.2 - Raman spectra for carbon thin films varying from diamond at the top to polycrystalline diamond at the bottom. ....	34
Figure 3.3 - Schematic of the micro-raman system. ....	35
Figure 3.4 - XPS analysis geometry and variable designations. ....	37
Figure 3.5 - XPS survey scan of carbon deposited on Si. ....	38
Figure 3.6 - High resolution XPS scan of the C(1s) peak. ....	39
Figure 3.7 - High resolution XPS scan of the Si(2p) peak. ....	39
Figure 3.8 - Symmetric x-ray diffraction geometry and variables. ....	43
Figure 4.1 - (a) SEM of diamond nuclei deposited by MPCVD on clean silicon substrates and (b) raman spectrum for isolated nuclei.....	47
Figure 4.2 - Schematic of the carbon evaporation system for controlled carbon deposition in the carbon pretreatment experiments.....	49
Figure 4.3 - Morphology of a polycrystalline diamond film deposited on diamond scratched silicon substrate. ....	53
Figure 4.4 - (a) Nuclei deposited by the ion-assisted process (b) Diamond film grown by unbiased MPCVD on top of bias-deposited nuclei.....	55
Figure 4.5 - Substrate isolation experimental set-up for investigating the role of the energetic ion flux. ....	57
Figure 4.6 - Nucleation density as a function of the applied bias voltage with constant time-integrated bias current to the substrate.....	61
Figure 4.7 - Maximum nucleation size as a function of the bias time with constant time-integrated bias current to the substrate.....	61
Figure 4.8 - Nucleation density as a function of the integrated bias flux to the substrate.....	63

Figure 4.9 - Nucleation density as a function of substrate temperature for the ion-assisted nucleation process under constant voltage and constant integrated bias current.....	64
Figure 4.10 - Nucleation density vs. carbon concentration at constant integrated bias current.....	68
Figure 4.11 - Bias current vs. time for various carbon concentrations.....	68
Figure 4.12 - Maximum nuclei size as a function of CH <sub>4</sub> /H <sub>2</sub> concentration for constant integrated bias current.....	69
Figure 4.13 - Bias current as a function of the bias time in a 100% H <sub>2</sub> followed by methane addition to 2% CH <sub>4</sub> /H <sub>2</sub> environment under the same conditions.....	70
Figure 4.14 - Raman spectra for sample BEN017 deposited in the sequential reactor under bias conditions: (a) Biased hydrogen emitter/scratched substrate, (b) Biased carbon emitter & scratched substrate, (c) Biased carbon emitter & unscratched substrate.....	73
Figure 4.15 - Measured bias current as a function of time during several similar ion-assisted nucleation pretreatments.....	75
Figure 4.16 - Initial bias current as a function of substrate temperature under constant bias voltage conditions.....	79
Figure 4.17 - Initial bias current as a function of carbon concentration in the gas phase under constant bias voltage conditions.....	80
Figure 4.18 - Initial experimental bias current as a function of the applied negative bias voltage.....	80
Figure 4.19 - Schematic of the retarding field probe for the ion energy distribution measurements in the MPCVD system.....	82
Figure 4.20 - Total current ( $I_{total}$ ), electron current ( $I_e$ ), and resulting ion current ( $I_{ion}$ ) from retarding probe measurements.....	83
Figure 4.21 - Response function for ions using the retarding probe.....	84
Figure 4.22 - Measured ion current (circles) and the ion current calculated (solid line) using the convolution theorem.....	85
Figure 4.23 - Calculated ion energy from the retarding probe measurements. A gaussian peak shape and the convolution theorem were used.....	86
Figure 4.24 - SEM images typical of bias-deposited nuclei as the pretreatment time is increased from approximately 10 minutes (a) to 20 minutes (b) to 60 minutes (c).....	88
Figure 4.25 - Raman spectrum for 1 hour bias-deposited carbon film.....	90

Figure 4.26 - Raman spectra: (a) 15 minute bias deposition, (b) 120 minute bias deposition, (c) 15 minute bias deposition plus 3 hour unbiased MPCVD.....	90
Figure 4.27 - Raman spectra for diamond films grown by MPCVD with (a) diamond scratching and (b) ion-assisted pretreatment.....	91
Figure 4.28 - Si(2p) high-resolution angle-resolved XPS scans.....	94
Figure 4.29 - C(1s) high-resolution angle-resolved XPS scans.....	94
Figure 4.30 - Schematic of substrate surface for XPS model. ....	96
Figure 4.31 - Experiment (open data points with dashed line) and analytical model data (solid lines) for SiC/SiO <sub>2</sub> , Si, and C for uniform overlayers of carbon and oxycarbide on the silicon substrate.....	97
Figure 4.32 - Experiment (open data points with dashed line) and analytical model data (solid lines) for SiC/SiO <sub>2</sub> , Si, and C for optically thick carbon clusters on a uniform oxycarbide on the silicon substrate.....	99
Figure 4.33 - Experiment (data points with dashed lines) and analytical model data (solid lines) for SiC, Si, and C for carbon clusters on a silicon oxycarbide overlayer on the silicon substrate. ....	100
Figure 4.34 - XPS survey scan for a carbon film deposited by ion-assisted pretreatment for 1 hour.....	102
Figure 4.35 - Symmetric x-ray synchrotron diffraction scans for a bias-deposited carbon film.....	103
Figure 4.36 - Symmetric x-ray synchrotron diffraction scan of bias-deposited carbon.....	106
Figure 4.37 - Dark field TEM image showing diamond nuclei (bright specks) in bias-deposited carbon film. ....	108
Figure 5.1 - Free energy for nuclei as a function of the radius. ....	114
Figure 5.2 - Relative abundance of ions in mass spectrometer due to electron impact ionization at 70 eV.....	117
Figure 5.3 - Maxwellian electron energy distribution for electrons with an average energy of 2 eV.....	119
Figure 5.4 - Schematic of sheath region under bias conditions.....	127
Figure 5.5 - Ion energy distributions for -275 V bias from the Monte Carlo simulations Iontrans for different neutral/ion temperatures. ....	134
Figure 5.6 - Ion energy distributions from the Monte Carlo simulations Iontrans for a number of applied bias voltages. ....	135



Figure 5.7 - Number of ions versus incident angle for ions with energies ranging from 18 - 46 eV.....	135
Figure 5.8 - Number of ions versus ion energy for both $H_2^+$ and $CH_4^+$ at -275V bias.....	136
Figure 5.9 - Bombardment of surface carbon cluster by an energetic ion to produce a temperature/pressure spike.....	139
Figure 5.10 - Temperature profile for thermal spike as a function of time following impact by a 20 eV atom.....	142
Figure 5.11 - Temperature profile for thermal spike one picosecond after impact of various energy atoms.....	142
Figure 5.12 - Carbon phase diagram showing stability regions for diamond and graphite.....	143
Figure 5.13 - Binding energies of hexagonal and tetrahedral carbon species as a function of the H/C ratio.....	144
Figure 5.14 - Schematic of shallow implantation (subplantation) of an energetic ion into a carbon cluster on the silicon substrate.....	147
Figure 5.14 - Penetration probability of $C^+$ ions into an amorphous carbon target from TRIM calculation.....	148
Figure A.1 - Schematic for XPS overlayer calculations.....	167

## CHAPTER 1 - Introduction

This chapter introduces the subject of diamond thin films and provides the motivation for this thesis as well as other areas of diamond research. Various aspects of diamond thin film deposition including the material properties, synthesis, and applications are discussed. A brief background of previous research in diamond and diamond nucleation is provided to set the stage for the experiments and results of this thesis. The goals of the thesis are detailed to indicate the scope of the research.

### 1.1 Diamond Thin Films - Properties, Synthesis, Applications

Diamond has been studied with increasing excitement during the past 20 years since it was confirmed that this material could be prepared in low pressure environments by chemical vapor deposition (CVD) [1-3]. Diamond is a versatile and important material because of its excellent mechanical, thermal, chemical, optical, and electrical properties. For example, diamond is the hardest known material, it has a room temperature conductivity five times greater than that of copper, it is optically transparent over a large range of wavelengths from the ultraviolet (UV) to the infrared (IR), it is extremely resistance to chemical attack and inert to nearly all chemicals, and it possesses useful electrical/semiconducting properties. These are only a sample of the excellent properties of diamond and a more complete list is given in Table 1.1. Two important points should be made concerning the properties of diamond. First, it is often the combination of two or more material properties which makes diamond so desirable as an engineering material. Second, the properties listed in Table 1.1 are those for natural bulk diamond, an important distinction since diamond thin films deposited by CVD often have properties which differ significantly from the bulk material. Typically, the properties for the thin diamond films are not as impressive as those for natural diamond due to the polycrystalline nature of these films. However, in a few cases, synthetic diamond films can be produced with properties superior to natural diamond; for example, the thermal conductivity of diamond can be increased by limiting contaminants and using isotopically pure  $C^{12}$  gas feeds [4-7].

Property	Value	Comments
Density (g/cm <sup>3</sup> )	3.51	Graphite → 2.25
Refractive index	2.42	@ 0.6 μm
Lattice Parameter (Å)	3.567	Diamond cubic lattice [8]
Bond Length (Å)	1.54	Tetrahedral bonds (sp <sup>3</sup> )
Electrical Resistivity (Ω cm)	> 10 <sup>16</sup>	ρ varies with doping
Scratch Hardness (Moh's scale)	10	Highest hardness
Indentation Hardness (Knoop - kg/mm <sup>2</sup> )	9000	Highest hardness
Modulus of Elasticity (GPa)	1050	Highest modulus
Thermal Conductivity (W/m K)	22	@ 300 K
Specific Heat (J/mol K)	6.2	@ 25 K [9]
Band Gap @ 25°C (eV)	5.4	Indirect band gap [8]
Thermal Expansion Coefficient (°C <sup>-1</sup> )	1 × 10 <sup>-6</sup>	[8]
Electron Mobility (cm <sup>2</sup> /V s)	1800	[10]
Hole Mobility (cm <sup>2</sup> /V s)	1200	[10]
Electron Saturation Velocity (cm/sec)	2.5 × 10 <sup>7</sup>	[11]
Breakdown Field (V/cm)	1 × 10 <sup>7</sup>	[12]
Dielectric Constant	5.7	[13]
Transmissivity	UV→IR	Widest transmissivity
Coefficient of Friction	0.05	Same value as for teflon

Table 1.1 - Properties of natural diamond.

As a result of its superb material properties, diamond could impact a wide range of advanced technologies [3, 8, 12]. For many applications, diamond is the optimum engineering material because it uniquely possesses the best properties in several categories. Its extreme hardness makes diamond an ideal candidate for protective coatings on cutting tools, ball bearings, turbine blades, etc. Diamond is an excellent passive coating for severe environments, i.e. corrosion, radiation, since it is extremely chemically inert. The biocompatibility of carbon coupled with diamond's excellent wear and corrosion properties offer possibilities in protective coatings for biomedical implants. The wide wavelength range over which diamond transmits light efficiently combined with its high

strength make it a logical choice for coatings for optical sensors since both sensor lifetime (due to wear resistance) and signal-to-noise (due to transmissivity) are improved. The high thermal conductivity of diamond make it an excellent heat sink material for high power laser diode and other solid state systems where thermal transport is a limiting factor. The heat transfer properties of diamond, combined with its excellent electrical resistivity, allow applications for silicon-on-insulator and multi-chip module technology. The low scattering efficiency of carbon and its high modulus allow very thin x-ray windows to be made which can support large pressure changes for vacuum chambers. Although pure diamond has an extreme resistivity, doped diamond has semiconducting properties which make it attractive for high-frequency and high-power transistors. Diamond also has unique electron emission characteristics including a negative electron affinity for the {111} crystal face. This is only a brief listing of the numerous potential uses for diamond thin films.

In light of the properties and applications for diamond, attempts to produce synthetic diamond date back to the beginning of this century or earlier. Diamond was first synthesized (intentionally) in the laboratories of General Electric Corporation in 1954 using high pressure - high temperature (HTHP) processes which operated in a regime where diamond was the stable phase of carbon. In essence, these processes mimicked the earth's natural process to form diamond by moving into a thermodynamically stable region of the carbon phase diagram. However, Russian researchers in the mid-1970's discovered that diamond could also be grown at lower pressures by chemical vapor deposition in a pressure and temperature regime where diamond is metastable [14]. Since that discovery, diamond has been grown in low pressure environments by a variety of methods including, but not limited to, hot filament chemical vapor deposition (HFCVD), microwave plasma chemical vapor deposition (MPCVD), dc arc-jets, combustion torches, electron cyclotron resonance (ECR) MPCVD, oxyacetylene torches, flat plate burners, laser-excitation methods, and sequential exposure to sputtered carbon and atomic hydrogen sources. There is considerable literature detailing and reviewing the various methods for diamond film synthesis [1-3].

From a simplified point of view, the critical requirement for all diamond deposition techniques is the coupling of energy to a carbon/hydrogen mixture to produce a complex chemical environment which contains the proper precursors for diamond deposition. There has been extensive discussion and research into the exact nature of the precursors for diamond deposition and the growth mechanisms which lead to the formation of diamond thin films. Although significant experimental evidence exists for the

methyl radical as the diamond growth precursor, this has not been unambiguously proven and research in this area continues [15-20]. It is known, however, that a significant excess of atomic hydrogen with respect to the carbonaceous growth species is required to grow high-quality diamond films. There are various models which attempt to explain the need for such copious amounts of atomic hydrogen. There has been significantly less research attention given to the nucleation of diamond thin films, a process critical for the realization of diamond in nearly all technological applications.

Despite the potential applications for diamond and the progress which has been made in this field over the past few decades, the use of diamond is still not widespread in technology. Deposition limitations still prevent most diamond applications from being fully realized. These problems include high deposition temperatures, slow growth rates, doping problems, shaping and machining difficulties, production costs, and nucleation problems. Each of these difficulties represents a complex problem which could form the basis for a doctoral thesis. This thesis focuses on the last of the problems, nucleation, which severely limits the use of diamond thin films.

## 1.2 Nucleation of Diamond

Nucleation is critical in diamond research since it limits many of the potential applications for this material. As mentioned, the superb properties of diamond detailed in the previous section generally apply only to single crystal diamond. These properties are usually degraded for the polycrystalline films which are grown by the current low pressure CVD processes. Nucleation controls many aspects of the morphology of diamond thin films including grain size, surface roughness, texturing, minimum full film thickness, and interface structure. In turn, the morphology and structure of diamond thin films directly impact the properties of the film, and therefore, potential applications. For example, low nucleation densities prevent deposition of continuous diamond films less than ~100 nm because diamond nucleates by a 3-dimensional island mechanism and the coalescence of the nuclei leads to film formation. Associated with this problem is that of relatively large surface roughness which results when low-density nuclei grow to sizes greater than a micron before coalescing into a full film. Surface roughness can affect optical and tribological properties of diamond thin films. Furthermore, the grain boundaries in such polycrystalline films strongly affect both the electrical and thermal conduction properties, typically in an undesirable way. Diamond nucleation also impacts the interface structure of the deposited films. The full impact of the interface structure is

unknown, but is likely to be critical for the adhesion and electrical properties of these films. The fact that diamond nucleation results in polycrystalline rather than heteroepitaxial films has the largest impact on active electrical devices which require high quality single crystal films for their operation.

Diamond nucleates extremely poorly on nearly all heterogeneous substrates including silicon (Si) which was used as the substrate for nearly all of the experiments in this thesis. Nucleation of diamond has been attempted on a variety of substrates including metals, semiconductors, oxides, and various carbon materials; poor nucleation has resulted for all substrates without specific pretreatments which are described in future sections of this thesis. Cubic boron nitride (c-BN) is perhaps the only material which shows some promise for nucleation of diamond, but this material is as difficult to deposit as diamond itself [21]. Typically, the nucleation density for diamond ranges from  $10^3$  -  $10^5$   $\text{cm}^{-2}$  for pristine silicon and polished refractory metals to the maximum values of  $10^8$   $\text{cm}^{-2}$  for graphite and c-BN.

Nucleation density vs. crystallite size is plotted in Figure 1.1 for an idealized diamond film in which the growing nuclei are assumed to be cubic in shape and have just coalesced to form a continuous thin film.

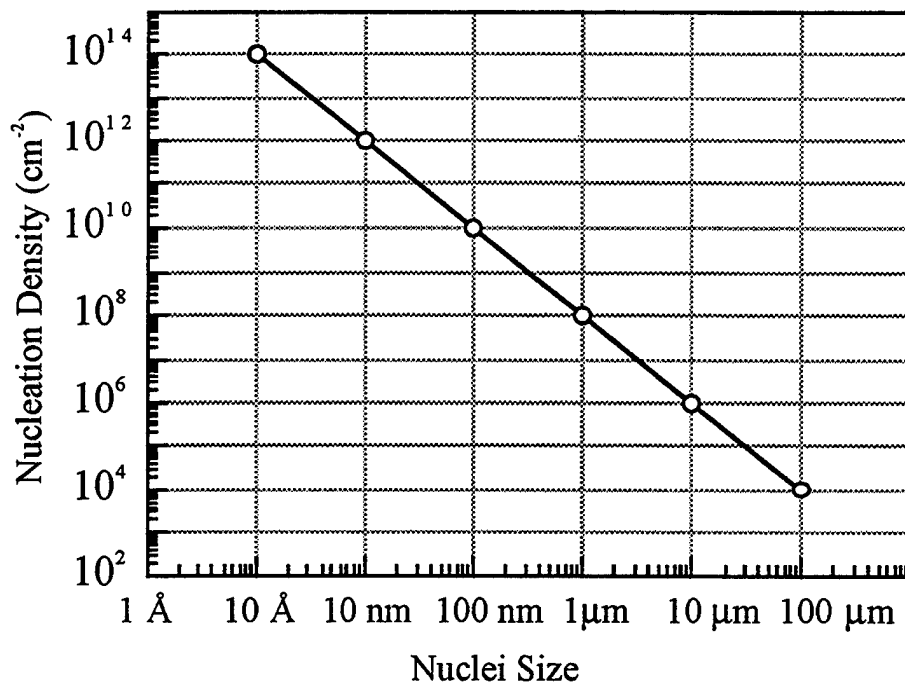


Figure 1.1 - Nucleation density vs. particle size for a single layer film composed of cubic nuclei.

Although this graph only approximates the true situation, it gives an order of magnitude estimate for nucleation density/grain sizes at various film thicknesses. At a nucleation density of  $10^8 \text{ cm}^{-2}$ , a crystallite size of approximately  $1 \mu\text{m}$  is required for a complete film. The nuclei size decreases to  $100 \text{ nm}$  at levels of  $10^{10} \text{ cm}^{-2}$ . At nucleation levels of  $10^4 \text{ cm}^{-2}$  which are typical for substrates with no pretreatment, the crystal size for completion of a layer of diamond is approximately  $100 \mu\text{m}$ . Not only is the deposition time for such a film unacceptable, significantly thinner complete films are required for most diamond thin films applications.

Research has demonstrated that surface carbon plays an important, yet undetermined, role in the diamond nucleation process. Nucleation enhancement attributed to surface carbon has been observed and studied by many researchers. As mentioned, without surface pretreatment the nucleation of diamond on heterogeneous substrates is extremely poor. Limited nucleation enhancement to densities less than  $10^8 \text{ cm}^{-2}$  using carbon sources as varied as vacuum pump oil, evaporated carbon, fingerprints, and microscopic carbon fibers has been reported on silicon [22, 23]. Diamond-like carbon (DLC), amorphous carbon, graphite, and glassy carbon films have also been investigated for enhancement of diamond nucleation [24-27]. However, some of these experimental studies involved surface carbon pretreatments which were applied to diamond-scratched substrates; the two effects cannot easily be separated in this case. Moreover, the results in most of these studies were neither uniform nor reproducible. Diamond nucleation on graphite is enhanced slightly relative to other substrates, but is still quite poor and generally unacceptable. In all of these nucleation studies, the role which surface carbon plays is poorly understood. The experimental evidence suggests a critical form of carbon required on the surface for nucleation enhancement, however, the configuration of this carbon and its formation mechanism are not known. Other studies have suggested that carbides [28-31] and surface topography [32, 33] play a role in nucleation of diamond.

Various schemes have been developed to overcome the problems associated with the poor nucleation of diamond. In the past, the most common nucleation pretreatment involved processes in which the substrate was seeded with diamond powder. Direct scratching with diamond powders or ultrasonic agitation in diamond slurries were the main methods by which the diamond was seeded on the substrate. The mechanism of nucleation for these methods was determined recently after many years of controversy. Initially, researchers postulated that diamond nucleation was aided by the scratches left behind by the scratching process. High energy surface and other morphological arguments were invoked to explain the enhanced nucleation [32]. Although scratches and topography on the substrate surface do play a role in diamond nucleation which is not fully

understood, Iijima, *et al.*, showed very convincingly that diamond seeding was the dominant process for diamond scratching or ultrasonic agitation pretreatments [34, 35]. Therefore, diamond scratching or abrasion techniques do not provide critical insights into nucleation mechanisms since diamond simply grows homoepitaxially on residual microscopic diamond seeds from the various pretreatments. Although abrasive/seeding pretreatments are suitable for many applications, many more applications do not allow this rather crude and harsh mechanical means of pretreatment. For examples, diamond optical coatings and semiconductor thin films cannot tolerate scratching of the substrate surface. In addition, the nucleation density of diamond cannot be well controlled using these techniques which are limited by the size of the diamond powder and the ability to uniformly and reproducibly distribute the seed particles. Most importantly, since growth occurs homoepitaxially for these pretreatments, studies involving seeding do not shed any light on the process by which diamond nucleates heterogeneously; therefore, little basic understanding of the nucleation process is gained for controlling and making improvements to this process.

Nucleation enhancement to densities significantly greater than that for diamond scratching/abrasion techniques has been observed by several groups without diamond seeding [36-39] using an applied negative bias on the substrate. This process, termed bias-enhanced nucleation (BEN) by several research groups in the late 1980's in both the US and Japan [36-38], overcomes many of the problems of nucleation of diamond. BEN involves the application of a negative bias to the substrate during the initial stages of deposition in an MPCVD system. This *in-situ* pretreatment enhances the nucleation of diamond by several orders of magnitude compared to scratching/abrasion techniques. Reproducible nucleation densities in the range of  $10^{10}$  -  $10^{11}$   $\text{cm}^{-2}$  have been reported using BEN on pristine silicon [36-38, 40]. The nucleation density have also been shown to be somewhat controllable using the bias pretreatment time. Research has suggested that a critical current density, critical bias voltage, and critical carbon concentration may be required for enhancement. Perhaps more importantly, this technique shows potential for the heteroepitaxy of diamond [41-43]. Careful deposition of thick diamond films by MPCVD following BEN pretreatments has produced very smooth diamond films containing only low angle grain boundaries on the upper surface and crystallographic registry of the diamond to underlying silicon or silicon carbide substrates. However, although this process is both effective and reproducible, the critical parameters are not well understood and few explanations have been offered regarding the atomistic mechanisms which control this process. It is not surprising that the bombardment of the substrate under bias conditions leads to significantly different results than without these



energetic particles. Ion bombardment assisted deposition (IBAD) has been used extensively in thin film deposition technology to modify the surface or develop unique materials properties [44-47].

### **1.3 Scope and Approach of this Thesis**

Although significant advances in diamond thin film technology have been made in the past decade, there are still many unanswered questions. This lack of understanding limits the use of diamond films in many applications today. Many of these questions involve the nucleation stage of diamond film growth. Since diamond film properties depend critically on nucleation, it is important to study this phenomenon. The inherent difficulties in diamond nucleation are probed in this thesis which focuses on understanding the physical processes which control the techniques used for nucleation enhancement.

Following this introductory chapter, a discussion of the experimental considerations for the nucleation and deposition of diamond by three different techniques is provided in Chapter 2. The characterization techniques for analysis of diamond, and more generally, carbon thin films are then discussed in Chapter 3. The analytical techniques used in this thesis are reviewed and the relevant considerations for the specific analysis of diamond and carbon materials are discussed. Chapter 4 is a description of the experimental results and observations. Nucleation on untreated, carbon-pretreated, and diamond-scratched substrates is discussed briefly, followed by a detailed discussion of the ion-assisted nucleation process. The main issues in this chapter focus on the nature of the ion-assisted process and the material it deposits. In Chapter 5, the experimental process and characterization results are used to model various aspects of the nucleation process. Calculations, simulations, and modeling help to explain the experimental observations in terms of a nucleation mechanism under bias conditions. The thesis results are summarized in Chapter 6.

### **1.4 References**

1. J. Angus and C. Hayman, *Science*, **241**, 913 (1988).
2. W. Yarbrough and R. Messier, *Science*, **247**, 668 (1990).

3. P. Bachmann and R. Messier, *Chemical and Engineering News*, **May 15**, 24 (1989).
4. T. R. Anthony, J. L. Fleischer, J. R. Olson, and D. G. Cahill, *J. Appl. Phys.*, **69**, 12 (1991).
5. W. F. Banholzer and T. R. Anthony, *Thin Solid Films*, **212**, 1 (1992).
6. A. Tokmakoff, W. F. Banholzer, and M. D. Fayer, *Applied Physics A*, **1**, 87 (1993).
7. T. D. Ositinskaya, A. P. Podoba, and S. V. Shmegeera, *Diamond Rel. Mater.*, **2**, 1500 (1993).
8. M. Ohring, *The Materials Science of Thin Films*, Academic Press, Inc., Boston (1992).
9. *Handbook of Chemistry and Physics*, The Chemical Rubber Company, Cleveland (1970).
10. S. M. Sze, *Physics of Semiconductor Devices*, John Wiley and Sons, New York (1981).
11. H. Shiomi, Ph. D. Thesis - *Characterization of Diamond Films and their Application for Electrical Devices*, Stanford University (1993).
12. K. V. Ravi, in *Synthetic Diamond: Emerging CVD Science and Technology*, ed. K. E. Spear and J. P. Dismukes, John Wiley and Sons, New York (1994).
13. J. Fontanella, R. Johnston, J. Colwell, and C. Andeen, *Applied Optics*, **16**, 2949 (1977).
14. B. V. Derjaguin and D. V. Fedeseev, *Scientific American*, **233**, 102 (1975).
15. S. J. Harris, A. M. Weiner, and T. A. Perry, *Appl. Phys. Lett.*, **53**, 1605 (1988).
16. S. J. Harris and L. R. Martin, *J. Mater. Res.*, **5**, 2313 (1990).
17. S. J. Harris, *Appl. Phys. Lett.*, **56**, 2298 (1990).
18. S. J. Harris, D. N. Belton, and R. J. Blint, *J. Appl. Phys.*, **70**, 2654 (1991).
19. C. E. Johnson, W. A. Weimer, and F. M. Cerio, *J. Mater. Res.*, **7**, 1427 (1992).
20. M. Frenklach and K. E. Spear, *J. Mater. Res.*, **3**, 133 (1988).
21. W. A. Yarbrough, *Journal of Vacuum Science & Technology A*, **9**, 1145 (1991).
22. A. Morrish and P. Perhsson, *Appl. Phys. Lett.*, **59**, 417-419 (1991).

23. P. E. Pehrsson, J. Glesener, and A. Morrish, *Thin Solid Films*, **212**, 81 (1992).
24. K. V. Ravi and C. A. Koch, *Appl. Phys. Lett.*, **57**, 348 (1990).
25. T. Hartnett, R. Miller, D. Montanari, C. Willingham, and R. Tustison, *J. Vac. Sci. Technol. A*, **8**, 2129 (1990).
26. M. Terranova, R. Polini, V. Sessa, M. Braglia, and G. Cocito, *Diamond Rel. Mater.*, **1**, 969 (1992).
27. J. Angus, *et al.*, in *Proceedings of the 2nd International Symposium on Diamond Materials*, ed. A. J. Purdes, The Electrochemical Society, vol. 91-9, 125 (1991).
28. S. D. Wolter, J. T. Glass, and B. R. Stoner, *J. Appl. Phys.*, **77**, 5119 (1995).
29. P. A. Dennig, Ph. D. Thesis - *Fundamental Studies of the Nucleation of Diamond Thin Films*, Stanford University (1995).
30. R. Haubner and B. Lux, *Diamond Films and Technology*, **3**, 209 (1994).
31. P. Joffreau, R. Haubner, and B. Lux, *International Journal of Refractory and Hard Metals*, **7**, 186 (1988).
32. P. Dennig and D. Stevenson, *Appl. Phys. Lett.*, **59**, 1562 (1991).
33. P. Dennig, H. Shiomi, D. Stevenson, and N. Johnson, *Thin Solid Films*, **212**, 63 (1992).
34. S. Iijima, Y. Aikawa, and K. Baba, *Appl. Phys. Lett.*, **57**, 2646 (1990).
35. S. Iijima, Y. Aikawa, and K. Baba, *J. Mater. Res.*, **6**, 1491 (1991).
36. S. Yugo, T. Kanai, T. Kimura, and T. Muto, *Appl. Phys. Lett.*, **58**, 1036 (1991).
37. B. R. Stoner, B. E. Williams, S. D. Wolter, K. Nishimura, and J. T. Glass, *J. Mater. Res.*, **7**, 257 (1992).
38. B. R. Stoner, G.-H. M. Ma, S. D. Wolter, and J. T. Glass, *Phys. Rev. B*, **45**, 11067 (1992).
39. R. J. Meilunas, R. P. Chang, S. Liu, and M. Kappes, *Appl. Phys. Lett.*, **59**, 3461 (1991).
40. S. Yugo, T. Kimura, and T. Kanai, *Diamond Rel. Mater.*, **2**, 328 (1992).

41. B. R. Stoner, *et al.*, *Diamond Rel. Mater.*, **2**, 142 (1993).
42. D. K. Milne, *et al.*, *Diamond Rel. Mater.*, **4**, 394 (1995).
43. X. Jiang, *et al.*, *Diamond Rel. Mater.*, **2**, 407 (1992).
44. H. F. Winters, W. Eckstein, and H. J. Coufal, in *Proceedings of the Photons and Low Energy Particles in Surface Processing Symposium*, ed. C. Ashby, J. H. Brannon, and S. W. Pang, Materials Research Society, vol. 236, 273 (1992).
45. J. M. E. Harper, J. J. Cuomo, R. J. Gambino, and H. R. Kaufman, in *Ion Bombardment Modification of Surfaces: Fundamentals and Applications*, ed. O. Auciello and R. Kelly, Elsevier, Amsterdam (1987).
46. J. E. Greene, A. Rockett, and J.-E. Sundgren, in *Proceedings of the Photon, Beam, and Plasma Stimulated Chemical Processes at Surfaces Symposium*, ed. V. M. Donnelly, I. P. Herman, and M. Hirose, Materials Research Society, vol. 74, 39 (1987).
47. B. W. Dodson, in *Proceedings of the Proceedings of Processing and Characterization of Materials Using Ion Beams Symposium*, ed. L. E. Rehn, J. Greene, and F. A. Smidt, Materials Research Society, vol. 128, 137 (1989).

## CHAPTER 2 - Experimental Considerations

Multiple diamond deposition techniques were used in the research of this thesis. While a detailed description of each of these techniques is not the goal of this chapter, it is important to understand the capabilities and limitations of the different deposition processes. The similarities and differences among the methods are important considerations when analyzing and comparing the results obtained in each. In addition, associated with these deposition techniques are several experimental issues which affect the experiments and their interpretation.

As mentioned in Chapter 1, diamond has been deposited by a wide variety of techniques [1-3]. Most of these techniques differ mainly in the manner by which energy is coupled into the carbon-containing gas to produce the chemical species required for diamond deposition. This is not an insignificant point since these different processes lead to deposition condition differences in gas pressure, reactive species concentrations, ion/neutral species fluxes, heat flux, and the mode of reactive species transfer to the surface (diffusion and/or convection). The fact that diamond can be deposited by so many different techniques infers indirectly that the mechanism for growth is similar in all these processes.

Three different diamond deposition techniques were used in the research of this thesis to probe the nucleation and early growth stages of diamond thin film deposition: HFCVD, MPCVD, and Sequential Deposition. Each of these deposition systems is shown schematically along with a brief discussion of relevant aspects of each system and the associated experimental parameters. A detailed description of each technique is beyond the scope of this thesis and can be found in the literature.

### 2.1 Hot Filament Chemical Vapor Deposition (HFCVD)

Hot filament chemical vapor deposition (HFCVD) is the simplest diamond deposition method from an equipment requirement perspective. In this method, the hydrogen-rich carbon containing feed gas (typically  $\text{CH}_4/\text{H}_2$ ) is activated thermally by a refractory metal filament, such as tantalum or tungsten, heated above  $2000^\circ\text{C}$ . The

resulting gas species including atomic hydrogen and various carbonaceous radicals and molecules are transported to the nearby substrate mainly through diffusion; convective transport plays a relatively minor role for the gas flow rates usually used [4]. At elevated substrate temperatures (600 - 1000°C), diamond is deposited on substrates that have been pretreated to enhance nucleation. Numerous articles in the literature detail the various aspects of diamond deposition by the HFCVD method [4-6].

The HFCVD system used for diamond growth and nucleation experiments in this thesis is shown schematically in Figure 2.1. It consisted of a 20 mil (0.020 inch) tantalum wire coiled into a filament and located approximately 5 - 10 mm from the substrate. Tantalum was chosen over tungsten, another common filament material, since its lower recrystallization temperature allows easy shaping of the filament at room temperature.

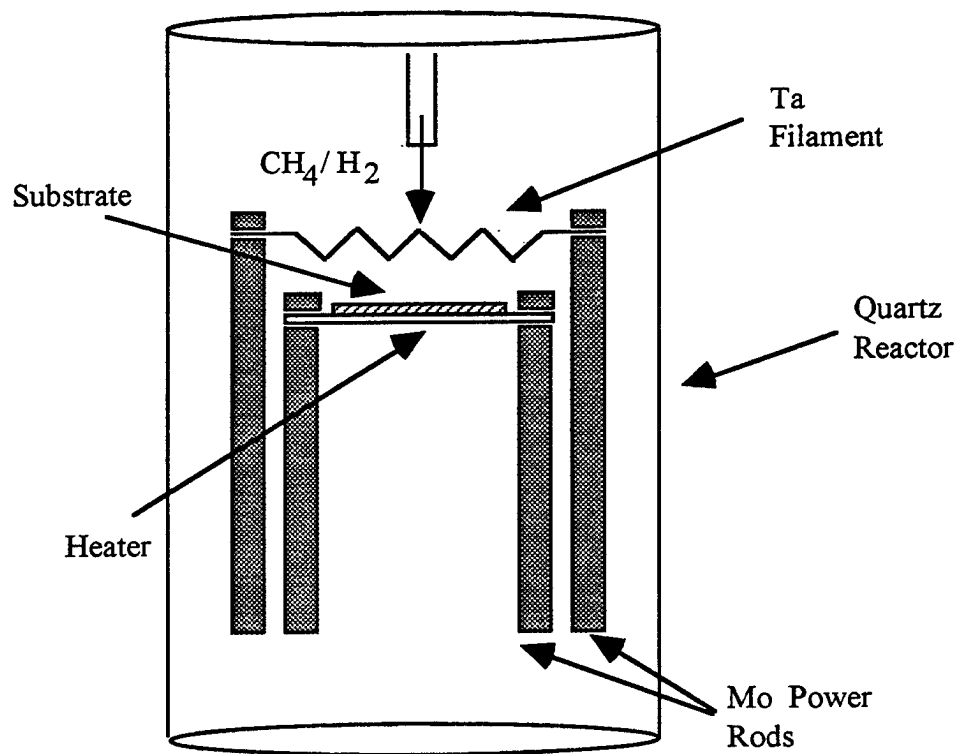


Figure 2.1 - HFCVD diamond reactor schematic.

New filaments were "conditioned" for deposition by a rapid heating ( $\sim 1$  minute) in rough vacuum ( $\sim 20$  mtorr) to  $\sim 2000^\circ\text{C}$  to release stress and remove contaminants, followed by a carburization period of 1 - 2 hours in 1%  $\text{CH}_4/\text{H}_2$  mixtures at  $\sim 2000^\circ\text{C}$ . Carburization changed the filaments from a silver to gold color and the carburized filaments performed

better and produced more reproducible results in this system. The substrate was mounted on a resistively-heated molybdenum substrate assembly in a 2" quartz tube as shown in figure 2.1. The system was pumped by a mechanical pump which reached a base pressure of ~20 mtorr. A standard four-lead feedthrough provided power into the reactor for both the filament and heater by vacuum connection to 0.25 inch molybdenum rods on which the filament and substrate heater were mounted. The tantalum filament was heated to 2000 °C for deposition.

Biasing capability in this system was accomplished rather easily since the filament and substrate were mounted on an electrically isolated feedthrough. A negative substrate bias was applied by grounding the filament to the reactor and connecting the negative lead of the bias power supply to the substrate. Application of the bias resulted in the formation of a violet glow discharge between the filament and the substrate. Quartz tubes were placed over the substrate power rods to minimize glow discharge formation away from the substrate region.

Typical HFCVD diamond growth conditions are shown in Figure 2.1. Diamond film growth rates under these conditions were ~0.5  $\mu\text{m}/\text{hour}$  on silicon substrates pretreated by hand abrasion with 4 - 6  $\mu\text{m}$  diamond powder. Such conditions allow the deposition of highly faceted films with good quality as determined from Raman spectroscopy as will be shown in later sections of this thesis.

Gas Composition	0.5 - 1.0% CH <sub>4</sub> in H <sub>2</sub>
Gas Flow Rate	~ 200 cm <sup>3</sup> /min (sccm)
Filament Temperature	~ 2000 °C
Substrate to Filament Distance	5 - 8 mm
Substrate Temperature	700 - 900 °C
Pressure	20 - 30 torr

Table 2.1 - Typical experimental conditions for HFCVD.

Despite the simplicity of the HFCVD system and its ease of operation, there are several disadvantages in this type of reactor. One drawback for the HFCVD system is the potential for metallic contamination from the filament. At filament temperatures less than 1800 °C, the level of atomic hydrogen formation is insufficient for good diamond growth. But at the higher filament temperatures which produce sufficient atomic

hydrogen, metallic contamination in the films rises due to evaporation of the filament. However, no significant metallic filament contamination was typically observed in the HFCVD diamond films deposited in this system as evidenced by x-ray photoelectron spectroscopy (XPS) analyses which indicated the presence of only carbon with slight oxygen contamination due to surface adsorption of water vapor. This does not mean that no metallic impurities exist in these films, just that the level of metallic contamination is below the detection limit of the XPS system ( $\sim 0.1\%$ ). The HFCVD system used for this research was also limited in terms of substrate size. Due to the geometry of the reactor, substrates larger than 10 mm x 30 mm could not be used. Furthermore, given the geometry of the filament size and shape with respect to the substrate, non-uniform film profiles were deposited on the substrate. These problems, however, are not inherent to HFCVD systems which can, in general, be scaled with the addition of more filaments to uniformly coat extremely large substrates.

## **2.2 Microwave Plasma Chemical Vapor Deposition (MPCVD)**

Microwave plasma chemical vapor deposition (MPCVD) is a more complicated method for deposition of diamond both from an equipment and chemical environment perspective. In this method, the feed gas is excited in a plasma ball formed by the interaction of microwave radiation with the gaseous environment. Since the plasma is composed of high energy electrons and somewhat lower energy ions, this deposition technique offers the ability to produce extremely reactive chemical species, often in higher concentrations and at lower temperatures than would be available by thermal methods [7]. However, this higher reactivity leads to a chemical environment which is extremely complex and difficult to fully characterize.

Most of the research included in this thesis utilized the MPCVD system rather than the HFCVD system for the following reasons:

- larger substrate capability (4-inch diameter compared to several centimeters)
- reduced contamination issues (lower leak rate and no metal incorporation)
- improved reproducibility and process control
- more stable substrate bias environment

Drawbacks to MPCVD deposition included a strong coupling of the process parameters such that individual adjustment of parameters was difficult, if not impossible. For



example, the chemical environment in the plasma (electron and ion densities, radical concentrations, etc.) was coupled both to the gas pressure and the microwave power. Although the temperature control was independent of microwave power above  $\sim 400$  °C, it was still affected by plasma conditions.

The MPCVD system used for diamond growth and nucleation experiments in this thesis is shown schematically in Figure 2.2. This system is similar others described in the literature for diamond deposition and substrate bias pretreatments [8-11].

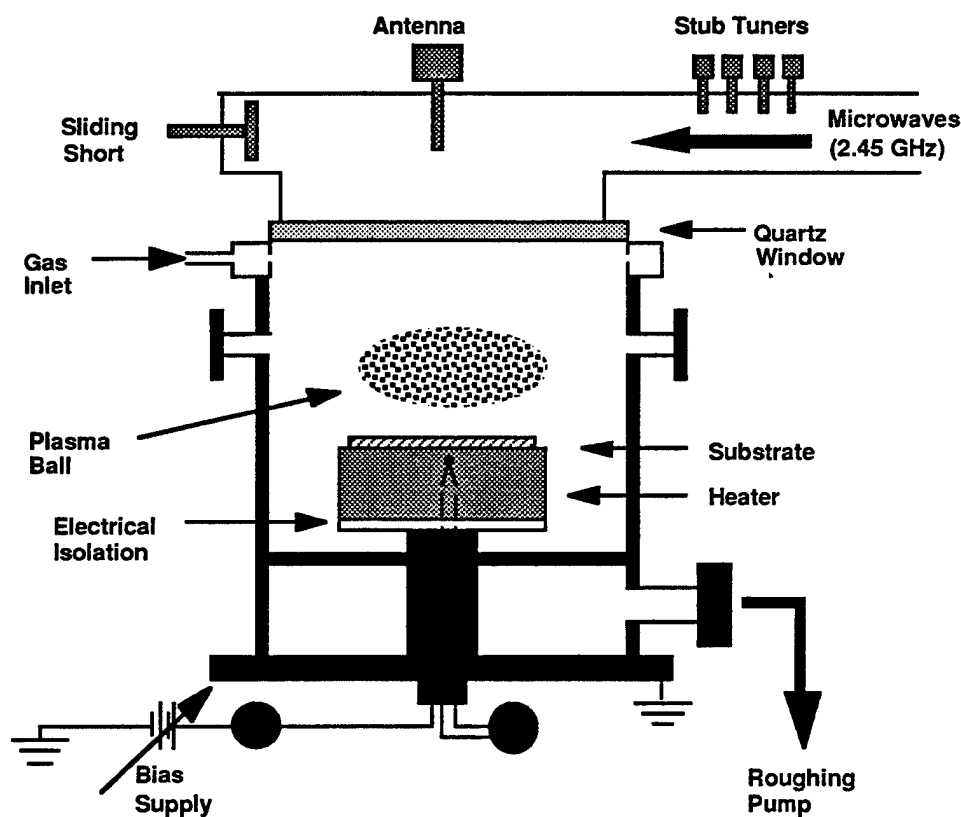


Figure 2.2 - Schematic of MPCVD system used in this thesis.

The system was computer controlled using the experimental control and data collection program *LabView*<sup>TM</sup> (National Instruments) and a *Macintosh*<sup>TM</sup> computer. A baratron gauge with feedback control to a small bypass valve controlled the system pressure. Pumping was done with a mechanical roughing pump which provided an ultimate base pressure of 10 mtorr. Gases were admitted to the chamber through calibrated 100 sccm mass flow controllers. Since these flow controllers are less accurate at low flow rates

below 10 sccm, methane diluted heavily with hydrogen was mixed with pure hydrogen to obtain  $\text{CH}_4/\text{H}_2$  ratios in the 0 - 5 % range. Radiation from a resistively-heated tungsten filament allowed substrate heating to temperatures above those attained with the plasma alone ( $\sim 450^\circ\text{C}$ ). This filament was located in an enclosed molybdenum heater assembly, the top of which served as the substrate susceptor (4-inch diameter). Electrical isolation of the substrate heater assembly with respect to the grounded chamber allowed the application of a negative bias to the substrate. A bias circuit resistance greater than  $1\text{ M}\Omega$  was ensured prior to each experiment so the leakage current was negligible compared to the bias current collected at the substrate. For substrate bias experiments, the power (negative) lead of a 1 kW dc-sputter power supply was connected to the heater assembly while the ground lead was connected to the chamber.

Electrical isolation of the heater assembly from the rest of the system for biasing purposes was one of the most difficult equipment issues faced for this process for several reasons. First, since the system was typically operated at  $800^\circ\text{C}$  it was difficult to find a material with both a good electrical resistance and adequate thermal shock resistance to provide electrical isolation at this temperature. Second, conductive carbon (soot) deposited readily on nearly all parts of the heater assembly at elevated temperatures in the  $\text{CH}_4/\text{H}_2$  environment. This led to the repeated formation of a conductive path across the electrical isolation from the heater to ground over time. This problem was eventually circumvented with small ceramic rods upon which the entire heater assembly rested; these ceramic pieces were removed periodically and cleaned to maintain electrical isolation.

Microwave plasma CVD has the added difficulty that the stability of the plasma is critically dependent upon a number of parameters including the pressure, gaseous environment, geometry, etc. The geometry of the MPCVD reactor prevented clear visual observation of the plasma and substrate during deposition, but the substrate was located within several millimeters of the visible boundary of the plasma ball. Unfortunately, these limitations also precluded optical spectroscopic investigation. Additionally, the plasma ball was constrained between the quartz coupling window and substrate in such a way that both of these were immersed in the edge of plasma. This is different from many otherwise similar systems in the literature in which both the coupling window and the substrate are slightly remote from the plasma itself.

The following standard procedure was used for all unbiased MPCVD depositions in this thesis except as noted. Substrates were cleaned (see section 2.5), and loaded into the system which was subsequently pumped down to  $\sim 20$  mtorr over less than two hours prior to deposition. The system was then backfilled with pure  $\text{H}_2$  and plasma ignition was initiated by adjusting the microwave tuning parameters and heater position at  $\sim 6$  torr

pressure, a substrate position of ~25 mm (distance measured from the bottom of the height adjustment rod), a substrate temperature greater than 400 °C, and a microwave power greater than ~200 W. Plasma ignition was extremely difficult, if not impossible, at pressures higher than 12 torr and low temperatures. The plasma power was increased to deposition levels with simultaneous adjustment of the process pressure and tuning parameters to maintain a stable plasma discharge. All depositions were done at positions within several millimeters of each other and a pressure of  $20 \pm 2$  torr. The plasma, pressure, and temperature were stabilized for 10 minutes prior to the addition of CH<sub>4</sub> to the desired CH<sub>4</sub>/H<sub>2</sub> concentration. This exposure of the substrate to the H<sub>2</sub> plasma also removed residual contaminants. For unbiased depositions, the CH<sub>4</sub> was simply added and the deposition was monitored for the desired time. For biased depositions, the system was stabilized following the CH<sub>4</sub> addition for an additional 10 minutes prior to the application of the bias for the desired time. The geometry of the MPCVD reactor prevented clear visual observation of the plasma and substrate, but the substrate was located in close proximity to the edge of the plasma ball. Following the ion-assisted pretreatment, the bias voltage was removed, the CH<sub>4</sub>/H<sub>2</sub> ratio adjusted to diamond growth conditions, and the power typically increased to 800 W for improved deposition. Shutdown consisted of exposure of the substrate to pure H<sub>2</sub> plasma alone for 2 - 5 minutes prior to plasma extinction and cooling in a H<sub>2</sub> environment.

Numerous standard diamond depositions on diamond-scratched Si substrates (to ensure diamond nucleation) were done under various process conditions to confirm high-quality growth in the MPCVD system. Table 2.2 lists experimental conditions which resulted in highly faceted films with raman spectra corresponding to high quality diamond (see Chapters 3 and 4). The typical growth rate for this process as determined by SEM cross-sectional thickness measurements was 0.3 μm/hour which is comparable with those of other researchers.

Additional experimental considerations arose for the ion-assisted pretreatment process. First, 4-inch Si wafers which entirely covered the molybdenum substrate susceptor were used as substrates to reduce the bias instability and process variability which were observed when smaller substrates were used. Since the bias process involves energetic ions which interact with the substrate and heater assembly, the large substrates also minimized contamination concerns due to the exposed molybdenum, diamond, and diamond-like carbon (DLC) surrounding the silicon when small substrates were used. Some of these problems have been observed by Stoner, *et al.*, and have been linked to diamond deposits on the substrate susceptor [12]. Second, due to the instability of the microwave plasma under bias conditions, the microwave power during the ion-assisted

pretreatments was limited to 650 W; higher microwave powers produced secondary glows and unstable discharge problems in the chamber, especially at the quartz coupling window. The process parameters for the ion-assisted pretreatment are listed in Table 2.2 and are slightly different from those optimized for unbiased diamond deposition. A higher CH<sub>4</sub>/H<sub>2</sub> ratio was used in the bias pretreatments since crystalline quality is not as important a factor for the ion-assisted nucleation compared to growth of high quality diamond. Note that optimal ion-assisted nucleation conditions were not good growth conditions; poorer quality films and some etching results from continued growth under biased condition. The bias parameters shown in Table 2.2 and the effects of varying them are discussed in detail in Chapter 4.

Process Parameter	Unbiased	Biased
Microwave Power	800 W	650 W
Gas Composition	1% CH <sub>4</sub> /H <sub>2</sub>	2% CH <sub>4</sub> /H <sub>2</sub>
Pressure	20 torr	20 torr
Substrate Temperature	800 °C	800 °C
Bias Current	----	30 - 100 mA
Bias Voltage	----	- 250 V
Bias Time	----	15 minutes

Table 2.2 - Typical parameters for (a) unbiased MPCVD deposition and (b) ion-assisted MPCVD pretreatments.

The application of a negative substrate bias produced an additional visible glow discharge located between the substrate and the microwave plasma ball. The bias voltage was held constant throughout the experiments, and the bias current typically increased significantly during the bias pretreatment. However, it was difficult to maintain constant process conditions in the bias experiments due to the inherent instability of this process. This phenomenon will be discussed in more detail in later sections. For successful bias pretreatments, a deposition area as large as 2 inches in diameter was visible in the central region of the wafer. No deposition or contamination was observed around the outside edge of the silicon substrate. Bias nucleation research by Stoner, *et al.*, found that nucleation started at the edge and moving inward which is opposite of what was observed in these experiments [12].

## 2.3 Sequential Deposition

Sequential deposition was accomplished using a novel reactor which allowed separation of experimental conditions which are coupled in both the MPCVD and HFCVD reactors. A schematic of this reactor is shown in the figure 2.4.

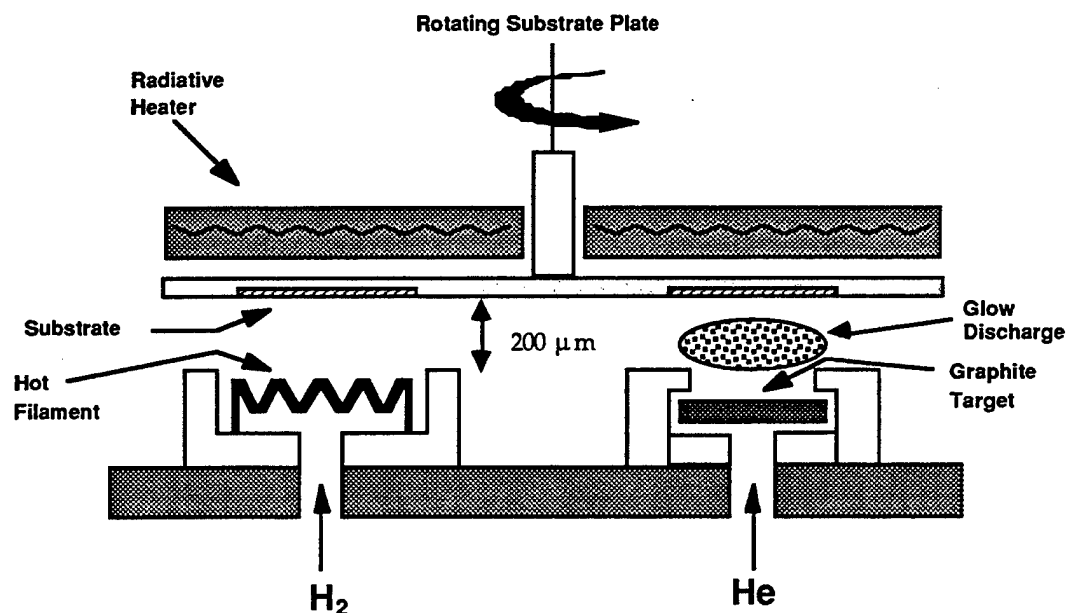


Figure 2.4 - Schematic of sequential deposition reactor for diamond deposition.

Briefly, a heated substrate plate is rotated past chemical sources, or emitters, which have separate and isolated chemical environments. Up to 4 chemical emitters can be used in this system, and the small distance between the emitters and the substrate plate ensures that cross contamination of the chemicals in adjacent emitters is not significant [13]. In the standard deposition mode, two emitters were used and the substrate rotated sequentially over atomic hydrogen ( $H^{\cdot}$ ) and carbon atom ( $C^{\cdot}$ ) sources. The  $H^{\cdot}$  flux was formed by thermal dissociation of  $H_2$  with a heated ( $\sim 2000^{\circ}C$ ) tungsten filament while the  $C^{\cdot}$  flux was created by sputtering carbon off a polycrystalline graphite target (cathode) in a dc-glow discharge of an inert gas such as helium (He) or argon (Ar). Sequential exposure of a scratched Si substrate at  $800^{\circ}C$  to these chemical environments

produced thin diamond films of good quality. Previous research with this novel system has provided insight into the role of atomic hydrogen, carbon, and atomic oxygen fluxes in the mechanism of diamond growth [14-19].

The sequential reactor just described was modified slightly for bias nucleation experiments. The rotating plate was electrically isolated from the rest of the system with a ceramic shaft. A brush contact to the rotating substrate plate was designed to apply a bias voltage to the substrate during a portion or the entire rotation cycle. Periodic application of the bias provided the means to study the effect of ion bombardment by any individual species in this system. Table 2.3 shows typical parameters for the bias pretreatments carried out in the sequential reactor. Unbiased sequential diamond deposition uses similar parameters with the exception of the bias application. The hydrogen emitter power for the bias experiments is slightly lower than for unbiased depositions to prevent the nuclei from being etched off by a high  $H^+$  flux. Also note that the bias time for the sequential experiments is much longer than for the MPCVD bias pretreatment since the cyclic nature of the former process results in approximately an 8-fold duty factor.

Process Parameters	
Hydrogen Emitter Power	250 W
Carbon Emitter Voltage	700 V
Carbon Emitter Gas	Helium
Chamber Pressure	12 torr
Substrate Temperature	800 °C
Bias Current	30 - 50 mA
Bias Voltage	-100 to -150 V
Bias Time	4 hours

Table 2.3 - Typical parameters for biased sequential deposition.

## 2.4 Temperature and Pressure Issues

Since both nucleation and deposition are typically temperature-dependent processes, the ability to measure and control the substrate temperature during

experiments was extremely important. Two methods of temperature measurement were used in the experiments of this thesis: thermocouples and optical pyrometry. Both techniques have limitations and, in general, accurate temperature measurement is extremely difficult. Thermocouple measurements are typically more straightforward than optical pyrometric measurements. Due to the Seebeck effect, when two metals are joined an electrical potential develops between them which can be related to the temperature at the point of dissimilar metal contact. The main problems for this method of temperature measurement are the thermal contact between the thermocouple and the region being investigated, and the stability of the thermocouple metals in the measurement environment. Optical pyrometry is advantageous due to its non-intrusive nature, but this method is problematic mainly due to the uncertainty in the emissivity. Optical pyrometers measure the intensity of the radiation emitter over a small wavelength range and compare this intensity to that expected from a blackbody at elevated temperature. The emissivity corrects for the fact that most materials do not emit radiation perfectly. To accurately measure the temperature using a pyrometer, either the emissivity (for a single wavelength pyrometer) or the slope of the emissivity curve (for a dual wavelength pyrometer) is required. The emissivity varies for materials and is dependent upon a variety of parameters including wavelength, angle of detection, and surface condition. It is extremely difficult to obtain accurate emissivity values, and furthermore, once a film is deposited on the substrate the emissivity changes. Additional concerns arise for plasma environments since radiation is emitted which may be measured by the pyrometer and attributed solely to temperature effects; the pyrometer cannot distinguish between radiation from the plasma and that from the substrate at temperature.

It is also important to note the difference between accuracy and precision when considering temperature measurements. Precise temperature measurements are those which, when repeated over time, consistently produce the same value with small deviations around this value. Accuracy refers to the difference between the true value and that measured. For these studies, precision was more desirable than accuracy since it was easier to recalibrate precise temperature measurements than to control imprecise readings.

Temperatures in the HFCVD system were measured both by thermocouple and pyrometer. These temperatures were consistent since good thermal contact was ensured by the colloidal graphite paste. The small substrate sizes also minimized temperature uniformity problems. Temperatures in the sequential reactor were estimated using the optical pyrometer since thermocouple contact was precluded by the rotating substrate. In this system, an method by which to calibrate the accuracy of the temperature measurements which were precise to  $\pm 25$  °C was not readily available. Substrate

temperature measurements were a larger concern in the MPCVD system for several reasons. First, most of the bias experiments were done in this system. Second, the effect of temperature on nucleation was studied in this system. Finally, because 4-inch substrates were used and heating occurred due to both the substrate heater and plasma ball, temperature non-uniformity across the substrates was expected and observed.

In the MPCVD system, temperatures were measured using a C-type thermocouple (W - 5% Re / W - 26% Re) positioned just below the substrate surface in a hole drilled through the center of the molybdenum susceptor. These measurements were compared to those obtained using a single wavelength optical pyrometer (Minolta Cyclops #152A, 0.8 - 1.1  $\mu\text{m}$  spectral response). Due to the reflective losses of the quartz coupling window through which the optical measurements were taken, emissivities were multiplied by 0.93 to account for the  $\sim 3.5\%$  loss per quartz surface [20]. Literature emissivity values for silicon and molybdenum were approximately 0.6 and 0.4, respectively [21]. The optical pyrometer and thermocouple measurements are plotted against each other in Figure 2.5 for the molybdenum susceptor and a both a silicon and molybdenum substrate without the plasma on to minimize errors in the optical measurement.

Since the thermal contact between the substrates and the heater is not perfect, it was expected that the thermocouple (which measures the temperature of the heater it was in good thermal contact with) would give a higher substrate temperature than that given by the pyrometer. This is observed in Figure 2.5 where, for a given thermocouple reading, the Mo susceptor is approximately 30 - 50  $^{\circ}\text{C}$  hotter than either the Mo or Si substrate as measured by optical pyrometry. In fact, the pyrometer also measured a higher susceptor temperature than the thermocouple which may be due to poor thermal contact between the susceptor and the thermocouple and/or inaccuracies in the emissivity values.

Therefore, although the precision of these measurements was good, the accuracy was a problem. As mentioned previously, this was a tolerable problem since precise measurements allowed the same temperature, although not known accurately, to be maintained from experiment to experiment. The thermocouple was used in these experiments to obtain precise control of the substrate temperature. This measurement was then used to estimate the actual substrate temperature during the deposition. The calibration in Figure 2.5 indicates that the substrate temperature is 30 - 50  $^{\circ}\text{C}$  less than that measured by the thermocouple in the heater. However, recall these measurements were taken without the plasma which, fortunately, will heat the substrate relative to the heater and tend to compensate for the temperature discrepancy. Although the plasma heating of the substrate compared to the heater cannot be accurately measured, simple



energy balance calculations suggest this temperature difference is on the order of the original thermocouple error. Therefore, the thermocouple measurements were reported for substrate temperature measurements and are estimated to be accurate to  $\pm 25$  °C. In terms of temperature uniformity across the substrates, temperature variations were less than  $\pm 10$  °C across the 4-inch heater without the plasma because to the large thermal mass of the molybdenum susceptor and the uniform heating provided by the heater. However, the spatial temperature uniformity was expected to decrease upon interaction with the plasma ball since it occupies only the central 2 inches of the heater; this non-uniformity was not estimated accurately but temperature gradient effects including crystal slip were observed on the Si substrates.

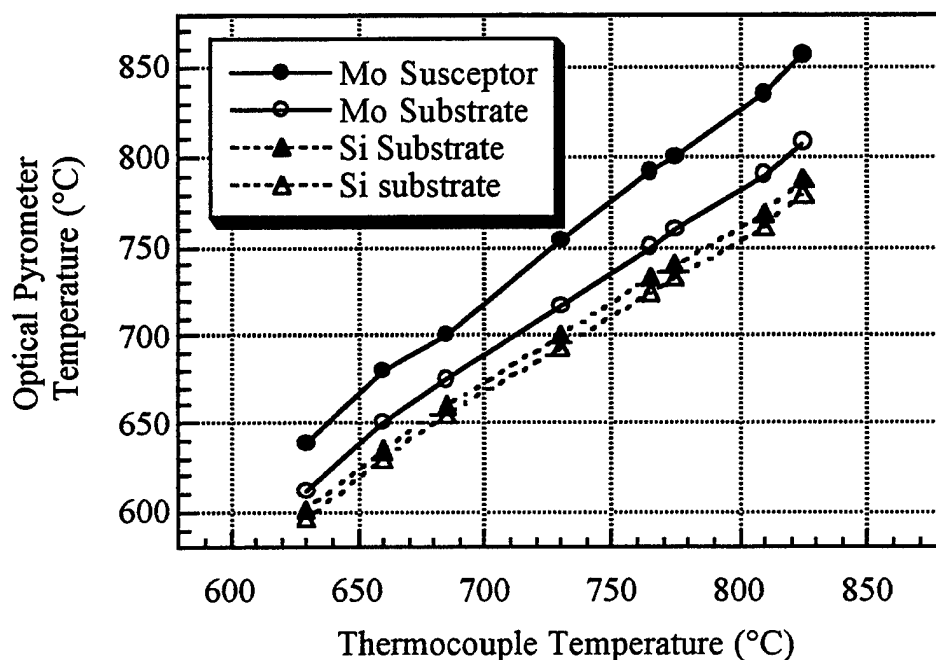


Figure 2.5 - Temperature calibration data for the MPCVD system.

Since all three deposition processes used pressures in the range of 10 - 30 torr, ultra-high vacuum (UHV) conditions were not required. However, the leak rates were considered since the addition of oxygen to the gaseous environment has been shown to affect diamond growth rates and may therefore also play a role in nucleation [22, 23]. In

each of these systems, the air leak rate was insufficient to add oxygen in levels which would significantly affect the results.

## 2.5 Substrates and Substrate Preparation

Silicon (Si) wafers were used as substrates for nearly all of the experiments in this thesis. There were several reasons for this choice. First, silicon is relatively inexpensive and can be obtained in chemically pure, perfect single crystal form. This eliminated many of the concerns regarding the role of contaminants and defects in the nucleation process. Second, strong interest in diamond deposition on silicon wafers for electronic applications makes this substrate an obvious choice. All of the experiments of this thesis used silicon wafers from the same manufacturing batch. These wafers were of "*prime*" quality and were n-type (Sb-doped) Si substrates upon which a thin n-type (P-doped) epitaxial layer was deposited. The resistivity of these wafers was approximately  $0.020 \Omega \cdot \text{cm}$ .

Substrate preparation is generally an issue of critical concern for nucleation studies. Since as-received "*prime*" Si wafers possess extremely clean surfaces, further processing is often more likely to result in a reduced level of cleanliness. The surface state required for the experiments described in this thesis was a Si surface without oxide or other carbonaceous contaminants. More importantly, however, was the ability to obtain a level of surface cleanliness which could be reproduced easily and quickly. Perfectly clean substrates were not required since heteroepitaxy was not possible at this stage of diamond processing. For this reason, the as-received wafers received minimal additional cleaning prior to deposition. Extensive research into ultra-clean semiconductor surfaces has shown that treatment of silicon surfaces with a hydrofluoric acid (HF)/deionized water (DI H<sub>2</sub>O) solution removes the native oxide layer ( $\sim 30 \text{ \AA}$ ) and leaves the surface terminated with hydrogen. Si surfaces produced in this manner have been shown to remain oxide free and hydrogen terminated in atmospheric environments for at least several hours. The wafers used in all experiments were therefore dipped for  $\sim 2$  minutes in a 10:1 solution of HF/DI H<sub>2</sub>O followed by a thorough 5 minute DI H<sub>2</sub>O rinse. These substrates were blown dry with nitrogen and then directly loaded in the MPCVD chamber for processing.

XPS analysis of the surface of the HF-etched Si wafers indicates that only residual amounts ( $<10\%$ ) of carbon and oxygen remain at the surface following this process. These contaminants are hypothesized to result from the adsorption of carbonaceous species and water vapor on the substrate surface. Si-O bonds detected from the XPS chemical shift of

the Si(2p) peak for the as-received wafers due to the native oxide (SiO<sub>2</sub>) disappear upon etching in the HF/H<sub>2</sub>O solution.

## 2.6 References

1. J. Angus and C. Hayman, *Science*, **241**, 913 (1988).
2. W. Yarbrough and R. Messier, *Science*, **247**, 668 (1990).
3. P. Bachmann and R. Messier, *Chemical and Engineering News*, **May 15**, 24 (1989).
4. T. Debroy, K. Tankala, W. A. Yarborough, and R. Messier, *J. Appl. Phys.*, **68**, 2424 (1990).
5. F. Jansen, I. Chen, and M. A. Machonkin, *J. Appl. Phys.*, **66**, 5749 (1989).
6. F. Jansen, M. A. Machonkin, and D. E. Kuhman, *J. Vac. Sci. Technol. A*, **8**, 3785 (1990).
7. J. Musil, *Vacuum*, **36**, 161 (1986).
8. S. Yugo, T. Kanai, T. Kimura, and T. Muto, *Appl. Phys. Lett.*, **58**, 1036 (1991).
9. B. R. Stoner, G.-H. M. Ma, S. D. Wolter, and J. T. Glass, *Phys. Rev. B*, **45**, 11067 (1992).
10. X. Jiang, *et al.*, *Diamond Rel. Mater.*, **2**, 407 (1992).
11. J. Gerber, M. Weiler, O. Sorh, K. Jung, and H. Ehrhardt, *Diamond Rel. Mater.*, **3**, 506 (1994).
12. B. R. Stoner, *et al.*, *Diamond Rel. Mater.*, **2**, 142 (1993).
13. D. S. Olson, Ph. D. Thesis - *The Sequential Deposition of Diamond Thin Films From Carbon and Atomic Hydrogen*, Stanford University (1992).
14. M. A. Kelly, D. S. Olson, S. Kapoor, and S. B. Hagstrom, *Appl. Phys. Lett.*, **60**, 2502 (1992).
15. M. A. Kelly, S. Kapoor, D. S. Olson, and S. B. Hagstrom, in *Proceedings of the Wide Band Gap Semiconductors Symposium*, ed. T. D. Moustakas, J. I. Pankove, and Y. Hamakawa, Materials Research Society, vol. 242, 51 (1992).

16. D. S. Olson, M. A. Kelly, S. Kapoor, and S. B. Hagström, in *Proceedings of the Wide Band Gap Semiconductors Symposium*, ed. T. D. Moustakes, J. I. Pankove, and Y. Hamakawa, Materials Research Society, vol. 242, 43 (1992).
17. D. S. Olson, M. A. Kelly, S. Kapoor, and S. B. Hagström, in *Proceedings of the Novel Forms of Carbon Symposium*, ed. C. L. Renschle, J. J. Pouch, and D. M. Cox, Materials Research Society, vol. 270, 335 (1992).
18. D. S. Olson, M. A. Kelly, S. Kapoor, and S. B. Hagström, *J. Appl. Phys.*, **74**, 5167 (1993).
19. D. S. Olson, M. A. Kelly, S. Kapoor, and S. B. Hagström, *J. Mater. Res.*, **9**, 1546 (1994).
20. Minolta Land Corporation, *personal communication* (1994).
21. *Handbook of Chemistry and Physics*, The Chemical Rubber Company, Cleveland (1970).
22. Y. Liou, A. Inspektor, R. Weimer, D. Knight, and R. Messier, *J. Mater. Res.*, **5**, 2305 (1990).
23. S. Kapoor, Ph. D. Thesis - *Growth of Diamond Films by Cyclic Exposure to Different Chemistries*, Stanford University (1994).

## CHAPTER 3 - Characterization Techniques

To study the nucleation and growth of diamond, multiple characterization techniques were required to probe the chemical composition, the atomic configuration, the film morphology, and the amount of material deposited on the substrate; no single technique could completely determine the nature of the carbon films deposited for the research of this thesis. The analytical techniques which include scanning electron microscopy (SEM), raman spectroscopy, x-ray photoelectron spectroscopy (XPS), x-ray diffraction (XRD), and transmission electron diffraction (TEM)/selected area electron diffraction (SAD) are discussed briefly in this chapter. The basic principles, advantages, and limitations of each of these techniques as is relevant for the study of diamond nucleation and growth are the focus. General discussions and detailed treatises on these techniques are available in the literature referenced in each section of this chapter.

### 3.1 Scanning Electron Microscopy (SEM)

Scanning Electron Microscopy (SEM) is a routine characterization technique for imaging the surface of materials at the microscopic level [1]. In this technique, a narrow beam of relatively high-energy electrons (typically 5 - 25 keV) is rastered across the surface of the specimen under analysis. Interaction of these electrons with the specimen results in the emission of electrons and photons which can be collected and analyzed as the basis for an image. All of the SEM images in this thesis are *secondary electron images* obtained by the collection of secondary electrons which have energies less than ~50 eV. Electrons emitted from the surface with higher energies form the basis of *backscattered images*, however, this technique was not used for this thesis. The contrast mechanism for SEM is the difference between electron emission at various points on the sample. These differences arise for several reasons including the atomic number of the element, the electronic structure of the material, and the surface morphology. A Hitachi S-800 Field Emission SEM was used to obtain most of the SEM images in this thesis.

One potential problem for the analysis of diamond by SEM is the insulating nature of this material. Since the SEM image is based on electrons emitted from the

surface due to interaction with a high-energy electron beam, insulating samples often become charged over time since there is no conductive path to ground to provide charge compensation. Typically, insulating samples are coated with a relatively thin layer of Au or Au-Pd alloy ( $\sim 200$  Å) to minimize charging effects. Charging effects cause problems for analysis of the surface morphology, especially at high magnifications, since charging alters the normal emission of electrons and, thereby, degrades the imaging capability. However, for nearly all of the samples analyzed in this research by SEM, charging was not a serious issue since the imperfect quality of the "diamond" deposited provided sufficient conductivity to minimize charging. In fact, the effects of sample charging in the SEM provided a qualitative means to judge the quality of the deposited material. Furthermore, the differences between the electron emission characteristics of high-quality diamond (insulating) and non-diamond carbon assisted for some of nucleation density analyses since it provided strong contrast between these two forms of carbon on the substrate.

SEM was used in this thesis primarily for analysis of nucleation densities and sizes as well as for investigating the morphology of the films and nuclei deposited. A wide variety of morphologies are observed for carbon and diamond materials. Figure 3.1 shows three of the numerous morphologies observed for carbon films deposited during the research of this thesis. These morphologies range from highly crystalline films in which  $\{100\}$ ,  $\{110\}$ , and  $\{111\}$  facets were readily observed (3.1a) to slightly defective crystalline films with heavy twinning and secondary nucleation (3.1b) to non-crystalline carbon films with what has been referred to as "cauliflower" morphology (3.1c). Although many interesting morphological differences were observed, these are not the focus of this thesis and are not be described in significant detail.

The primary function of the SEM analysis in this thesis was the *ex-situ* determination of nucleation densities. Several issues must be considered when using this technique for nucleation analyses. Many reports in the literature determine nucleation densities for various nucleation pretreatments followed by normal MPCVD growth. Such processes typically produce complete polycrystalline diamond films with thicknesses of a micron or greater. This presents a problem because crystallite counting procedures are extremely difficult for complete films. Moreover, the nucleation density of diamond crystallites at the surface of these films is not necessarily an accurate measure of the original nucleation density due to the coalescence and secondary nucleation which occurs during the growth process. Therefore, whenever possible, deposition conditions were intentionally chosen for the nucleation experiments in this thesis to produce incomplete films of individual, separated nuclei.

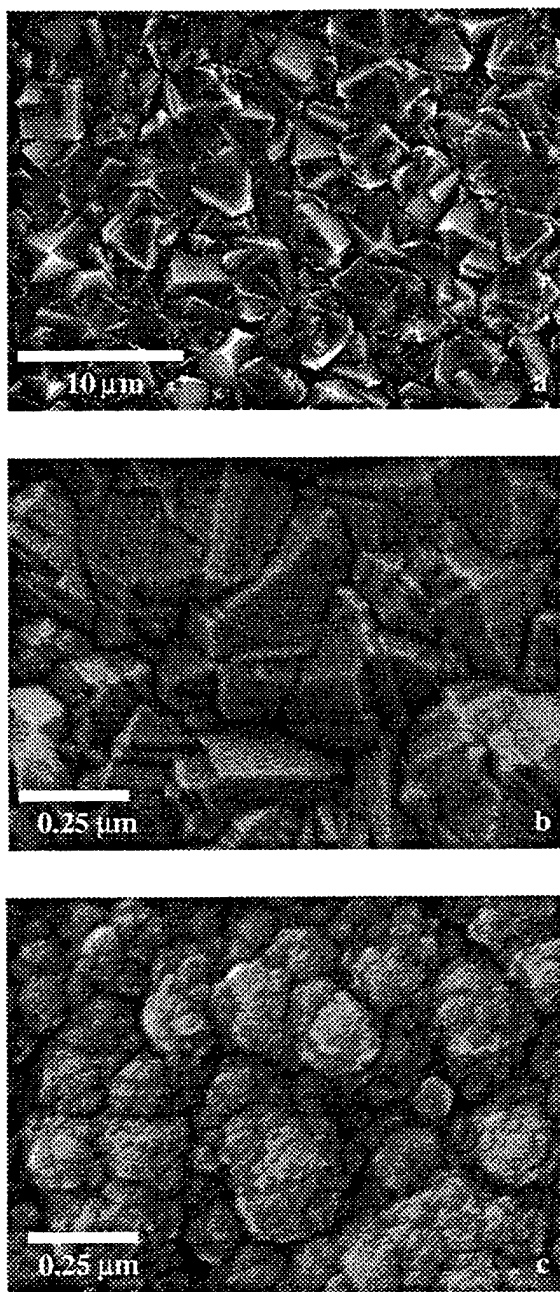


Figure 3.1 - SEM images indicating variations in carbon thin film surface morphologies observed by this technique.

It is also important to realize that SEM analyses do not provide an absolute measure of nucleation density. It is likely that stable carbon nuclei exist at sizes significantly smaller [2] than the resolution of the microscope ( $\sim 100\text{\AA}$ ). Nucleation often results from critical nuclei composed of only a few atoms. Therefore, SEM analysis does not allow study of the actual nucleation event, but rather, the evidence of the nucleation event at a short time after it has taken place. This is an important distinction when considering ramifications of this work. All nucleation events on the substrate were not accounted for in the SEM images and nucleation densities were estimated from clusters which had grown to a resolvable size. It follows that the nucleation densities listed in this research are lower limits, but still useful for relative comparisons.

Statistical issues are also important for nucleation analyses, and often neglected in discussions of diamond nucleation experiments. Several sources of error arise in the nucleation densities reported in this thesis including:

- **Counting errors** - variations in the number of nuclei imaged by the SEM and the number of nuclei actually counted.
- **Spatial uniformity error** - variations in the nucleation density at different sample locations due to spatial nonuniformity on a given sample.
- **Run-to-run error** - variations in the nucleation density among a number of samples deposited under similar conditions.

The counting errors were the smallest of the three as determined by multiple counting of the nuclei in a given SEM image. This type of error was typically less than 5%. Spatial uniformity error as assessed by multiple measurements from different regions of the same sample were typically less than 10%. While the counting error decreased at higher magnification since there were fewer nuclei to count in the image, the spatial uniformity error increased since the sampled region was smaller. Nucleation density tables in this thesis list the statistical mean and standard deviation for the nucleation densities as determined from multiple measurements (typically 4 to 6) on the same sample. Run-to-run variations were the largest source of uncertainty in the nucleation densities reported in this thesis. However, time constraints prevented multiple runs for each experiment. From a limited number of samples run under identical process conditions, the run-to-run variation was estimated to be approximately 15%. These errors are shown by the error bars for the nucleation density plots of this thesis.



## 3.2 Raman Spectroscopy

Raman spectroscopy relies upon the inelastic scattering of light due to interaction with phonon modes of a solid to probe the structure of the material [3]. In the past, this form of spectroscopy has been used mainly by chemists for the analysis of liquids and gases. However, in recent years the technique has gained popularity for the analysis of solid samples and thin films. Raman spectroscopy is a bulk technique since a laser has a significant penetration depth in most materials, as is the case for high quality diamond which is more or less transparent in the wavelength range of interest. For even the thickest films analyzed by raman spectroscopy in this thesis ( $\sim 5 \mu\text{m}$ ), the silicon substrate signal could be observed through the film indicating the transparency of the deposited diamond. This is not the case for graphite which absorbs light strongly relative to diamond; for this reason, the sampling depth is considerably shorter for graphite compared to diamond in this technique.

Diamond has a very strong raman scattering and a peak at much higher shifts than most materials due to the strong bonding of this material. The shortcomings of this technique for analysis of diamond include the lack of surface sensitivity and the quantification problems due to different cross-sections for diamond and other forms of carbon [4-6]. Raman spectra for extremely thin or incomplete films may look deceptively poor due to small amount of diamond and also due to large number of grain boundaries which contain non-diamond carbon material. This point is discussed in detail in Chapter 4. Since raman signal intensities are proportional to the amount of material present, the intensities can be used to estimate the relative amounts of material deposited under different conditions as long as the measurements were obtained under the same spectroscopic settings.

The raman spectra in figure 3.1 are from a natural diamond and a sputtered carbon film from the sequential reactor. The intensities have been scaled for this graph; in reality, the bulk diamond sample has a much stronger intensity than the thin carbon film. Diamond intensities are typically much stronger than for graphite even though the cross-section for graphite is 50 times higher than for diamond [7] since the penetration depth for diamond is large compared to the relatively opaque graphite. Single crystal graphite has a single peak, referred to as the G band, at  $1580 \text{ cm}^{-1}$ . For polycrystalline graphite, a peak at  $1345 \text{ cm}^{-1}$  referred to as the D band, arises due to relaxed selection rules. The D and G bands are characteristic of graphitic and other carbon structures. However, even after significant research in this area, there is no universal agreement that the D/G ratio is a

good measure of the quality of a diamond thin film [8]. Although it is not be discussed in detail, stress also has an affect on the raman spectra.

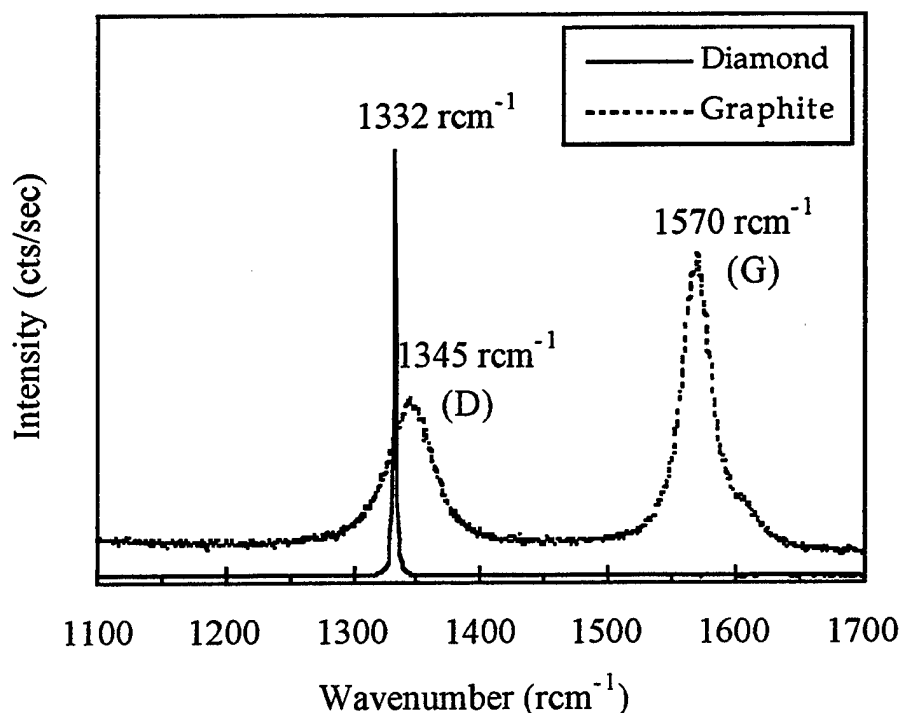


Figure 3.1 - Raman spectra for diamond and polycrystalline graphite.

Figure 3.2 shows raman spectra for a series of films in which the quality of the carbon deposited varies significantly. The lowest spectrum has a diamond-like carbon signature with two broad bands centered approximately at 1340 and 1580 rcm<sup>-1</sup>. The next three spectra show the diamond peak at 1332 rcm<sup>-1</sup>, but still non-diamond bonded carbon present in bands between 1500 and 1600 rcm<sup>-1</sup>. The uppermost spectrum is a good quality diamond film with a strong, narrow diamond peak at 1332 rcm<sup>-1</sup> and little non-diamond carbon background across the rest of the wavelength range. These spectra indicate that a wide range of structures can be differentiated, at least qualitatively, by raman spectroscopy.

An ISA U-1000 Raman Spectrometer with micro-raman analysis capability was used for all of the raman spectra reported. A schematic of the system in the micro-raman configuration is shown in Figure 3.3. This system employs an argon-ion laser operated at

a wavelength of 514.532 nm (green) and a double pass spectrometer with a photomultiplier tube or charge-coupled device (CCD) for detection. Both macro-raman and micro-raman configurations were available, but micro-raman analysis was used almost exclusively due to the ease of obtaining good spectra. Unless otherwise noted, all raman spectra were obtained using the micro-raman configuration, the photomultiplier detector, and the spectroscopic conditions listed in Table 3.1. These conditions were chosen to provide good signal-to-noise for most samples in a reasonable amount of time. Significantly lower laser powers were required for non-diamond carbon films which were quickly damaged or destroyed at the power listed in the table. The raman spectra in this thesis have intensities plotted against the relative wavenumber ( $\text{rcm}^{-1}$ ) which is the reciprocal of the wavelength difference between the emitted radiation and the laser. This is a standard way of representing raman spectra and is useful since the position of the raman peaks by this method are independent of the exciting laser wavelength.

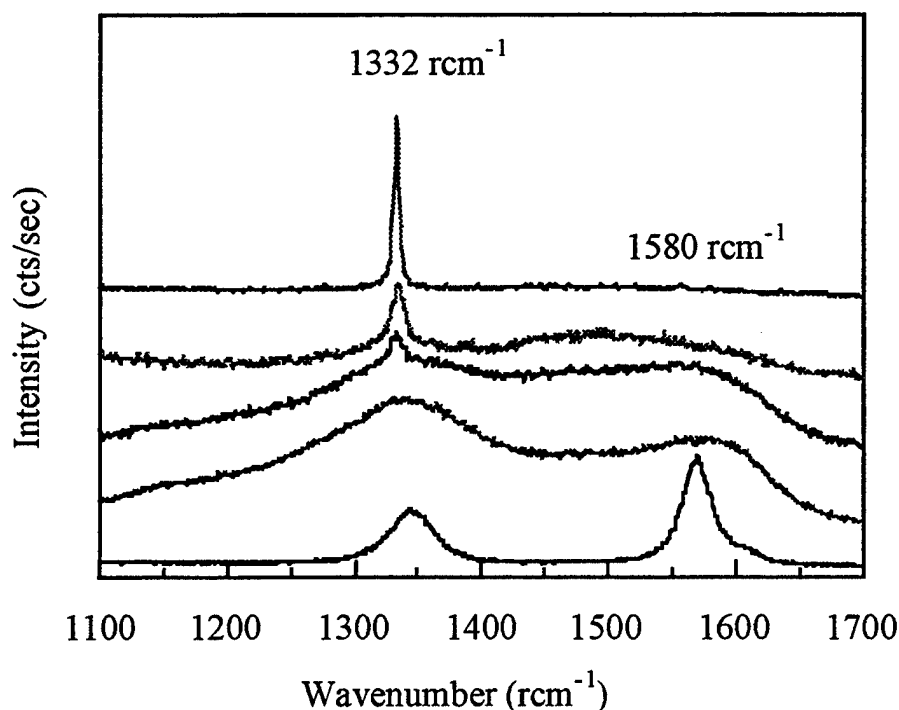


Figure 3.2 - Raman spectra for carbon thin films varying from diamond at the top to polycrystalline diamond at the bottom.

Characterization Parameters	
Laser Power	400 mW (at the source)
Slit widths	200 microns (all 4 slits)
Scan rate	1 $\text{cm}^{-1}$ per second
Integration time	1 second
Microscope objective	80X

Table 3.1 - Typical raman parameters for analysis of diamond films/nuclei.

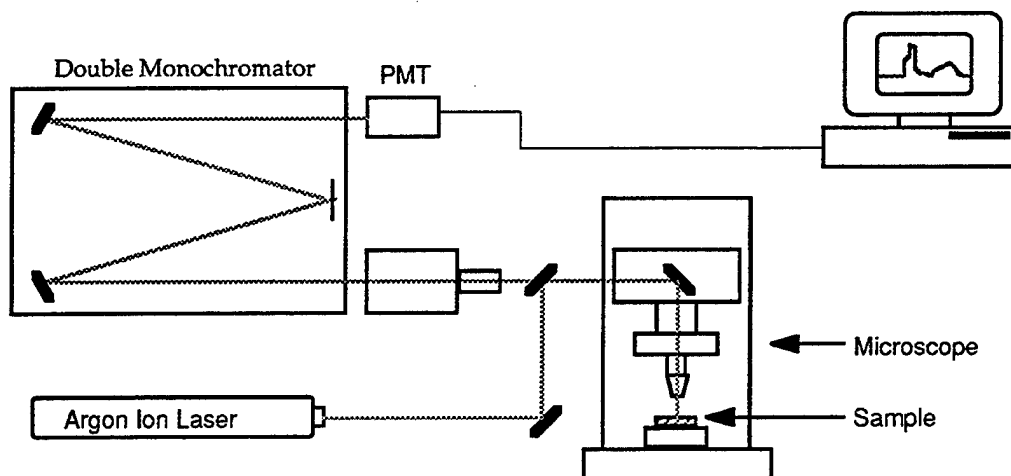


Figure 3.3 - Schematic of the micro-Raman system.

### 3.3 X-Ray Photoelectron Spectroscopy (XPS)

X-ray photoelectron spectroscopy (XPS) is an excellent technique for surface chemical analysis [9]. XPS is based on the emission of electrons from surface atoms due to interaction with x-rays. This form of electromagnetic radiation has an energy greater than the binding energy of the electrons in the atom and therefore can eject the electrons. Electrons are emitted from atoms throughout the entire region of penetration for the x-ray radiation. For electrons which are not scattered as they travel through the material to the

surface, the kinetic energy (KE) of the emitted electrons is the difference between the energy of the incident x-rays and the binding energy (BE) of the electron in the atom from which it was emitted. This is expressed mathematically as follows:

$$KE = h\nu - BE \quad 3.1$$

In equation 3.1 the x-ray energy is written as the product of Planck's constant,  $h$ , and the frequency of the radiation,  $\nu$ . Since each electron in a given atom has a specific binding energy, the energy of the emitted electrons can be analyzed to identify the elements present in the near surface region. Moreover, bonding information can also be obtained from this technique since electrons in atoms which have shared bonds have binding energies which are shifted slightly from their original position. This *chemical shift* is on the order of tenths of an eV to several eV from the unshifted positions.

The surface sensitivity of XPS arises due to the nature of the interaction of the photoemitted electrons with the atoms in the near surface region. As electrons are generated due to interaction of the atoms with the incident x-rays, they travel through the material and escape without energy loss if they are not inelastically scattered. Those electrons which are scattered in the material lose energy and are not useful for chemical analysis. The probability that an electron will be scattered over a given distance is described by the mean free path,  $\lambda$ , of the electron. The mean free path is dependent upon the electron energy, but is on the order of 10 - 20 Å for the electron energies under consideration for general XPS analysis [10]. Mathematically, the probability,  $P$ , of an electron not scattering as it exits a material and therefore retaining useful energy information is given by equation 3.2:

$$P \propto \int_0^d \exp(-z / \lambda \cos \theta) dz \quad 3.2$$

In this equation  $z$  is the distance from the surface,  $\lambda$  is the mean free path,  $\theta$  is the "takeoff" angle of the detector with respect to the sample normal, and  $d$  is the thickness of the layer. The geometry for this analysis is shown schematically in figure 3.4. The form of this exponential function is such that the probability of no scattering over a distance equal the mean free path is  $P = 1/e$  (37%) for  $\theta = 90^\circ$ . Since ~95% of the electrons have scattered over a distance equal to 3 mean free paths, XPS has a depth

resolution on the order of  $3\lambda$  or  $60\text{\AA}$ . For detector angles not normal to the surface, the depth resolution is even shallower due to the cosine factor in equation 3.2.

Although XPS is an excellent substrate characterization method, there are limitations for carbon analysis. Detection of carbon in the surface region of a sample typically presents no problems, however, detailed bonding information based on chemical shifts is limited. The binding energy chemical shifts for the different forms of carbon, i.e. DLC, graphite, and diamond are only on the order of 0.1 eV. Furthermore, the insulating nature of diamond and some DLC films presents problems since charging prevents accurate determination of peaks positions. XPS analysis of graphite does show subtle differences between diamond and graphite for the loss structure due to a  $\pi$ - $\pi$  plasmon at  $\sim 6$  eV higher binding energy than the C(1s) peak.

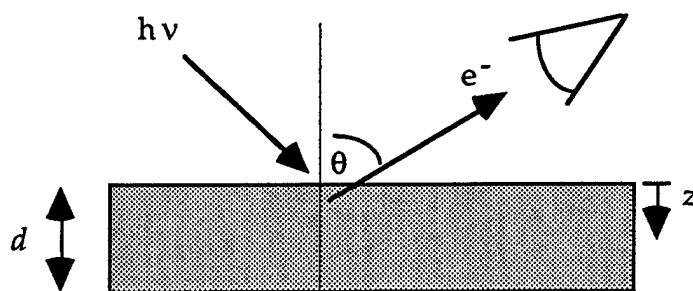


Figure 3.4 - XPS analysis geometry and variable designations.

As an example of the use of XPS for surface chemical analysis, Figure 3.5 shows a survey scan for carbon deposited upon a Si substrate. Silicon, carbon, and oxygen are observed and the presence of Si indicates that the deposited carbon is either very thin or not a continuous film. Table 3.2 details the XPS data obtained from the survey scan. A sensitivity factor,  $\sigma$ , for each element with respect to carbon ( $\sigma = 1$ ) allows determination of relative chemical compositions from the areas under the peaks in the spectrum. Although XPS is sensitive to sub-monolayer coverages, the accuracy of the relative composition data is on the order of several percent.

Figures 3.6 and 3.7 show typical high resolution scans of the C(1s) and Si(2p) regions, respectively. Least-squares fitting of these peaks yields the data shown in Tables 3.3 and 3.4. In the C(1s) region, several bonding states can be identified; C-Si

bonds are present at 283.0 eV while C-C bonds are located at 284.6 eV. Additional bonding of carbon to oxygen shows up at higher binding energies in the 286 range. The presence of the carbide is observed in the Si(2p) region as well. Here, Si-Si bonds are observed at ~100 eV, the carbide (Si-C) is at 100.6 eV and the oxide (Si-O) occurs at binding energies >102 eV. Notice the sum of the Si(2p) and C(1s) contributions in the high-resolution scans approximately add up to percentages found survey scan.

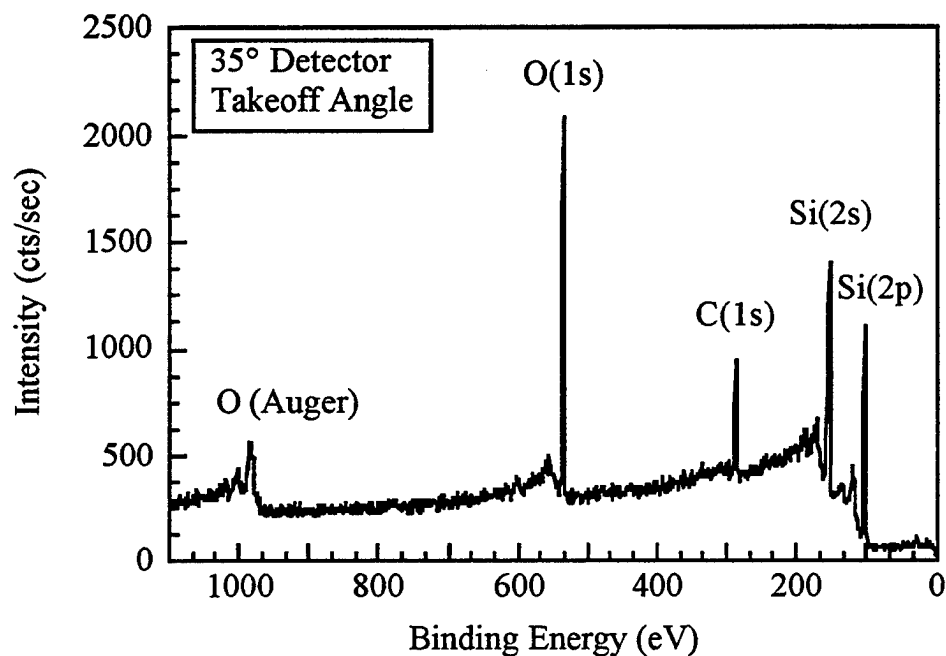


Figure 3.5 - XPS survey scan of carbon deposited on Si.

Peak	Binding Energy (eV)	Sensitivity Factor	Normalized Area	Relative Area	Atomic Percent (%)
C(1s)	284.6	1.00	5322	5322	22.3
Si(2p)	100.5	0.90	11233	12442	53.7
Si(2s)	151.8	1.03	13121	12765	----
O(2s)	534.0	2.49	14196	5700	24.0

Table 3.2 - XPS data for survey scan shown in Figure 3.5.

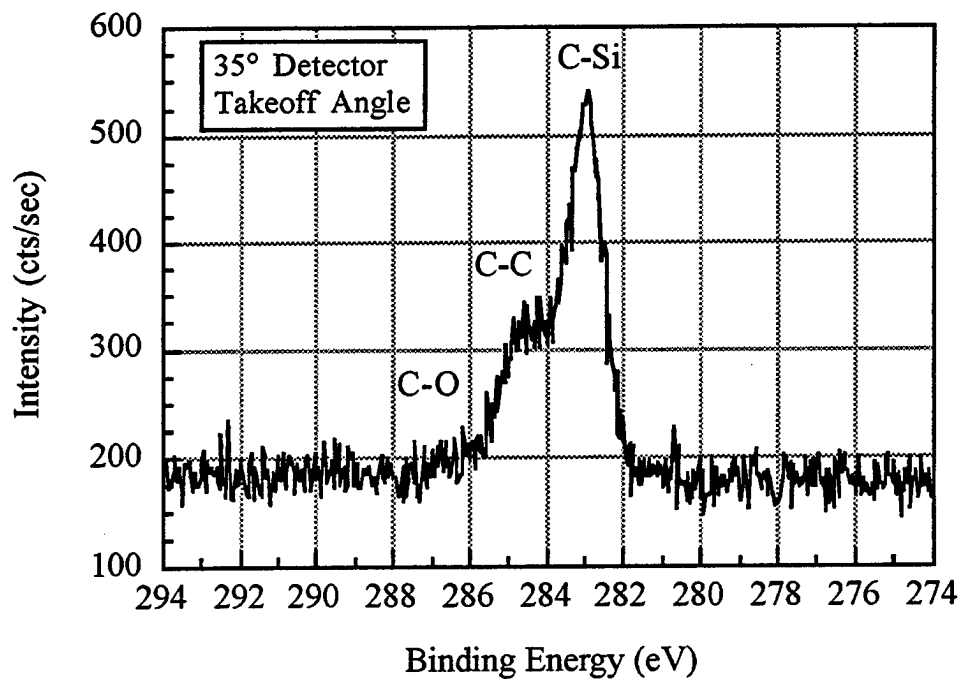


Figure 3.6 - High resolution XPS scan of the C(1s) peak.

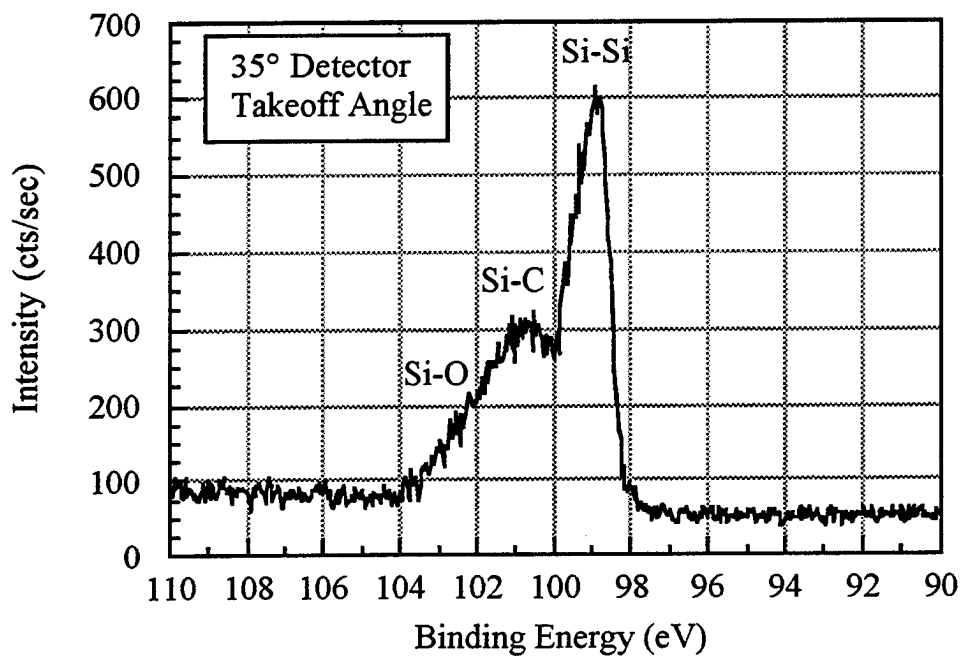


Figure 3.7 - High resolution XPS scan of the Si(2p) peak.



Peak	Position (eV)	Width (eV)	Atomic Percent (%)
C-C	284.5	1.55	9
C-Si	283.0	1.03	14
			23

Table 3.3 - XPS peak fit data for C(1s) high resolution scan.

Peak	Position (eV)	Width (eV)	Atomic Percent (%)
Si-Si	98.9	0.78	18
Si-Si	99.5	0.75	9
Si-C	100.6	1.41	13
Si-O	101.9	1.94	12
			52

Table 3.4 - XPS peak fit data for Si(2p) high resolution scan.

The XPS peak assignments are consistent with the binding energy ranges given in a standard reference handbook for XPS values [11]. Furthermore, peak positions from XPS analysis in diamond research in the literature also compare closely to those in this thesis as shown in Table 3.5 [12, 13].

Peak Positions (eV)		
Peak	Thesis Data	Literature Data
Si-Si	99.1 ± 0.1	99.0 [12]
Si-C	100.6 ± 0.1	100.3 [12]
Si-O	101.9 ± 0.1	102.7 [12]
C-C	284.5 ± 0.1	284.3 [12]
C-Si	283.0 ± 0.1	282.7 [12]

Table 3.5 - Comparison of XPS peak assignments to literature values.

A Surface Science Instruments S-probe system was used for all of the XPS analyses in this thesis. The x-ray radiation source was the  $AlK\alpha$  line with energy of 1486.6 eV. The ultimate base pressure of this cryopumped system is less than  $10^{-9}$  torr. XPS data in this thesis were analyzed using the software provided with the system. Curve-fitting utilized a least-squares routine with gaussian-shaped peaks. In reality, XPS peaks have both gaussian and lorentzian character, but accurate determination of the contributions from each type of peak is difficult. Therefore, only gaussian peaks were assumed for consistency. A Shirley background was employed for the baseline rather than a linear background [14].

A few comments should be made regarding the *ex-situ* nature of the XPS analyses. To energy analyze the emitted electrons in XPS, a high-vacuum environment is required to prevent scattering of the electrons by gas atoms before they reach the energy detector. This results in practical limitations of XPS to vacuum pressures less than  $\sim 10^{-8}$  torr. Therefore, electron-based spectroscopies like XPS cannot be used for *in-situ* surface analysis during diamond thin film growth which occurs at pressures greater than 1 torr. This means that XPS analysis either is done *ex-situ*, or *in-vacuo* by interrupting the process and then transferring the sample under high vacuum conditions into the XPS system. The *in-vacuo* analysis option was not available for the MPCVD system used for this research. Therefore, samples were removed from the MPCVD reactor following deposition and then loaded into the XPS system. The atmospheric transfer of the sample allowed for the possibility of contamination or modification of the surface state during the transfer. Atmospheric contamination and/or oxidation were real concerns since the XPS analyzes only the top several monolayers of the surface. All precautions were taken in this work to prevent these problems. In addition, surfaces which were exposed to atmosphere for differing periods of time were analyzed by XPS and only minor differences were observed. In general, nearly all samples exposed to atmospheric conditions had limited hydrocarbon and water contamination. However, the presence of the minor contaminants did not jeopardize the experiments nor change the conclusions made from the XPS data.

### 3.4 X-Ray Diffraction (XRD)

X-ray diffraction is based on the coherent scattering of x-ray by crystalline planes of atoms in the sample. Bragg's law governs x-ray diffraction and is written in terms of  $\lambda$ , the wavelength of the x-rays, and  $\theta$ , the Bragg angle:

$$\lambda = 2d_{hkl} \sin \theta \quad 3.3$$

The lattice spacing,  $d_{hkl}$ , is given by the following relationship containing the lattice spacing,  $a$ , and the Miller plane indices,  $(h, k, l)$ :

$$d_{hkl} = \frac{a_0}{\sqrt{h^2 + k^2 + l^2}} \quad 3.4$$

Given the energy  $E$  (eV) of the x-ray source, the wavelength  $\lambda$  (nm) can be determined from the expression:

$$\lambda = \frac{1240}{E} \quad 3.5$$

The d-spacings and relative intensities for random polycrystalline samples are shown in Table 3.6 for diamond and graphite [15]. Bragg angles can be obtained from equation 3.1 given the wavelength of the x-ray radiation. The structure factor in x-ray diffraction governs the atomic planes for which diffraction can be observed for a polycrystalline sample. Since diamond has an FCC lattice, planes with mixed  $(hkl)$  indices (even and odd values) will necessarily be missing in the diffraction pattern [16]. Furthermore, since diamond has a two-atom basis, planes for which  $(h + k + l) = 2n$  where  $n$  is an odd integer will also be missing. The first seven planes which are allowed from the structure factor are shown in Table 3.6. A detailed calculation of the structure factor for diamond is given in the Appendix A.4.

X-ray diffraction attempts using conventional lab sources were unsuccessful due to the poor scattering of carbon coupled with the relatively thin carbon films deposited. For films a micron in thickness, faint diamond peaks were observed with a lab diffractometer, but had extremely poor signal-to-noise and therefore were not very useful. Therefore, the synchrotron at Stanford Synchrotron Radiation Lab (SSRL) was used since the high x-ray flux provided by this facility offer the potential to overcome the scattering inefficiencies of these carbon films. For the synchrotron diffraction analysis, symmetric reflection geometry was used as shown in Figure 3.8. In this geometry, the scattering wave vector,  $k$ , is perpendicular to the sample surface and only lattice planes which are approximately parallel to the sample's surface contribute to diffraction peaks.  $\theta - 2\theta$  scans were done in the angular regions where crystalline diamond peaks were expected.

The system was limited to  $2\theta$  values less than approximately  $90^\circ$  due to mechanical constraints. The wavelength of the synchrotron radiation was 8500 eV which corresponds to 1.46 Å from equation 3.3.

DIAMOND			GRAPHITE		
d-spacing (Å)	Intensity	(hkl)	d-spacing (Å)	Intensity	(hkl)
2.059	100	(111)	3.348	100	(002)
1.261	25	(220)	2.127	3	(100)
1.075	16	(311)	2.027	15	(101)
0.8917	8	(400)	1.795	3	(102)
0.8183	16	(331)	1.674	6	(004)
0.7281	---	(422)	1.5398	4	(103)
0.6864	---	(333)	1.3154	1	(104)
0.6864	---	(511)	1.2280	4	(110)
			1.1529	6	(112)
			1.1333	1	(105)
			1.1160	1	(006)
			1.0503	1	(201)

Table 3.6 - d-spacings and relative integrated intensities for diamond and graphite planes.

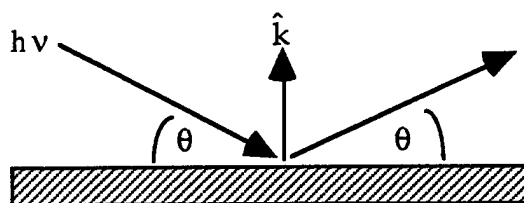


Figure 3.8 - Symmetric x-ray diffraction geometry and variables.

### 3.5 Transmission Electron Microscopy (TEM)

Transmission electron spectroscopy is one of the most useful characterization techniques for high resolution imaging of the atomic structure of materials. In this technique, high energy (100 ~ 400 keV) electrons are focused on a thin sample and the detector image is based on the electrons which are transmitted through the sample. Sample thicknesses are typically less than 200 nm to allow a significant portion of the electron beam to be transmitted. The transmitted beam consists both of diffracted and undiffracted electrons. Two modes are available, imaging and diffraction mode. In diffraction mode, the electron diffraction pattern is focused on the detector. Selected area electron diffraction (SAD) involves the use of apertures to select a region of the sample from which the diffraction pattern is collected. TEM imaging can be done using either bright-field or dark-field microscopy. For bright-field images, the objective aperture is used to block all diffracted electrons while those which are transmitted (undiffracted) through the sample are collected. Contrast in such images results both from differences in atomic mass and structure. Regions consisting of atoms with high atomic number appear darker in bright-field images since they scatter more strongly than low atomic number atoms. Crystalline regions in multiphase material and defects in highly crystalline material also appear darker in bright-field images since these areas diffract more strongly. For dark-field images, on the other hand, the objective aperture is positioned around a diffracted beam from the electron diffraction pattern. In this case, bright-regions correspond to those which diffract into the objective aperture. The contrast mechanisms are the same for dark-field images, but now the gray-scale image is essentially inverted. A detailed description of the general TEM techniques is given in the literature [17].

Several considerations are important for the TEM analysis of carbon thin films. The interaction of electrons with the target atoms is considerably higher than for x-rays since  $f_e \sim 10^4 f_x$  where  $f_e$  and  $f_x$  are the atomic scattering factors for electrons and x-rays, respectively. The scattering factor increases with atomic number,  $Z$ , so electron diffraction has the potential to be very useful for carbon materials compared to x-ray diffraction. However, electron diffraction analyses have limitations due to the extremely small volume of material being sampled and the strong possibility of texture or preferred orientation. Furthermore, the SAD pattern of graphite is quite similar to that of diamond [8]. Several researchers have mistakenly identified diamond when microcrystalline graphite was actually present. Therefore, extreme care in the indexing of SAD patterns from unidentified phases in carbon films is required.

### 3.6 References

1. J. B. Bindell, in *Encyclopedia of Materials Characterization - Surfaces, Interfaces, Thin Films*, ed. C. R. Brundle, Butterworth-Heinemann, Boston (1992).
2. S. Yugo, T. Kimura, and T. Kanai, in *Proceedings of the 1st International Conference on New Diamond Science and Technology*, ed. S. Saito, O. Fukunaga, and M. Yoshikawa, KTK Scientific Publishers, 119 (1990).
3. H. Baranska, A. Labudzinska, and J. Terpinski, *Laser Raman Spectrometry: Analytical Applications*, Ellis Horwood Limited, Chinchester (1987).
4. R. J. Nemanich, J. T. Glass, G. Lucovsky, and R. E. Shroder, *J. Vac. Sci. Technol. A*, **6**, 1783 (1988).
5. D. S. Knight and W. B. White, *J. Mater. Res.*, **4**, 385 (1989).
6. R. E. Shroder and R. J. Nemanich, *Phys. Rev. B*, **41**, (1990).
7. N. Wada, P. J. Gaczi, and S. A. Solin, *J. of Non-Crystalline Solids*, **35/36**, 543 (1980).
8. W. Yarbrough and R. Messier, *Science*, **247**, 668 (1990).
9. C. R. Brundle, in *Encyclopedia of Materials Characterization - Surfaces, Interfaces, Thin Films*, ed. C. R. Brundle, Butterworth-Heinemann, Boston (1992).
10. M. P. Seah and W. A. Dench, *Surface and Interfacial Analysis*, **1**, (1979).
11. C. D. Wagner, *Handbook of XPS*, Perkin-Elmer, (1979).
12. D. Belton, S. Harris, S. Schmieg, and T. Perry, *Appl. Phys. Lett.*, **54**, 416 (1989).
13. M. Waite and S. Shah, *Appl. Phys. Lett.*, **60**, 2344 (1992).
14. D. Shirley, *Phys. Rev. B*, **5**, 4709 (1972).
15. *JCDPS Powder Diffraction File*, International Centre for Diffraction Data, Swarthmore (1990).
16. B. D. Cullity, *Elements of X-Ray Diffraction*, Addison-Wesley Publishing Company, Reading (1978).
17. K. Sickafus, in *Encyclopedia of Materials Characterization - Surfaces, Interfaces, Thin Films*, ed. C. R. Brundle, Butterworth-Heinemann, Boston (1992).

## CHAPTER 4 - Results and Discussion

This chapter focuses on experiments designed to investigate the process of diamond nucleation. The nucleation of diamond was studied primarily using Si substrates and a variety of potential nucleation pretreatments including carbon deposition, diamond powder abrasion/scratching, and ion bombardment. Each deposition method reviewed in Chapter 2 is discussed in this chapter. However, the majority of the work focuses on MPCVD and the ion-assisted nucleation process developed in this system; this process is clearly the most promising of those studied and provides the most significant insights into the nucleation of diamond. The results for all of the nucleation experiments, as well as the characterization of the deposited material, are discussed in detail in this chapter.

### 4.1 Diamond Nucleation on Pristine Substrates

As previously stated, the heterogeneous nucleation of diamond without any substrate pretreatment is extremely poor. Numerous attempts to deposit diamond onto pristine Si wafers using HFCVD, MPCVD, and Sequential Deposition consistently resulted in poor nucleation with densities between  $10^3$  and  $10^5$   $\text{cm}^{-2}$ . These low nucleation levels are consistent with those of other researchers using similar methods. Deposition onto other substrates including molybdenum (Mo), stainless steel, quartz ( $\text{SiO}_2$ ), zirconia ( $\text{ZrO}_2$ ), lanthalaminate ( $\text{LaAl}_2\text{O}_3$ ), and palladium (Pd) also yielded low nucleation densities with levels similar to those for silicon. The SEM image shown in the figure 4.1 shows diamond nuclei deposited by MPCVD on an untreated silicon substrate. The nucleation density for this sample is  $\sim 5 \times 10^4$   $\text{cm}^{-2}$  and is typical for each of the 3 deposition processes of this thesis. Although the nucleation density was low for pristine substrates, the quality of the individual crystallites was good as inferred by faceted crystals and a sharp  $1332$   $\text{cm}^{-1}$  in the raman spectrum.

The low diamond nucleation densities on pristine silicon substrates provided inadequate statistics to show valid correlations between the nucleation density and deposition parameters such as substrate temperature, pressure, methane concentration, or excitation level (power). At these low densities, run-to-run nucleation density variations

were on the same order as the differences due to changing process conditions, and therefore, were inconclusive. Since the potential to gain useful insights into the nucleation process by continued experimentation on substrates which nucleated so poorly was low, other methods were investigated to increase the nucleation densities to levels amenable for research and reasonable for diamond thin film applications.

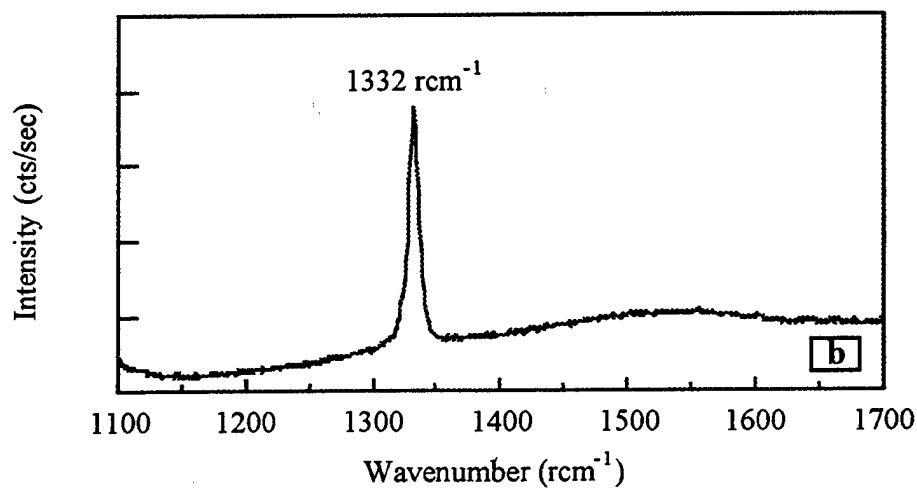
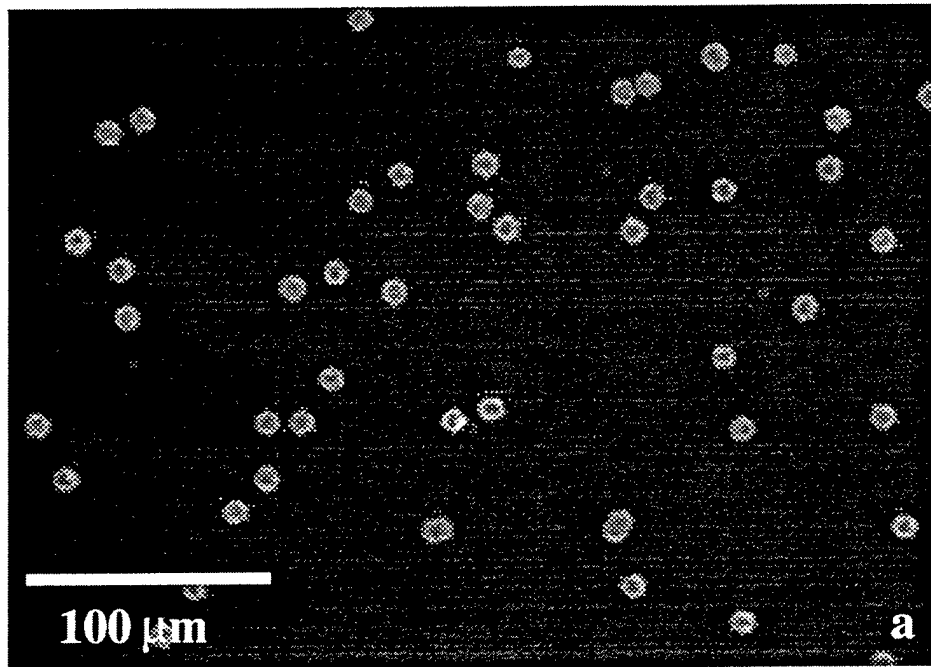


Figure 4.1 - (a) SEM of diamond nuclei deposited by MPCVD on clean silicon substrates and (b) raman spectrum for isolated nuclei.



## 4.2 Carbon Pretreatments and Nucleation Enhancement

Since diamond deposition is a product of the interaction of carbon and hydrogen species at the growth surface, surface carbon was assumed to play a significant role in the initial stages of nucleation of the diamond film. This hypothesis has further support from researchers who have observed varying degrees of nucleation enhancement due to fingerprints, contaminants, and hydrocarbon solvent residue left on the surface either intentionally or by accident, and various carbon thin films [1-3]. However, nucleation enhancement reports in the literature were never significant with densities only 1 - 2 orders of magnitude higher than those for untreated silicon. More importantly, this enhancement was typically neither uniform nor reproducible so few conclusions were inferred from these numerous studies. Therefore, the only conclusion from previous nucleation research is that some forms of carbon at the surface lead to nucleation enhancement.

To study the role of surface carbon on diamond nucleation, carbon was deposited on Si and then pretreated in various ways in attempts to form the specific carbon configurations which would lead to favorable sites for diamond nucleation [4]. Thin carbon films were deposited under controlled conditions onto untreated silicon substrates to study the effect of surface carbon on the nucleation of diamond. Two pure graphite electrodes (AESAR, 99.995% Carbon) were placed in contact, and carbon was thermally evaporated at low pressure ( $<10^{-5}$  torr) by passing ~60 amps at 5 volts through these electrodes. The substrate was mounted on a resistively-heated molybdenum foil located ~50 mm below the carbon electrodes. The resistive heater assembly provided substrate heating up to 1100 °C. The experimental set-up is shown schematically in Figure 4.2.

The amount of carbon deposited on the substrate was controlled by the electrode to substrate distance and the deposition time. XPS analysis provided an estimate of the amount of carbon deposited on the substrates. The carbon thin films were subjected to the subsequent processing steps listed in table 4.1 in attempts to promote the formation of stable carbon/diamond clusters. Following the carbon deposition and pretreatments, each sample was exposed to typical diamond growth conditions in the HFCVD system for 5 hours (0.5% CH<sub>4</sub>/H<sub>2</sub>, 2000 °C filament temperature, 8 mm substrate to filament distance, 800 °C substrate temperature, and 30 torr pressure). The HFCVD deposition was also done on a polycrystalline graphite substrate (nuclear grade) and a diamond-scratched Si substrate (4 - 6 μm powder) for comparison. Each sample was analyzed

using XPS prior to the deposition of carbon, following the pretreatment, and following HFCVD deposition.

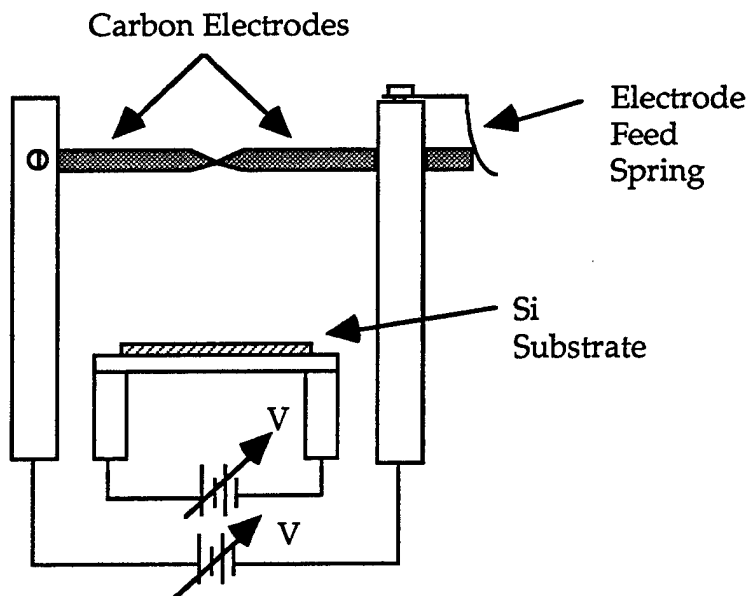


Figure 4.2 - Schematic of the carbon evaporation system for controlled carbon deposition in the carbon pretreatment experiments.

	Substrate Temperature	Deposition Environment	Additional Process
i	Low (< 100 °C)	10 <sup>-5</sup> torr	none
ii	Low (< 100 °C)	10 <sup>-5</sup> torr	30 min. anneal, 1150 °C, 10 <sup>-5</sup> torr
iii	High (850°C)	10 <sup>-5</sup> torr	none
iv	High (850°C)	10 <sup>-4</sup> torr H <sub>2</sub>	none
v	High (850°C)	10 <sup>-4</sup> torr H <sub>2</sub>	30 min. e <sup>-</sup> bombardment, -500V, 15 mA

Table 4.1 - Carbon thin film deposition and pretreatment processes prior to HFCVD.

Table 4.2 lists the nucleation densities following HFCVD for both the carbon pretreated and standard substrates. The nucleation densities tabulated in table 4.2 suggest that little, if any, nucleation enhancement occurred for any of the carbon pretreatment

processes. Nucleation densities for HF-etched silicon were essentially the same as for the carbon-pretreated silicon given run-to-run variations. If the carbon pretreatments played a role in nucleation, the effect was too small to observe in these experiments.

High-resolution XPS analysis of the C(1s) and Si(2p) regions confirmed the formation of silicon carbide (SiC) and the presence of carbon-carbon bonds in the near surface region following each of the pretreatments. The relative amounts of surface carbon and carbide formation varied for each pretreatment, but were difficult to quantify accurately. Although the XPS analysis showed various carbon/carbide compositions for the pretreatments, analysis following HFCVD indicated very similar surface compositions. First, the surface composition was within several percent for all samples. Second, SiC was observed at 100.4 eV in the Si(2p) region and 283.0 eV in the C(1s) region and the relative amount of the carbide was nearly identical for all samples [4]. The observation of carbide formation was not surprising as carbides have been observed with XPS during the diamond deposition process on Si and other carbide-forming substrates [5-7]. Raman spectra indicated the carbon deposited by these pretreatments was graphitic or amorphous in nature. Since these forms of carbon erode faster than diamond in the HFCVD growth environment, it was concluded that the deposited carbon was etched from the surface and did not lead to stable carbon configurations for nucleation.

Substrate (Orientation)	Pretreatment Process	Nucleation Density (cm <sup>-2</sup> )	Additional Comments
Silicon (100)	HF-etch	$3.5 \pm 0.7 \times 10^5$	1-2 $\mu\text{m}$ maximum nuclei size
Silicon (100)	Pretreatment (i)	$3.4 \pm 0.7 \times 10^4$	"
Silicon (100)	Pretreatment (ii)	$3.1 \pm 0.8 \times 10^5$	"
Silicon (100)	Pretreatment (iii)	$1.6 \pm 0.4 \times 10^5$	"
Silicon (100)	Pretreatment (iv)	$3.8 \pm 1.6 \times 10^4$	"
Silicon (100)	Pretreatment (v)	$1.2 \pm 0.3 \times 10^4$	"
Graphite	Solvent clean	$6.5 \pm 2.1 \times 10^6$	Nucleation on sharp features
Silicon (100)	Diamond abrasion	$2.0 \pm 1.0 \times 10^8$	Continuous film

Table 4.2 - Nucleation Densities for HFCVD of Diamond

These experiments indicated that, independent of the amount or process by which carbon was deposited on the substrate, the final surface state after the pretreatment was essentially the same. This suggests that the carbon pretreatments produced a form of carbon which did not survive in the deposition environment. Therefore, nucleation was not affected and simply the presence of carbon on the surface of a substrate was insufficient for nucleation enhancement.

These results are consistent with the poor nucleation enhancement observed by other researchers on SiC, graphite, amorphous carbon, and glassy carbon when no diamond seeds or special pretreatments are utilized [2, 5, 8]. Other cases of dramatic nucleation enhancement on SiC and C<sub>70</sub> buckyball films were observed only when negative-bias MPCVD pretreatment was utilized [5, 9, 10]. Poor nucleation by comparison was observed when growth was attempted directly on these materials without pretreatment. Therefore, a special configuration of carbon on the substrate surface appears to be responsible for nucleation of diamond on silicon. Two possibilities for this configuration are diamond nanocrystals or a non-diamond carbon configuration which is similar to diamond and allows for nucleation. Angus, *et al.*, have argued for the nucleation of diamond on the edges of the graphite basal plane [11, 12]. However, thin graphitic carbon layers present on the substrate surface in the diamond growth environment are most likely unstable since H<sup>+</sup> etches graphite considerably faster than diamond [13]; the removal of the surface carbon due to etching does not appear to lead to nucleation. Nucleation enhancement on graphite substrates is possible when the entire film is of sufficient thickness so that it is not completely etched away and nucleation sites may be formed through the etching of less stable configurations. This could explain the slightly higher nucleation densities observed on the graphite substrates in this experiment. On the other hand, nucleation enhancement on DLC layers suggests a non-diamond carbon phase may enhance diamond nucleation [14]. However, this carbon form may itself contain small amounts of diamond phase which are not easily identified. The carbon pretreatment experiments of this thesis do not confirm either of these hypotheses, but given the arguments above, it is more likely that the critical carbon configuration is a small diamond-phase cluster. Raman analysis of the carbon pretreatment layers produced by negative-bias MPCVD which led to significant nucleation enhancement indicated some diamond phase present [5]. Additionally, theoretical calculations by Badziag, *et al.*, suggest that extremely small carbon clusters which are hydrogen-terminated may be more stable as diamond than as graphite [15]. This argument is discussed in more detail in Chapter 5.

Some researchers have suggested that hydrocarbon cage molecules may serve as molecular precursors or templates for the nucleation of diamond [16]. One promising hydrocarbon candidate is adamantane,  $C_{10}H_{16}$ , the smallest molecule with complete diamond-carbon bonding (all the carbon-carbon bonds are staggered and all of the six-membered rings have the chair configuration). This saturated hydrocarbon molecule is essentially a ten-carbon diamond nucleus with complete hydrogen termination. Both HFCVD and MPCVD on self-assembled monolayers (SAM) of adamantane on Si with thicknesses of 10 Å and 80 Å was attempted [17]. Typical diamond deposition conditions produced no nucleation enhancement. It is postulated that the high temperature and/or the H<sup>+</sup> concentration in the deposition environment led to poor stability of this molecular SAM and prevented the formation of stable diamond nuclei.

### 4.3 Nucleation by Diamond Scratching/Abrasion Pretreatments

Given the poor heterogeneous nucleation of diamond and the prohibitively high cost of diamond substrates for most applications, methods have been developed to enhance nucleation. Diamond powder scratching/abrasion of substrates has typically been the method of choice to produce complete diamond films with adequate nucleation density [18]. Diamond powder scratching was used successfully in each of the deposition systems studied in this thesis. Two main techniques for diamond abrasion were used:

- simple hand-scratching of the substrate using dry 4 - 6  $\mu\text{m}$  diamond powder (Beta Diamond Co.) and a "Q-tip" applicator
- ultrasonic agitation of silicon substrates in solutions containing small amounts of 4 - 6  $\mu\text{m}$  diamond powder in methanol

With little variation between the various deposition systems, diamond nucleation was enhanced significantly as compared to the untreated Si case using either diamond abrasion technique. Nucleation densities typically ranged from  $10^7$  -  $10^8$   $\text{cm}^{-2}$  which is comparable to densities observed by other researchers for a variety of deposition techniques. Figure 4.3 shows a typical SEM for a diamond films deposited by MPCVD on Si which was scratched using 4 - 6  $\mu\text{m}$  diamond powder. This research also verified, although not in as much detail as Iijima [19, 20], that diamond scratching techniques leave residual

nanocrystalline diamond crystals on the substrate which serve as nucleation seeds for subsequent homoepitaxial growth. Scratching with other powders such as boron carbide (BC), silicon carbide (SiC), and alumina ( $\text{Al}_2\text{O}_3$ ) produced slight levels of nucleation enhancement in the deposition systems used in this thesis, but these enhancements were several orders of magnitude lower than for scratching with diamond powder.

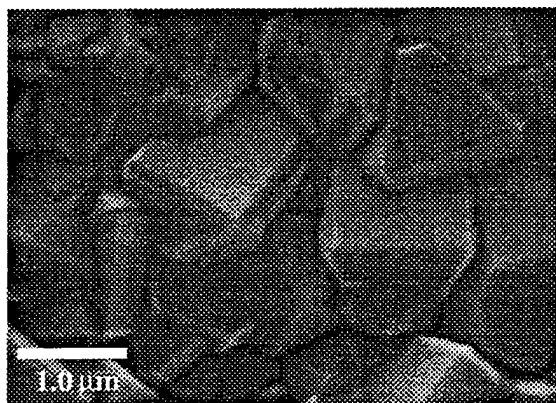


Figure 4.3 - Morphology of a polycrystalline diamond film deposited on diamond scratched silicon substrate.

A noticeable difference in the distribution of nuclei sizes was observed for scratched as compared to pristine Si substrates. For scratched substrates, a narrow nuclei size distribution was typically observed which is consistent with homoepitaxial growth on residual diamond seeds which are small compared to the final nuclei size. The residual diamond seeds are often less than 100 nm in size, and therefore, extremely difficult to image using SEM. On unscratched silicon, a significantly broader size distribution (as well as a lower density) of nuclei were observed suggesting nucleation events which occurred randomly in time during the deposition. These findings suggest that mathematical analyses of nucleation size distributions are inaccurate for experiments in which diamond scratching or abrasion was employed [21, 22]. Furthermore, parametric studies in the literature in which nucleation densities were investigated as a function of process parameters such as pressure, temperature, gas composition, etc. are invalid when diamond seeds were left behind from the scratching process; in fact, these studies actually study the effects of the parameters on diamond growth rather than nucleation [21, 23].

In summary, diamond scratching is a technique for diamond nucleation when damage to the substrate surface is acceptable. However, insight regarding nucleation

mechanisms cannot be gained from such studies. Furthermore, nucleation enhancement by scratching/abrasion suffers from other practical application issues. Since the nucleation density and uniformity are controlled by the seeding process, it is difficult to reproduce nucleation densities, grain sizes, and surface morphologies. The process is also *ex-situ* which introduces the possibility of contamination. Finally, extremely thin diamond films cannot be deposited with this method since the lower nucleation density requires the nuclei to be larger when coalescing to form a complete film.

#### 4.4 Ion-Assisted Nucleation of Diamond

Due to the poor heterogeneous nucleation of diamond on untreated substrates, and the fundamental and practical limitations imposed by diamond abrasion techniques, the bulk of this thesis research focused on diamond nucleation under applied bias voltages. This method was briefly described in Chapter 1 and has been termed *bias-enhanced nucleation* (BEN) by other researchers studying this process [5, 23-27]. As the experiments in this section indicate, significant progress in understanding this process has been made. The role of ions has been confirmed to control this process, and therefore, this process is referred to as *ion-assisted nucleation* since this term more accurately describes the underlying mechanism of this technique.

Bias pretreatment processes involve the application of a negative bias to the substrate under deposition conditions which are otherwise quite similar to those used for normal growth of diamond films. Under these bias conditions a visible glow discharge forms between the substrate and the microwave plasma ball. This secondary glow discharge is basically a dc-discharge between the substrate (cathode) and the plasma (anode). For most ion-assisted nucleation experiments, no further growth was done following the bias pretreatment to ensure that only the ion-assisted process was studied. Analysis of films prepared using bias pretreatments and subsequent deposition processes is more complicated. The level of nucleation enhancement for ion-assisted nucleation depends on a variety of factors which this section discusses in detail. In general, the nucleation density on Si substrates is increased several orders of magnitude above that observed for diamond abrasion techniques to densities greater than  $10^{10}$  cm<sup>-2</sup>. Figure 4.4 shows both the bias-deposited nuclei following a 15 minute ion-assisted pretreatment (4.4a) and a complete diamond film growth by 2 hour unbiased MPCVD (4.4b) following such an ion-assisted nucleation pretreatment. Note that the morphology of the nuclei deposited in the ion-assisted process is significantly different that for the complete film

grown on top of these nuclei. The nuclei size and film grain size are similar, but signs of crystallinity are observed in the faceting of the polycrystalline film.

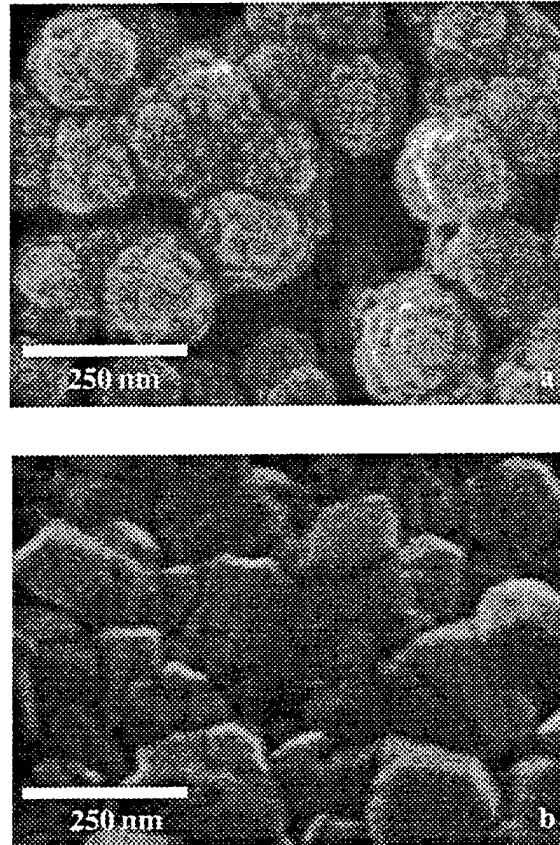


Figure 4.4 - (a) Nuclei deposited by the ion-assisted process (b) Diamond film grown by unbiased MPCVD on top of bias-deposited nuclei.

Experiments using an applied negative bias pretreatment were also done in the HFCVD system. Diamond nucleation enhancement to densities similar to those observed in the MPCVD process were obtained on Si substrates [28]. However, these results were not as reproducible as those in the MPCVD system. Furthermore, the samples often contained metallic contamination from the filament, and the filament condition changed rapidly under bias conditions leading to difficulties in maintaining constant process parameters within and between experiments. Therefore, these experiments are not detailed in this thesis.



The ion-assisted nucleation experiments of this thesis differ from other similar biased nucleation studies in two important respects [25, 29, 30]. First, the bias current depended on various process parameters including the substrate position, the applied bias voltage, and the substrate temperature. Therefore, the time-integrated bias current rather than the total bias time was maintained for parametric experiments since this current is related to the incident ion flux to the surface. To unambiguously determine the role of ionic species in the nucleation process, it is necessary to maintain the total number of ions incident upon the surface when comparing the effects of bias voltage or any parameter which changes the level of the bias current. Constant bias time experiments typically do not maintain the total ion flux and result in the variation of more than one parameter for a given experimental set. A constant time-integrated current, on the other hand, corresponds to the same ion flux incident upon the substrate for each experiment if the electron component of the measured current does not vary significantly. In previous bias-enhanced nucleation literature, bias current levels have generally not been reported and bias processes were run for constant times. Second, bias pretreatment times (integrated fluxes) were chosen specifically to produce incomplete films of individually separated nuclei. Analysis of the substrates and deposited nuclei directly followed the bias pretreatment without any unbiased growth so that only the ion-assisted nucleation process was studied. As discussed in the characterization section of this thesis, this improves the accuracy of the nucleation density estimates determined using *ex-situ* scanning electron microscopy (SEM). Nucleation densities estimated for complete diamond polycrystalline films may be inaccurate due to coalescence and secondary nucleation during the growth process [31].

#### 4.41 Role of Energetic Species (Ions/Neutrals)

The fact that application of a negative bias to normal MPCVD is so effective in increasing nucleation density suggests that ions are important in this process. Initial nucleation research using applied voltages by Yugo, *et al.*, suggested that the bias voltage played an important role in the nucleation of diamond [23]. After further research, the following effects of biasing in MPCVD systems were postulated by Stoner, *et al.*, in enhanced nucleation studies using applied negative bias processes [5]:

- Increased flux of positively charged carbon ions to the surface
- Reduced flux of electrons and negatively charged ions to the surface

- Higher energy transfer from the ions to the surface, resulting in increased surface mobilities of adsorbed species
- Enhancement of reactions and molecular dissociation just above the substrate as a result of an increase in, and higher energy from, ion-neutral collisions within the sheath region
- Reduction and suppression of oxide formation on the surface

The experiments discussed in this chapter were designed to test these postulates and to determine in more detail the effects of each in the nucleation mechanism of diamond under bias conditions.

The importance of energetic ion bombardment during the bias pretreatment was initially confirmed in the following experiment. A small (5 x 5 x 0.5 mm) Si substrate was mounted at the center of a 4-inch Si wafer on top of a slightly larger sapphire ( $\text{Al}_2\text{O}_3$ ) substrate which provided electrical isolation. Figure 4.5 schematically shows the set-up for this experiment.

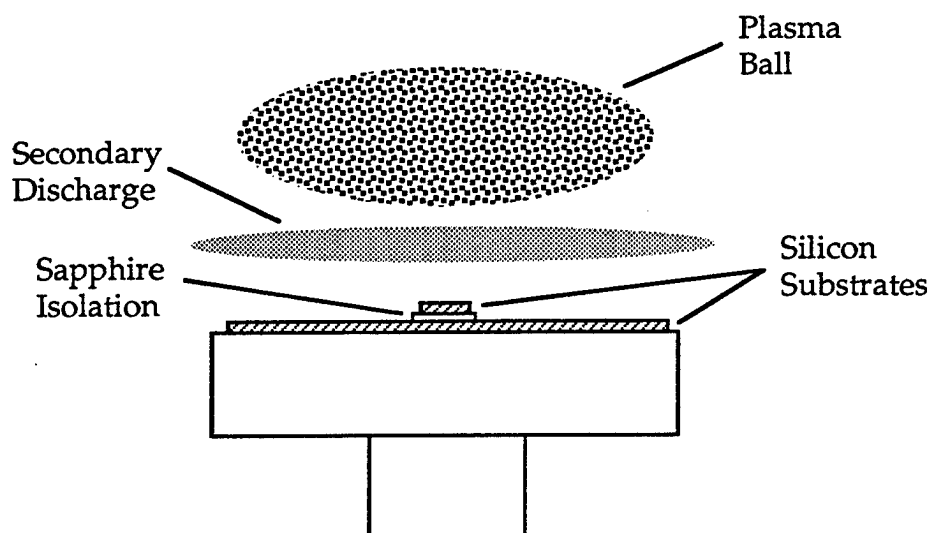


Figure 4.5 - Substrate isolation experimental set-up for investigating the role of the energetic ion flux.

This substrate arrangement was exposed to a 20 minute bias pretreatment at -300 V with a bias current which increased from 57 to 76 mA. The biased-silicon substrate showed

heavy nucleation with a density of  $9.0 \pm 0.7 \times 10^9 \text{ cm}^{-2}$ , while the electrically-isolated substrate nucleated extremely poorly with a density of  $2.0 \pm 1.0 \times 10^4 \text{ cm}^{-2}$ . This experiment indicates that energetic ion bombardment plays a significant role in the bias-enhanced nucleation of diamond since the only difference between these substrates is the bombardment of the biased Si substrate by energetic cations. If gas-phase species created by the application of the bias rather than energetic species controlled nucleation, enhanced densities of nuclei would be observed on both substrates due to diffusion. An ion bombardment nucleation mechanism has been previously postulated in the literature, but never proven explicitly [5, 32]. Previous work by Aisenberg, *et al.*, on carbon deposition by energetic ion beams supports this general conclusion as it was stated that "..... the role of energetic ions is more important in transporting momentum and energy to the substrate atoms than in transporting deposition material [16]." Recent work by Jiang, *et al.*, also led to the same conclusion regarding the critical role of energetic ions in ion-assisted nucleation; in this research Si substrates with etched vias were biased and nucleation was only observed on the normal surfaces which were exposed to energetic species [33].

In contrast to energetic ion control, nucleation enhancement due to a more reactive near-surface chemical environment created as a result of the bias process has been postulated [32, 34, 35]. Evidence to support this conclusion include the following: (i) the observed secondary discharge is significantly brighter than original microwave discharge suggesting that this region is quite reactive, (ii) optical emission spectroscopy (OES) by Shigesato, *et al.*, suggests that the  $\text{H}^+$  concentration is increased, as well as the electron temperature, in the region of the bias [35]. However, the modest  $\text{H}^+$  increase of less than 25% is not likely to increase nucleation densities five orders of magnitude. Furthermore, OES data by Beckmann, *et al.*, which indicate slight decreases in  $\text{H}^+$  concentrations at higher bias voltage also argue against this mechanism [30]. Moreover, this mechanism cannot explain the results of the isolated substrate experiment because the chemical environments are similar for the biased and electrically-isolated silicon substrates. If nucleation were the result of any low-energy gas phase species created by the bias, enhanced nucleation would be expected on both the biased and isolated substrates due to diffusion of the reactive species to the substrates. The only difference between these substrates is the bombardment of the biased silicon substrate by energetic cations; although cations also bombard the electrically isolated substrate, these species have much lower energies since the potential across which they are accelerated is not the bias potential (300 V), but rather, the floating potential which is typically only 10 - 15 volts negative due to the higher mobility of electrons in the system [36].

A nucleation mechanism controlled by the bombardment of energetic ions may possess a critical voltage below which the process is not activated and nucleation enhancement is not observed. This postulate was tested by studying the effects of ion impingement energy on the nucleation density. At first glance, it may seem possible to study the effect of the bias species energy by changing the total pressure in the system since the mean free path of the ions is inversely proportional to the pressure. In turn, the mean free path directly affects the energy accumulated by these ions as they traverse the sheath region before bombarding the substrate. However, changes in pressure also affect the sheath thickness; unfortunately, the product of sheath thickness and pressure in dc-glow discharges has been observed to be constant. Therefore, variations in the pressure will not significantly change the number of collisions within the sheath and this parameter cannot be used to probe the energetic characteristics of the bias ions [36].

A more direct method for investigating the effects of ion energy involved varying the applied bias voltage while maintaining the other process parameters. However, as discussed in detail in the next chapter, the bias voltage is only an indication of the energy of the impinging species since much of the bias potential is lost due to ion-neutral collisions in the sheath. This limitation cannot be avoided in the MPCVD system so the overall bias voltage was varied and energies losses were accounted for later. The time-integrated bias current was maintained within 10% while the bias voltage was varied for a set of substrates. The deposition parameters were maintained at  $20 \pm 1$  torr, 2% CH<sub>4</sub>/H<sub>2</sub>,  $800 \pm 10$  °C, and  $650 \pm 10$  W during all experiments. Table 4.3 shows the bias parameters for the voltages investigated in this set of experiments. Note that large differences in the total bias time were required to obtain the same integrated bias current to the surface. The bias current increased with time during the process for all successful ion-assisted nucleation experiments. This phenomenon is discussed in more detail in later sections. From Table 4.3, it is observed that conditions producing low nucleation densities correlated with small increases in the bias current during the process. Therefore, it may be possible to use the bias current or changes in the bias current as an *in-situ* method of process control for nucleation density.

The ion-assisted nucleation densities are plotted versus the applied negative bias voltages in Figure 4.6. At a critical bias voltage of approximately -200 V, the nucleation density increased nearly five orders of magnitude above the unbiased case. At the high-voltage end of these experiments, the small nucleation density decreases were attributed to increased sputtering/destruction of nuclei by higher energy ions. Alternatively, the coalescence of more densely packed clusters would also lead to decreases in the nucleation density. More experiments are required to fully explain the nucleation dependence at high

bias voltages. Similar nucleation density trends for critical bias voltages between -100 V and -250 V have been observed by other researchers; however, in these reports the bias currents for each voltage were not reported and the total ionic flux to the surface was most likely not maintained [25, 29]. The existence of a critical voltage is consistent with a mechanism in which nucleation is controlled by the energetic cations impinging upon the surface. Below the critical voltage, the impinging species do not possess enough energy to overcome the nucleation barrier(s). From these measurements, the critical energy for nucleation can be estimated by accounting for ion-neutral collisions which occur between the sheath and substrate. Detailed estimates of the ion energy distribution at the substrate are provided in the next chapter.

Bias Voltage (V)	Bias Current (mA)	Bias Time (minutes)	Integrated Bias Current (mA·sec)	Nucleation Density (cm <sup>-2</sup> )
0	---	300	---	$5.0 \pm 2.0 \times 10^3$
-102	6 → 8	110	49700	$1.0 \pm 0.5 \times 10^4$
-155	10 → 11	85	55400	$2.1 \pm 0.1 \times 10^7$
-206	14 → 29	42	54600	$4.3 \pm 0.5 \times 10^9$
-231	20 → 57	23	47000	$1.2 \pm 0.1 \times 10^{10}$
-257	35 → 78	16	53700	$1.4 \pm 0.1 \times 10^{10}$
-283	50 → 88	13	48100	$1.8 \pm 0.2 \times 10^{10}$
-307	53 → 104	12	51600	$1.1 \pm 0.1 \times 10^{10}$
-333	62 → 94	12	55600	$7.3 \pm 0.9 \times 10^9$

Table 4.3 - Bias voltages, parameters, and nucleation densities for ion-assisted nucleation voltage experiments.

The maximum nucleus size is plotted as a function of the bias time for constant integrated bias current in Figure 4.7. Under these conditions, approximately the same number of ions were incident on each substrate, due to the voltage dependence of the bias current, even though the bias times varied. Since the maximum nucleus size increases with bias time rather than with integrated bias current, the ions cause nuclei formation but do not significantly contribute to the continued growth of the nuclei. Therefore, although energetic ions enhance nucleation, the neutral species which possess only thermal energies are the main contributors to the growth process.

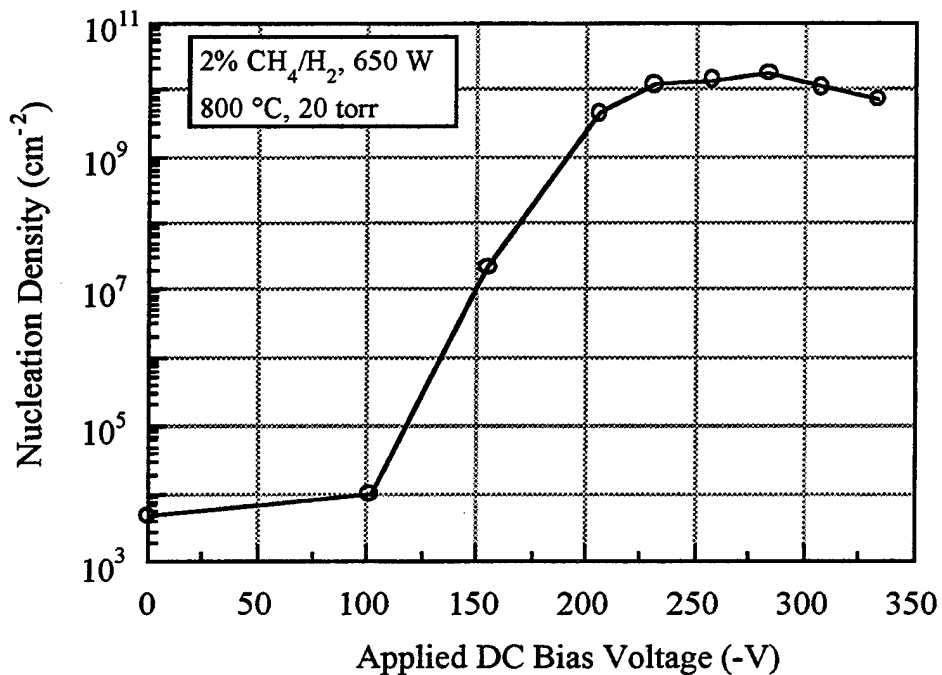


Figure 4.6 - Nucleation density as a function of the applied bias voltage with constant time-integrated bias current to the substrate.

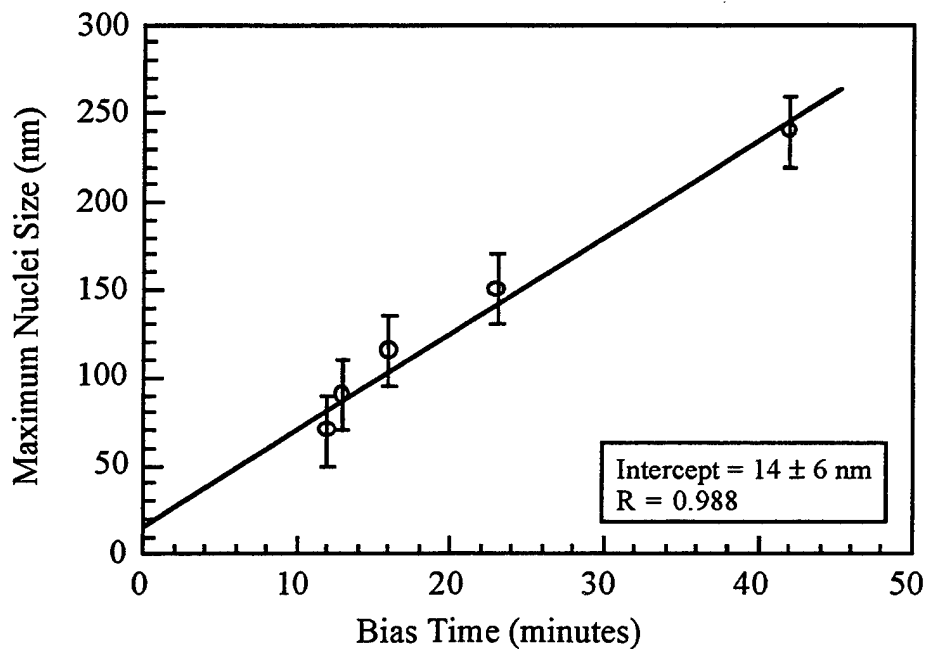


Figure 4.7 - Maximum nucleation size as a function of the bias time with constant time-integrated bias current to the substrate.

The relatively linear growth rate with time observed in Figure 4.7 is consistent with the following growth model. Consider, for simplicity, the nuclei to be perfect hemispheres on the substrate surface. The mass growth rate,  $dm/dt$ , can be written as:

$$\frac{dm}{dt} = \rho \frac{dV}{dt} = FSM \quad 4.1$$

In this equation  $V$  is the volume of the nuclei,  $F$  is the flux of growth species ( $\text{cm}^{-2}\text{s}^{-1}$ ),  $S$  is the sticking coefficient of growth species (unitless),  $A$  is the surface area of the nuclei ( $\text{cm}^2$ ), and  $M$  is the molecular weight of the nuclei atoms in amu ( $\text{kg}^{-1}$ ). For cluster growth where hemispheres are assumed:

$$V = \frac{2}{3}\pi r^3 \quad \longrightarrow \quad dV = 2\pi r^2 dr \quad 4.2$$

$$A = 2\pi r^2 \quad 4.3$$

Substitution of equations 4.2 and 4.3 into equation 4.1 and subsequent integration yields the time dependence of the growth rate:

$$2\rho\pi r^2 \frac{dr}{dt} = 2\pi r^2 FSM \quad 4.4$$

$$r(t) = \int_0^t dr = \int_0^t \frac{FSM}{\rho} dt = \frac{FSM}{\rho} t \quad 4.5$$

The y-intercept, at zero bias time, corresponds to the onset of nucleation. Least squares fitting of the experimental data gives a critical nuclei size of  $14 \pm 6$  nm. This value may be an overprediction given the errors (shown by the error bars in the figure) in the nuclei size measurements.

Figure 4.8 shows the nucleation density as a function of the integrated ion flux to the substrate. For complete analysis more data is necessary at shorter times, but this is difficult experimentally due to the limited accuracy of the MPCVD system mass flow controllers at low flow rates. However, the trend is similar to that observed by Gerber with nucleation density increasing rapidly with time and leveling out [26]. However, these results suggest induction periods less than 4 minutes in contrast to longer induction periods suggested by other researchers. Induction periods are very difficult to assess

since the resolution of the microscope limits the nuclei size which can be observed and results in overestimates of the induction time.

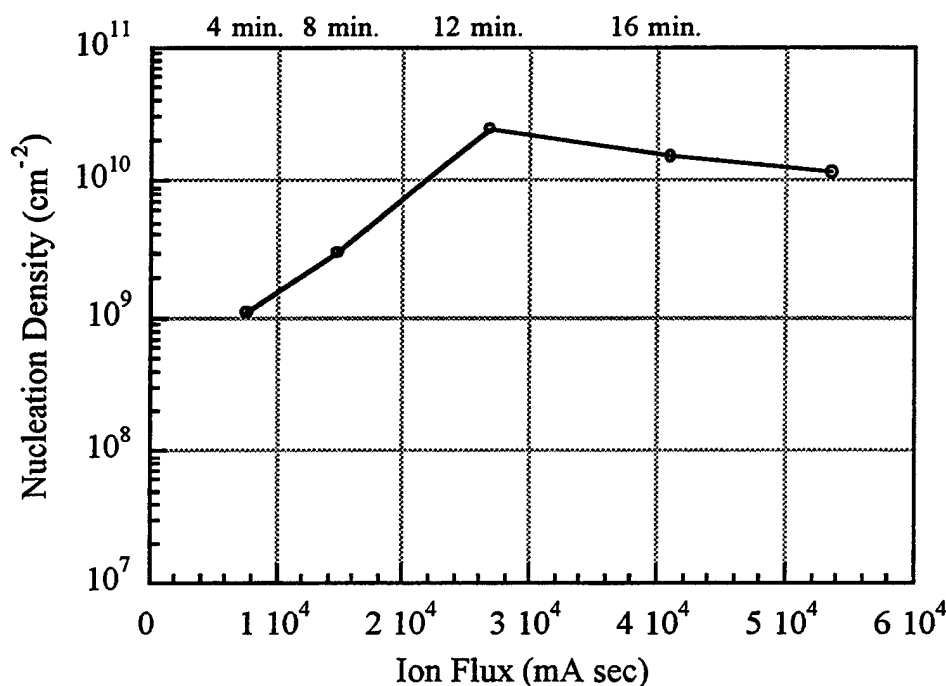


Figure 4.8 - Nucleation density as a function of the integrated bias flux to the substrate.

In any case, nucleation density increases with ion flux to the surface before leveling out, and therefore, this parameter should be used for process control of nucleation density rather than overall bias time. Additional studies of nucleation density as a function of ion flux for a variety of temperatures, voltages, and methane concentrations are required to ensure that ion flux alone can be used as a calibration curve for nucleation densities under varied process conditions.

#### 4.42 Role of Substrate Temperature

The temperature dependence of nucleation under applied negative bias also provides insight into the mechanism of ion-assisted nucleation. An important check for an energetic ion controlled nucleation process is whether or not the process is thermally



activated. Thermally-activated process have a temperature dependence which can be studied to determine quantitative activation barriers. However, an ionic mechanism may be temperature insensitive since the energy of the incoming cations is much higher than any energy provided due to thermal effects at the temperatures under consideration. Sheldon, *et al.*, observed carbon film thicknesses during biased deposition that did not change significantly with temperature which implies a non-chemical mechanism due to the absence of thermal activation [32].

In this thesis, the nucleation density was measured as a function of the substrate temperature under constant bias voltage and constant ion flux to the surface. The data are plotted in Figure 4.9. All other process variables were held constant and the ion-assisted nucleation process was run at temperatures from 450 °C to 950 °C. Higher temperature measurements were limited by the heater power supply output, while lower temperatures were impossible due to the heating from the plasma. From the discussion of the substrate temperature measurement in Chapter 2, although the thermocouple measurement does not exactly match that of the surface of the silicon, the quoted values are believed to be accurate within  $\pm 25$  °C.

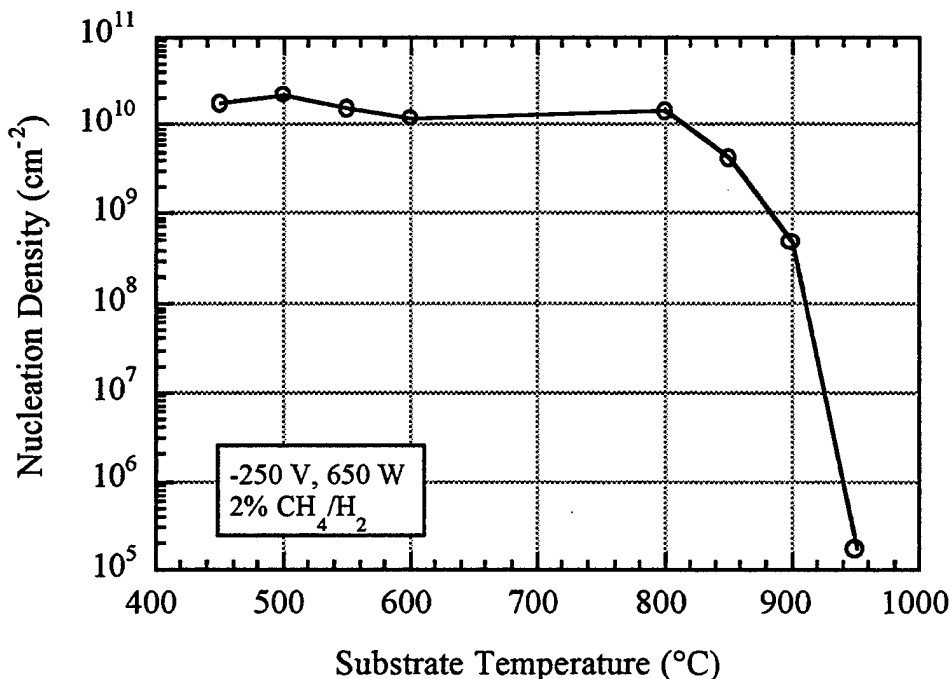


Figure 4.9 - Nucleation density as a function of substrate temperature for the ion-assisted nucleation process under constant voltage and constant integrated bias current.

Table 4.4 shows the nucleation densities and measured experimental parameters for ion-assisted nucleation pretreatments at various temperatures. The integrated bias currents were maintained as close as experimentally possible and differences in the bias times result from bias current variations from run to run. SEM analyses confirm that high nucleation densities persist down to 450 °C even though the material deposited during the ion-assisted nucleation pretreatment was not visible by eye below 600 °C. This is explained by the strong temperature dependence of the growth rate of diamond; although the nuclei are formed, the growth rate is slow at low temperatures resulting in smaller nuclei for the same ion flux [37, 38]. This temperature dependence differs from that observed by other researchers [25, 26] who do not observe high nucleation densities at low substrate temperature [13, 21]. This result is most likely due an ion flux to the surface which was not constant in their experiments and/or nuclei resolution difficulties. Above 900 °C, the nucleation density is observed to decrease dramatically in Figure 4.9. The reduction in nucleation density at higher temperatures was also confirmed in the numerous, less controlled experiments. Often, the plasma interaction with the substrate during the ion-assisted pretreatment resulted in a local "hot spot" in the center of the wafer. It is estimated that this "hot spot" was several hundred degrees hotter than the surrounding substrate regions. At substrate temperatures in the range of 700 - 800 °C, the hot spot region contained nucleation densities several orders of magnitude below that of the rest of the substrate.

Substrate Temp. (°C)	Bias Current (mA)	Bias Time (minutes)	Integrated Bias Current (mA·sec)	Nucleation Density (cm <sup>-2</sup> )
450	27 → 41	24	51900	$1.7 \pm 0.2 \times 10^{10}$
500	40 → 48	20	53800	$2.2 \pm 0.4 \times 10^{10}$
550	34 → 60	18	50900	$1.5 \pm 0.2 \times 10^{10}$
600	28 → 65	20	52000	$1.2 \pm 0.2 \times 10^{10}$
800	35 → 78	16	53700	$1.4 \pm 0.1 \times 10^{10}$
850	30 → 43	23	50100	$4.2 \pm 0.2 \times 10^9$
900	26 → 31	28	48200	$4.8 \pm 0.5 \times 10^8$
950	27 → 28	30	50100	$1.7 \pm 0.3 \times 10^6$

Table 4.4 - Process parameters and nucleation data for ion-assisted nucleation process at various substrate temperature

Note that similar to the critical voltage results in Table 4.3, conditions producing lower nucleation densities correlated with smaller increases in the bias current during the process. Although it is discussed in more in later sections, note that the initial bias was relatively constant over the substrate temperature range which provides information concerning the source of the current. Additionally, SEM analyses determined that the average nucleus size increased from ~60 nm at 500 °C to ~200 nm at 800 °C despite the increase in total deposition time for the former case; this confirms the strong temperature dependence of the growth process.

The observed temperature dependence of this process is consistent with the proposed ion-assisted nucleation mechanism. Since the energy of the incident species (greater than 10 eV) is several orders of magnitude greater than the thermal energies (less than 0.1 eV), the nucleation density should be independent of temperature and nucleation densities should not decrease at low substrate temperatures. The experimental results follow this behavior except at higher temperatures where additional mechanisms may dominate. For example, both hydrogen abstraction and desorption of surface carbon increase at elevated temperatures which may account for the decrease in nucleation density above 800 °C [39].

#### 4.43 Effect of Carbon Concentration and Plasma Chemistry

The effect of gas-phase carbon concentration on ion-assisted nucleation provides additional insight into the nucleation process. Specifically, the concentration dependence provides information about the flux of carbon ions incident at the substrate. The effects of this parameter were investigated by varying the CH<sub>4</sub>/H<sub>2</sub> ratio from 0.5% to 3.0% under constant voltage, constant integrated bias current, and constant deposition parameters. Table 4.5 details the nucleation densities and process parameters for these experiments.

Figure 4.10 shows the nucleation density as a function of the carbon species overall concentration. The nucleation density is relatively flat for CH<sub>4</sub>/H<sub>2</sub> ratios above 1%. Jiang, *et al.*, also observed a drop in nucleation density at lower concentrations but did not report the bias currents for these processes which makes comparisons difficult [25]. The reason for the abrupt decrease in nucleation density is not fully understood. However, since the growth of the nuclei was shown to be dominated by gas phase species rather than the ions, the final nuclei size for the low CH<sub>4</sub> concentration experiments may be extremely small; therefore, the nucleation densities for these experiments may be

inaccurate due to SEM resolution limitations. From the bias currents listed in Table 4.5 and the plot of bias current versus time at various CH<sub>4</sub>/H<sub>2</sub> concentrations in Figure 4.11, the addition of carbon to the gas mixture does not appear to significantly change the initial bias current. This suggests that the carbon ions are not the dominant species for the bias current which is composed of both carbonaceous and hydrogenic ions incident on the substrate as well as electrons emitted from the substrate. This slight increase in the bias current as the carbon concentration was increased differs from the results of Beckmann, *et al.*, who observed decreases in bias current with increasing carbon concentration [30]. Furthermore, since the initial bias current is only slightly higher than that observed for the case with no CH<sub>4</sub> in the system, this indicates that the bulk of the ion current at the substrate during the bias process is carried by hydrogenic ions rather than CH<sub>x</sub><sup>+</sup> ions.

CH <sub>4</sub> /H <sub>2</sub> Ratio (%)	Bias Current (mA)	Bias Time (minutes)	Integrated Bias Current (mA·sec)	Nucleation Density (cm <sup>-2</sup> )
3.0	25 ---> 71	18	51180	1.6 ± 0.1 x 10 <sup>10</sup>
2.0	24 ---> 52	22	52440	1.8 ± 0.1 x 10 <sup>10</sup>
1.0	23 ---> 47	25	58755	1.8 ± 0.2 x 10 <sup>10</sup>
0.5	21 ---> 41	28	59730	2.7 ± 0.2 x 10 <sup>7</sup>
0.0	19 ---> 19	---	-----	-----

Table 4.5 - Nucleation data for studies of the effects of carbon concentration on ion-assisted nucleation.

A control experiment in which the bias was applied in a pure H<sub>2</sub> environment was also done to ensure that carbon species were necessary for the nucleation process. For this case, the bias current did not increase with time as is typical for the ion-assisted process when carbon is present. Following an ion-assisted pretreatment in H<sub>2</sub>, no evidence of nucleation was observed either by Raman spectroscopy or SEM. Normal unbiased MPCVD following this process also resulted in no nucleation enhancement. Therefore, modification of the substrate due to hydrogen ion bombardment in the form of surface roughness, creation of high energy ledges and kinks, or other surface defects is not sufficient for diamond nucleation. These avenues for diamond nucleation have been postulated by other researchers [40, 41].

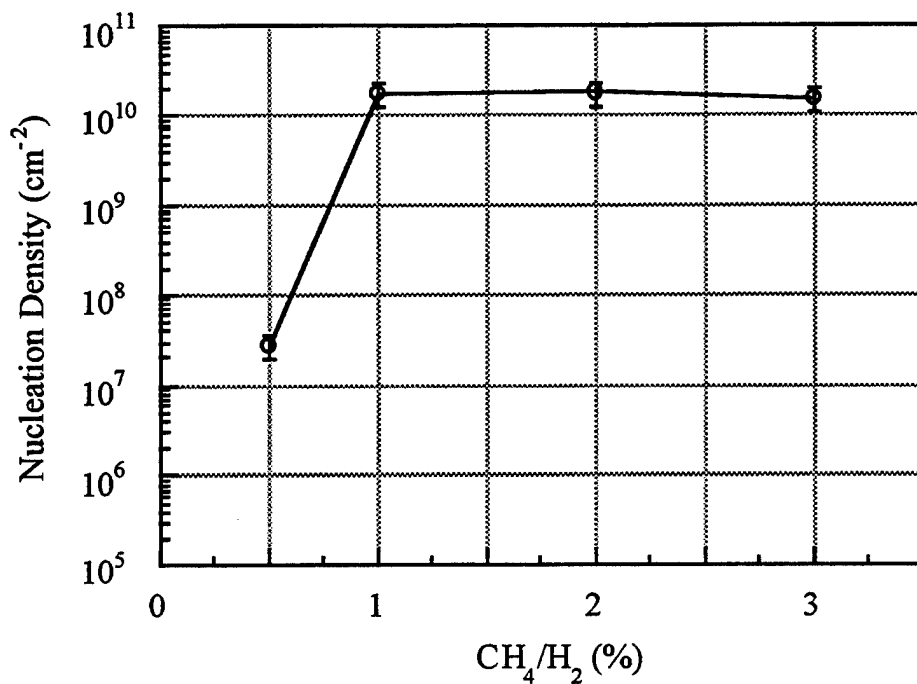


Figure 4.10 - Nucleation density vs. carbon concentration at constant integrated bias current.

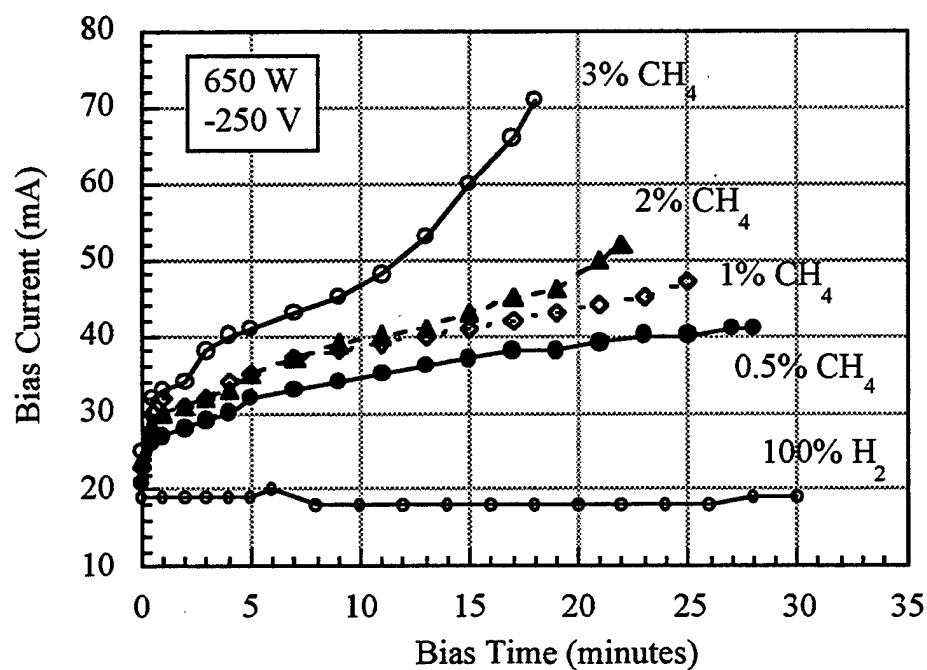


Figure 4.11 - Bias current vs. time for various carbon concentrations.

Nuclei sizes for ion-assisted nucleation pretreatments with different carbon concentrations were estimated from the SEM images and are shown in Figure 4.12. Without sophisticated image analysis and statistical methods only rough approximations were made, but useful information was still obtained. The nuclei size increased approximately linearly as shown in Figure 4.12, despite the decreased deposition time required to maintain the integrated bias current as the carbon concentration increased. The data point for the 0.5%  $\text{CH}_4/\text{H}_2$  experiment is not shown since the nuclei could not be resolved with SEM following the ion-assisted pretreatment. The nucleation density for this case was estimated by deposition under unbiased MPCVD conditions for 30 minutes to grow the nuclei to a resolvable size.

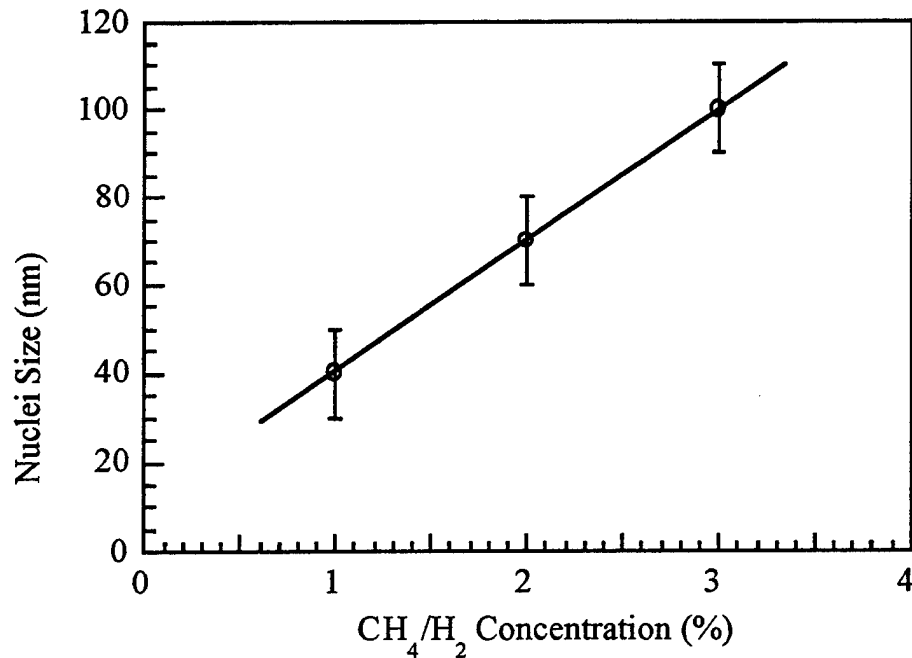


Figure 4.12 - Maximum nuclei size as a function of  $\text{CH}_4/\text{H}_2$  concentration for constant integrated bias current.

Direct measurements of the absolute ion species' fluxes under various conditions were desirable, but not possible, in the MPCVD system. Therefore, estimates of the relative ion species' fluxes were made simply by measuring the bias current under conditions which were essentially identical except for the gas phase chemical environment. Since the plasma conditions were intimately coupled to the gaseous

environment in this system, this measurement is not ideal due to plasma differences (dissociation fraction, ion temperature, electron temperature, etc.) as the carbon concentration varies. The negative substrate bias was applied for a pure  $H_2$  plasma and later 2%  $CH_4$  was added to the plasma environment. The bias current versus time was measured for both environments and a typical set of data is shown in Figure 4.13. At -250 V bias conditions, the bias current measured in pure hydrogen was 20 mA and relatively stable over time. Methane (2%  $CH_4/H_2$ ) was added to this system without any other changes and the bias current immediately increased to 36 mA. This behavior is different from that reported by other researchers who observed a decrease in total bias current with additions of methane [30]. Continued bias in the 2%  $CH_4/H_2$  environment led to bias current increases with time as observed in Figure 4.13; such increases in bias current with time were always observed for successful ion-assisted nucleation and are attributed to ion-induced electron emission. This phenomenon will be discussed in detail in a later section and in chapter 5.

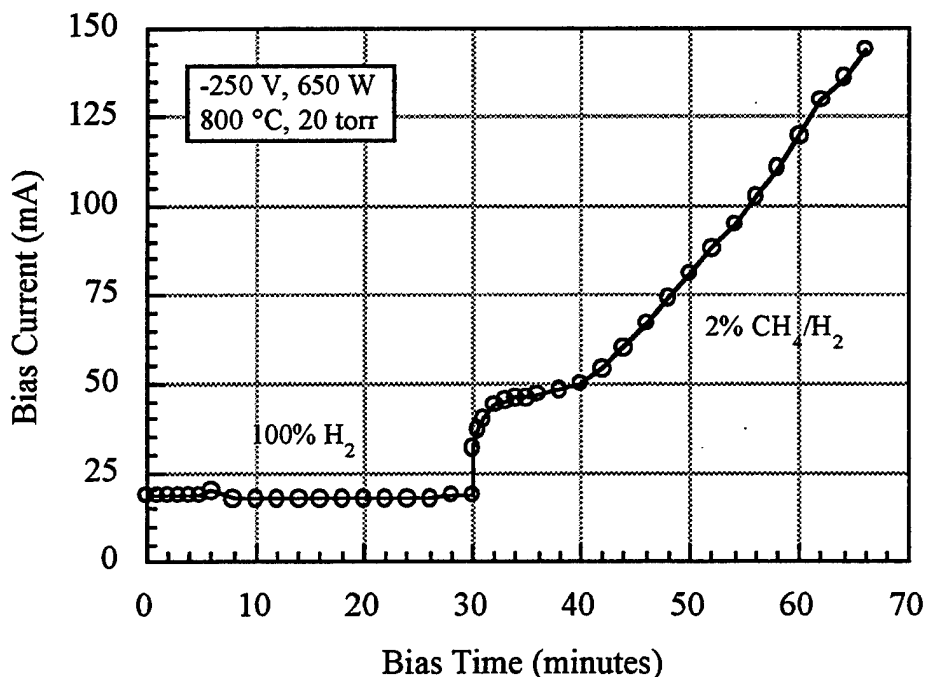


Figure 4.13 - Bias current as a function of the bias time in a 100%  $H_2$  followed by methane addition to 2%  $CH_4/H_2$  environment under the same conditions.

#### 4.44 Sequential Deposition Using Bias

As important as the roles of ion energy, ion flux, and substrate temperature are for ion-assisted nucleation, plasma chemistry issues also are critical for understanding the mechanism of this process. Although the substrate isolation experiments confirmed the role of ion energy as a controlling parameter for nucleation enhancement, the significance of the chemical nature of the ions for the process was still not clear. Were energetic particles required to simply provide energy to overcome the nucleation barrier(s), or was the chemical nature of the energetic species critical for the nucleation mechanism? If energy transfer alone is the critical issue, nucleation enhancement should not depend on the chemical nature of the energetic species; carbon ions or another energetic species such as argon should be equivalent. If, however, energy transfer is not the only issue, then a specific chemical species such as energetic carbon ions may be required. Unfortunately, investigation of the role of chemistry in this process is not an easy task. It is very difficult to probe the complex chemical environment of the plasma with any certainty, much less determine what the near-surface ion species are present. Optical emission spectroscopy (OES), laser-induced fluorescence (LIF), and resonance-enhanced multiphoton ionization (REMPI) are among the techniques which can be used for ion and neutral species spatial measurements, but these were not options in the available deposition systems.

The sequential reactor described previously (see section 2.3) was used to investigate the role of ion chemistry under bias conditions. A brush contact was added to the rotating substrate plate such that a negative bias was applied only while the substrate resided over a specific emitter. In this scheme, one substrate on the rotating plate was only exposed to the bias during its residence over the hydrogen emitter while the second substrate was exposed to bias conditions only while it passed over the carbon emitter. During the rest of the cycle, the substrate was unbiased. This experiment provided a means to separate the effects of hydrogenic ion bombardment ( $H^+$ ,  $H_2^+$ ,  $H_3^+$ ) and carbon ion bombardment ( $CH_4^+$ ,  $CH_3^+$ , etc.) under otherwise identical nucleation conditions.

The deposition conditions and results for the sequential bias experiments using only a hydrogen-filament emitter and a glow-discharge sputtered carbon emitter are shown in table 4.6. For these experiments, half of each Si substrate was pre-scratched with diamond powder as a control. Substrate temperatures between 750 and 800 °C were used for each experiment. Following the bias pretreatment, the substrates were exposed



to normal growth conditions (either in the sequential reactor or MPCVD) for a quick, but non-quantitative, assessment of the nucleation enhancement.

Sample	Bias Time	Bias Voltage	H <sub>2</sub> -Emitter Scratched	H <sub>2</sub> -Emitter Unscratched	C-Emitter Scratched	C-Emitter Unscratched
BEN013	60 min	-300 V	normal film	no film	no film	no film
BEN014	80 min	-200 V	normal film	no film	no film	no film
BEN017	250 min	-150 V	normal film	no film	normal film	<b>thin film</b>
BEN018	250 min	-100 V	normal film	no film	normal film	<b>thin film</b>
SBEN099	300 min	-130 V	normal film	no film	normal film	<b>thin film</b>

Table 4.6 - Deposition conditions and results for sequential deposition with separate carbon and hydrogen applied bias.

The results can be summarized as follows. At bias voltages of -200 V or higher (more negative), no film deposition was observed on the unscratched region of either the carbon biased or hydrogen biased substrate. Although a film typical of unbiased sequential deposition was observed on the scratched region for the hydrogen biased sample, no film was deposited on the scratched region of the carbon biased sample. At bias voltages between -100 V and -150 V, films typical of unbiased deposition were observed on both of the scratched substrates, but the carbon biased films were slightly thinner as estimated from interference fringes. This suggests that the carbon ion bombardment reduced the nucleation/growth on the scratched samples with the effect being larger at higher bias voltages. While no deposition was observed on the unscratched Si exposed to the hydrogen bias between -100 V and -150 V, a thin film was deposited on the unscratched substrate region exposed to the carbon bias. Here, the carbon bias produced nucleation on untreated Si in the sequential deposition scheme. Note that the pretreatments times are considerably longer compared to non-sequential methods due to the duty cycle for sequential deposition. Raman spectra are shown in Figure 4.14 for each of the regions where sequential ion-assisted pretreatments were successful for sample BEN017. Unbiased sequential deposition was continued on this sample for 10 hours at 850 °C and sequential deposition conditions which deposit good quality diamond films. All of the region have similar Raman spectra with a distinct 1332  $\text{cm}^{-1}$  diamond peak and non-diamond features between 1400 and 1600  $\text{cm}^{-1}$ .

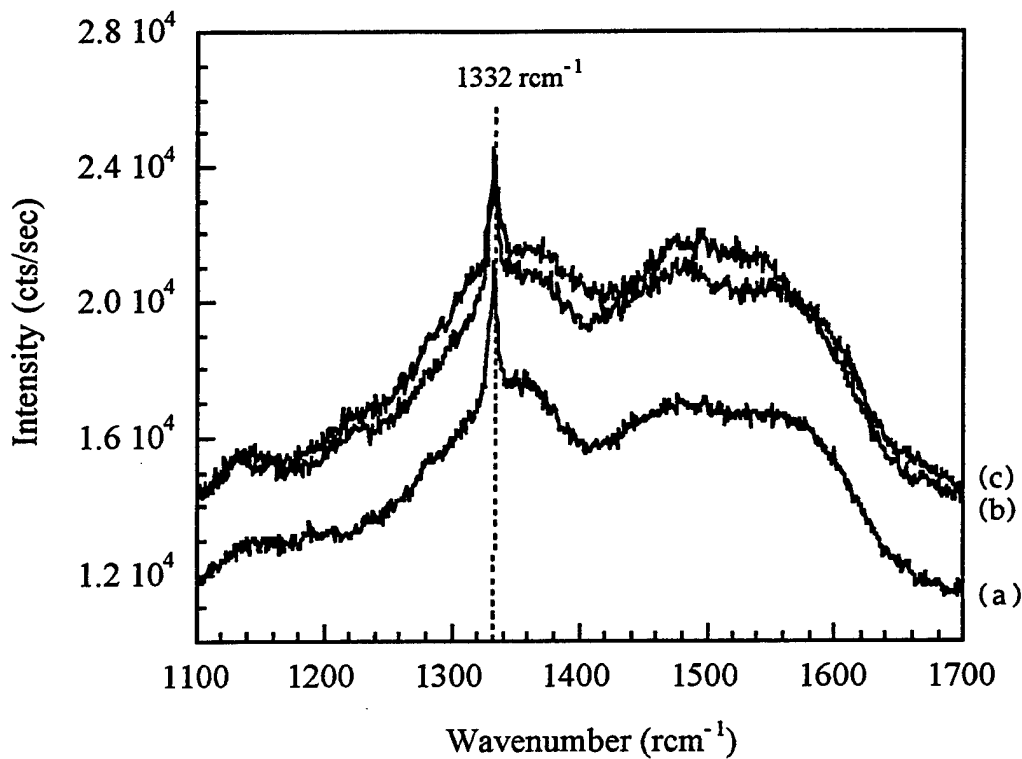


Figure 4.14 - Raman spectra for sample BEN017 deposited in the sequential reactor under bias conditions: (a) Biased hydrogen emitter/scratched substrate, (b) Biased carbon emitter & scratched substrate, (c) Biased carbon emitter & unscratched substrate.

Although the sequential deposition experiments suggest that the carbon ions lead to nucleation enhancement while the hydrogen ions do not, another experiment was required to confirm this effect. Since the carbon emitter is simply a glow discharge in He which sputters carbon off a graphite target, the effects observed may be attributed to energy transferred from the He ions to the substrate surface rather than a result of carbon ion bombardment. To check this hypothesis, the sequential reactor was set up with unbiased hydrogen and carbon emitters and a biased He emitter following the carbon emitter exposure. The emitter exposure sequence was unbiased hydrogen, unbiased carbon, biased He, and then back to the start of the cycle. No deposition was observed on the unscratched region of the substrate in this scheme which indicates that the effects of He bombardment did not lead to nucleation enhancement. Growth was still observed on the scratched half of the substrate showing that the conditions were otherwise correct

for diamond deposition. A similar experiment was also done with an Ar biased emitter instead of a He biased emitter following the hydrogen and carbon unbiased exposure. Results similar to those for He bias were observed with growth only on scratched regions. The parameters for these experiments are shown in Table 4.7.

Sample	Bias Time	Bias Voltage	Bias Emitter	Bias Emitter Unscratched	Bias Emitter Scratched	No Bias Scratched
BEN020	240 min	-150 V	Helium	no film	normal film	normal film
BEN021	210 min	-150 V	Helium	no film	normal film	normal film
BEN022	135 min	-240 V	Helium	no film	normal film	normal film
SBEN100	265 min	-150 V	Argon	no film	normal film	normal film

Table 4.7 - Deposition conditions and results for sequential deposition with exposure to hydrogen, carbon, and biased He or Ar.

These results strongly suggest that energetic carbon ions are required for nucleation enhancement in this process. The bombardment of the substrate with non-carbon energetic species produced no significant nucleation enhancement. Therefore, an energy transfer mechanism alone cannot account for enhanced diamond nucleation under sequential bias conditions. The importance of carbon ions for the ion-assisted nucleation process also points out that the integrated bias current is not the most appropriate parameter to maintain to gain the most information. Although not possible given the experimental set-up, it would be better to maintain a constant carbon ion flux to the surface since these ions control the process.

#### 4.45 Role of Secondary Electron Emission

For constant bias voltage conditions in the MPCVD system, the bias current was observed to increase significantly during the ion-assisted bias pretreatment for CH<sub>4</sub>/H<sub>2</sub> environments. This was shown previously in Figures 4.11 and 4.13 and is illustrated again in Figure 4.15 for several experiments under similar conditions. Although run-to-run variability due a number of factors is clearly present, the overall trend is similar. Increased nucleation densities were correlated with increased bias current as discussed previously with regard to Tables 4.3 and 4.4. For H<sub>2</sub> plasmas under applied bias, the bias

current remained relatively constant (see Figures 4.11, 4.13) without the increases with time observed for the  $\text{CH}_4/\text{H}_2$  environments.

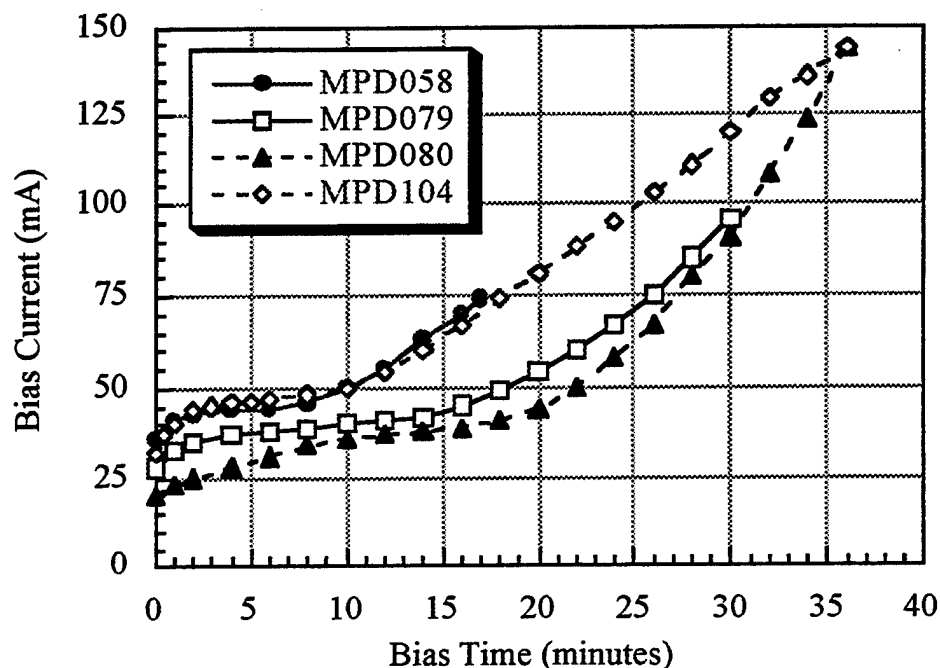


Figure 4.15 - Measured bias current as a function of time during several similar ion-assisted nucleation pretreatments.

These bias current phenomena are attributed to ion-induced electron emission in the ion-assisted diamond nucleation process. Increases in bias current due to increased electron emission for diamond films compared to the substrate material have been previously observed [30, 42]. It has also been reported that diamond or DLC material in close proximity to Si substrates during MPCVD bias pretreatments was required to obtain high bias currents and high nucleation densities [34, 43]. These results suggest that diamond and/or DLC emit electrons more efficiently than silicon and other substrate materials. In fact, Stoner, *et al.*, have utilized the electron emission properties of diamond compared to metals to develop an etching process for diamond based on the ion-bombardment and emission of electrons in ion-assisted hydrogen plasmas to selectively and anisotropically etch diamond [42].

*Secondary electron emission* is the generic term for the process by which electrons are emitted from the surface through interaction with electrons, ions, neutrals, metastables, etc. This is a very complicated area of surface physics which has been

studied in great detail. Secondary ion emission due to ion bombardment, referred to in this thesis as *ion-induced electron emission*, is characterized by  $\gamma$ , the 2nd Townsend coefficient, which is defined as the ratio of electrons emitted per incident ion. The physical property which governs electron emission is the work function, defined as the difference between the vacuum and Fermi levels, which is related to the energy required to remove an electron from the material. The work function is extremely sensitive both to surface structure and contamination. Low work function surfaces naturally yield higher electron emission than do surfaces with high work functions under the same conditions [44]. From a compilation of the limited available data, the following expression has been formulated to describe the qualitative dependence of  $\gamma$  [45]:

$$\gamma = \alpha(\beta W_i - 2W_f) \quad 4.6$$

In this equation,  $\alpha$  and  $\beta$  are constants determined from a least-squares fitting of the experimental data,  $W_i$  is the potential energy of the bombarding species, and  $W_f$  is the work function of the surface. For species bombardment in the low-energy regime (< 1 keV) it has been determined that the electron emission is not strongly dependent on the kinetic energy of the incident species, but rather is dominated the potential energy of the species [45]. Therefore, for a given potential energy, the induced electron emission will be greater for surfaces with lower work functions. Estimates for the work functions of various forms of carbon and silicon are listed in Table 4.8.

Material	Work Function (eV)	Comments/Reference
Silicon	4.85	n-type [46]
"	4.91	(100) orientation [47]
"	4.60	p-type, (111) orientation [46]
"	4.33	n-type, $N_D = 7 \times 10^{14} \text{ cm}^{-3}$ [48]
"	4.4 - 4.7	[47]
SiC	4.8	(0001) crystal face [49]
Carbon	4.0 - 4.8	Graphite [47]
Diamond	2.7	Intrinsic diamond (H-terminated) [50]
DLC	3.6	[48]

Table 4.8 - Carbon and silicon work functions.

Since the work function is extremely dependent upon both the structure and the surface characteristics of the material under investigation, the different forms of carbon may possess different work functions. For the ion-assisted nucleation process, the excess of atomic hydrogen in the system is thought to result in the hydrogen termination of the surfaces. Therefore, the work function for surfaces which are hydrogen-terminated are most relevant, but this data is typically not available.

Ion-induced electron emission from the substrate during the ion-assisted nucleation process explains the experimentally measured bias current increases in the following way. The measured bias current is the sum of the ions incident on the surface and the electrons emitted from the surface. Since the voltage is held constant during the ion-assisted process, increased electron emission and/or the creation of additional ions in the sheath are the only means for this current to increase. The electrons emitted from the Si surface under bias conditions result from photoemission and from ion-induced electron emission. The effects of photoemission in microwave plasma discharges are not well understood. However, the photoemission yield of most materials for photons in the visible and near ultraviolet wavelength (UV) range is typically several orders of magnitude smaller than the emission of electrons by ion bombardment so this contribution was ignored [36].

If carbon has a higher 2nd Townsend coefficient,  $\gamma$ , than silicon, the number of electrons emitted will increase as carbon is deposited on the Si substrate during the nucleation process. This is a simplification of the true situation since there is a thin interfacial SiC region at the surface as well. In either case, an increase in  $\gamma$  will increase the bias current since the electrons leaving the surface will be accelerated by the sheath field. Electrons emitted from the surface due to bombardment by an incident ion have an energy typically of 5 - 10 eV [36] and a mean free path on the order of the sheath thickness. However, the mean free path is the distance at which  $1/e = 36\%$  (see equation 3.2) have not collided, meaning that 63% of the emitted electrons have collided. Since the electrons are accelerated away from the substrate by the sheath field (which is strongest near the substrate), they can gain enough energy to ionize gaseous species in the sheath upon collision. This produces an ion and an additional electron which, in turn, can be accelerated and cause further ionization. In this manner, a small increase in  $\gamma$  can increase the measured bias current significantly.

This bias current model depends upon a change in the electron emission for carbon with respect to Si under carbon and hydrogen ion bombardment. Many materials have ion-induced electron emission variations of at least a factor of two with as little as a monolayer of adsorbed material [36]. Any experimental data for the 2nd Townsend

coefficient for both carbon and Si in the literature is scarce. The electron emission coefficient for carbon (structure not reported) under bombardment by slow (energy not reported)  $H_2$  ions has been reported as 0.014 [44]. This low value means that only a small fraction of incident ions causes electron emission and so the experimentally measured bias current is dominated by ions with electrons as the minority carrier. This parameter is extremely sensitive to the form of the material at the surface and it also depends upon the ion bombarding species and energies. None of these are known accurately. However, the work functions for carbon compared to silicon and the emission characteristics of diamond and DLC films reported in the literature suggests this explanation may be valid.

For the bias process in a pure  $H_2$  environment, the bias current should remain relatively constant with time as was observed in Figure 4.11. Under these conditions, the Si surface is relatively stable and its 2nd Townsend coefficient should not vary with time. On the other hand, if carbon is deposited during in the ion-assisted process in a  $CH_4/H_2$  environment, this model predicts that the bias current will increase with time since the increasing level carbon on the surface results in emission of more electrons due to the higher 2nd Townsend coefficient. However, when a full film of carbon has been deposited and no Si is left at the surface, the measured bias current would be expected to level out. This behavior was not observed in the bias experiments of the previous section, but more time may be required to see this effect; the deposition time for the experiments above was limited by the plasma stability which often required process shutdown at longer times. The leveling of the current at longer bias times, and in some cases current decreases, has been observed by other researchers [51-53]. Decreases in the bias current may be caused by ion-induced damage to the carbon films which may reduce the electron emission.

Plotting the initial bias current versus temperature from Table 4.4 produces Figure 4.16. The temperature independence of the bias current confirms that thermionic emission of electrons does not play a dominant role in the measure bias current. If this process were significant, the bias current would rise steeply with temperature due to the strong temperature dependence of thermionic electron emission. This temperature independence of the bias current has been observed by other researchers in similar experiments [30].

The dependence of the initial bias current on carbon concentration for the ion-assisted process is shown in Figure 4.17. The bias current increases slightly as carbon concentration is increased. This result differs from that of Beckmann, *et al.*, who found that increasing the methane concentration in the gas phase decreased the overall ion density in the plasma and led to lower overall current [30]. As previously observed in

Figure 4.11, although the initial bias current is not significantly different for the different carbon concentrations, the increase in bias current with time is more rapid for higher carbon concentrations. This result is consistent with the electron emission arguments since more carbon is deposited on the surface at a given time for a higher carbon concentration.

While the initial bias current was not a strong function of either the carbon concentration or the substrate temperature, it did vary significantly with bias voltage as shown in Figure 4.18. This behavior, too, is explained by ion-induced secondary electron emission. The bias current increases with increasing voltage most likely result from the stronger electric field in the sheath which accelerates the emitted electrons and therefore increases the ion flux through the ionization probability. Furthermore, the size of the secondary discharge over the substrate appeared to be dependent upon the applied bias voltage. Larger voltages produced secondary discharges which covered more of the substrate and therefore, due to the larger area, the higher total bias current.

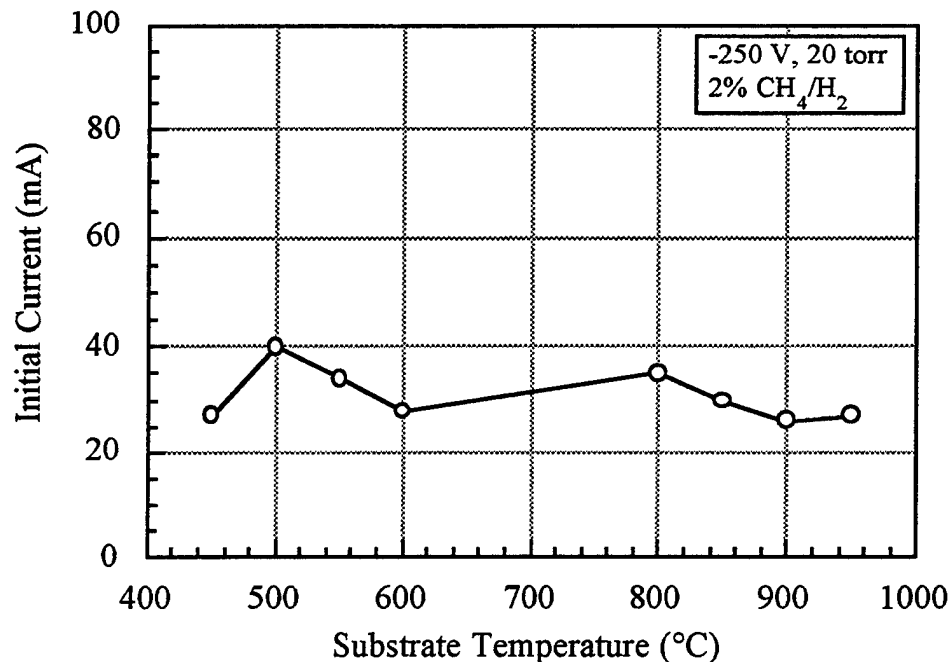


Figure 4.16 - Initial bias current as a function of substrate temperature under constant bias voltage conditions.



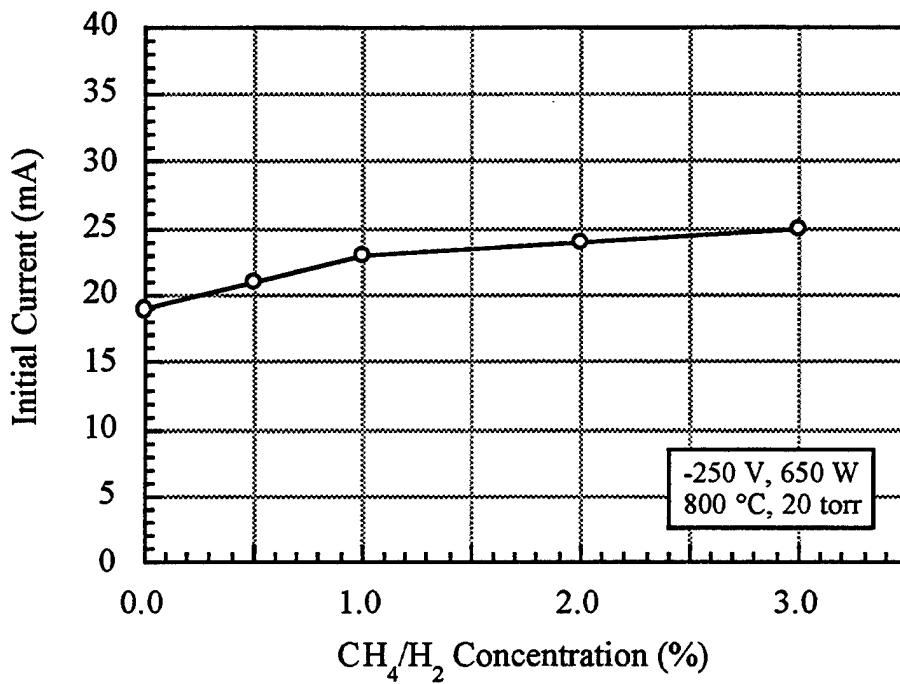


Figure 4.17 - Initial bias current as a function of carbon concentration in the gas phase under constant bias voltage conditions.

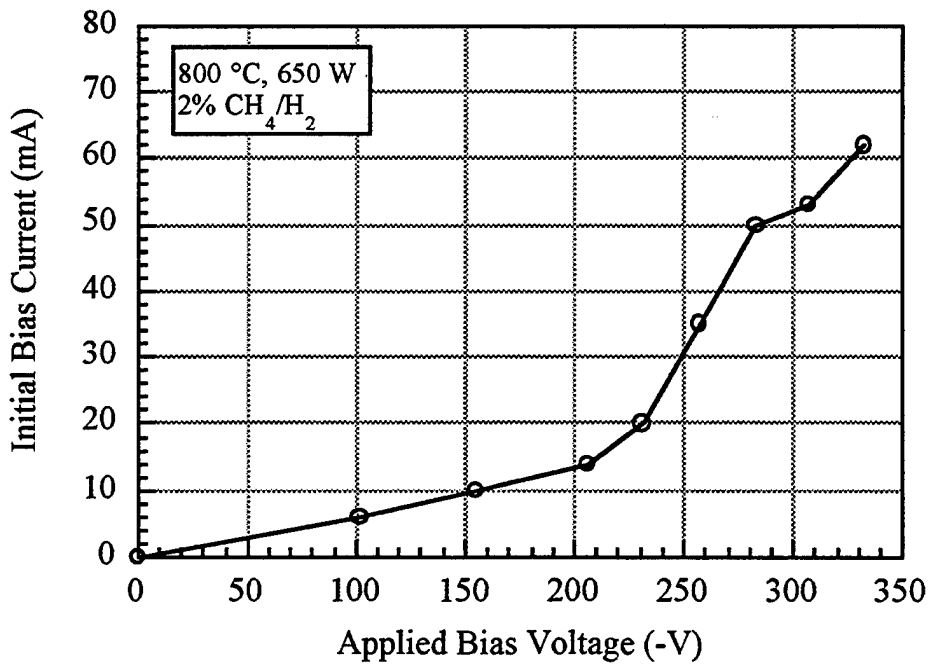


Figure 4.18 - Initial experimental bias current as a function of the applied negative bias voltage .

#### 4.46 Retarding Field Probe Measurements

The distribution of ion energies at the surface of the substrate during the bias is an important parameter for understanding the physical processes which occur for nucleation. Experimental measurements of this distribution are difficult, but critical for modeling of the ion-assisted process. Researchers have previously reported average ion energies encompassing a large range from 10 - 200 eV [32, 54]. Given the relatively high pressure in this system, it is unlikely that the ions possess the full bias voltage when they reach the substrate due to collisions in the sheath region. This subject will be discussed in more detail in the next chapter.

Accurate experimental measurement of ion energy distributions is best done with a collection probe at the substrate surface connected to an energy analyzer or a mass spectrometer (ionizer off to measure process ions). This measurement option was not available in the MPCVD experimental set-up. However, a reasonable estimate of the ion energy distribution was obtained using a simple retarding field probe. The basic idea for a retarding probe measurement involved electrical isolation of a probe at the substrate surface. This probe was then biased with respect to the substrate and the collected current was measured. When the probe is biased positive with respect to the surrounding substrate, incident ions (cations) with energies less than the voltage difference between the probe and substrate will not be collected. By varying the probe voltage and measuring the current collected, the ion energy distribution was estimated.

The experimental set-up for the probe is shown schematically in Figure 4.19. A 0.125" diameter hole was drilled through the molybdenum substrate susceptor to accommodate the probe. The probe itself consisted of an outer stainless steel tube (OD = 0.125") with an inner alumina 2-hole thermocouple tube for electrical isolation. A platinum wire threaded through the ceramic tube and spot-welded to a small stainless steel plate served as the collector. The end of the ceramic tube was beveled so that the collector was positioned slightly below the level of the top of the stainless tube. A fine nickel mesh (75% transparent) was spot-welded to the top of the outer tube to ensure that the outer tube and top of the probe were at the same bias potential. This mesh also helped to minimize electric field distortion under bias conditions due to the probe geometry. Since the probe fit tightly in the hole in the substrate, the outer probe tube was at the same potential as the substrate under bias conditions. The top of the probe was positioned so that its surface was even with that of the substrate. The leakage between the probe and substrate was  $\sim 2 \mu\text{amp}$  at 40 volts and 800 °C.

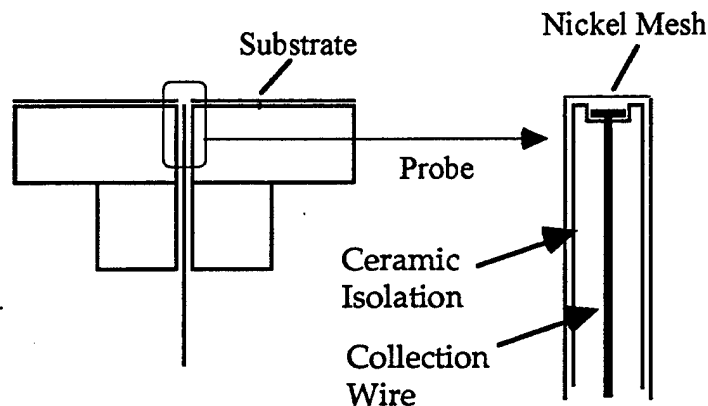


Figure 4.19 - Schematic of the retarding field probe for the ion energy distribution measurements in the MPCVD system.

Figure 4.20 shows the total retarding probe current as a function of probe voltage with respect to the substrate under ion-assisted pretreatment conditions of -275 V, 2% CH<sub>4</sub>/H<sub>2</sub>, 800 °C, and 20 torr. As the probe voltage increased, ions were repelled from the collector and the current measured decreased. Electrons in the probe vicinity were also collected as evident from the current passing through zero and changing from positive (ion dominated) to negative (electron dominated) values as the probe was biased more positive with respect to the substrate. Electron collection was not desirable since the contribution from electrons must be removed from the total probe current to obtain the ion current.

The electron current was estimated by measuring the collection efficiency of electrons as a function of the probe bias voltage. In a vacuum ( $\sim 10^{-6}$  torr) environment, the probe was placed within an inch of a thoriated-tungsten filament which served as an electron source. The electrons emitted from this filament at high temperature ( $\sim 2000$  °C) were accelerated (+5 V) in the direction of the probe which measured the collected electron current as a function of bias voltage. This curve is also shown in figure 4.20 and it is observed that the collection of electrons (negative current) increases and levels with increasing bias voltage. Since the actual electron current collected from the filament was orders of magnitude lower than the total current measured under bias conditions in the MPCVD system, this curve was scaled so the high voltage tail matched closely with that for the total current. This is valid since the total current is nearly all electrons at the high

bias voltages. To obtain the ion current as a function of probe voltage for the bias experiment, the electron current was subtracted from the total current in figure 4.20.

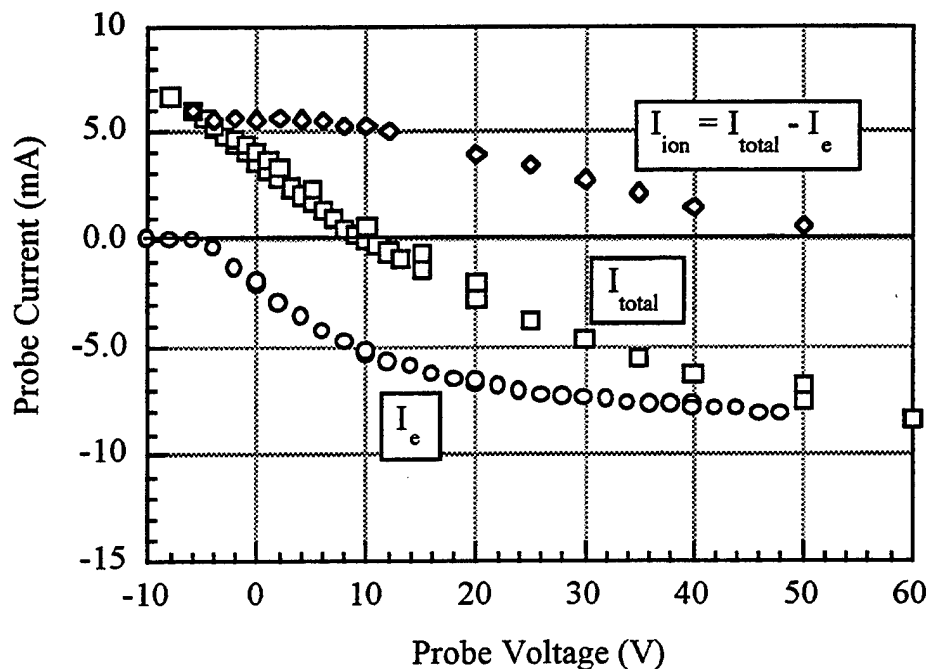


Figure 4.20 - Total current ( $I_{total}$ ), electron current ( $I_e$ ), and resulting ion current ( $I_{ion}$ ) from retarding probe measurements.

Determination of the ion energy distribution from the ion current versus probe voltage data was not a straightforward process due to physics of the charged species collection. Not only was subtraction of the electron current necessary, but the dependence of the efficiency of ion and electron collection on the collection voltage had to be considered. The measured ion current was a convolution of the ion energy distribution and the ion collection efficiency of the probe. Therefore, simple differentiation of the ion current with respect to voltage does not give the proper distribution of ion energies since this assumes that the collector efficiency is constant for all probe voltages. The ion collection efficiency was estimated from the measured electron current as a function of probe voltage. Since the electrons were accelerated through a voltage large compared to their energy distribution, the probe "sees" a roughly monoenergetic electron beam at  $\sim 5$  V. The ion collection efficiency was assumed to be similar to that of the electrons since the mechanism of collection is no different for ions other than the opposite charge effects.

Therefore, the electron data was reversed as shown in figure 4.21 to obtain the ion collection efficiency. At low probe voltages the collection efficiency is near unity, but this value drops to zero with increasing probe voltage since the ions are retarded. This collector is not an ideal collector which would have an abrupt, step-like, cut-off.

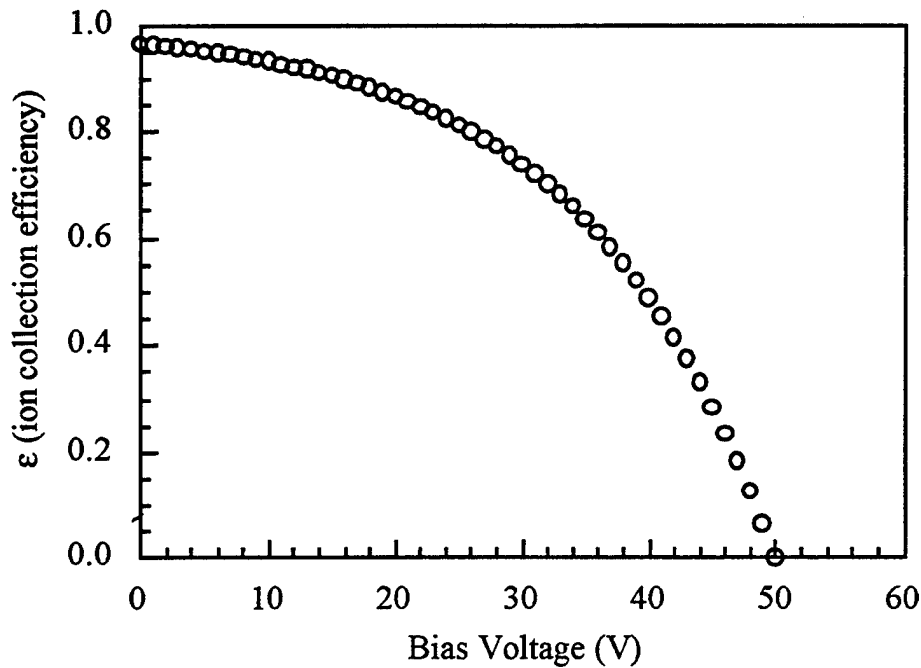


Figure 4.21 - Response function for ions using the retarding probe.

Given the measured ion current and the ion collection efficiency, the convolution theorem can be applied to deconvolute the ion energy distribution. The ion current,  $I(E)$ , is the convolution of the ion energy distribution,  $N(E)$ , and the collection efficiency  $\epsilon(E)$ . This convolution is written mathematically as follows:

$$I(E) = \int_{-\infty}^{\infty} n(x)\epsilon(E-x)dx = n(E)*\epsilon(E) \quad 4.7$$

The convolution theorem states that the Fourier transform,  $F$ , of a convolution is equal to the product of the Fourier transforms of the two convoluted functions:

$$F[I(E)] = F[n(E)] \cdot F[\epsilon(E)] \quad 4.8$$

Dividing the Fourier transforms of the ion current and collection efficiency and taking the inverse Fourier transform,  $F^{-1}$ , of this ratio gives the ion energy distribution.

$$n(E) = F^{-1} \left[ \frac{F[I(E)]}{F[\epsilon(E)]} \right] \quad 4.9$$

In theory this deconvolution is possible, but in reality, it is not a simple task. Depending upon the form of the functions, numerical deconvolution may or may not be feasible [55]. Attempts at this problem both using Fourier transform and Laplace transform methods did not give a solution. The Fourier method resulted in unstable oscillations, likely due to high frequency harmonics [56], while the method using Laplace transforms was too difficult to solve. Therefore, a estimate was obtained simply by assuming a gaussian peak shape for the ion energy distribution and convoluting it with the ion collection efficiency using equation 4.7. The parameters of the gaussian (mean and width) were adjusted until the best fit of the ion current data was obtained. The measured ion current and calculated ion current are shown in Figure 4.22.

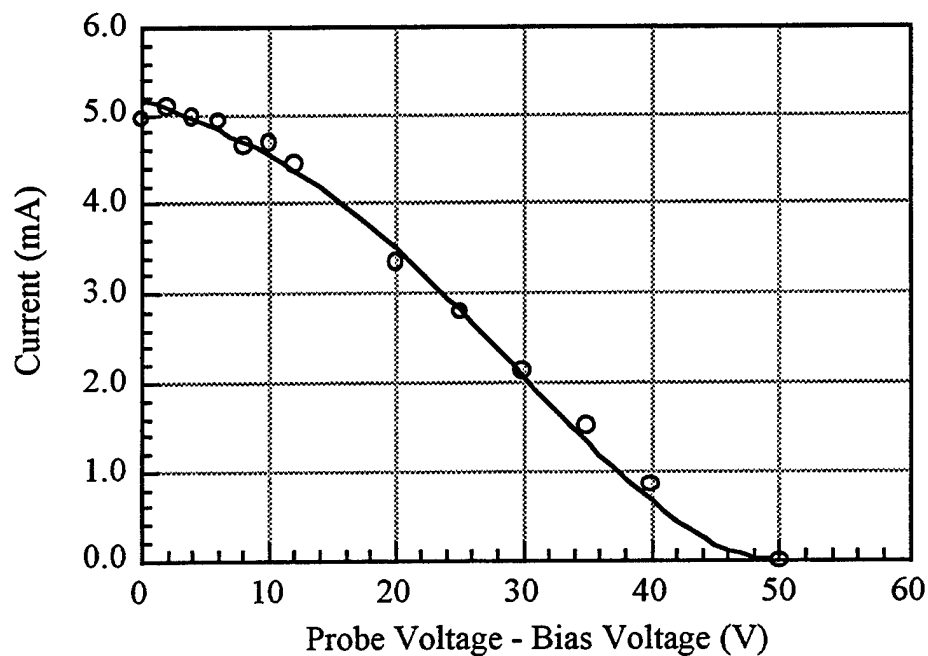


Figure 4.22 - Measured ion current (circles) and the ion current calculated (solid line) using the convolution theorem.

The gaussian peak which was used to obtain this fit is shown in Figure 4.23. The convolution of the ion energy distribution and collector efficiency was also done assuming a maxwellian distribution, but the fit to the ion current experimental data was significantly better for the gaussian distribution. Gerber, *et al.*, also measured the ion energy distribution with a retarding field probe [26] during bias pretreatment in a similar system and found the ion energy distribution peaked at  $\sim 80$  eV for a  $-250$  V applied bias. The discrepancy between these two values is small enough to be explained by differences in the plasma systems and process parameters which affect the ion energy distributions. Furthermore, the ion energy distributions estimated by Gerber, *et al.*, did not consider the ion collection efficiency and were obtained by simply differentiating the bias current with respect to energy.

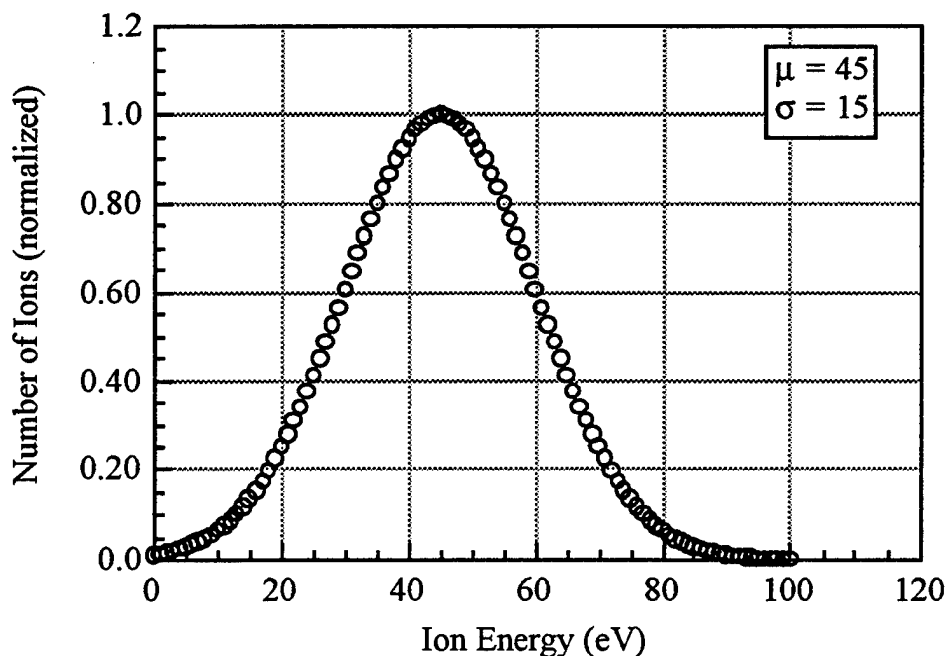


Figure 4.23 - Calculated ion energy from the retarding probe measurements. A gaussian peak shape and the convolution theorem were used.

#### 4.47 Characterization of Bias-Deposited Material

The research of this thesis, along with that in the literature, confirm that high quality, fine-grained diamond films can be deposited by using the ion-assisted

pretreatment process. However, the nature of the material deposited using a negative substrate bias has been a source of contention. To fully exploit this process, it is important to distinguish whether the ion-assisted process forms diamond nanocrystals, or rather, forms non-diamond carbon configurations which are conducive to subsequent growth of high density polycrystalline films. If the nature of the material deposited in the bias pretreatment is understood, it may be possible to deposit this material using easier and/or more efficient methods. In the past, researchers have suggested that diamond can be nucleated effectively on non-diamond carbon. However, the results from the various carbon surface pretreatments of this thesis did not nucleate diamond effectively. Furthermore, the enhanced diamond nucleation claimed in the literature on SiC and C<sub>60</sub>/C<sub>70</sub> films was only realized under bias deposition conditions [9, 34, 57]. The surface carbon pretreatments discussed in the beginning of this chapter suggest that diamond phase material is the only efficient nucleation site for diamond thin films. All other claims of enhanced nucleation in the literature are not nearly as efficient as the ion-assisted or bias processes which produce nucleation densities several orders of magnitude higher than any other method to date. To fully characterize the material deposited under bias conditions, the techniques discussed in Chapter 3 were used.

Figure 4.24 shows SEM images which are typical for depositions under different ion-assisted pretreatment times. Nuclei produced with bias pretreatments times less than 5 minutes are too small to image clearly. For short pretreatment times, the clusters are isolated with a non-faceted morphology and a broad nuclei size distribution centered around 100 nm or less as observed in Figure 4.24(a). This distribution of nuclei sizes indicates that the clusters are formed throughout the nucleation process rather than at the same time [31]. With increased bias-deposition time, these spherically-shaped clusters grow and then coalesce into a complete film as seen in Figures 4.24(b) and 4.24(c), respectively. The ability to image these films using SEM with only minor charging effects indicated that these films were not extremely resistive as would be expected for high quality diamond; however, this was not a quantitative measure of the electrical properties of these films. The morphology of the deposited nuclei and coalesced film is not characteristic of the facetting observed for high-quality diamond crystals. As discussed previously in this chapter, nucleation densities on the order of  $10^{10}$  cm<sup>-2</sup> were typically observed, but this value is a lower limit since stable carbon nuclei may be significantly smaller than the resolution of the microscope [18]. The resolution limitations imposed by SEM preclude any further structural analysis of the bias-deposited film using this characterization technique. Other more structure-sensitive techniques were required to understand the bias-deposited carbon.



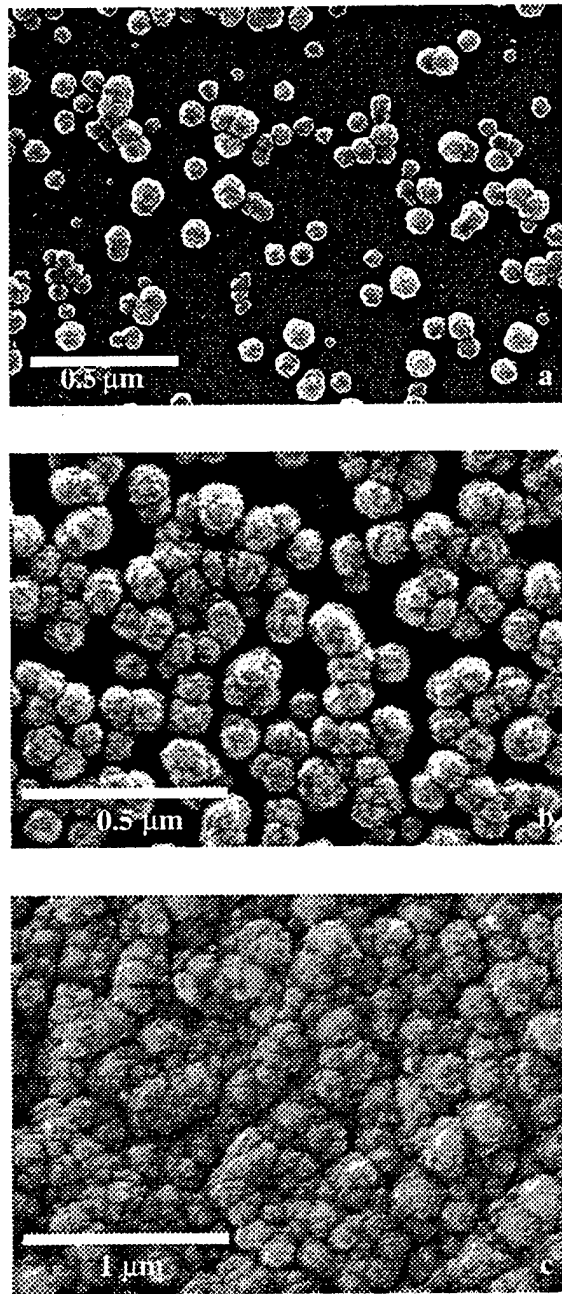


Figure 4.24 - SEM images typical of bias-deposited nuclei as the pretreatment time is increased from approximately 10 minutes (a) to 20 minutes (b) to 60 minutes (c) .

The structure of the films deposited by the ion-assisted pretreatments was better probed with Raman spectroscopy. Micro-Raman spectra were taken for samples deposited under various conditions by the ion-assisted nucleation process. A typical Raman spectrum for material deposited by the ion-assisted nucleation process is shown in Figure 4.25. This spectrum has good signal-to-noise since a relatively large amount of material (full film) was deposited during the 1 hour ion-assisted pretreatment process. Spectra for shorter pretreatment times show no qualitative differences, only reduced signal-to-noise due to the smaller amounts of material deposited on the substrate. The bias-deposited carbon Raman spectrum shows no distinct diamond phonon peak at  $1332\text{ cm}^{-1}$  and has broad non-diamond peaks centered around  $1340$  and  $1590\text{ cm}^{-1}$ . Some researchers have claimed these features to be characteristic of DLC, however, the differences between the peaks shapes and positions for DLC compared to other non-diamond carbon forms are often not distinctive [58, 59]. Comparing to spectra from other bias processes, this spectrum is nearly identical to that of Gerber, *et al.*, [29] but different from that of Stoner, *et al.*, [5] who observed a small "diamond" peak around  $1332\text{ cm}^{-1}$ . Variations in the bias deposition conditions produced similar spectra although the peak positions and shapes varied slightly from those in Figure 4.25. The Raman spectra for different bias voltages, carbon concentrations, and substrate temperatures during the ion-assisted nucleation process are not shown in this thesis since there were no significant differences among them.

The fact that the Raman spectra for the bias-deposited material shows no  $1332\text{ cm}^{-1}$  peak does not necessarily indicate that diamond is not present. It is possible that nanocrystalline diamond in these films may not be observed in the Raman spectra; the high cross-section of non-diamond carbon relative to diamond may obscure the diamond peak ( $1332\text{ cm}^{-1}$ ) within the broad non-diamond peak at  $1350\text{ cm}^{-1}$ . Support for this postulate is shown in the Raman spectra in figure 4.26. These spectra correspond to films deposited by ion-assisted pretreatments of different times (2%  $\text{CH}_4/\text{H}_2$ , -300 V, 15 and 120 minutes, 650 W,  $800\text{ }^\circ\text{C}$ ) as well as that for a similar ion-assisted pretreatment plus subsequent unbiased MPCVD (1%  $\text{CH}_4/\text{H}_2$ , 800 W,  $800\text{ }^\circ\text{C}$ ). The Raman spectra for the two different length bias pretreatments are similar to that shown in Figure 4.25, but subsequent diamond MPCVD shows the  $1332\text{ cm}^{-1}$  peak emerges from within the broad peak at  $\sim 1340\text{ cm}^{-1}$ . These spectra are consistent with the growth of diamond from nanocrystalline diamond nuclei which are not initially observed by Raman spectroscopy due to their size.

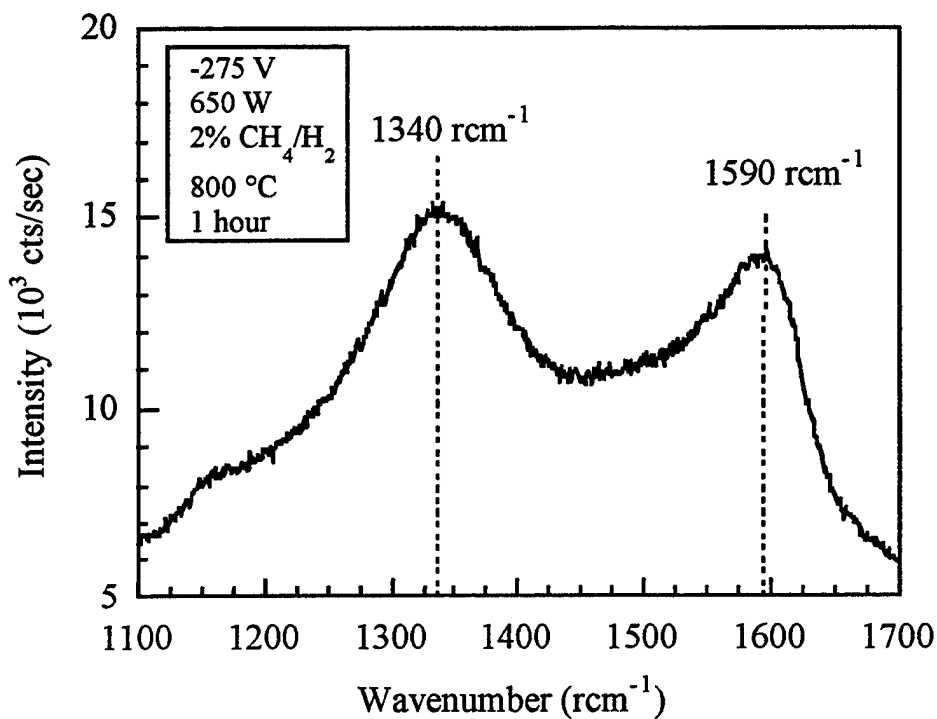


Figure 4.25 - Raman spectrum for 1 hour bias-deposited carbon film.

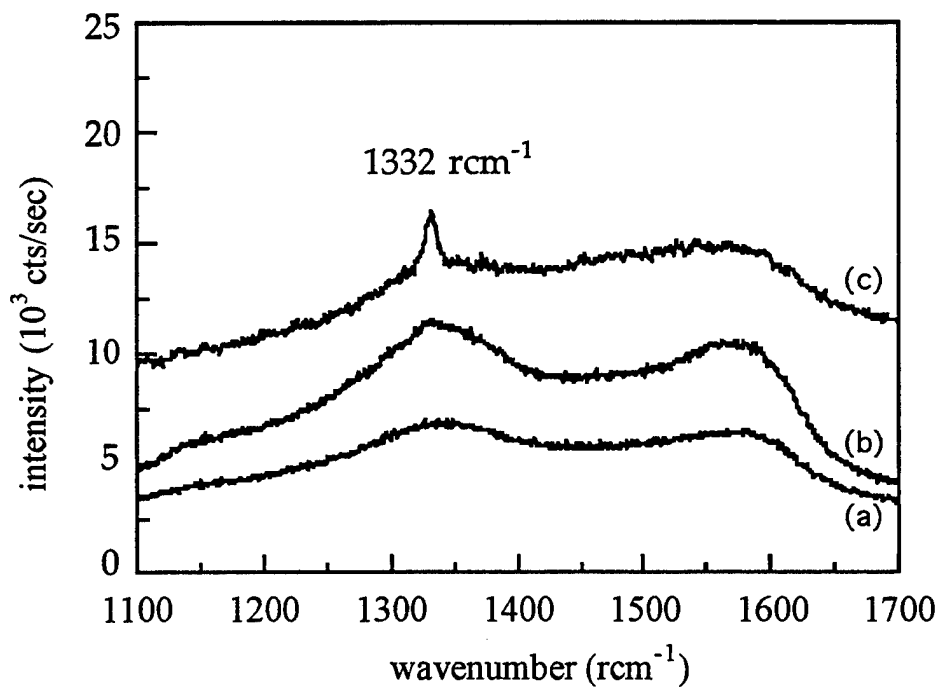


Figure 4.26 - Raman spectra: (a) 15 minute bias deposition, (b) 120 minute bias deposition, (c) 15 minute bias deposition plus 3 hour unbiased MPCVD.

The high nucleation density of the bias-deposited films may also contribute to the apparent poor raman spectra with a large non-diamond component and small diamond peak. Non-diamond carbon is hypothesized to exist at the grain boundaries between diamond crystals and the high sensitivity of this material may mask the small diamond particles. Furthermore, the full width half maximum (FWHM) peak values have been shown in the literature to increase with decreasing crystal size [60, 61].

To investigate the effects of grain size on the raman spectra, diamond was deposited simultaneously on two substrates in the MPCVD reactor to ensure identical deposition conditions. However, the two substrates were pretreated with different processes; one was scratched with 4 - 6  $\mu\text{m}$  diamond powder while the other was nucleated using typical ion-assisted pretreatment conditions. Subsequent MPCVD was carried out for 5 hours at 800°C and 0.5%  $\text{CH}_4/\text{H}_2$ . These conditions produced films several microns thick. The raman spectra for these films are shown in Figure 4.27. The highly nucleated bias-deposited film has a spectrum which is significantly poorer than the scratched sample even though they were deposited under identical growth conditions.

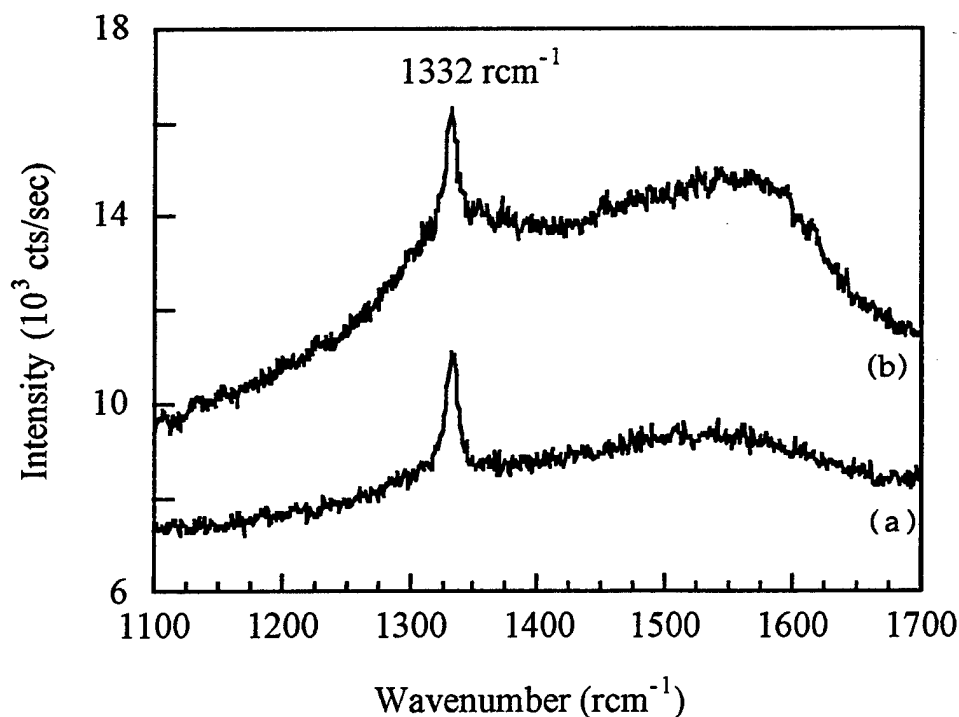


Figure 4.27 - Raman spectra for diamond films grown by MPCVD with (a) diamond scratching and (b) ion-assisted pretreatment.

These results support the postulate that the quality of the films deposited by subsequent MPCVD on bias-deposited carbon is better than indicated by the raman spectra. The non-diamond features in the raman spectra of these films may arise from the carbon deposited at the interface by the ion-assisted nucleation pretreatment and/or the grain boundary material in the nanocrystalline films. Since diamond is relatively transparent to the raman laser light, the material at the interface is probed even for films greater than 10  $\mu\text{m}$  in thickness. The non-diamond carbon present in the interfacial region has a higher sensitivity to raman than diamond, and therefore, may dominate the spectrum.

On the other hand, nanocrystalline films like those produced by the ion-assisted nucleation process and subsequent MPCVD growth have more total grain boundary area than films with micron-sized grains. The surface area to volume ratio is independent of the thickness of these films and gives an estimate of the relative amount of grain boundary area; this intergranular material is expected to be some form disordered carbon and will therefore have significant non-diamond character which leads to the broad peaks around  $1550\text{ cm}^{-1}$ . Simple calculations of the grain boundary vs. diamond volume can be used to estimate the effects of grain boundaries and grain size on the raman spectra. Typically, full diamond films grown on scratched substrates have grain sizes on the order of 1  $\mu\text{m}$  while similar deposited using ion-assisted pretreatments have grain sizes on the order of 100 nanometers. For simplicity, consider films composed of perfect cubes which have coalesced. The surface area to volume ratio for a single cube with sides of length,  $L$ , is given by  $6/L$ . For 1  $\mu\text{m}$  grains, the surface area to volume ratio is  $6 \times 10^4\text{ cm}^{-1}$ . Now consider the same cube volume of material in which the grain size has been reduced a factor of 10 to 100 nm. There are now 1000 smaller grains in this same volume and the surface area to volume has increased  $33/L$  which is  $3.3 \times 10^5\text{ cm}^{-1}$ . Therefore, the increase in the relative grain boundary area as the grain size drops a factor of 10 is only a factor of  $\sim 5.5$ . Similarly, the increase in the relative grain boundary area as the grain size drops a factor of 100 to 10 nm is a factor of  $\sim 50$ . This value differs dramatically from that of Dotter, *et al.*, who have estimated a relative grain boundary surface increase of  $10^4$  for grain sizes for nanocrystalline films in comparison with those in the micrometer range [62]. These estimates do not fully explain the raman results observed for bias-nucleated films since the sensitivity of raman to non-diamond carbon is approximately 50 times higher than for diamond. Although this calculation is too simplistic to be accurate, it suggests that the non-diamond features in the raman spectra are probably not dominated by grain boundary material, but rather arise from the interfacial material deposited by the bias pretreatment.

X-ray photoelectron spectroscopy (XPS) was used to analyze the surface of the Si substrate following both biased and unbiased MPCVD processes of varying duration. This technique provided a quantitative estimate of the relative amounts of material deposited on the substrate under both processes as well as the surface chemical state(s) present. Although unbiased MPCVD on pristine silicon does not produce high densities of diamond nuclei, it is important to understand the nature of the substrate surface prior to the application of the bias. Recall, in all ion-assisted nucleation experiments in this thesis, the substrate was cleaned *ex-situ* with an HF chemical etch, then cleaned with an *in-situ* exposure to a H<sub>2</sub> plasma, and then finally exposed to a CH<sub>4</sub>/H<sub>2</sub> plasma for several minutes to stabilize the system. This *pre-bias* surface is of interest for modeling the ion-assisted nucleation process.

Angle-resolved XPS measurements were done on Si substrates exposed to a 2% CH<sub>4</sub>/H<sub>2</sub> plasma at 650 W, 20 torr, and 800 °C for 15 minutes. Following cool-down in H<sub>2</sub>, the sample was transferred immediately to the XPS system to minimize surface contamination. As the detector takeoff angle (angle between the surface plane and the line from the surface to the detector) is made more glancing (smaller angles), XPS becomes more sensitive to the surface; the effective escape depth of the electrons is shorter due to the longer path length resulting from the low angle. Survey scans indicated the presence of only carbon, silicon, and oxygen and are not shown. High-resolution XPS scans as a function of the detector angle for the Si(2p) and C(1s) regions are shown in Figures 4.28 and 4.29, respectively. As the detector takeoff angle is increased, the Si-Si peak (~99 eV) increases with respect to the Si-C (~101 eV) and Si-O peaks (>102 eV), respectively, in Figure 4.28. This signifies that the carbide and oxide are on top of the Si substrate since the signals for these components become stronger relative to the substrate as the detector angle becomes more and more glancing.

In figure 4.29, the C-Si carbide peak (~283 eV) increases with respect to the C-C peak (~284.6 eV) as the detector angle is increased. This indicates that the carbon-bonded material is on top of the SiC which has formed on top of the Si substrate. The oxygen present in the samples appears to be bound to both the silicon and the carbon. Accurate analysis of the bonding state of this element is difficult due to the relatively small amount present. Since carbon monoxide (CO) and carbon dioxide (CO<sub>2</sub>) are thought to be unstable on the surface, it is assumed that most of the oxygen is bound to the silicon and carbon in the form of oxycarbides.

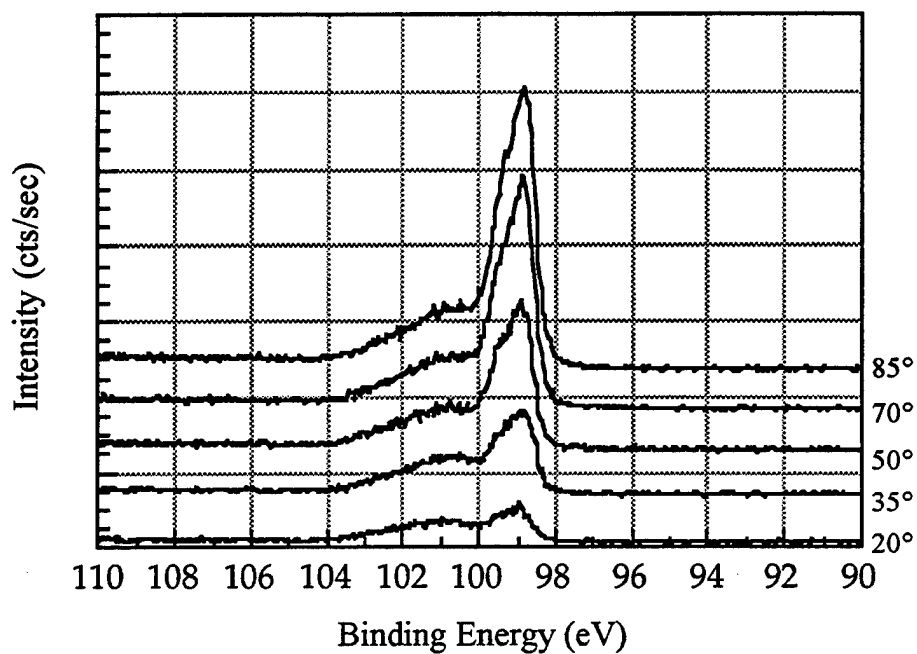


Figure 4.28 - Si(2p) high-resolution angle-resolved XPS scans.

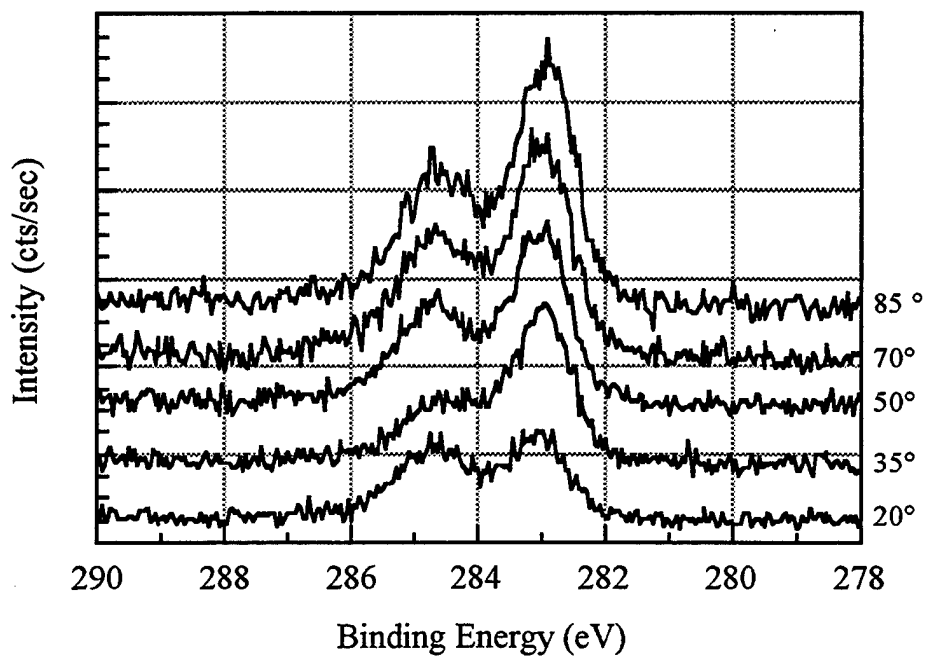


Figure 4.29 - C(1s) high-resolution angle-resolved XPS scans.

The carbon, carbides, and oxycarbides observed by XPS may be present in layers and/or clusters on the silicon substrate. In theory, the thickness of thin films or the coverage of the surface by clusters can be determined using angle-resolved measurements with an XPS system. Consider the attenuation of the silicon substrate signal by a uniform overlayer which is given equation 4.10.

$$\frac{I_{Si}(d)}{I_{Si}(\infty)} = \exp\left[\frac{-d}{\lambda_{Si} \overline{\cos\theta}}\right] \quad 4.10$$

$$\overline{\cos\theta} = \frac{\cos(\theta + \Delta\theta) + \cos(\theta - \Delta\theta)}{2} \quad 4.11$$

In these equations,  $d$  is the layer thickness,  $\lambda$  is the mean free path,  $\theta$  is the detector take-off angle, and the average cosine term,  $\overline{\cos\theta}$ , accounts for the acceptance angle of the detector. For a perfectly uniform overlayer with no intermixing at the interface, the Si attenuation ratio is such that the layer thickness,  $d$ , is constant with angle. For the data from Figures 4.28 and 4.29, the overlayer thicknesses were calculated for the various angles and are shown in Table 4.9.

Detector Take-off Angle (°)	Calculated Effective Overlayer Thickness (Å)
20	11.2
35	15.0
50	16.2
70	17.4
85	17.7

Table 4.9 - Calculated overlayer thickness at various angles for a perfectly uniform single overlayer.

Since the effective overlayer thicknesses calculated using equation 4.10 are not constant with varying detector angles, the single uniform overlayer model on the silicon substrate is not adequate. That is not surprising given the chemical complexity observed in the high resolution scans. It is likely that multiple layers are present which may or may not be



complete and/or uniform. In this case, a model to predict the data becomes more difficult. Analysis of XPS peaks and determination of film thicknesses when compounds form at interfaces, when film layers are not complete, and when surface roughness is present can be extremely complex. Two relatively simple cases are considered for analysis of the angle-resolved XPS data. These are shown schematically in Figure 4.30.

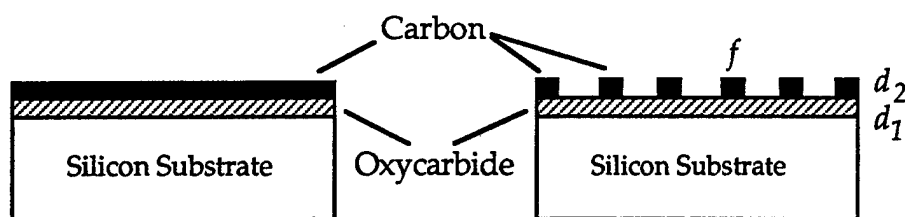


Figure 4.30 - Schematic of substrate surface for XPS model.

The first case shown on the left half of figure 4.30 is two uniform layers, the lower one of silicon carbide/silicon oxide (oxycarbide) with thickness  $d_1$  and the upper layer of carbon with thickness  $d_2$ . The equations which govern this bilayer system are shown below and are based on a more general analysis shown in the Appendix A.3. The symbols in these equations are defined as in Figure 3.4 with the addition of  $A_i$  which refers to the XPS peak area for chemical state  $i$  which may be carbon (C), silicon (Si), or oxycarbide (o-c).

$$A_C \approx \sigma_C \int_{d_1}^0 C_C(z) \exp\left[\frac{-z}{\lambda_C \cos \theta}\right] dz = \sigma_C C_C \lambda_C \overline{\cos \theta} \left[1 - \exp\left(\frac{-d_1}{\lambda_C \cos \theta}\right)\right] \quad 4.12$$

$$\begin{aligned} A_{o-c} &\approx \sigma_{Si} \int_{d_1+d_2}^{d_1} C_{Si_{o-c}}(z) \exp\left[\frac{-z}{\lambda_{Si} \cos \theta}\right] dz \\ &\approx \sigma_{Si} C_{Si_{o-c}} \lambda_{Si} \overline{\cos \theta} \left[ \exp\left(\frac{-d_1}{\lambda_{Si} \cos \theta}\right) - \exp\left(\frac{-(d_1+d_2)}{\lambda_{Si} \cos \theta}\right) \right] \end{aligned} \quad 4.13$$

$$A_{Si} \approx \sigma_{Si} \int_{\infty}^{d_1+d_2} C_{Si}(z) \exp\left[\frac{-z}{\lambda_{Si} \cos \theta}\right] dz = \sigma_{Si} C_{Si} \lambda_{Si} \overline{\cos \theta} \exp\left(\frac{-(d_1+d_2)}{\lambda_{Si} \cos \theta}\right) \quad 4.14$$

The electron mean free path for C(1s) electrons,  $\lambda_C$ , and for Si(2p) electrons,  $\lambda_{Si}$ , are both  $\sim 20 \text{ \AA}$  [63] and the photoionization cross-sections for C(1s) and Si(2p) are  $\sigma_C = 1.0$  and  $\sigma_{Si} = 0.9$ . In equation 4.13 for the oxycarbide, the values for Si were used since the data for comparison to the analytical model were taken from the high resolution Si scan. In theory, the carbon signal could be used to give the same results, however, the Si XPS data was better for these experiments. The average cosine term was defined previously and accounts for the acceptance angle of the detector which is approximately  $15^\circ$  so  $\Delta\theta \sim 7^\circ$ . Figure 4.31 compares the "two-layer" model to the experimental XPS data. The experimental peak areas for the chemical states were normalized to the total peak areas of the components being measured. The signals from Si bound both to oxygen and carbon were combined to determine the oxycarbide relative percentage. The values shown in Figure 4.32 are for  $(d_1 + d_2) = 15 \text{ \AA}$  since this is the approximate average of the overlayer calculations of Table 4.9. It is easily observed that the model does not fit the data closely although the overall trends are correct.

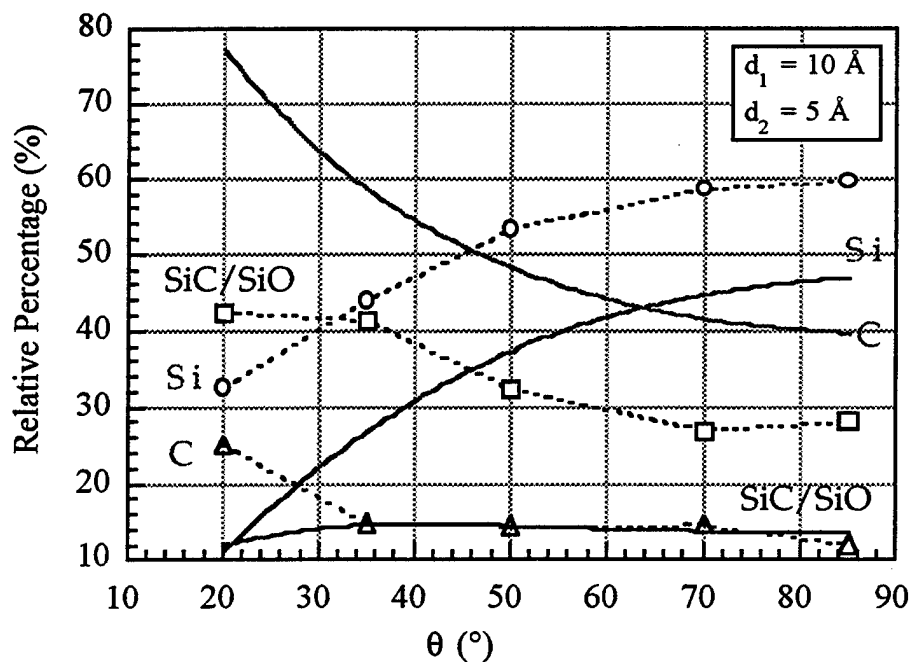


Figure 4.31 - Experiment (open data points with dashed line) and analytical model data (solid lines) for SiC/SiO, Si, and C for uniform overlayers of carbon and oxycarbide on the silicon substrate.

The second case shown on the right half of figure 4.30 is a "cluster + layer" model consisting of carbon clusters with height  $d_2$  on a uniform oxycarbide of thickness  $d_1$ . The equations for this model are similar to those for the previous model except now an additional parameter,  $f$ , corresponding to the areal surface fraction covered by the carbon clusters is also required. In the limit of  $f \rightarrow 1$ , this model is the same as the uniform bilayer model. Mathematically, this model is slightly more complicated since signal can originate in the case from regions at the surface or underneath the clusters.

$$A_C = f\sigma_C \int_{d_1}^0 C_C(z) \exp\left[\frac{-z}{\lambda_C \cos \theta}\right] dz = f\sigma_C C_C \lambda_C \overline{\cos \theta} \left[1 - \exp\left(\frac{-d_1}{\lambda_C \cos \theta}\right)\right] \quad 4.15$$

$$\begin{aligned} A_{o-c} &\approx (1-f)\sigma_{Si} \int_{d_2}^0 C_{Si_{o-c}}(z) \exp\left[\frac{-z}{\lambda_{Si} \cos \theta}\right] dz + f\sigma_{Si} \int_{d_1+d_2}^{d_1} C_{Si_{o-c}}(z) \exp\left[\frac{-z}{\lambda_{Si} \cos \theta}\right] dz \\ &\approx (1-f)\sigma_{Si} C_{Si_{o-c}} \lambda_{Si} \overline{\cos \theta} \left[1 - \exp\left(\frac{-d_2}{\lambda_{Si} \cos \theta}\right)\right] \\ &\quad + f\sigma_{Si} C_{Si_{o-c}} \lambda_{Si} \overline{\cos \theta} \left[\exp\left(\frac{-d_1}{\lambda_{Si} \cos \theta}\right) - \exp\left(\frac{-(d_1+d_2)}{\lambda_{Si} \cos \theta}\right)\right] \end{aligned} \quad 4.16$$

$$\begin{aligned} A_{Si} &= (1-f)\sigma_{Si} \int_{\infty}^{d_2} C_{Si}(z) \exp\left[\frac{-z}{\lambda_{Si} \cos \theta}\right] dz + f\sigma_{Si} \int_{\infty}^{d_1+d_2} C_{Si}(z) \exp\left[\frac{-z}{\lambda_{Si} \cos \theta}\right] dz \\ &\approx (1-f)\sigma_{Si} C_{Si} \lambda_{Si} \overline{\cos \theta} \left[\exp\left(\frac{-d_2}{\lambda_{Si} \cos \theta}\right)\right] \\ &\quad + f\sigma_{Si} C_{Si} \lambda_{Si} \overline{\cos \theta} \left[\exp\left(\frac{-(d_1+d_2)}{\lambda_{Si} \cos \theta}\right)\right] \end{aligned} \quad 4.17$$

An extreme case of this "layer + cluster" model was initially tested in which the carbon clusters were assumed to be thick enough ( $d_2 = 5\lambda = 100 \text{ \AA}$ ) so essentially none of the emitted electrons from the region below them could escape without scattering. The

fraction  $f$  was adjusted so the Si experimental data matched well to the model. The oxycarbide layer thickness was left the same as in the previous case. It is seen in Figure 4.32 that for these conditions the oxycarbide percentages follow the correct trend with angle, but were under-predicted quantitatively. The carbon concentration was not only over-predicted quantitatively, but also did not show the correct trend. For optically thick clusters, there was no angular dependence which is clearly incorrect in light of the experimental data.

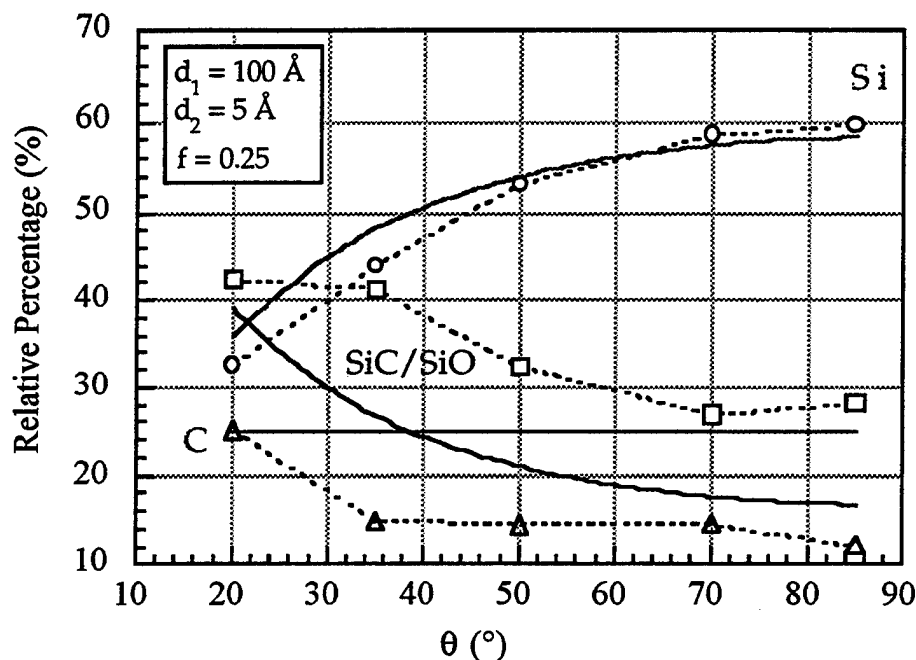


Figure 4.32 - Experiment (open data points with dashed line) and analytical model data (solid lines) for SiC/SiO, Si, and C for optically thick carbon clusters on a uniform oxycarbide on the silicon substrate.

Since these two extreme cases did not follow the experimental data adequately, the parameters for the "layer + cluster" model were adjusted to better match the experimental data. A good qualitative and quantitative fit was obtained with only minor modifications of the oxycarbide layer and carbon cluster thicknesses from the original two limiting cases. The results are plotted in figure 4.33. The model fits the data well both in terms of the angular dependence and the quantitative values. Therefore, the XPS data indicates that prior to the application of the bias in the MPCVD system, silicon carbide and oxide form

a thin layer on the Si substrate. On top of the oxycarbide, carbon clusters several monolayers in height cover approximately one quarter of this surface. The size of these clusters cannot be obtained from these measurements and model, but probably could be determined using methods such as atomic force microscopy (AFM).

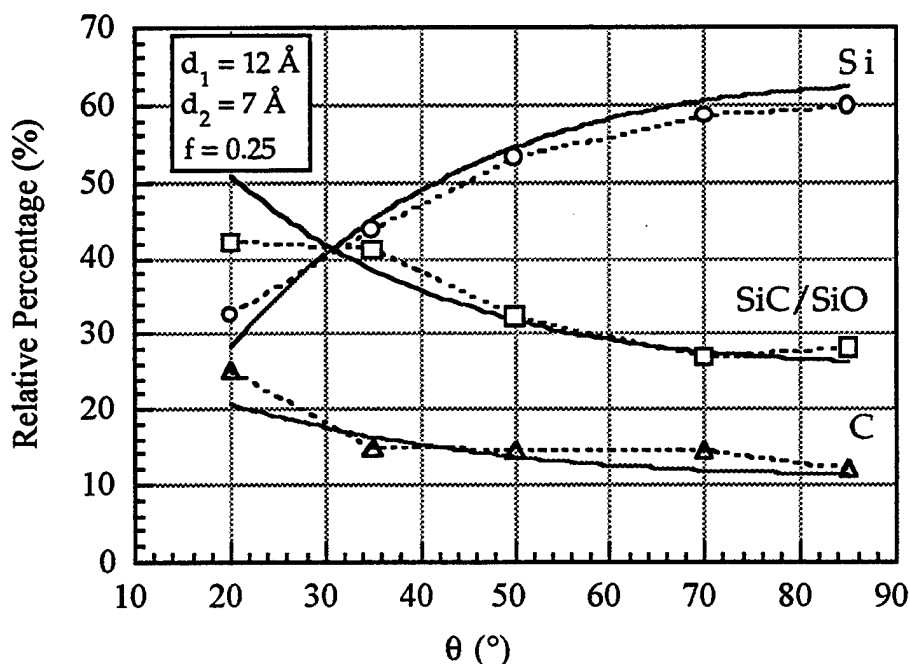


Figure 4.33 - Experiment (data points with dashed lines) and analytical model data (solid lines) for SiC, Si, and C for carbon clusters on a silicon oxycarbide overlayer on the silicon substrate.

Following the ion-assisted nucleation process, but before continued MPCVD deposition, XPS was also used to evaluate the level of carbon deposition and the surface chemical states. A bias pretreatment at -300 V, 800 °C, 20 torr, 650 W, and 2% CH<sub>4</sub>/H<sub>2</sub> was carried out for 15 minutes. The XPS survey and high resolution C(1s) and Si(2p) scans for this sample were qualitatively similar to those shown previously so will not be shown here. Quantitatively, however, there are significant differences between biased and unbiased samples with the same deposition time and similar conditions. In the biased case, the Si(2p) peak is smaller and the carbide is significantly enhanced as compared to the unbiased case. In the C(1s) bias spectra, the C-C peak is very strong with only a small carbide peak indicating the presence of significantly more carbon at the surface.

These statements are quantified in the surface composition data of Table 4.10. Since the biased Si XPS data indicates mainly carbon at the surface, little more insight can be derived from additional XPS studies along these lines.

Substrate	Carbon (%)	Oxygen (%)	Silicon (%)
Unbiased Si	20.2	28.0	51.8
Biased Si	70.2	10.8	19.1

Table 4.10 - XPS surface composition data for biased and unbiased MPCVD deposition on silicon.

A few comments should be made regarding the presence of the carbide observed in the XPS. Carbide formation was observed on Si substrates for all depositions in which the process conditions allowed XPS analysis of the interfacial region; i.e. short pretreatments which produced very thin or incomplete films. The presence of SiC has been reported by other researchers with XPS and other techniques such as transmission electron diffraction and TEM [6, 32, 41, 64]. The driving force for silicon and carbon to form SiC at the deposition temperatures is strong so the observation of a carbide is expected. Hypotheses have been made in the past concerning the role of SiC, and other carbides, in the nucleation and growth of diamond [41, 65, 66]. The role of carbides in the nucleation process is not understood, and the data in this thesis does not suggest whether SiC is necessary or sufficient for good diamond nucleation in the ion-assisted pretreatments on Si substrates. Since this issue is not the focus of this thesis, no further discussion or conclusions from the XPS carbide observations are made.

Relatively thick, continuous bias-deposited carbon films were also analyzed by XPS. A typical survey scan for these films is shown in Figure 4.34. The C(1s) peak was the only significant peak detected although oxygen was also present at levels less than 5%, most likely due to adsorption of water on the surface during atmospheric transport. The high-resolution C(1s) region is not shown since no distinction can be made between the form of the bias-deposited carbon by chemical shifts; as stated in Chapter 3, the chemical shifts for the different forms of carbon are less than 1 eV and charging issues make it extremely difficult to distinguish between them from the core peak chemical shift. The absence of all other chemical species on this surface is important because it signifies

that no contamination is present and also that potential sputtering of the substrate by energetic bias ions was not significant.

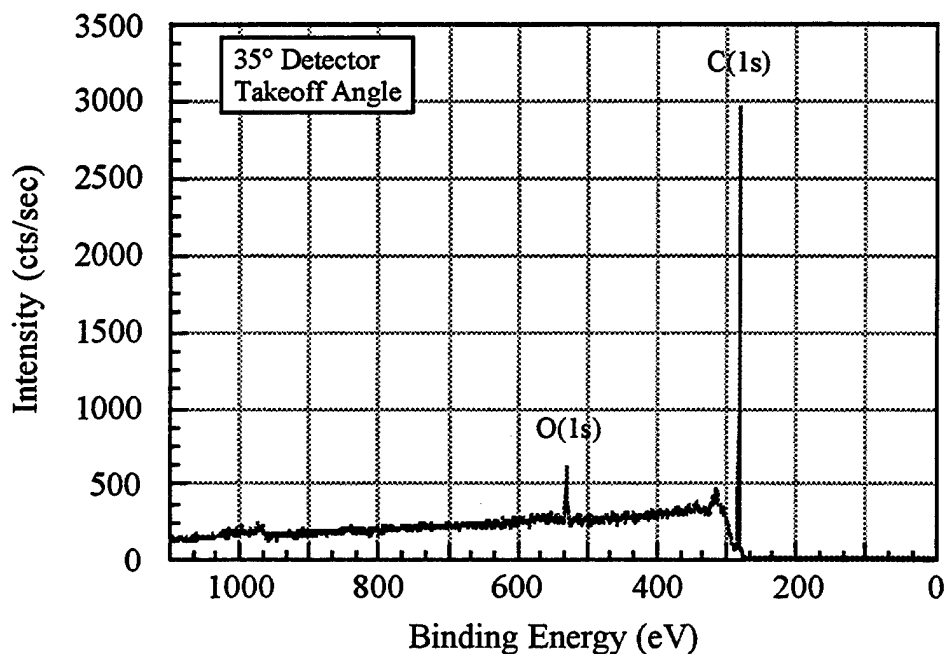


Figure 4.34 - XPS survey scan for a carbon film deposited by ion-assisted pretreatment for 1 hour.

Since XPS does not provide structural or phase information while Raman spectroscopy and SEM have limitations for diamond, other methods were used to probe the nature of the bias-deposited films. Specifically, x-ray diffraction techniques were used to detect crystallinity. X-ray diffraction is much more sensitive to the crystalline phases than the non-crystalline phases. This contrasts raman spectroscopy which has a higher sensitivity to non-diamond carbon, a characteristic which appears to limit the utility of this technique for these carbon films. Since the scattering of carbon by x-rays is relatively poor and the films were thin, symmetric x-ray diffraction scans were done at the *Stanford Synchrotron Radiation Lab (SSRL)* which offers a superior photon flux compared to typical lab diffraction facilities. All attempts to confirm the presence of diamond using conventional lab diffractometers were unsuccessful. The samples were mounted on the x-ray goniometer and standard calibration procedures were used to ensure accuracy of the measured angles. The synchrotron diffraction data is plotted on a log-

intensity scale in Figure 4.35. Table 4.11 compares the experimental peaks positions to those expected for diamond and graphite given the experimental conditions. Within experimental error, the x-ray diffraction peaks match the first three allowed reflections for diamond. Higher angle peaks for diamond were not accessible due to angular range limitations for the diffractometer. The expected Bragg angles correspond to the d-spacing from Table 3.6 for  $E = 8501.3$  eV and  $\lambda = 1.4586$  Å. Graphite peaks would appear at positions listed in Table 4.11 near the observed peaks, but these are not as close as the expected diamond peak positions. Evidence of the graphite {100} peak, however, is observed upon close inspection of the shoulder of the diamond {111} peak.

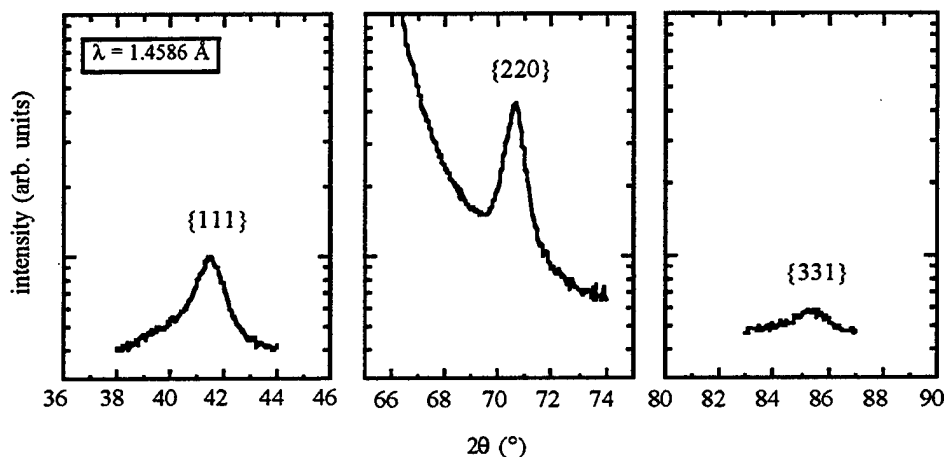


Figure 4.35 - Symmetric x-ray synchrotron diffraction scans for a bias-deposited carbon film.

Experimental $2\theta$ (°)	Peak Width FWHM (°)	Integrated Area (cts)	Diamond $2\theta$ (°) - {hkl}	Graphite $2\theta$ (°) - {hkl}
$41.5 \pm 0.1$	1.1	7343	41.49 - {111}	40.10 - {100} 42.17 - {101}
$70.6 \pm 0.1$	0.72	32076	70.67 - {220}	72.87 - {110}
$85.3 \pm 0.1$	1.6	3250	85.44 - {311}	87.95 - {201}

Table 4.11 - Experimental X-ray diffraction Bragg angles.



In theory, x-ray diffraction also allows for estimation of the grain size in polycrystalline films through the Scherrer formula shown in equation 4.18. This x-ray analysis assumes diffraction peak broadening only due to small crystal size and not due to instrumental broadening or inhomogeneous strain broadening [67, 68].

$$\Delta\theta_{FWHM} = \frac{0.9\lambda}{L \cos \theta} \quad 4.18$$

In this expression,  $\lambda$  is the wavelength,  $\Delta\theta_{FWHM}$  is the full width in radians at half of the maximum intensity, and  $L$  is the crystal size. Since little, if any, strain is suggested in the diamond film from the close agreement of the peaks to their expected positions, the assumption of small inhomogeneous strain may be reasonable. However, the data do not follow the expected angular dependence of equation 4.18 which gives increased broadening at higher angles. For the three peaks observed, the calculated crystal sizes were 73 Å, 128 Å, and 64 Å. This result is difficult to explain, but given the low signal-to-noise for the smaller peaks, the curve fitting parameters used to calculate the crystal sizes may have been inaccurate leading to errors in the peak  $\Delta\theta_{FWHM}$ . Crystal sizes of ~20 nm have been estimated using XRD for diamond films [62]. However, this report and other XRD analyses [25, 62] have been for diamond films grown on top of biased deposited films to give a thick diamond layer.

The observed intensities of the peaks in this diffraction pattern raise questions concerning the texture of these films since the intensities are not consistent with those for a randomly oriented polycrystalline film. The {111} peak is expected to be four times as intense as the {220} peak for a random polycrystalline diamond sample. The opposite intensity is observed for this data with the {220} being over four times as intense as the {111}. This suggests texturing, but rocking curves about the {220} did not confirm this hypothesis. However, the diamond {220} rocking curve may have been dominated by the tail of the strong silicon (004) substrate peak nearby. Wild, *et al.*, observed random crystal orientation by XRD for thin diamond films, but an increasing {110} texture as films were grown [69].

These diffraction questions indicate the complexity of the structure of these carbon films and indicate that further analysis is required. Despite of the unanswered questions regarding the texture, the x-ray analysis provides conclusive evidence of diamond in the bias-deposited films. These results confirm the postulate made earlier that, despite raman spectra which do not conclusively show a diamond phonon peak, diamond is present in the bias-deposited films. No other literature shows evidence of

diamond nuclei by XRD in films deposited only under bias conditions. Recall that no unbiased deposition was done following the ion-assisted pretreatment for the samples analyzed by XRD. This ensures that the presence of diamond can be attributed only to the bias-deposition process. Other researchers have reported x-ray diffraction measurements for bias-enhanced nucleation of diamond, but only for relatively thick diamond films grown by unbiased MPCVD on top of biased deposited films [25, 62].

Cross-sectional transmission electron microscopy (TEM) was used to further study the structure of the bias-deposited carbon film and interface region. The sample analyzed by TEM was deposited under conditions of -250 V bias, 800 °C, and 2% CH<sub>4</sub>/H<sub>2</sub> for 1 hour. The raman spectrum for this film was shown in Figure 4.26(b). The surface morphology of this sample was nearly identical to that of the sample shown in Figure 4.24(c) and is therefore not shown. This continuous bias-deposited film was chosen for TEM analysis to minimize the potential for damage of the interfacial region during the cross-sectional sample preparation. Standard TEM cross-section sample preparation techniques based on the Bravman-Sinclair method were used [70]. A detailed description of the TEM sample preparation is given in Appendix A.5. Since TEM cross-section samples are prepared by gluing the samples face-to-face to produce a sandwich structure, the gluing of films with nuclei which have not fully coalesced can lead to damage and ambiguity in the interfacial region.

Figure 4.36 shows the selected area electron diffraction (SAD) pattern for this film. The continuous and sharp ring character of the SAD pattern indicates that the sample is polycrystalline with little, if any, preferred texture; a textured film would have incomplete rings or diffraction spots depending upon the level of texture. In contrast, the scattering from amorphous material would result in diffuse diffraction halos rather than the well-defined rings observed in this diffraction pattern. A simultaneously acquired electron diffraction pattern for the single crystal (100) Si substrate allowed calibration of the TEM camera constant for d-spacing calculations. Equation 4.19 relates the d-spacing for the diffracting planes,  $d_{hkl}$ , to the radial distance on the diffraction pattern,  $R_{hkl}$ , the electron wavelength,  $\lambda$ , and the camera constant,  $L$  [71].

$$\frac{1}{d_{hkl}} = \frac{R_{hkl}}{\lambda L} \quad 4.19$$

The average camera constant and wavelength product,  $\overline{\lambda L}$ , was determined using the experimentally measured  $R_{hkl}$  for 6 of the Si diffraction spots and the corresponding Si plane spacings from the JCPDS-ICDD standard [51]. This average product for the

camera constant and wavelength was used with the radial distances,  $r_{hkl}$ , measured for the polycrystalline rings to back-calculate the d-spacings from Figure 4.7. Both the substrate spots and film diffraction rings were analyzed using the original TEM negative, a light table, and an optical lupe for accurate measurements and complete error analysis. Although only three diffraction rings are clearly visible in Figure 4.36 due to contrast limitations in the image, at least seven diffraction rings are visible on the original negative.

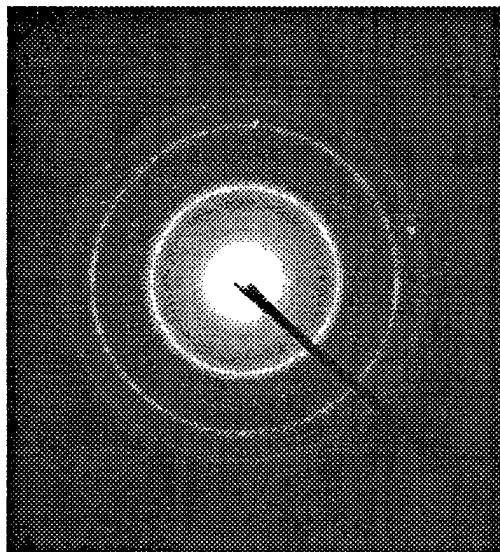


Figure 4.36 - Symmetric x-ray synchrotron diffraction scan of bias-deposited carbon.

The results are shown in Table 4.12 which compares the experimentally determined d-spacings to those expected for diamond [72] and graphite [73]. Statistical error analysis was used to obtain the errors listed in this table. The diamond planes listed in this table correspond to the first seven reflections allowed from the structure factor of diamond; due to its FCC lattice with a two-atom basis, diamond has missing reflections for all  $(hkl)$  mixed and all  $(h + k + l) = 2n$  where  $n$  is an odd integer. The d-spacings for these seven planes all agree with those observed experimentally when the errors in the calculated d-spacings are considered. The agreement of the experimental spacings with the graphite planes listed in the table are not as close as for the diamond planes and generally are outside of the error in the measurement. Furthermore, relatively strong intensity graphite rings, especially the basal plane  $\{002\}$  at  $3.357\text{\AA}$  which is the strongest expected graphite reflection in a polycrystalline sample, are missing from the diffraction pattern. The only

explanation for the absence of this intensely diffracting plane would be a sample with no graphite {002} planes oriented parallel to electron beam in the diffraction condition; this is highly unlikely since the diffraction rings show no indication of texturing. Therefore, we conclude that diamond is present in this bias-deposited carbon film.

Experimental d-spacing (Å)	Diamond d-spacing (Å) - {hkl}	Graphite d-spacing (Å) - {hkl}
....	....	3.357 {002}
....	....	2.133 {100}
2.05 ± 0.01	2.059 {111}	2.033 {101}
....	....	1.679 {004}
1.25 ± 0.01	1.261 {220}	1.232 {110}
1.07 ± 0.01	1.075 {311}	1.067 {200}
0.896 ± 0.007	0.8917 {400}	0.900 {204}
0.819 ± 0.007	0.8183 {331}	0.828 {116}
0.729 ± 0.007	0.7281 {422}	0.711 {300}
0.686 ± 0.007	0.6864 {511}	0.694 {118}
	0.6864 {333}	

Table 4.12 - Comparison of experimental TED d-spacings to those expected for diamond and graphite.

A dark-field image of the film was obtained by positioning the objective aperture around a portion of the innermost polycrystalline diffraction ring in Figure 4.36, corresponding to diamond {111} planes. In this figure, the deposited film is in the upper half of the image and the interface is observed as a line running horizontally through the middle of the image. The small bright particles in film region of the dark-field image in Figure 4.37 represent only those regions which have {111} planes diffracting in a direction which allows them to pass through the off-axis objective aperture. The size distribution of these diamond nuclei ranges from approximately 25 - 150 Å. Assuming that these particles are distributed uniformly throughout the film so that the areal density in film cross-section is the same as for plan-view, the nucleation density was estimated at  $\sim 10^{11} \text{ cm}^{-2}$ . Since the size and position of the objective aperture for this dark field image

allows less than one-tenth of the diffracting regions to be observed, the nucleation density is expected to be at least an order of magnitude higher than the value measured from this image [74]. Therefore, this TEM analysis suggests that nucleation densities estimated using SEM may be several orders of magnitude too low. As was the case for the SEM nucleation density measurements, the TEM measurements are a lower bound since it is difficult to accurately count all the small crystals in the TEM images. Surface roughness was also observed with numerous pits on the order of 100 Å deep throughout the interface region.

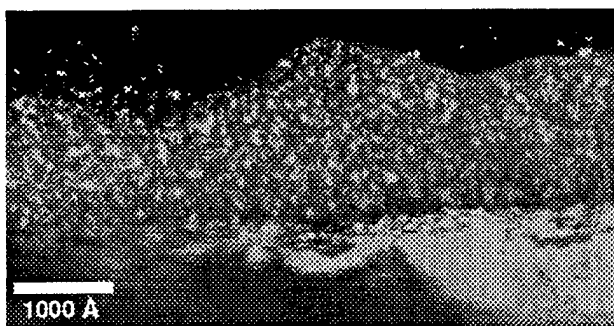


Figure 4.37 - Dark field TEM image showing diamond nuclei (bright specks) in bias-deposited carbon film.

The x-ray and electron diffraction data are clear evidence of the presence of diamond in the bias-deposited carbon films. This indicates that under some conditions, SEM and raman analysis are poor indicators of the diamond phase. Therefore, analysis of the material deposited by ion-assisted nucleation pretreatments suggests a mixture of diamond and non-diamond carbon in the nucleating clusters.

## 4.5 References

1. P. Barnes and R. Wu, *Appl. Phys. Lett.*, **62**, 37 (1993).
2. A. Morrish and P. Perhsson, *Appl. Phys. Lett.*, **59**, 417-419 (1991).
3. P. E. Pehrsson, J. Glesener, and A. Morrish, *Thin Solid Films*, **212**, 81 (1992).

4. S. P. McGinnis, M. A. Kelly, T. M. Gür, and S. B. Hagström, in *Proceedings of the 3rd International Symposium on Diamond Materials*, ed. J. P. Dismukes and K. V. Ravi, The Electrochemical Society, vol. 93-17, 153 (1993).
5. B. R. Stoner, G.-H. M. Ma, S. D. Wolter, and J. T. Glass, *Phys. Rev. B*, **45**, 11067 (1992).
6. M. Waite and S. Shah, *Appl. Phys. Lett.*, **60**, 2344 (1992).
7. D. Belton and S. Schmieg, *J. Vac. Sci. Technol. A*, **8**, 2353 (1990).
8. T. Hartnett, R. Miller, D. Montanari, C. Willingham, and R. Tustison, *J. Vac. Sci. Technol. A*, **8**, 2129 (1990).
9. R. J. Meilunas, R. P. Chang, S. Liu, and M. Kappes, *Appl. Phys. Lett.*, **59**, 3461 (1991).
10. B. R. Stoner, B. E. Williams, S. D. Wolter, K. Nishimura, and J. T. Glass, *J. Mater. Res.*, **7**, 257 (1992).
11. Z. Li, *et al.*, *J. Appl. Phys.*, **73**, 711 (1993).
12. W. R. L. Lambrecht, *et al.*, *Nature*, **364**, 607 (1993).
13. W. L. Hsu, *J. Vac. Sci. Technol. A*, **6**, 1803 (1988).
14. K. V. Ravi and C. A. Koch, *Appl. Phys. Lett.*, **57**, 348 (1990).
15. P. Badziag, W. Verwoerd, W. Ellis, and N. Grenier, *Nature*, **343**, 244 (1990).
16. S. Matsumoto and Y. Matsui, *Journal of Materials Science*, **18**, 1785 (1983).
17. D. A. Offord and J. H. Griffin, *Langmuir*, **9**, 3015 (1993).
18. S. Yugo, T. Kimura, and T. Kanai, in *Proceedings of the 1st International Conference on New Diamond Science and Technology*, ed. S. Saito, O. Fukunaga, and M. Yoshikawa, KTK Scientific Publishers, 119 (1990).
19. S. Iijima, Y. Aikawa, and K. Baba, *J. Mater. Res.*, **6**, 1491 (1991).
20. S. Iijima, Y. Aikawa, and K. Baba, *Appl. Phys. Lett.*, **57**, 2646 (1990).
21. E. Molinari, R. Polini, M. Terranova, P. Ascarelli, and S. Fontana, *J. Mater. Res.*, **7**, 1778 (1992).
22. E. Molinari, R. Polini, and M. Tomellini, *Appl. Phys. Lett.*, **61**, 1287 (1992).

23. S. Yugo, T. Kimura, and T. Muto, *Vacuum*, **41**, 1364 (1990).
24. B. R. Stoner and J. T. Glass, *Appl. Phys. Lett.*, **60**, 698 (1992).
25. X. Jiang, *et al.*, *Diamond Rel. Mater.*, **2**, 407 (1992).
26. J. Gerber, S. Sattel, K. Jung, H. Ehrhardt, and J. Robertson, *Diamond Rel. Mater.*, **4**, 559 (1995).
27. J. Robertson, *et al.*, *Appl. Phys. Lett.*, **66**, 3287 (1995).
28. R. Higa, Master's Thesis - *Bias-Enhanced Nucleation of Diamond in a Hot Filament Chemical Vapor Deposition Reactor*, Stanford University (1995).
29. J. Gerber, M. Weiler, O. Sorh, K. Jung, and H. Ehrhardt, *Diamond Rel. Mater.*, **3**, 506 (1994).
30. R. Beckmann, B. Sobisch, W. Kulish, and C. Rau, *Diamond Rel. Mater.*, **3**, 555 (1994).
31. S. P. McGinnis, M. A. Kelly, and S. B. Hagström, *Appl. Phys. Lett.*, **66**, 3117 (1995).
32. B. W. Sheldon, R. Csencsits, J. Rankin, R. E. Boekenhauer, and Y. Shigesato, *J. Appl. Phys.*, **75**, 5001 (1994).
33. X. Jiang, in *Proceedings of the 4th International Symposium on Diamond Materials*, ed. K. V. Ravi, The Electrochemical Society, (1995).
34. B. R. Stoner, *et al.*, *Diamond Rel. Mater.*, **2**, 142 (1993).
35. Y. Shigesato, R. Boekenhauer, and B. Sheldon, *Appl. Phys. Lett.*, **63**, 314 (1993).
36. B. Chapman, *Glow Discharge Processes*, John Wiley and Sons, New York (1980).
37. E. Kondoh, T. Ohta, T. Mitomo, and K. Ohtsuka, *J. Appl. Phys.*, **73**, 3041 (1993).
38. C. J. Chu, R. H. Hauge, J. L. Margrave, and M. P. D'Evelyn, *Appl. Phys. Lett.*, **61**, 1393 (1992).
39. S. J. Harris and A. M. Weiner, *J. Appl. Phys.*, **75**, 5026 (1994).
40. P. Dennig and D. Stevenson, *Appl. Phys. Lett.*, **59**, 1562 (1991).
41. P. A. Dennig, Ph. D. Thesis - *Fundamental Studies of the Nucleation of Diamond Thin Films*, Stanford University (1995).

42. B. Stoner, G. Tessmer, and D. Dreifus, *Appl. Phys. Lett.*, **62**, 1803 (1993).
43. S. D. Wolter, B. R. Stoner, and J. T. Glass, *Diamond Rel. Mater.*, **3**, 1188 (1994).
44. J. D. Cobine, *Gaseous Conductors, Theory and Engineering Applications*, Dover Publications, Inc., New York (1958).
45. P. Varga and H. Winter, in *Particle Induced Electron Emission II: Springer Tracts in Modern Physics*, ed. G. Höhler and E. A. Niekisch, Springer-Verlag, Berlin (1992).
46. H. D. Hagstrum, in *A Physicist's Desk Reference*, ed. H. L. Anderson, American Institute of Physics, New York (1989).
47. *Handbook of Chemistry and Physics*, The Chemical Rubber Company, Cleveland (1970).
48. T. Mandel, M. Frischholz, R. Helbig, and A. Hammerschmidt, *Applied Physics*, **64**, 3637 (1994).
49. R. C. Glass, L. M. Spellman, and R. F. Davis, *Appl. Phys. Lett.*, **59**, 2868 (1991).
50. P. T. Choong, K. V. Ravi, L. A. D'Cruz, and G. L. Hatch, in *Proceedings of the 28th Intersociety Energy Conversion Engineering Conference*, American Chemical Society, vol. 1, 555 (1993).
51. D. K. Milne, *et al.*, *Diamond Rel. Mater.*, **4**, 394 (1995).
52. M. Schreck, T. Baur, and B. Stritzker, *Diamond Rel. Mater.*, **4**, 553 (1995).
53. P. Emmert, *personal communication* (1995).
54. S. Yugo, T. Kimura, and T. Kanai, *Diamond Rel. Mater.*, **2**, 328 (1992).
55. W. H. Press, B. P. Flannery, S. A. Teukolsky, and W. T. Vetterling, *Numerical Recipes: The Art of Scientific Computing*, Cambridge University Press, Cambridge (1989).
56. D. Kirillov and G. J. Reynolds, *Appl. Phys. Lett.*, **65**, 1641 (1994).
57. R. J. Meilunas and R. P. Chang, *J. Mater. Res.*, **9**, 61 (1994).
58. D. S. Knight and W. B. White, *J. Mater. Res.*, **4**, 385 (1989).
59. W. Yarbrough and R. Messier, *Science*, **247**, 668 (1990).
60. Y. Namba, E. Heidarpour, and M. Nakayama, *J. Appl. Phys.*, **72**, 1748 (1992).



61. P. K. Bachmann, *et al.*, *Diamond Rel. Mater.*, **3**, 1308 (1994).
62. W. Dotter, R. Erz, K. Jung, and H. Ehrhardt, in *Proceedings of the 3rd International Symposium on Diamond Materials*, ed. J. P. Dismukes and K. V. Ravi, The Electrochemical Society, vol. 17, 746 (1993).
63. M. P. Seah and W. A. Dench, *Surface and Interfacial Analysis*, **1**, (1979).
64. B. E. Williams and J. T. Glass, *J. Mater. Res.*, **4**, 373 (1989).
65. R. Haubner and B. Lux, *Diamond Films and Technology*, **3**, 209 (1994).
66. P. Joffreau, R. Haubner, and B. Lux, *International Journal of Refractory and Hard Metals*, **7**, 186 (1988).
67. B. D. Cullity, *Elements of X-Ray Diffraction*, Addison-Wesley Publishing Company, Reading, MA (1978).
68. B. E. Warren, *X-Ray Diffraction*, Dover Publications, Inc., New York (1990).
69. C. Wild, N. Herres, and P. Koidl, *J. Appl. Phys.*, **68**, 973 (1990).
70. J. C. Bravman and R. Sinclair, *Journal of Electron Microscopy Technique*, **1**, 53 (1984).
71. D. McKie and C. McKie, *Essentials of Crystallography*, Blackwell Scientific Publications, Oxford (1986).
72. *JCDPS Powder Diffraction File*, International Centre for Diffraction Data, Swarthmore (1990).
73. K. Kitahama, *Appl. Phys. Lett.*, **53**, 1812 (1988).
74. R. Alvis, *personal communication* (1995).

## CHAPTER 5 - Nucleation Mechanisms

The experimental results discussed in the previous chapter provide a wealth of insight into diamond nucleation phenomena, especially the ion-assisted nucleation of diamond thin films. This chapter discusses process modeling and atomistic mechanisms to account for the experimental results of this thesis. The goal of this chapter is to develop a nucleation mechanism which advances the understanding of diamond nucleation. Such a nucleation model must account for a number of experimentally observed phenomena including the following:

- Application of the bias changes the MPCVD process from one in which almost no carbon is deposited to one in which carbon nucleates heavily in small clusters which grow linearly with bias deposition time to form complete carbon layers.
- Below a critical bias voltage, the nucleation density decreases rapidly.
- Nucleation under applied bias is independent of substrate temperature from 450 ~ 800°C, but decreases significantly at higher temperatures.
- Bombardment of the surface with energetic species requires carbon species for nucleation enhancement while hydrogen, argon, and helium species do not produce enhanced nucleation.
- Not only does carbon deposit more efficiently under bias, but diamond-phase nanocrystallites are formed in a matrix of non-diamond carbon.
- Growth under biased MPCVD conditions produces poorer quality films than unbiased MPCVD following the ion-assisted nucleation pretreatment.

Since the MPCVD system was used for most of the nucleation experiments of this thesis, modeling efforts will focus on this deposition technique and use appropriate plasma parameters. However, many of the general concepts developed in this chapter are not limited to MPCVD and could be applied to HFCVD, sequential deposition, and other diamond growth techniques.

## 5.1 Nucleation Theory and Diamond Nucleation Considerations

Nucleation theory is an appropriate place to begin any discussion of modeling of nucleation phenomena. Standard nucleation theory considers the stability of small clusters which are deposited upon and removed from the substrate surface in a complex dynamic process. Species deposited on the substrate may move on the surface depending upon their mobility. These species can react with the substrate, form bonds with other species, or desorb back the vapor. Thermodynamic considerations predict that once a cluster of atoms on the surface grows to a certain size, known as the critical nucleus, it is energetically favorable for that cluster to grow since the volumetric energy gained in condensation is greater than the surface energy required. At nucleus sizes below the critical size, however, it is not energetically favorable for the cluster to grow and it therefore shrinks and eventually disappears. The formation of clusters of any size is governed by the statistical nature of this dynamic process. The free energy for nuclei formation is shown as a function of radius,  $r$ , in Figure 5.1. The critical radius is denoted by  $r^*$  and the corresponding free energy at this point is  $\Delta G^*$ .

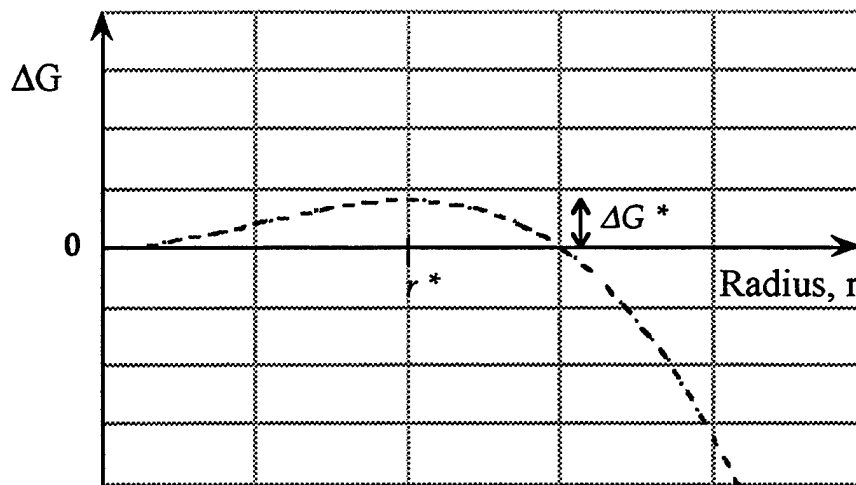


Figure 5.1 - Free energy for nuclei as a function of the radius.

This nucleation theory has been developed in detail [1]. In general, these concepts must hold for the case of diamond nucleation as well. However, diamond deposition is not as

simple as the standard condensation of a metal on a substrate which serves as the model for the nucleation theory just described. Simple nucleation theory does not account for many of the unique aspects of the diamond nucleation environment. First, due to the large concentration of H<sup>•</sup> in this system, carbon can be abstracted from the substrate surface as well as desorbed. However, since the chemical nature of the substrate surface is very complex and not understood on the atomic level, the rate constants for abstraction and desorption are not known accurately. Furthermore, the mobility (surface diffusion coefficient) of carbon on Si, on other substrates, or even on diamond is not known and is a source of contention in the diamond research community. Additionally, standard nucleation theory does not consider multiple phase formation as is the case for carbon with graphite, amorphous carbon, diamond-like carbon, and diamond structures possible. Given the elevated temperatures of diamond deposition, reactions of the surface carbon with the heterogeneous substrate, for example, carburization, are not accounted for in standard nucleation theory. Finally, bombardment of the surface by energetic species with energies considerably in excess of thermal energies is rarely treated by standard nucleation theory. For these reasons, diamond nucleation and ion-assisted nucleation of diamond will not be treated in detail with the standard models of nucleation, except for the use of some of these ideas conceptually as necessary and useful. Instead, other arguments and models will be invoked to explain the nucleation of diamond. Much of this work will draw heavily from concepts of nucleation in ion-beam assisted deposition (IBAD) processes.

## 5.2 Relevant Chemical Species and Fluxes

To accurately model the nucleation process in the MPCVD system, an understanding of the chemical species involved is required. Given the complexity of the plasma and the lack of in-situ diagnostics for this system, direct chemical characterization was not possible. Estimates of the dominant gas-phase plasma chemical species were made by considering the process parameters and known chemical reactions. The microwave plasma is an excited chemical environment in which energetic electrons ionize chemical species and drive chemical reactions to produce ions, radicals, and reactive species [2]. Therefore, electron-neutral reactions play a large role in the chemical nature of the plasma and a list of important reactions of this type are given in Table 5.1. Note that dissociation of H<sub>2</sub> and ionization of H<sup>•</sup> occur at electron energies less than the

ionization of  $H_2$ . Also note that ionization of the methyl radical ( $CH_3^\bullet$ ) requires less energy than ionization of methane ( $CH_4$ ).

Electron-Neutral Reaction	Threshold Energy (eV)	Reference
$H_2 + e^- \rightarrow H^\bullet + H^\bullet + e^-$	10.0	[3]
$H^\bullet + e^- \rightarrow H^+ + 2e^-$	13.6	[3]
$H_2 + e^- \rightarrow H_2^+ + 2e^-$	15.4	[3]
$H_2 + e^- \rightarrow H^+ + H^\bullet + 2e^-$	18.0	[3]
$CH_3^\bullet + e^- \rightarrow CH_3^+ + 2e^-$	9.8	[4]
$CH_4 + e^- \rightarrow CH_4^+ + 2e^-$	12.6	[5]
$CH_4 + e^- \rightarrow CH_3^+ + H^\bullet + 2e^-$	14.3	[4, 5]
$CH_4 + e^- \rightarrow CH_2^+ + 2H^\bullet + 2e^-$	15.1	[5]
$CH_4 + e^- \rightarrow CH^+ + 3H^\bullet + 2e^-$	22.2	[5]
$CH_4 + e^- \rightarrow C^+ + 4H^\bullet + 2e^-$	25.0	[5]

Table 5.1 - Important electron-neutral reactions and threshold values.

The cross-sections for these ionization reactions are strongly dependent on electron energy and tend to increase rapidly with energy from the threshold value before leveling out at energies several times higher than the threshold. The relative cross-sections for methane can be estimated from the cracking pattern of this gas in a mass spectrometer as shown in Figure 5.2. The data plotted are for ionization by 70 eV electrons which have much higher energy than those expected in typical microwave plasma systems where the average electron energy is 1 ~ 10 eV [2]. However, this plot graphically shows the relative cross-sections which follow the same trend at the lower electron energies present in the plasma [5]. Note that the peak at mass 17 originates from the  $C^{13}$  isotope which has a natural abundance relative to  $C^{12}$  of 1.1/98.9 [6].

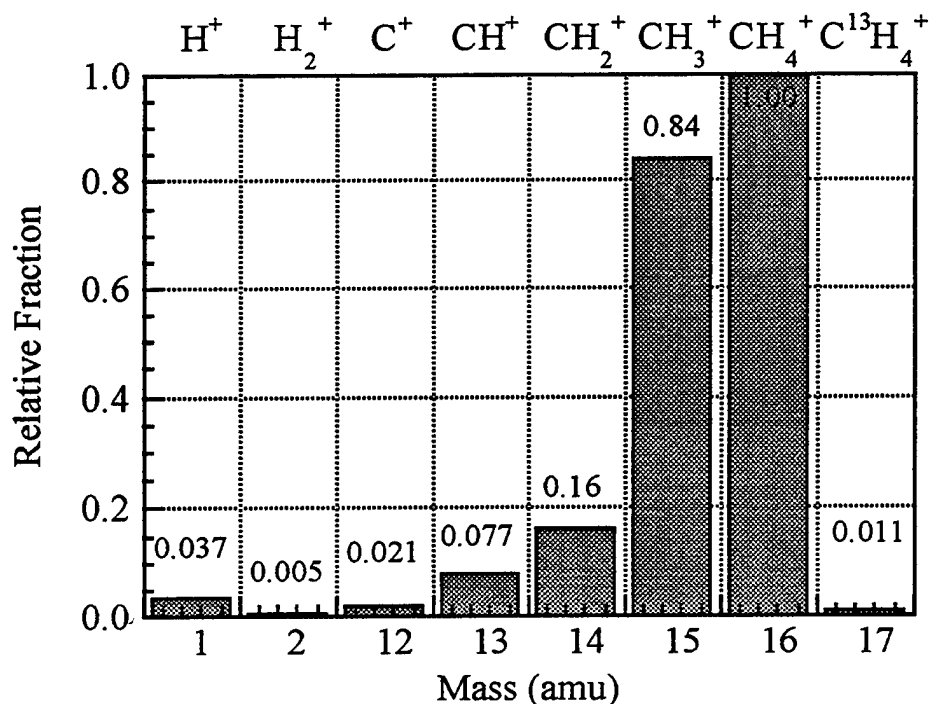


Figure 5.2 - Relative abundance of ions in mass spectrometer due to electron impact ionization at 70 eV [UTI Corporation].

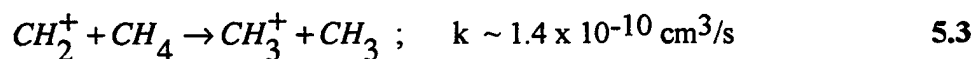
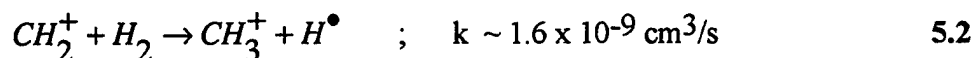
The important information to glean from the full cross-section vs. energy curves, which are not shown, is that the electron collision cross-section for neutral CH<sub>4</sub> to produce CH<sub>4</sub><sup>+</sup> is slightly larger than that to produce CH<sub>3</sub><sup>+</sup> at electron energies between 20 and 100 eV. Below 20 eV, the cross-section for CH<sub>4</sub><sup>+</sup> increases even more relative to CH<sub>3</sub><sup>+</sup> with decreasing energy due to the relative threshold values shown in Table 5.1 for these species [5]. From these arguments, CH<sub>4</sub><sup>+</sup> is expected to dominate CH<sub>3</sub><sup>+</sup> in this system since direct ionization to produce the former is energetically easier. Furthermore, the formation of the latter ion from CH<sub>3</sub><sup>·</sup>, although the ionization threshold is lower for this radical compared to the neutral species, is not expected to be significant due to the relatively low concentration of the CH<sub>3</sub><sup>·</sup> compared to CH<sub>4</sub> in the plasma environment.

Qualitative estimates of the plasma ionic species also require consideration of the ion-neutral reactions which play an important role in the plasma chemistry of this system. One such reaction which dictates the dominant hydrogenic ion in the reactor is shown in Equation 5.1:



The relatively large reaction rate and strong exothermicity for this reaction lead to extremely efficient production of  $H_3^+$ ; this species is typically the dominant hydrogen ion in hydrogen plasmas [7]. Furthermore, detailed simulations of the chemical reactions involved in a MPCVD hydrogen discharge have predicted that  $H_3^+$  is the dominant hydrogenic ion in these systems [3]. Although production of  $H^+$  through ionization of  $H$  is easier than production of  $H_2^+$  from ionization of  $H_2$  due to the lower ionization threshold of the former, the latter ion will predominate in the MPCVD system since the  $H_2$  concentration is orders of magnitude larger than the  $H$  concentration. However, the situation is complicated by the fact that the excess  $H$  in this system tends to drive reaction 5.1 back to the left.

Other ion-neutral reactions such as those listed below complicate estimates of the chemical environment [8]:



Additional reactions involving the ions and neutral species shown in these reactions also produce larger carbonaceous ions of the form  $C_xH_y^+$  [8]. However, since the concentrations of the precursor species for these larger ion formation reactions are relatively small and the overall reaction rates are quite low, it is expected that the single carbon ions discussed above are the most important ions for the ion-assisted process in the MPCVD system.

To accurately quantify the ionic and neutral species concentrations using the reactions listed above, the electron energy distribution function (EEDF) is required. Lacking the full EEDF, the electron temperature can be used to approximate the electron energies in the plasma. In an ASTEX deposition system similar to the MPCVD system used for this research, an electron temperature of 0.5 - 1.0 eV has been measured using a Langmuir probe [9]. However, Langmuir probe measurements in this relatively high pressure region are difficult and often inaccurate. Numerical modeling of  $H_2$  and  $H_2/CH_4$  microwave plasmas has provided estimates of the electron temperature at 2 eV [3]. In either case, these values indicate that only the energetic tail of the electron distribution controls the formation of species by electron-neutral reactions. This is seen in the Figure

5.3 which shows an assumed Maxwellian electron energy distribution for electrons with an average energy of 2 eV. Once again, the situation is more complex since research by Hsu has indicated that thermal reactions, as well as the electron impact dissociation discussed in this section, play significant roles in the MPCVD plasma chemistry [9]. In addition, it is important to realize that for consideration of the electron-neutral reactions in the sheath, the typical plasma electron energy distribution function is not valid; rather, this distribution is modified significantly by the electric fields in the sheath which increases the electron energies. The electron energy distribution in the sheath region is not known under bias conditions.

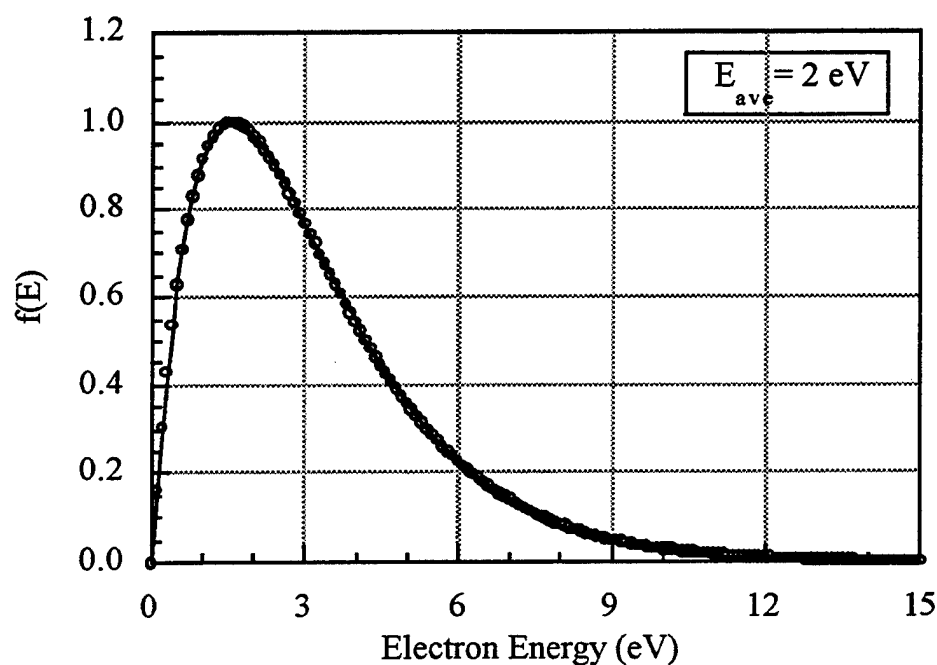
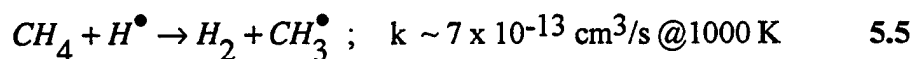
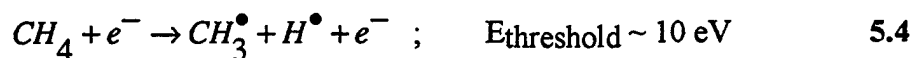


Figure 5.3 - Maxwellian electron energy distribution for electrons with an average energy of 2 eV.

The neutral species concentrations arise from the coupling of numerous species in large number of hydrocarbon chemical reactions. Some chemical models in the literature account for 50 - 100 hydrocarbon reactions [10, 11]. For a simple model to describe the ion-assisted nucleation process, methyl radical fluxes will be compared to carbonaceous ion fluxes. The methyl radical concentration is controlled by the following two reactions:





Given the estimated electron energy distribution and the abundance of  $H^\bullet$  in the plasma, Hsu concluded that the hydrocarbon concentrations ( $CH_3$ , etc.) is controlled by atomic hydrogen reactions rather than electron-induced dissociation [9].

### 5.3 Neutral and Ion Flux Considerations

The previous section considered the main species present in the plasma system. To understand the diamond nucleation mechanism during both biased and unbiased MPCVD, it is useful to know not only which species are present, but also to have an estimate of the fluxes of these species to and from the surface. The chemical fluxes and parameters of interest include the following:

- Methyl radical and atomic hydrogen neutral fluxes to the surface
- Carbon and hydrogen ion fluxes to the surface under bias conditions
- Carbon species' desorption and abstraction fluxes

Although the first two of these fluxes can be estimated with some accuracy, desorption and abstraction data is extremely limited for this system. Fortunately, it is expected that the neutral and ion fluxes dominate in the cases considered in this thesis. The mobility of carbon species on the surface may also play a role in the nucleation process. Ion bombardment has been used in other materials systems to impart energy to surface species and thereby enhance surface mobilities. However, little is known about carbon surface diffusion and no reports for this process are available in the literature. Given the strong bonding for most forms of carbon, it is assumed in this work that the effects of surface diffusion are not significant for the ion-assisted nucleation process.

Under MPCVD conditions similar (except the addition of  $\sim 10\%$  argon to the feed gas as an actinometer) to those used for unbiased growth of diamond films (800 W, 800  $^\circ\text{C}$ , 20 torr,  $\sim 1\%$   $CH_4/H_2$ ), the mole fractions of various relevant chemical species were measured by Hsu using a molecular beam mass spectrometer (MBMS) system which samples the near-surface region [9]. These deposition conditions produced extremely

poor nucleation of diamond,  $\sim 10^4 \text{ cm}^{-2}$ , without substrate bias. For these deposition conditions, the approximate flux of atomic hydrogen and methyl radical to the surface were estimated using equation 5.6 which relates diffusive flux of species  $i$  to the surface,  $J_i$  (number/cm<sup>2</sup> sec), to the partial pressure of species  $i$ ,  $P_i$  (atm), and the temperature,  $T$ (K), of the system:

$$J_i = \frac{P_i}{\sqrt{2\pi m_i kT}} \quad 5.6$$

The near-surface mole fractions measured by MBMS in the MPCVD system were approximately  $3 \times 10^{-4}$  for  $\text{CH}_3^{\cdot}$  and  $1 \times 10^{-3}$  for  $\text{H}^{\cdot}$ . Transforming these values to fluxes with equation 5.6 results in a  $\text{CH}_3^{\cdot}$  flux of  $1.6 \times 10^{18} \text{ cm}^{-2}\text{s}^{-1}$  and an  $\text{H}^{\cdot}$  flux of  $2.1 \times 10^{19} \text{ cm}^{-2}\text{s}^{-1}$  at 1073 K. Normalizing this flux to a per site basis by dividing by the number of surface sites available ( $\sim 10^{15}$ ) results in 1600 methyl radicals per second per site and 21,000 hydrogen atoms per second per site. The high ratio of atomic hydrogen to carbon growth species has been discussed in the literature [12-15]. Alternatively, this means there are 630 microseconds between methyl arrivals and 50 microseconds between atomic hydrogen arrivals on each site. This analysis only considers the methyl radical and no other carbon precursors. Inclusion of acetylene and other carbon precursors would increase the carbon flux to the surface by at least a factor of two [9].

The ion flux to the surface was estimated using a typical bias current measured during the bias pretreatment process. To determine the current density, a circular collection area with a 5 cm diameter was assumed which corresponds to the observed deposition area following the ion-assisted pretreatment. With this assumption, a current density of several mA/cm<sup>2</sup> is typical for the ion-assisted process. By ignoring secondary electron effects and assuming all the current results from incident ions, the following fluxes were calculated. The ion flux to the substrate is on the order of  $\sim 10^{16}$  ions/cm<sup>2</sup>-sec. Normalizing this flux by  $10^{15}$  sites/cm<sup>2</sup> results in 10 ions per second per site or, alternatively, 70 milliseconds between ion arrivals per site. From Chapter 4, ion-induced electron emission does occur during the ion-assisted process. If this electron emission were also considered, the effect would be the small reduction of the incident ion flux to the surface.

The neutral flux during the ion-assisted process was assumed to be similar to that estimated for the unbiased case in the previous paragraph. Small neutral flux differences most likely exist between these two cases due to the secondary glow discharge present in the case of the bias, but these differences cannot be quantified with any accuracy.

Although these numbers provide only a rough estimate of the neutral and ion fluxes, the important result is that the flux of ions to the surface is several orders of magnitude less than the methyl and atomic hydrogen neutral flux to the surface under bias conditions. Table 5.2 summarizes the flux estimates. These data are consistent with the experimental results of Figure 4.7 which indicated that the growth of the nuclei was controlled by the radical species flux rather than the energetic ion flux responsible for nucleation. However, there are still more than sufficient ions available to account for the nucleation densities observed. In fact, the efficiency of the ion-assisted process is very low given the estimates of  $10^{16} \text{ cm}^{-2}\text{s}^{-1}$  ion flux and the nucleation densities of only  $10^{10} \text{ cm}^{-2}$ .

Species	Flux ( $\text{cm}^{-2}\text{s}^{-1}$ )	# site <sup>-1</sup> second <sup>-1</sup>	Arrival Interval (s)
CH <sub>3</sub> <sup>·</sup>	$1.6 \times 10^{18}$	1600	$630 \times 10^{-6}$
H <sup>·</sup>	$2.1 \times 10^{19}$	21,000	$50 \times 10^{-6}$
Ions	$\sim 10^{16}$	10	$70 \times 10^{-3}$

Table 5.2 - Estimates for species flux in biased/unbiased MPCVD.

Considering the sequential reactor experiments which suggest that carbon ions control the ion-assisted process, it is important to know the relative fraction of carbon ions to hydrogenic ions in the total ion flux. As previously discussed, the bias current is the sum of the ion fluxes to the substrate plus the electron flux emitted from the substrate. Increases in the bias current with time were attributed to an increase in the ion-induced electron emission resulting from a larger 2nd Townsend coefficient,  $\gamma$ , due to the deposition of carbon on the Si substrate. Estimates of the carbon/hydrogen ion flux can be made using the threshold energies listed in Table 5.1. Since the threshold energies for hydrogenic ions and carbonaceous ions in this table are relatively close, it is expected that the hydrogenic ions will dominate since their concentration in the plasma is several orders of magnitude higher than that of the carbon species. Furthermore, if the carbon ions were a major current carrier in this process, the bias current would be sensitive to the gas-phase carbon concentration. This was not observed experimentally as the initial bias current was not a strong function of carbon concentration in Figure 4.18. Although this evidence suggests that hydrogen ions dominate carbon ions, quantitative species fluxes cannot be assessed with any accuracy.

The flux of carbon leaving the surface due to abstraction by  $H^{\cdot}$  was considered for both the biased and unbiased deposition processes. The data in the literature relevant to the erosion of carbon by hydrogen has been summarized by Hsu [16]. The yield, carbon atoms removed per incident atom, due to  $H^{\cdot}$  interaction with graphite appears to be at least an order of magnitude lower than the yield from hydrogen ion bombardment. The highest yields were observed for simultaneous exposure to both  $H^{\cdot}$  and energetic hydrogen ions - conditions similar to those for ion-assisted deposition. Hydrogen erosion yields are also temperature dependent which is an important consideration when examining the temperature effects of ion-assisted nucleation. The erosion yield of a:C-H films by energetic hydrogen was found to peak around 800 K and decreases rapidly both at higher and lower temperatures. The data varies significantly for the erosion of different forms of carbon by hydrogen, but the literature suggests that  $H^{\cdot}$  reacts to remove no more than 0.01 carbon atoms, either as  $CH_4$  or  $CH_3^{\cdot}$ , per incident hydrogen. Note that one must be careful in extending these numbers to diamond since the removal mechanism for methyl species from the diamond surface is probably not the same as the erosion of graphite by hydrogen; a methyl species on diamond may be removed by simple abstraction with hydrogen whereas a graphite carbon must be hydrogenated first and then removed as methyl or methane.

Assessment of the desorption of carbon from the surface during this process depends upon estimation of  $\tau_a$ , the average surface lifetime of species  $a$ . This average time before desorption is defined by equation 5.7.

$$\tau_a = \frac{1}{\nu_0} e^{E_a/kT} \quad 5.7$$

Here, the lifetime is assumed to be independent of the number of adatoms present on the surface,  $\nu_0$  is the vibrational frequency of the adatom on the surface ( $\nu \sim 10^{12} - 10^{13} \text{ s}^{-1}$ ), and  $E_a$  is the energy required to desorb it back into the vapor. Surface lifetimes as a function of adsorption energy are listed in Table 5.3. The carbon deposited on the surface is thought to chemisorb with energies around 3 eV for single C-C bonds or C-Si bonds depending upon the structure (see Appendix A.2). This result in a surface lifetime which is relatively long compared to the atomic hydrogen arrival rate. Equation 5.7 does not account for the abstraction of a species through chemical reaction so the overall surface lifetime is dominated by the shorter of the desorption and abstraction lifetimes. Even though the abstraction probability is estimated to be less than 0.01, the high  $H^{\cdot}$  flux makes this lifetime orders of magnitude shorter than that for desorption.

Adsorption Energy, $E_a$ (eV)	Surface Lifetime, $t_a$ (s)
0.1	$2.9 \times 10^{-12}$
0.5	$2.1 \times 10^{-10}$
1.0	$4.4 \times 10^{-8}$
1.5	$9.1 \times 10^{-6}$
2.0	$1.9 \times 10^{-3}$
2.5	0.40
3.0	82
3.5	$1.7 \times 10^3$
4.0	$3.6 \times 10^6$

Table 5.3 - Surface lifetime as a function of adsorption energy for  $T = 800$  °C,  $\nu = 10^{12}$  s<sup>-1</sup>.

Now that the relevant species' fluxes at the surface have been discussed, consider the following simple model of the carbon depositing on a Si substrate under MPCVD conditions. The XPS results of Chapter 4 indicate the presence of a thin silicon oxycarbide layer covered with small carbon clusters. A thin carbon layer has also been observed at the diamond-silicon interface by Sheldon, *et al.*, using TEM [17]. It is assumed in this thesis that diamond nucleation originates at the carbon clusters by mechanisms discussed later in this chapter. The formation of the carbon clusters occurs by the competitive deposition and removal of carbon from the substrate from the fluxes described in the previous section. Cluster or island formation, known as a *Volmer-Weber* growth model, is characterized by individual nuclei which grow three-dimensionally until they impinge to form a film. In general, this growth mode is observed when the atoms prefer to bond with each other rather than to the substrate; in other words, the bond strength between atoms in the cluster is higher than the bond strength between cluster atoms and substrate atoms. Since most carbon-carbon single bonds have an energy of approximately 3.6 eV while those for C-Si are 3.0 eV (see appendix A.2), the clustering phenomena is consistent with thermodynamic considerations.

Even though carbon deposits on untreated Si substrates under unbiased conditions, the poor diamond nucleation for this case is not understood. One hypothesis used in the literature to explain this phenomenon has been a low *sticking coefficient* of the

carbon precursor(s) for diamond nucleation on most substrates [18]. However, the concept of a sticking coefficient is perhaps not an appropriate method of visualizing diamond nucleation since this parameter is typically defined as the ratio of deposited material to the incident precursor flux. Therefore, this coefficient does not distinguish between chemical bonds which are never formed (i.e. the species reflect off the surface) and bonds which are formed then removed (abstracted) by chemical reaction. Due to the abundance of H<sup>•</sup> in this system, it is generally assumed that most sites on the surface are hydrogen-terminated. The ability of a precursor to bond (stick) to the surface depends on the availability of open sites since a hydrogen-terminated site is relatively passive. This is one explanation for diamond growth limitations at lower temperatures; the formation of open growth sites by H<sup>•</sup> abstraction decreases with temperature therefore limiting the bonding ability of the precursor. Alternatively, it is possible that carbon precursors bond (stick) readily to the substrate, but then are abstracted away rapidly by the abundance of H<sup>•</sup>, again the final result being that no carbon is deposited. From sequential deposition experiments, H<sup>•</sup> abstraction is known to play a significant role. When carbon is sputtered onto silicon at 800 °C in the sequential reactor in inert gas environments (Ar or He) polycrystalline graphite films form readily. If the substrate is rotated past an atomic hydrogen emitter, the carbon film will be reduced as the level of hydrogen excitation is increased [15]. Therefore, whether the carbon is prevented from bonding to the surface due to hydrogen termination or whether it bonds but is rapidly abstracted off the surface, the result is the same with little diamond deposited on the substrate.

The ion-assisted nucleation experiments found significantly more carbon deposited on the surface under biased relative to unbiased conditions. The difference between these processes is one of the critical questions addressed by this thesis. The species flux estimates of this chapter suggest that the neutral fluxes are approximately equivalent for biased and unbiased deposition, but there is clearly an additional energetic flux of hydrogen and carbon ions under bias conditions. Although this energetic flux is several orders of magnitude smaller than the neutral flux, the energy of these species is considerably higher due to the acceleration by the field in the sheath region. These energetic species may bond more readily to the surface by several mechanisms including implantation into subsurface regions or by displacement of surface-terminated hydrogen to create bonding sites. Both of these mechanisms increase the sticking coefficient significantly. However, recall that energetic hydrogen ions are more effective at removing carbon from the surface by abstraction so this must be considered. Ion bombardment of the surface may not only provide more efficient sticking, but at the same time provide energy at the substrate to surmount an activation barrier for nucleation of small diamond

nuclei. This explanation has been experimentally confirmed by the voltage, temperature and carbon concentration dependences for nucleation density under bias conditions. To further model the critical role bombarding ions play in this process, the ion energies were considered in more detail.

## 5.4 Ion Energy Distribution

The experimental results of Chapter 4 combined with the modeling of the previous section confirm an atomistic mechanism for ion-assisted nucleation which is controlled by the energy of the incident species. To accurately model the carbon deposition process under the bias conditions, the energy distribution of the bombarding species at the substrate surface is a critical parameter. The retarding probe measurements under bias conditions in Chapter 4 provide a good estimate of the ion energy distribution. Unfortunately, this is the total ion energy distribution. Given the importance of carbon ions relative to hydrogen ions as observed in the sequential deposition experiments, it is desirable to know the energy distribution for only the carbon ions. Furthermore, the retarding probe measurements were difficult and only taken for a limited number of processing conditions. A method to probe the ion energy distribution as a function of process parameters was required.

The energy distribution for impinging ions on the surface during the ion-assisted pretreatment is difficult to estimate due to the complexity of the plasma. Figure 5.4 schematically shows the substrate and sheath region in question. Note that the dimensions of this figure are not to scale. Ions present in the sheath are accelerated toward the substrate in the electric field produced by the applied bias voltage. These ions collide mainly with neutral species which dominate the gas environment and lose energy as they traverse the sheath and impinge upon the substrate. The average distance traveled between the ion-neutral collisions is given by the mean free path,  $\lambda$ . Several researchers have estimated this energy to be on the order of the applied bias voltage [19, 20]. However at 20 torr, the main ionic species ( $\text{CH}_4^+$ ,  $\text{H}_3^+$ ) have mean free paths which are at least several orders of magnitude smaller than the distance from the sheath edge to the substrate. Therefore, the energy of the impinging species is significantly less than the bias potential due to ion-neutral collisions in the sheath region. Sheldon, *et al.*, realized this fact and estimated the low-energy range of the ionic species by assuming that the ions transfer all of their energy upon collision [17]. In this calculation, the energy of the ions,  $E_a$ , was estimated by multiplying the mean free path,  $\lambda_a$ , of the ion species  $a$  by the field

strength which is given by the potential drop,  $\Delta V$ , divided by the sheath thickness,  $Z_s$  as shown in equation 5.8:

$$E_a = \lambda_a \frac{\Delta V}{Z_s} \quad 5.8$$

Using a collision diameter of 3 Å for  $\text{CH}_4^+$  which corresponds  $\lambda_a = 25 \mu\text{m}$ , a potential drop of 200 V, and a sheath thickness ranging from 0.1 - 1.0 mm, an ion energy of 2 - 20 eV calculated. This calculation is inaccurate for several reasons. First, since carbon ions are significantly heavier than the  $\text{H}_2$  molecules with which they mainly collide in the sheath, they do not transfer all of their energy upon collision. Furthermore, the mean free path used by Sheldon, *et al.*, was inaccurate and the field strength was assumed to be constant. A linear electric field in the sheath region has been observed in the experimental work of other researchers and is a better choice [21, 22].

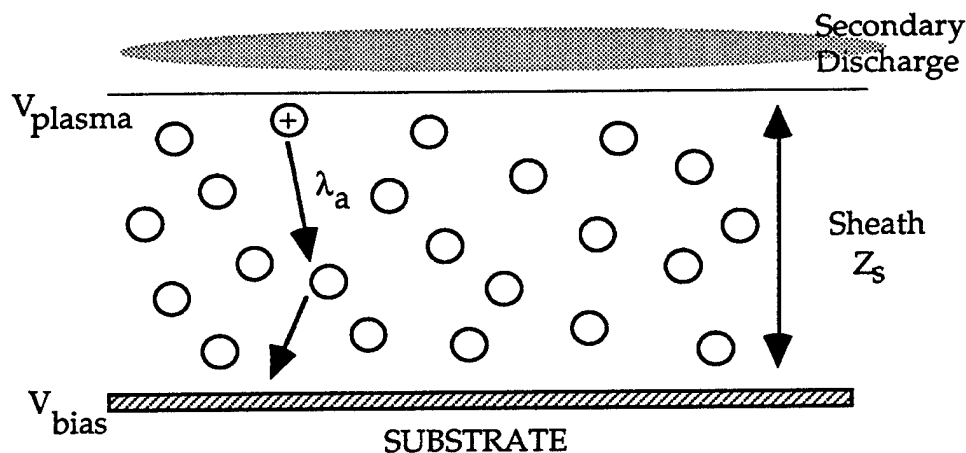


Figure 5.4 - Schematic of sheath region under bias conditions.

A more sophisticated model was developed to obtain a better estimate of the average energy of the incident ions. This model accounts for the loss of energy due to multiple elastic collisions in the sheath region and the energy gain from the electric field between collisions. The mean free path between collisions was calculated using the following expressions which account for the mass and size differences between the colliding species [23]:



$$\lambda_a = \frac{1}{\pi n_b d_{ab}^2 \sqrt{1 + m_a / m_b}} \quad 5.9$$

$$d_{ab} = (d_a + d_b) / 2 \quad 5.10$$

In these equations,  $\lambda_a$  is the mean free path of species  $a$  in  $b$ ,  $n_b$  is the gas density of the majority species  $b$ ,  $m_a$  and  $m_b$  are the masses of species  $a$  and  $b$  respectively, and  $d_{ab}$  is an average collision cross-section determined from the individual molecular diameters,  $d_a$  and  $d_b$ , of species  $a$  and  $b$ .

The use of the mean free path is not strictly valid in this situation since this parameter is typically used for elastic collisions between thermal molecules. A more accurate parameter is the collision cross-section which is a function not only of the size and type of species under consideration, but also its velocity (energy). However, elastic binary collisions with constant collision cross-sections (mean free paths) were assumed since no more accurate data was available. Cross-sections independent of energy are reasonably accurate in the low-energy range considered here and this is a common assumption in more complicated Monte Carlo ion collision simulations. The gas density in MPCVD system was estimated using the ideal gas law ( $PV = nRT$ ) under typical deposition conditions of 20 torr total pressure. Assuming the neutral gas temperature equal to that of the substrate at 1073 K results in a density of  $1.80 \times 10^{17} \text{ cm}^{-3}$ . Estimates of the molecular diameter for mean free path calculations were taken from Rohsenow, *et al.*, and these values are 2.74 Å for  $\text{H}_2$  and 4.14 Å for  $\text{CH}_4$  [24]. The mean free paths are temperature dependent due to changes in gas density with temperature. Table 5.4 shows the mean free paths for  $\text{CH}_4^+$  and  $\text{H}_2^+$  at various gas temperatures.

Gas Temperature (K)	$\lambda_{\text{CH}_4^+}$ ( $\mu\text{m}$ )	$\lambda_{\text{H}_2^+}$ ( $\mu\text{m}$ )
1073	5	17
2000	9	31
3000	14	47

Table 5.4 - Estimated mean free paths for  $\text{CH}_4^+$  and  $\text{H}_2^+$  as a function of gas temperature.

The dominant collision in the sheath considered was that of methane ions ( $\text{CH}_4^+$ ,  $m_a = 16$ ) with hydrogen molecules ( $\text{H}_2$ ,  $m_b = 2$ ) which make up the bulk of the plasma since the level of ionization is expected to be on the order of  $10^{-3}$ . Given the huge numbers of gas species colliding at all possible angles, an average was taken over the angles from  $0$  to  $90^\circ$  and this value was used to account for energy loss upon collision. The energy loss was estimated using a classical model in which the energy transfer ratio,  $E_a/E_b$ , is dependent upon the mass of the colliding species ( $m_a, m_b$ ) and the angle of collision,  $\theta$ . The functional form of this expression is given by:

$$\frac{E_a}{E_b} = 4 \frac{m_a m_b}{(m_a + m_b)^2} \cos^2 \theta \quad 5.11$$

Here  $E_a$  is the energy transferred upon collision which is always less than or equal to  $E_b$ . This term must be modified for the variation in collision probability as a function of the collision angle which is maximized for collisions at  $45^\circ$  and approaches zero for both head-on ( $\theta = 0^\circ$ ) and glancing collisions ( $\theta = 90^\circ$ ). This modifies equation 5.11 as follows:

$$\frac{E_a}{E_b} = 8 \frac{m_a m_b}{(m_a + m_b)^2} \cos^3 \theta \sin \theta \quad 5.12$$

To determine the average energy retained over all angles, the above expression is subtracted from unity, integrated from  $0$  to  $90^\circ$ , and divided by the range of  $90^\circ$ . Using this model for a single collision, approximately 87% of the methane ion energy is retained, on average, upon collision with  $\text{H}_2$ .

The average energy for a  $\text{CH}_4^+$  ion at the substrate surface was estimated in the following way. The ion was started at the sheath edge with no energy (velocity) and gained energy from the linear electric field (assumption) in the sheath over the distance of one mean free path. The energy of the ion following the first collision was calculated using the energy gained over the first mean free path multiplied by the average energy retained upon collision. To this resulting energy was added the energy gained by acceleration from the electric field over another mean free path, and then the new total energy was multiplied again by the energy retention factor. This sequence was continued until the total sheath distance had been traversed by an ion traveling the distance of exactly one mean free path between the collisions. The results of this model show that

for a -275 V substrate bias, the average ion energy of the impinging ions is approximately 35 eV for a sheath thickness of 1 mm. This value is a strong function of the sheath distance since the electric field model was linear. Additionally, the average energy was observed to decrease monotonically with decreasing bias voltage in this model.

This model provides only an approximate value for the average ion energy since only one ion species was considered, and also since this ion was assumed to travel exactly one mean free path between each collision and subsequent loss of energy. In reality, a distribution of distances are traversed prior to collision and this affects the amount of energy gained by acceleration and subsequently lost due to collision. A better estimate of the average ion energy can be obtained by considering a large number of ions which travel different distances between collisions with the mean free path being the average distance traveled. A Monte Carlo program, *IONTRANS*, has been developed at Stanford University to compute the ion angular and energy distributions as part of a larger plasma etch and deposition simulation known as *SPEEDIE* [25]. This simulation follows the path of many ions through the sheath and assumes that the degree of ionization is very low ( $<10^{-3}$ ) so that ion-ion collisions are relatively unlikely compared to ion-molecule collisions. Each ion trajectory is calculated independently from the others through numerical integration of the equation of motion until the ion undergoes a collision or reaches the substrate [26]. The initial velocity and trajectory of ions at the edge of the sheath are sampled randomly from the thermal distribution function at the gas temperature. Collisions occur at distances randomly sampled from the distribution function defined by the mean free path. New trajectories and energies following collisions are calculated from hard-ball elastic and charge transfer collisions. This simulation was used to provide more accurate estimates of the entire ion energy distribution at the substrate surface. Table 5.5 shows typical values for the input parameters of the *IONTRANS* simulation. The simulation calculates the mean and standard deviation for the number of ion-neutral collisions in the sheath, the mean and standard deviation for the incident angle of the ions with respect to the surface, and the number of ions at the substrate as a function of both energy and incident angle.

The number of ions used in all the simulations in this thesis was 10,000. Considering the computational time required on the workstations for these simulations, this value was a compromise between calculation time and statistical validity. Simulations for 100,000 ions took an order of magnitude longer time, ~100 minutes compared to ~10 minutes, and resulted in insignificant differences in the final ion energy distributions. Extremely short simulations for 1000 ions, on the other hand, sacrificed the accuracy of the results.

Parameter	Value
Number of Particles	10,000
Pressure (mTorr)	20,000
Neutral Gas Temperature (K)	1000 - 3000
dc Sheath Potential (V)	- 100 to - 300
ac Sheath Potential (V)	0.00
dc Sheath Thickness (mm)	1.00
ac Sheath Thickness (mm)	0.00
Frequency (cps)	0.000010
Gas Molecular Weight (amu)	2.0
Ion Molecular Weight (amu)	16.0
Maxwell Ion Temperature (K)	1500 - 3500
Momentum Transfer Cross-Section (m <sup>2</sup> )	1.1 x 10 <sup>-18</sup>
Charge Transfer Cross-Section (m <sup>2</sup> )	0.00
Field model	Linear Variation

Table 5.5 - Input parameters for *IONTRANS* Monte Carlo simulation.

Sheath thickness is a critical value since the ion energy is a function of the number of ion collisions in the sheath which, in turn, is dependent upon the sheath thickness/mean free path ratio. This parameter is also very difficult to measure experimentally since it is defined by the ion species concentrations between the plasma and the substrate. The sheath thickness was estimated as ~1 mm under bias conditions from a visual observation of the cathode dark space. This estimate is expected to be accurate within approximately a factor of 2. Equation 5.13 has been shown to be an appropriate sheath scaling law in the pressure regime for "materials processing discharges" in which the pressure is higher than that for the Child-Langmuir sheath law which assumes a collisionless sheath region [27]:

$$J = \epsilon_0 \left( \frac{500}{243\pi} \right)^{\frac{1}{2}} \left( \frac{2e}{m_i} \right)^{\frac{1}{2}} \frac{V^{\frac{3}{2}} \lambda_i^{\frac{1}{2}}}{s^{\frac{5}{2}}} \quad 5.13$$

In this equation,  $J$  is the current density,  $\epsilon_0$  is the permittivity of free space,  $m_i$  is the ion mass,  $V$  is the sheath potential,  $\lambda_i$  is the ion mean free path, and  $s$  is the sheath thickness. Inserting appropriate parameters for this system ( $J = 5 \text{ mA/cm}^2$ , 3 g/mol for  $\text{H}_3^+$  ions or 16 g/mol for  $\text{CH}_4^+$  ions, 275 V sheath potential, and 9  $\mu\text{m}$  or 31  $\mu\text{m}$  for the mean free path of  $\text{H}_3^+$  or  $\text{CH}_4^+$  ions, respectively) the sheath thickness determined using equation 5.13 ranges from 0.80 - 1.4 mm. Simulations using larger sheath thicknesses led to shifts in the ion energy distribution to lower energies as a result of more ion collisions and subsequent energy loss. Although the simulation code also accounts for an ac-component to the sheath thickness as may be present for capacitive sheaths in RF systems, this was not required for the conditions of this system. Plasma frequency equations rule out the possibility of an ac-component to the sheath thickness for this model [21] since neither the electrons or the ions can respond to the microwave plasma frequency.

Collision cross-sections,  $\sigma$ , were estimated from a simple equation which relates this parameter to the mean free path,  $\lambda$ , and gas density,  $n$ :

$$\sigma = \frac{1}{\lambda n} \quad 5.14$$

As discussed previously, the cross-sections were assumed to be independent of energy. By definition, collision-cross sections are independent of temperature since mean free path and gas density have inverse linear dependences on temperature. The *IONTRANS* simulation also allows for charge transfer effects which are dominant in some plasmas and can dramatically affect the energy distribution of ions and neutrals in the sheath. The probability of collision leading to charge transfer is typically greater for atomic ions colliding with parent atoms or molecular ions colliding with parent molecules (*symmetrical resonant charge transfer*) as shown in equation 5.15 than is charge exchange for collisions of unlike species (*asymmetric charge transfer*) as shown in equation 5.16 which tends to be less efficient [21].



For this reason, charge transfer reactions were not considered for simulations involving  $\text{CH}_4^+/\text{CH}_3^+$  ions colliding with  $\text{H}_2$ . Charge transfer reactions result in the formation of a new ion and a fast neutral. However, the fast neutral cannot gain more energy in the field

since it is no longer charged, and the new ion has an energy less than or equal to that of the original ion; therefore, these reactions cannot create more energetic species than are created in the elastic collisions already considered. Therefore, the simulations to determine the hydrogen ion energy distribution resulting from collisions of hydrogen ions and molecules also did not consider the effects of charge transfer.

The neutral gas temperature impacts the *IONTRANS* simulation primarily through its effect on the density of neutrals in the plasma and sheath. This parameter is difficult to measure experimentally and a wide range of values from 1000 - 5000 K have been reported in the literature [9]. In most plasmas, the ion temperature is typically higher than the neutral temperature since the ions can interact with the fields in the plasma [21]. For this thesis, the neutral and ion temperatures were adjusted so that the simulation data showed close agreement with that measured by the retarding probe under similar conditions. Figure 5.5 shows the ion energy distributions calculated for three different ion/neutral temperatures as well as that measured with the retarding probe at -275 V. The effect of increasing the neutral and ion temperatures is a shift in the ion energy distribution to higher energy values due to the decrease in gas density and concomitant increase in mean free path. A neutral temperature of 3000 K and ion temperature of 3500 K give close agreement as observed in Figure 5.5 for the average ion energy calculated by the model and measured with the retarding probe. These are reasonable values for the temperatures in the plasma [9]. The calculated average ion energy from *IONTRANS* at 3000/3500 K is slightly higher than that determined experimentally due to the shapes of these curves. The experimental data was calculated using an assumed Gaussian distribution while that simulated by the model was not symmetric and showed more ions at energies greater than the peak value.

The results of numerous *IONTRANS* simulations show that the ion energy distribution is affected by changes in the input parameters. The sensitivity of the results to the parameters depends on the particular parameter in question and the magnitude of the variations. Since many of the parameters for this process were not known accurately, the results of the simulations were not used as absolute ion energies but rather to obtain rough estimates, and more importantly, to observe the trends when parameters were adjusted. Figure 5.6 shows that the ion energy distribution varies depending upon the substrate bias voltage. The plots in this figure show the ion energy distributions for a number of applied bias voltages, with the neutral/ion temperatures at 2000/2500 K and the other parameters as listed in Table 5.5. The average ion energies increased with increasing bias due to the larger electric field in the sheath.

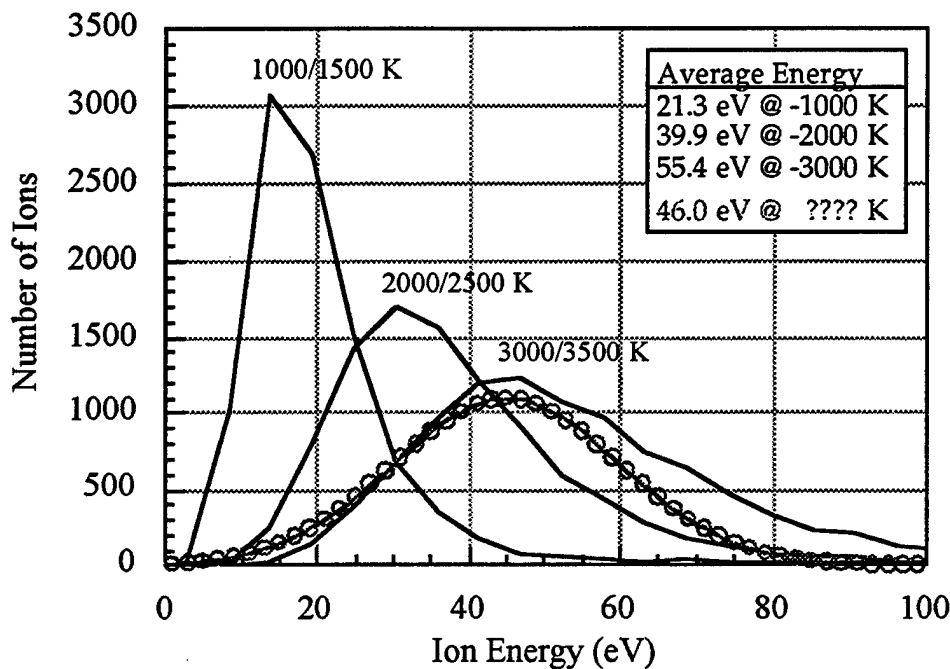


Figure 5.5 - Ion energy distributions for -275 V bias from the Monte Carlo simulations *Iontrans* for different neutral/ion temperatures. The curve through the circles shows experimentally determined energy distribution from retarding probe under similar bias conditions.

The *IONTRANS* simulation also provided the angular distribution of the energetic ions at the substrate surface. Figure 5.7 is a plot of the number of ions versus incident angle for ions with energies ranging from 18 - 46 eV under typical bias deposition conditions. The incident angle in this case is defined between the direction of the incoming ion and the surface normal. Although a large number of collisions occur due to the relatively high process pressure and the short mean free paths, the ions bombard the surface at angles almost normal to the surface. The effect of the slight deviation from perfectly perpendicular bombardment is simply less energy transferred in the direction normal to the surface. Energy transfer efficiency, sputtering yields, and implantation depths are all affected by the angle of incidence of bombarding species, but the narrow angular distribution in Figure 5.7 suggests that the effects in this system are not significant.

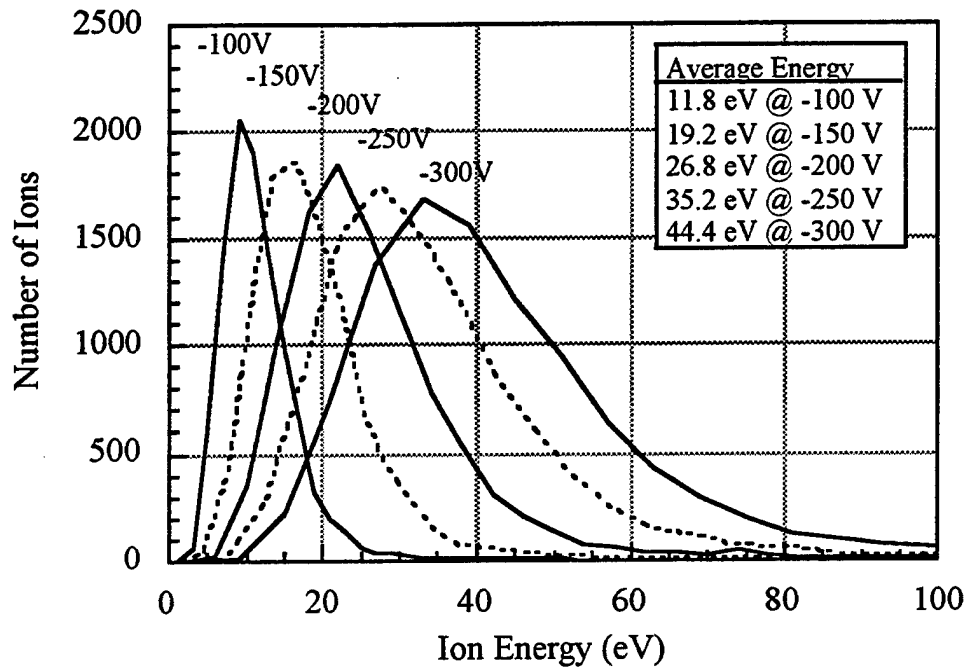


Figure 5.6 - Ion energy distributions from the Monte Carlo simulations *Iontrans* for a number of applied bias voltages.

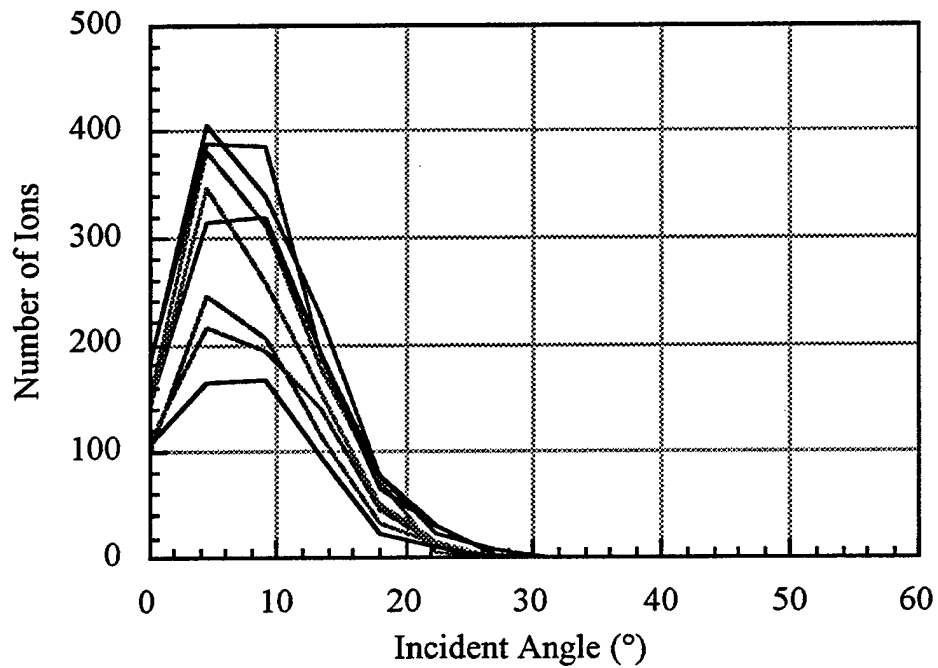


Figure 5.7 - Number of ions versus incident angle for ions with energies ranging from 18 - 46 eV.



The ion species also affect the simulated ion energy distribution both through mass and mean free path considerations. The collision dynamics depend upon the masses of the ion and neutral species as seen in equations 5.9 and 5.11. Recall from Table 5.4 that the mean free path for methane is shorter than for hydrogen ions in the primarily hydrogen gas environment. Therefore, the hydrogen ions travel farther between collisions with hydrogen molecules and gain more energy from the electric field. However, since the mass of the hydrogen ions is closer to the hydrogen molecules than for methane ions, the former also lose more energy upon collision since their energy transfer is more efficient. The result is effectively a cancellation of the two effects and the ion energy distribution calculated by *IONTRANS* for  $H_2^+$  is similar to that for the  $CH_4^+$  ions as shown in figure 5.8. This is fortunate for modeling considerations since it eliminates the need to consider different ion energy regimes for the various ion species present in the system.

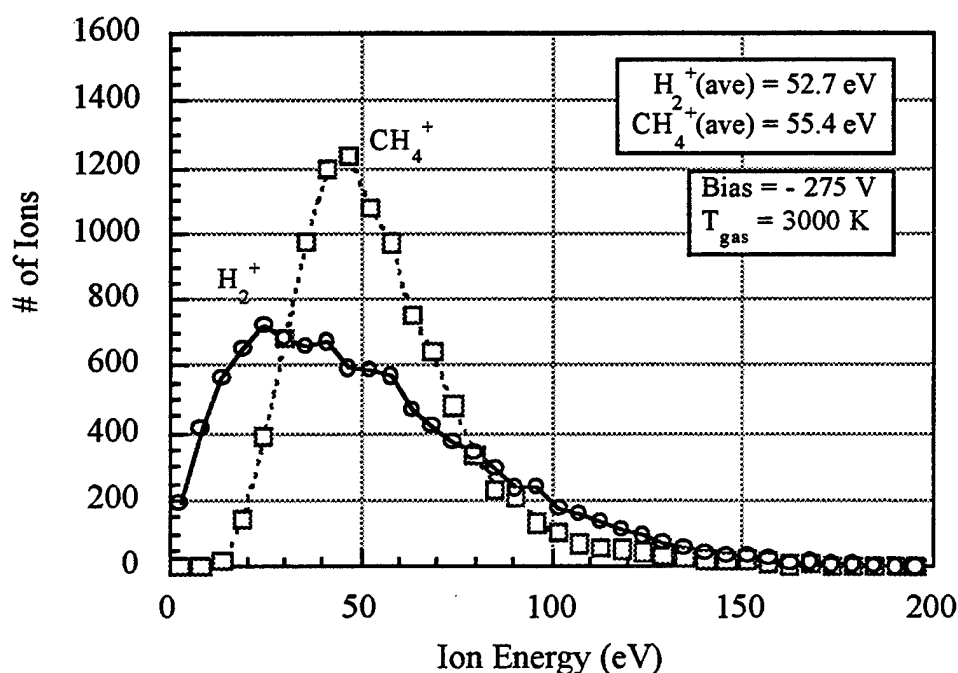


Figure 5.8 - Number of ions versus ion energy for both  $H_2^+$  and  $CH_4^+$  at -275V bias.

## 5.5 Ion-Assisted Diamond Nucleation Mechanisms

The experimental results of Chapter 4 indicate that ions play a critical role in the nucleation of diamond nanocrystals during the ion-assisted process. The previous

sections of this chapter provided details concerning the ionic species, fluxes, and energies. The retarding probe measurements and Monte Carlo simulation results have important implications for the possible ionic mechanisms leading to nucleation since they bracket the critical energy and, therefore, limit the potential atomic processes. Several potential nucleation mechanisms based on energetic ion bombardment including preferential sputtering, thermal spikes, and carbon subplantation are discussed in this section. Variations of each of these mechanisms have been proposed in the literature for the growth of DLC and diamond under energetic ion bombardment.

### 5.51 Preferential Sputtering

Since the substrate is bombarded with an energetic ion flux during the ion-assisted process, sputtering of both the substrate and deposited material must be considered. The sputtering of contaminants from the depositing surface during ion-beam assisted deposition (IBAD) is an important factor in other materials systems. *Physical sputtering* is based purely on the momentum transfer from the energetic incident species to the surface atoms of the substrate. If enough energy is transferred to an atom at the surface it may be ejected, or *sputtered*. *Chemical sputtering* may also occur in which a chemical reaction between the incoming energetic species and the substrate atoms causes removal of material from the surface. The atomistic mechanisms for physical sputtering are understood quite well while the processes occurring in chemical sputtering are not fully understood. In both cases, sputtering has a threshold below which no atoms are ejected. For physical sputtering, this threshold has been estimated as approximately four times the binding energy,  $E_b$ , of the sputtered atom to the surface [28].

A mechanism for the evolution of a diamond phase in a growing film based on the preferential sputtering of non-diamond carbon with respect to diamond-bonded carbon can be envisioned [29]. Consider the deposition of a film which is composed of both non-diamond carbon and diamond. At incident ion energies where non-diamond carbon is sputtered at a significantly higher rate than diamond, the diamond phase could evolve preferentially in the growing film. However, this scenario depends on several characteristics of the process. First, both diamond and non-diamond material must be present at the surface. Second, the diamond sputtering rate must be less than its deposition rate or no net diamond growth will occur. Although the latter criteria may be satisfied in the ion-assisted process, the presence of diamond in the depositing film is problematic for this mechanism.

For carbon, the sputter yields are known to differ significantly for the various allotropes. The displacement energies for carbon in a diamond structure and carbon in a graphitic structure have been estimated as 80 eV and 25 eV, respectively [30]. However, more recent direct measurements of these energies report values which differ by a much smaller amount with graphite at 35 eV and diamond at 37 - 47 eV depending upon the crystallographic orientation [31, 32]. However, graphite in-plane bonds are expected to sputter less than out-of-plane bonds due to the large differences in bond strengths, 7.43 and 0.86 eV, respectively [30]. The sputter yield for amorphous carbon, graphite, and diamond with 100 eV carbon ions at near-normal incidence has been calculated to be approximately 0.1, 0.01, and 0.001, respectively [33]. These values were calculated using TRIM code and estimated surface binding energies of 2 eV, 3.5 eV, and 7.4 eV for amorphous carbon, graphite, and diamond. Experimental values for these sputter yields were not available and the substantial yield differences from the calculations result due to the large differences assumed in the surface binding energies. Since sputter yields decrease with lower energy ions as are found in this process, the values just listed are maximum sputter yields. These sputter yields are quite low and make it difficult to explain the evolution of a diamond phase by carbon sputtering alone since the neutral depositing carbon species flux is several orders of magnitude higher than the ion flux.

However, the sputtering yield also depends upon the sputtering species and chemical sputtering may occur for species such as hydrogen and oxygen. This thesis has demonstrated that hydrogenic ions not only are present, but most likely are the dominant ions in the system. Hsu has reported chemical sputtering yields of diamond and graphite by energetic  $H^+$  in the 200 - 800 eV range [16]. These yields are temperature dependent and peak at 800 °C where the yield is 0.1 for graphite and 0.03 for diamond. As was the case for carbon ions, these sputter yields are small compared to the flux of depositing carbon neutrals, but could help explain the evolution of diamond in a non-diamond matrix.

Even if the physical and chemical sputtering account for diamond phase evolution in the depositing carbon films, such mechanisms do not provide the initial diamond nuclei required for such a model. A mechanism for diamond nucleation is still required for this phase to evolve in the growing film, and the preferential removal of material by sputtering does not provide a means to form diamond. Therefore, although it is likely that preferential sputtering does occur, albeit on a limited basis in this process, it cannot account for the diamond nucleation phenomenon.

## 5.52 Thermal Spikes

Alternatively, the concept of a *thermal spike* [34] may explain the formation of diamond nuclei under an energetic ion flux. This mechanism is shown schematically in Figure 5.9. A thermal spike is a product of the transfer of the incident ion energy to an extremely small and localized region at the substrate surface, thereby causing a brief, but extreme, temperature fluctuation. For impinging species with energies less than 100 eV, no major displacements of the atoms occur and the atoms instead impart their excess energy to the adjacent atoms around the site of impact. Through mutual interactions with neighboring atoms, a short-lived region of highly agitated atoms is produced [35]. Since XPS experiments prior to energetic ion bombardment indicated the presence of carbon clusters at the substrate surface, highly-activated clusters of carbon atoms may transform into diamond nuclei due to the thermal spike.

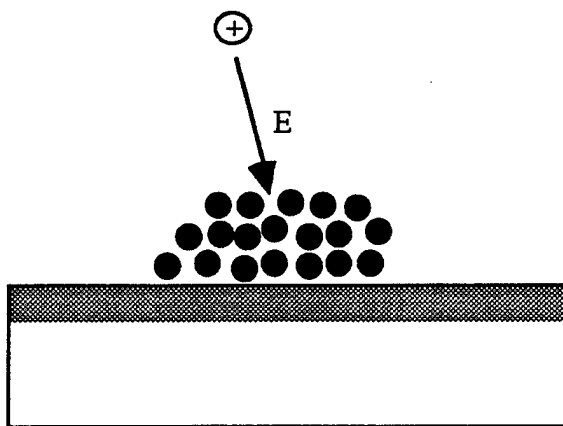


Figure 5.9 - Bombardment of surface carbon cluster by an energetic ion to produce a temperature/pressure spike.

The atomic processes which occur during the ion-solid interaction must be considered for assessment of the thermal spike mechanism. The thermal spike just described is different than a *displacement spike* in which the bombarding particles have higher energies (hundreds of eV) and atoms are actually displaced from their lattice sites. The energetic ion-solid interaction has been separated into three major regimes [36]:

- **Collisional regime** - the incoming ion transfers its kinetic energy to the solid and a structure of highly energetic or displaced atoms known as collision cascade forms. In the low-energy regime (10 - 1000 eV), the characteristic timescale for this process is a few tenths of a picosecond ( $10^{-12}$  s).
- **Thermalization of the cascade region** - the energetic atoms lose their excess kinetic energy through generation of phonons in the surrounding material. The thermalization regime ends when the cascade region has settled into local thermal equilibrium with the surrounding region. This occurs within a few picoseconds for cascades generated by low-energy interactions.
- **Long-term relaxation** - the damaged cascade region changes due to diffusional processes and interaction with other incoming atoms or ions. This time scale is dependent on the specific process and material and is varies widely ( $10^{-10}$  - 1 s) making it difficult to model atomistically.

A general model for the thermal spike was developed by Seitz, *et al.*, based on the instantaneous transfer of energy to the lattice in the form of heat which spreads according to the classical laws of heat transfer [34]. The temperature in the region surrounding the spike was assumed to obey the heat conduction equation:

$$\nabla^2 T = \frac{1}{D} \frac{\partial T}{\partial t} \quad 5.17$$

The thermal diffusivity,  $D$  ( $\text{cm}^2/\text{s}$ ), is related to the thermal conductivity,  $K$ , and the specific heat capacity,  $C_v$ , of the material. For the microscale regime, it is easier to work with thermal diffusivity in terms of the phonon velocity (speed of sound),  $v$ , and the phonon mean free path,  $\Lambda$ . The relationship between these variables is given by :

$$D = K / C_v \quad 5.18$$

$$K = C_v v \Lambda / 3 \quad 5.19$$

$$D = v \Lambda / 3 \quad 5.20$$

The solution to the heat transfer equation in terms of the radial distance from the point of energy transfer,  $r$ , and the time,  $t$ , given an incident energy,  $E$ , and an initial temperature,  $T_0$ , is given by the following expression:

$$T(r,t) = T_0 + \frac{E}{C_v(4\pi Dt)^{3/2}} e^{-r^2/4Dt} \quad 5.21$$

Applying this model to the ion-assisted nucleation process is not a straight forward insertion of values and calculation. Assuming the heat conduction equation is valid for this system, problems still remain for choosing the correct material physical properties to solve the equation. First, it is not clear whether the concepts of thermal conductivity and heat capacity hold for such localized regions. Second, these parameters are expected to vary for the different forms of carbon and an accurate value or estimate is difficult. The speed of sound in low H-content carbon films with densities of  $\sim 2 \text{ g/cm}^3$  has been measured as  $10^4 \text{ cm/s}$  [37]. Although the structure of this material was not well characterized, these carbon films were assumed amorphous since their densities were less than that for graphite ( $2.25 \text{ g/cm}^3$ ). Amorphous structures have extremely short phonon mean free paths due to the lattice disorder which scatters the lattice vibrations [38, 39]. The mean free path was estimated as  $\sim 5 \text{ \AA}$  for this case since it was postulated that the carbon was essentially amorphous prior to ion bombardment and diamond nucleation. These values result in a thermal diffusivity on the order of  $10^{-4} \text{ cm}^2/\text{s}$ . Although thermal diffusivity is temperature dependent, this was not accounted for in this simple analysis. The heat capacity,  $C_v$ , was approximated as  $3nk_B$  in the high-temperature Debye limit where  $n$  is the atomic density ( $\text{cm}^{-3}$ ) and  $k_B$  is the Boltzmann constant [40]. The initial temperature,  $T_0$ , was set at the substrate temperature of 1073 K.

Using equation 5.21, Figure 5.10 shows the thermal spike temperature as a function of radial position and time. Figure 5.11 shows the thermal spike temperature 1 picosecond after bombardment by ions of various energies. These plots clearly show the "spike" nature of this phenomenon. If the phonon mean free path is increased from  $5 \text{ \AA}$  to  $10 \text{ \AA}$ , the maximum temperature at 20 eV ions drops from 9100 K to 3900 K and the spike radius increases from  $4 \text{ \AA}$  to  $6 \text{ \AA}$ . All of the input parameters for this model may be inaccurate leading to significant differences in the absolute, but not qualitative, features of these curves. Other researchers using the formulation by Seitz [34] for thermal spikes have estimated that low energy ions incident on amorphous carbon and silicon produce a region consisting of nearly 100 atoms excited to a temperature of several thousand Kelvins which decays over a time period of  $10^{-11} \text{ s}^{-1}$  [41].

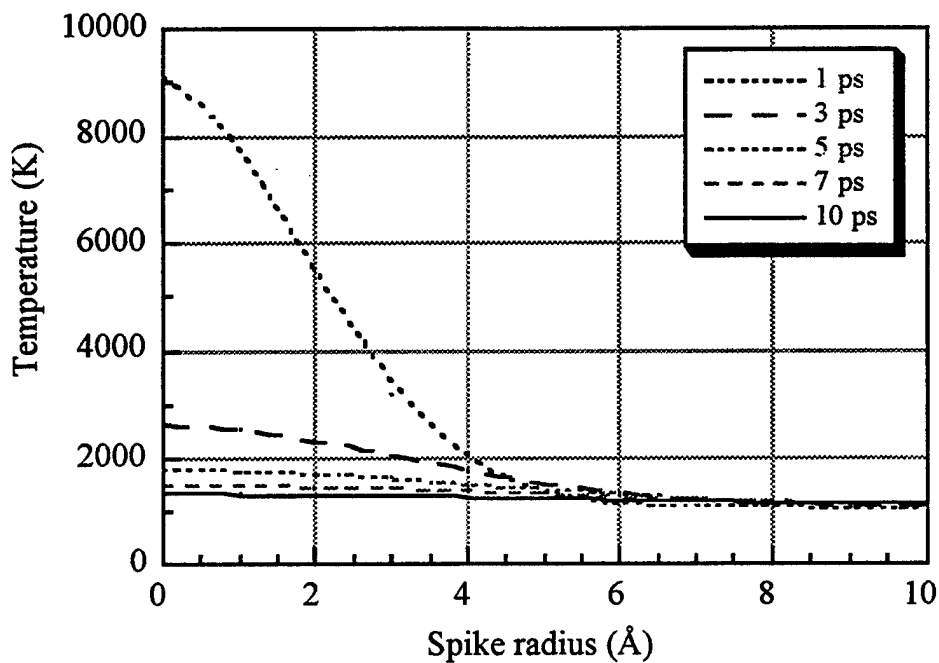


Figure 5.10 - Temperature profile for thermal spike as a function of time following impact by a 20 eV atom.

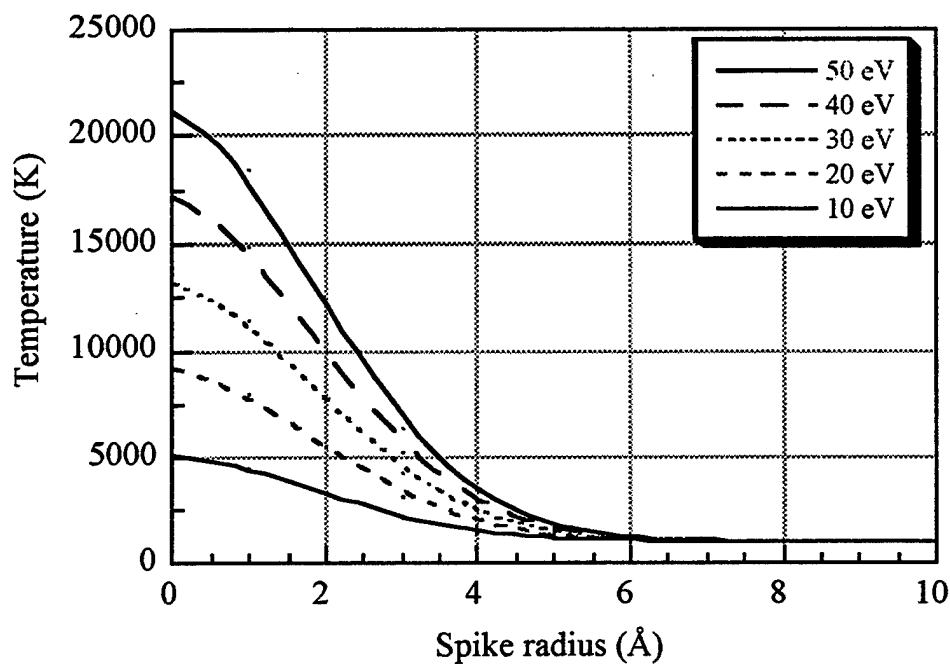


Figure 5.11 - Temperature profile for thermal spike one picosecond after impact of various energy atoms.

The argument for the transformation of a carbon cluster from an amorphous to diamond structure by a thermal spike is based upon thermodynamics. The carbon phase diagram is shown in Figure 5.12. At the high temperatures envisioned in the thermal spike, a corresponding increase in pressure must accompany the temperature rise to move the system state vertically from the graphite to the diamond stability region. Two possibilities exist to account for the pressure required for the thermodynamic transformation of carbon to diamond. First, the bombarding ion produces a pressure spike in addition to the thermal spike. Considering the bonds between the carbon atom as springs, bombardment of a carbon cluster with an energetic species will produce a very brief pressure wave which travels through the atoms in the cluster. Shock wave calculations have estimated a pressure rise in the spike region of 10 to 100 GPa depending upon the assumptions made in the calculations [41].

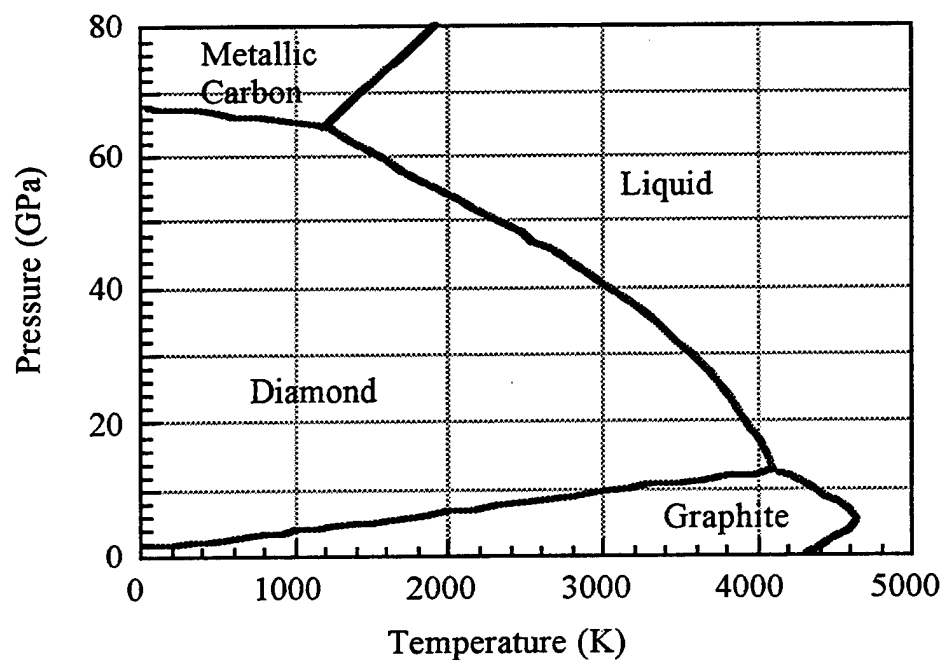


Figure 5.12 - Carbon phase diagram showing stability regions for diamond and graphite [42].

Alternatively, theoretical calculations by Badziag, *et al.*, argue that for nanocrystalline carbon clusters, diamond is more stable than graphite for hydrogen-terminated clusters below a certain size [43]. Figure 5.13 plots the binding energy per mole of carbon for various carbon molecules with hexagonal and tetrahedral geometries. These molecules



have been used to represent small graphite (hexagonal) and diamond (tetrahedral) hydrogen-terminated clusters. The binding energy of these species crosses as expected since graphite is more stable than diamond under normal conditions. This graph suggests that as the H/C ratio increases, the tetrahedral geometry is more stable if the carbon atoms are hydrogen-terminated. The crossover point of  $H/C = 0.24$  corresponds to a cluster of size of  $\sim 30\text{\AA}$ . Therefore, diamond clusters smaller than this size are considered stable compared to graphite due to hydrogen stabilization. If this postulate were true, it removes the high pressure restriction in the carbon phase diagram and allows for diamond stability because the abundance of H<sup>+</sup> in nucleation environment is expected to react and terminate unfilled carbon bonds.

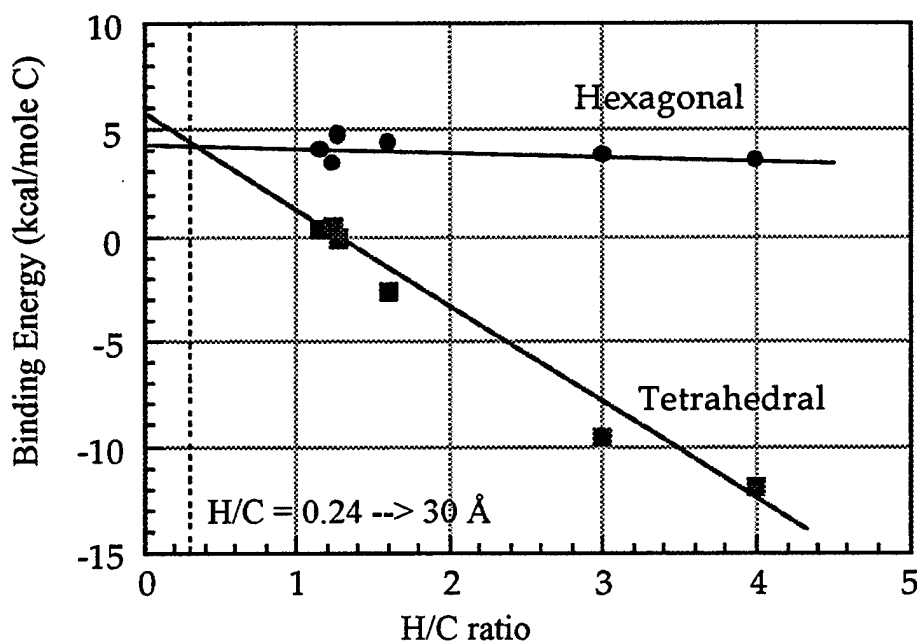


Figure 5.13 - Binding energies of hexagonal and tetrahedral carbon species as a function of the H/C ratio [43].

The interpretation of the thermal spike model and estimates is not straight forward since the concepts of "temperature" and "pressure" are not well-defined for such a small number of atoms over such brief time periods. However, these estimates, although not exact, indicate that it is possible for the system to pass through a diamond phase region during the thermal spike. The rapid decay of the spike may allow the

diamond phase to be quenched-in as the temperature cools and the system moves into the graphite stability region; diamond would be metastable in this state, but would not transform due the large activation barrier. Given the estimates on the short lifetime of the thermal spike, kinetics become important for evaluating this dynamic process. Thermodynamic phase equilibrium requires some time and it is not clear whether the diamond phase can kinetically be realized during the thermal spike. Pulsed laser annealing of amorphous silicon results in crystallization over the nanosecond time scale, but the thermal spike process is several orders of magnitude faster. However, the differences between the atomic positions for the various forms of carbon are not great. The transformation of diamond from an amorphous to diamond structure does not require significant atomic rearrangement. Amorphous carbon films (a-C) have a complicated structure which consists of both  $sp^2$  and/or  $sp^3$  bonding [44]. The first and second nearest neighbors in amorphous carbon can be compared to those for perfect diamond and graphite. The values for amorphous carbon shown in Table 5.6 are average values for a number of different amorphous carbon films [44]. The small difference in the structure for the various forms of carbon suggests that relatively long times on the scale of diffusional jumps may not be necessary to change the phase.

Carbon Form	1 <sup>st</sup> Nearest Neighbor (Å)	2 <sup>nd</sup> Nearest Neighbor(Å)
Graphite	1.42	2.44
a - Carbon	1.5	2.5
Diamond	1.55	2.52

Table 5.6 - Nearest neighbor distances for various forms of carbon.

Note that the thermal spike mechanism does account for the experimental observation of a critical nucleation voltage. In figure 5.11, the temperature of the spike one picosecond after impact is observed to vary dramatically for different energies. A low-energy ion may not possess sufficient energy to move the system into the diamond stability region of the phase diagram, thereby preventing nucleation during the thermal spike. As the ion energy increases, it becomes more likely for the system to enter the diamond stability region and lead to enhanced nucleation. Further energy increases may not necessarily improve the efficiency of this process.

Although the thermal spike model has characteristics which allow a thermodynamic explanation for nucleation, experimental observations reject this as the sole mechanism for ion-assisted nucleation. The thermal spike model is not sensitive to the chemical species imparting the energy into the substrate. As long as the species transfers energy with a similar efficiency, it should not matter whether the species is carbon or argon or another atom. Although methyl/methane ion to carbon atom transfer of energy in binary collisions is most efficient at 98% (see equation 5.12), the energy transfer from helium ions (64%) or argon ions (71%) to carbon atoms is only slightly less efficient. Therefore, if the only issue were energy transfer to the carbon atoms, argon and helium and other atoms should cause nucleation enhancement. The sequential reactor experiments discussed in section 4.44 are not consistent with this model. Nucleation enhancement was only observed for the case of carbon ions accelerated into the surface. Both helium and argon produced no enhancement of the nucleation. Therefore, the nucleation model must account for the specificity of the bombarding ions and the thermal spike is not sufficient to account for the results in this thesis.

### 5.53 Subplantation of Carbon

The fact that the bombardment of carbon ions into carbon clusters on the substrate leads to diamond nuclei points to *subplantation* as a potential nucleation mechanism. This model has been used extensively to account for the formation of diamond-like carbon, an extremely hard carbon phase with a density nearly that of diamond [33, 45]. Recently, this mechanism has been extended in attempts to account for nucleation of both diamond and cubic boron nitride [46, 47] (also reference c-BN). This mechanism relies on the implantation of energetic carbon ions in the near-surface region, or subplantation. A schematic of this process is shown in Figure 5.14. The incoming ion has sufficient energy to implant itself within the top several monolayers of the substrate/carbon clusters either by direct penetration into an interstitial site or by displacement of an atom present at the surface.

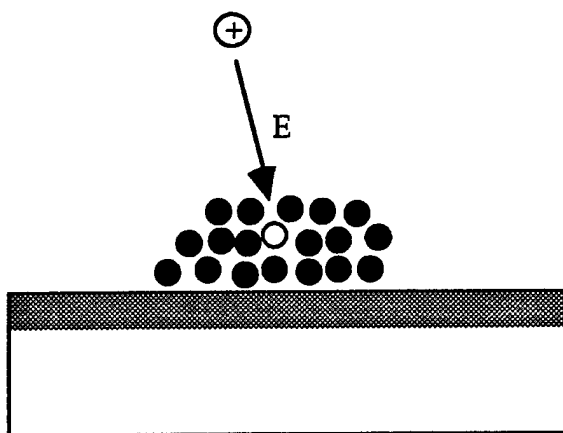


Figure 5.14 - Schematic of shallow implantation (subplantation) of an energetic ion into a carbon cluster on the silicon substrate.

Recall the ion energy distribution of the bombarding species for the ion-assisted process; nearly all ions possessed less than 100 eV and the average energy was approximately half this value depending on the bias voltage. A computer simulation known as *TRIM* (Target Range in Matter) provides the interaction of energetic atoms with a substrate [48]. The average implanted depth, or range, calculated using *TRIM* show that carbon ions ( $C^+$ ) and methane ions ( $CH_4^+$ ) with energies less than  $\sim 100$  eV will be stopped within  $5 \sim 10 \text{ \AA}$  of the surface of a carbon target [33, 49]. Furthermore, Robertson has estimated the probability of low energy carbon ion penetration into an amorphous carbon substrate as a function of the ion energy [50]. This data is plotted in Figure 5.14 for a  $2 \text{ g/cm}^3$  carbon target assuming a displacement energy,  $E_d$ , of 35 eV and a binding energy,  $E_b$ , of 7.4 eV. However, the results of these calculations must be interpreted carefully since their accuracy at these lower ion energies is questionable due to assumptions in the basic *TRIM* model [51]. The important characteristic of the penetration probability of Figure 5.14 is the rapid rise in this probability above the threshold energy of  $\sim 25$  eV. Superimposed on the penetration probability plot are the ion energy distributions calculated by the *IONTRANS* Monte Carlo simulation (Figure 5.6) for several different applied bias voltages. For bias voltages less than 100 V, there is little overlap of the high energy species with the penetration probability. This produces little nucleation since few ions are subplanted. At higher bias voltages, the overlap of the

higher energy ions and the penetration probability increases and the nucleation would increase dramatically if this mechanism controls.

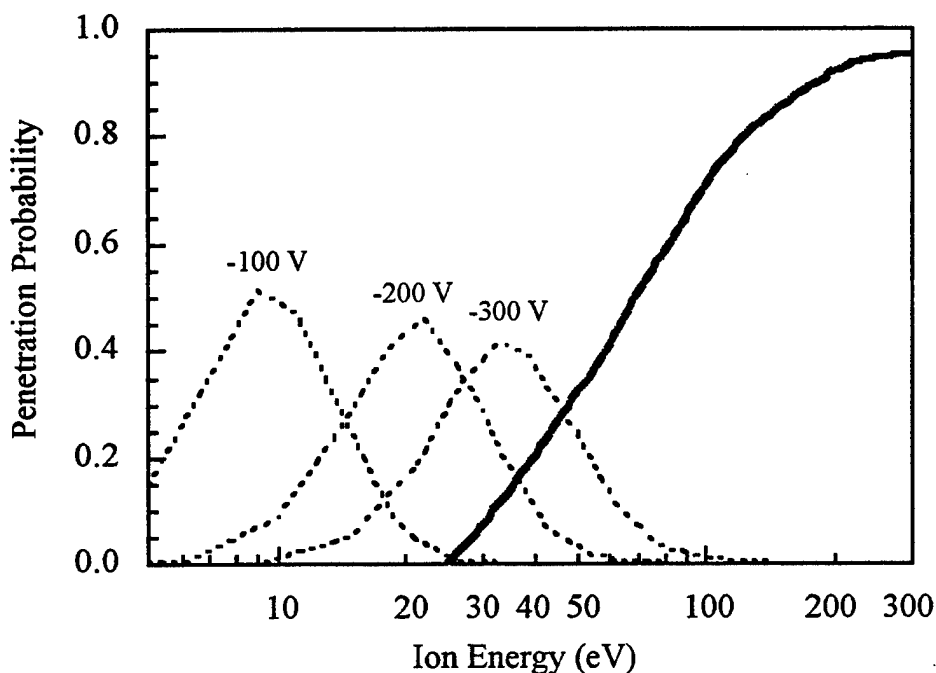


Figure 5.14 - Penetration probability of  $C^+$  ions into an amorphous carbon target from TRIM calculation. Data from Robertson [45].

For the ion-beam deposition of diamond-like carbon films (DLC), it has been shown that the both the density and hardness of these carbon films pass through a maximum with ion energy. These results coupled with electron energy loss spectroscopy (EELS) studies led to the conclusion that the formation of  $sp^3$  carbon relative to  $sp^2$  carbon shows a maximum with ion energy which is centered between 50 and 200 eV depending upon the system [33, 52]. A subsurface growth mechanism in this optimal ion energy range has also been confirmed with roughness measurements by atomic force microscopy surface [53]. The subplantation mechanism developed by Lifshitz, *et al.*, predicts this maximum to result from a competition between the probability of penetration and the annealing of  $sp^3$  phases by the thermal spikes from high-energy ion bombardment. An optimum energy results since low-energy ions do not penetrate

efficiently while high-energy ions cause large thermal spikes which anneal out the density increases.

As was the case for the thermal spike mechanism, the subplantation model for diamond nucleation can be evaluated from a thermodynamic perspective. Although the incident energies are too low for this process to cause significant atom displacement, subplanted carbon atoms produce a compressive stress in the growing film by an "ion-peening" process which has been explained in detail in the literature [54]. From the carbon phase diagram of Figure 5.12, the stress required to move across the stability line from graphite to diamond is only  $\sim 3$  GPa at typical ion-assisted nucleation substrate temperatures. Stress levels in this range have been observed in DLC films deposited by carbon ion-beam deposition [33]. The appropriate film stress for phase diagram considerations is hydrostatic stress; most ion-deposited thin films show biaxial compressive stress, but this stress can be reduced mathematically to two components - a hydrostatic stress and a shear distortion. The biaxial compressive stress,  $\sigma$ , in thin films as obtained from measurements of substrate curvature is related to the hydrostatic stress,  $P$ , by the following relation:

$$P = \frac{2}{3} \sigma \quad 5.22$$

McKenzie, *et al.*, found that film stress in ion-assisted deposited carbon films passed through a maximum which closely matched maxima in both the film density and  $sp^3/sp^2$  ratio. Comparing these stresses to the carbon phase diagram produced good agreement with the formation of a tetrahedral carbon phase when the stresses crossed the graphite/diamond stability line [55]. This compressive stress concept may also explain the formation of diamond nuclei for this ion-assisted process. Although stresses were not directly measured for the films of this thesis, they are expected to be compressive and in the range found by other researchers for similar processes. The stresses arising from the subplantation of carbon in the film lead to diamond stability according to the phase diagram. The fact that the entire bias-deposited film does not convert to diamond, but rather is composed of small diamond nuclei in a non-diamond matrix, may have several origins. The nonuniformity of the deposited carbon clusters may mean that only a small fraction of the implanted carbon ions reside in local regions where the stress is high enough for diamond to be stable. Alternatively, many regions of the film with the appropriate stress may be present, but kinetics may limit the degree of transformation to the diamond structure. Finally, the thermal spike associated with the subplantation

mechanism may destroy existing diamond phases or prevent the transformation of a local region.

A thermal spike, although not sufficient to explain diamond nucleation, does occur even in a subplantation mechanism and probably plays an important role. The optimum energy for subplantation in DLC formation has been postulated to result from competition between maximum implantation probability while minimizing thermal spike effects which can "anneal" out the diamond phase. Diamond surfaces begin to graphitize at temperatures between 600 and 1000 °C, and thermal spike is clearly "hotter" than this for a brief time period. This may explain the nucleation levels observed for the ion-assisted process. As discussed in the previous section, the thermodynamic arguments assume the kinetics allow the diamond phase to form in the short time the system exists in the diamond stability region. This assumption may not be accurate and the majority of the thermal spikes might not form diamond nuclei due to kinetic limitations. However, given the observed levels of diamond nucleation with respect to the ion flux, the ion-assisted nucleation process is not efficient. Over a 15 minute ion-assisted pretreatment, the ion dose to the surface is well over  $10^{15}$  ions/cm<sup>2</sup>. Nucleation densities observed by SEM were  $10^{10}$  cm<sup>-2</sup> and by TEM were  $10^{11}$  cm<sup>-2</sup> so an efficiency of 0.001 is more than enough to account for the experimental observations. Therefore, even if most of the thermal spikes resulted in amorphization or graphitization of the carbon clusters, relatively improbable diamond transformations can still account for the nucleation levels observed.

The ion energies measured and simulated for this ion-assisted nucleation process are somewhat lower than those considered to be optimum for DLC formation by subplantation. However, most subplantation research for DLC films has utilized mass-selected-ion-beams or other methods which allow tight control of the ion energies. This control is not present in the ion-assisted MPCVD process where the energy distribution is quite broad. Therefore, the small optimum energy discrepancies are not significant.

The ion-assisted diamond nucleation process is also quite different from the DLC processes due to the presence of large amounts of H<sup>+</sup> along with the neutral and ion fluxes. The atomic hydrogen in this process may assist stabilization of the diamond phase as discussed in the previous section and also minimizes non-diamond carbon bonding by virtue of the higher abstraction rate of this material compared to diamond. Experimental results indicate that hydrogen or energetic hydrogenic ions are critical for diamond nucleation. The deposition of carbon by energetic carbon beams without the presence of hydrogen has not lead to the formation of diamond, even though carbon films with high tetrahedrally-bonded sp<sup>3</sup> carbon percentages can be formed under these conditions [55].

Furthermore, unbiased MPCVD on most DLC and hard carbon films do not produce highly nucleated diamond films.

In addition to its consistency with the experimental results of this thesis, the carbon subplantation mechanism may be consistent with the limited heteroepitaxial nucleation of diamond on Si and SiC [18, 56, 57]. Since the incident ion energies are sufficiently low that displacement of the Si substrate atoms is unlikely, the registry of the deposited carbon film with the underlying substrate may not be affected. However, more experimental evidence is required to prove this point.

Table 5.7 below compares the attributes and deficiencies of each of the mechanisms discussed in this section. Each mechanism accounts for the control of nucleation by ion bombardment. The observed nucleation densities may be explained by inefficient thermal spike and subplantation mechanisms, whereas preferential sputtering does not adequately explain the formation of high densities of diamond nuclei. Both the thermal spike and subplantation mechanisms satisfy thermodynamic phase stability considerations under certain assumptions. However, kinetic arguments for the thermal spike are much more difficult to explain than for the subplantation mechanism. Finally, only the carbon subplantation mechanism is consistent with the experimental evidence for ion specificity observed in the sequential deposition scheme.

Experimental Observation	Preferential Sputtering	Thermal Spike	Carbon Subplantation
Ion Bombardment Control of Nucleation	Yes	Yes	Yes
Nucleation Density	No	Yes	Yes
Critical Bias Voltage	No	Yes	Yes
Temperature Independence	No	Yes	Yes
Thermodynamic Phase Stability/Kinetics	No	Maybe	Yes
Ion Specificity	No	No	Yes

Table 5.7 - Comparison of nucleation models for ion-assisted diamond nucleation process.



In spite of the apparent consistency of the subplantation mechanism for ion-assisted nucleation, neither this nor the other mechanisms adequately explains the nucleation ( $<10^4 \text{ cm}^{-2}$ ) which occurs for deposition without an applied bias. Other researchers have shown that substrate contamination, surface defects, and topography do contribute to small, but real, increases in the nucleation density [58]. These mechanisms may account for all nuclei which form without the presence of energetic species. Alternatively, the distribution of ionic and neutral species in the plasma is such that there is a small, but finite, number of species which have the energies that have been claimed to cause the nucleation enhancement. These may be sufficient in number to account for low level nucleation when no bias is applied.

## 5.4 References

1. D. A. Porter and K. E. Easterling, *Phase Transformations in Metals and Alloys*, Chapman and Hall, London (1981).
2. J. Musil, *Vacuum*, **36**, 161 (1986).
3. C. R. Koemtzopoulos, D. J. Economou, and R. Pollard, *Diamond Rel. Mater.*, **2**, 25 (1993).
4. H. Toyoda, H. Kojima, and H. Sugai, *Appl. Phys. Lett.*, **54**, 1507 (1989).
5. H. Chatham, D. Hils, R. Robertson, and A. Gallagher, *Journal of Chemical Physics*, **81**, 1770 (1984).
6. *Handbook of Chemistry and Physics*, The Chemical Rubber Company, Cleveland (1970).
7. T. Oka, *Reviews of Modern Physics*, **64**, 1141 (1992).
8. W. Zhang and Y. Catherine, *Plasma Chemistry and Plasma Processing*, **11**, 473 (1991).
9. W. Hsu, *J. Appl. Phys.*, **72**, 3102 (1992).
10. M. Frenklach and H. Wang, *Phys. Rev. B*, **43**, 1520 (1991).
11. S. J. Harris and D. G. Goodwin, *Journal of Chemical Physics*, **97**, 23 (1993).

12. D. S. Olson, M. A. Kelly, S. Kapoor, and S. B. Hagström, in *Proceedings of the Wide Band Gap Semiconductors Symposium*, ed. T. D. Moustakes, J. I. Pankove, and Y. Hamakawa, Materials Research Society, vol. 242, 43 (1992).
13. D. S. Olson, M. A. Kelly, S. Kapoor, and S. B. Hagström, *J. Appl. Phys.*, **74**, 5167 (1993).
14. D. S. Olson, M. A. Kelly, S. Kapoor, and S. B. Hagström, *J. Mater. Res.*, **9**, 1546 (1994).
15. D. S. Olson, Ph. D. Thesis - *The Sequential Deposition of Diamond Thin Films From Carbon and Atomic Hydrogen*, Stanford University (1992).
16. W. L. Hsu, *J. Vac. Sci. Technol. A*, **6**, 1803 (1988).
17. B. W. Sheldon, R. Csencsits, J. Rankin, R. E. Boekenhauer, and Y. Shigesato, *J. Appl. Phys.*, **75**, 5001 (1994).
18. X. Jiang, *et al.*, *Diamond Rel. Mater.*, **2**, 407 (1992).
19. S. Yugo, T. Kimura, and T. Kanai, *Diamond Rel. Mater.*, **2**, 328 (1992).
20. J. Gerber, M. Weiler, O. Sorh, K. Jung, and H. Ehrhardt, *Diamond Rel. Mater.*, **3**, 506 (1994).
21. B. Chapman, *Glow Discharge Processes*, John Wiley and Sons, New York (1980).
22. H. Chan, PhD Thesis - Department of Mechanical Engineering, Stanford University (1990).
23. W. G. Vincenti and C. H. Kruger, *Introduction to Physical Gas Dynamics*, Krieger Publishing Co., (1986).
24. W. M. Rohsenow and H. Choi, *Heat, Mass, and Momentum Transfer*, Prentice-Hall, Englewood Cliffs, New Jersey (1961).
25. J. P. McVittie, *et al.*, Stanford University - Integrated Circuits Laboratory, Version 2.5 (1993).
26. J. I. Ulacia and J. P. McVittie, in *Proceedings of the Seventh Symposium on Plasma Processing*, ed. G. S. Mathad and G. C. Schwatz, The Electrochemical Society, vol. 88-22, 50 (1988).
27. M. A. Lieberman, *J. Appl. Phys.*, **65**, 4186 (1989).
28. J. Bohdanky and J. Roth, *J. Appl. Phys.*, **51**, 2861 (1980).

29. E. G. Spencer, P. H. Schmidt, D. C. Joy, and F. J. Sansalone, *Appl. Phys. Lett.*, **29**, 118 (1976).
30. J. C. Angus, P. Koidl, and S. Domitz, in *Plasma Deposited Thin Films*, ed. J. Mort and F. Jansen, CRC Press, Inc., Boca Raton (1986).
31. H. J. Steffen, D. Marton, and J. W. Rabalais, *Physical Review Letters*, **68**, 1726 (1992).
32. J. Koike, D. M. Parkin, and T. E. Mitchel, *Appl. Phys. Lett.*, **60**, 1450 (1992).
33. Y. Lifshitz, S. R. Kasi, J. W. Rabalais, and W. Eckstein, *Phys. Rev. B*, **41**, 10468 (1990).
34. F. Seitz and J. S. Kohler, in *Progress in Solid State Physics*, ed. F. Seitz and D. Turnbull, Academic, New York (1956).
35. K. J. Klabunde, *Thin Films From Free Atoms and Particles*, Academic Press, Inc., Orlando, (1985).
36. B. W. Dodson, in *Proceedings of the Laser- and Particle-Beam Chemical Processes on Surfaces Symposium*, ed. A. W. Johnson, G. L. Loper, and T. W. T. W. Sigmon, Materials Research Society, Pittsburgh, PA, 1989, vol. 129, 29 (1988).
37. A. Ali, R. O. Dillon, N. J. Ianno, and A. Ahmad, in *Proceedings of the International Conference on Metallurgical Coatings and Films*, American Vacuum Society (1995).
38. K. E. Goodson, M. I. Flik, L. T. Su, and D. A. Antoniadis, *Journal of Heat Transfer*, **116**, 317 (1994).
39. K. E. Goodson and M. I. Flik, *Thermal Science and Engineering*, **2**, 191 (1994).
40. C. Kittel, *Introduction to Solid State Physics*, John Wiley and Sons, New York (1986).
41. C. Weissmantel, *Thin Solid Films*, **92**, 55 (1982).
42. G. C. Suits, *American Scientist*, **52**, 395 (1964).
43. P. Badziag, W. Verwoerd, W. Ellis, and N. Grenier, *Nature*, **343**, 244 (1990).
44. D. C. Green, D. R. McKenzie, and P. B. Lukins, in *Materials Science Forum: Properties and Characterization of Amorphous Carbon Films*, Trans Tech Publications, Switzerland (1990).

45. J. Robertson, *Diamond Rel. Mater.*, **3**, 361 (1994).
46. J. Robertson, *Diamond Rel. Mater.*, **4**, 549 (1995).
47. J. Robertson, *et al.*, *Appl. Phys. Lett.*, **66**, 3287 (1995).
48. J. P. Biersack and L. G. Haggmark, *Nucl. Instrum. Methods*, **174**, 257 (1980).
49. J. Angus and C. Hayman, *Science*, **241**, 913 (1988).
50. J. Robertson, *Diamond Rel. Mater.*, **2**, 984 (1993).
51. B. W. Dodson, in *Proceedings of the Proceedings of Processing and Characterization of Materials Using Ion Beams Symposium*, ed. L. E. Rehn, J. Greene, and F. A. Smidt, Materials Research Society, vol. 128, 137 (1989).
52. Y. Lifshitz, S. R. Kasi, and J. W. Rabalais, *Physical Review Letters*, **62**, 1290 (1989).
53. Y. Lifshitz, G. Lempert, and E. Grossman, *Physical Review Letters*, **72**, 2753 (1994).
54. H. Windischmann, *J. Appl. Phys.*, **62**, 1800 (1987).
55. D. R. McKenzie, D. Muller, and B. A. Pailthorpe, *Physical Review Letters*, **67**, 773 (1991).
56. B. R. Stoner and J. T. Glass, *Appl. Phys. Lett.*, **60**, 698 (1992).
57. B. Stoner, S. Sahaida, J. Bade, P. Southworth, and P. Ellis, *J. Mater. Res.*, **8**, 1334 (1993).
58. P. A. Dennig, Ph. D. Thesis - *Fundamental Studies of the Nucleation of Diamond Thin Films*, Stanford University (1995).

## CHAPTER 6 - Summary

This chapter reviews the main conclusions derived from both the experimental and modeling aspects of this thesis. These conclusions summarize the advances made in understanding the phenomenon of diamond nucleation, especially by an ion-assisted pretreatment process, from the research of this thesis. Despite these findings there are still many unanswered questions, and several research avenues provide the possibility for additional advances in the nucleation of diamond.

### 6.1 Experimental Conclusions

The experiments and characterization discussed in Chapter 4 were done to provide insights into the process of heterogeneous diamond nucleation. From this research, the following conclusions were made. Extremely poor nucleation with nuclei densities less than  $10^5 \text{ cm}^{-2}$  was observed for HFCVD, MPCVD, and sequential deposition techniques on Si and other substrates when no pretreatments were used. Initial experiments to enhance diamond nucleation focused on the role of carbon at the substrate surface. Carbon layers were deposited under various conditions in attempts to form suitable nucleation sites for diamond. Although varying amounts of carbon were deposited on the substrates and these samples were subjected to different pretreatments, no significant nucleation enhancement was observed for any of the carbon pretreatments. Furthermore, the deposited surface carbon was unstable in the diamond deposition environment. These experiments suggested that a specific configuration of carbon on the substrate surface leads to diamond nucleation. It was postulated that diamond nanocrystals are required for diamond nucleation, rather than a non-diamond form of carbon which is conducive to nucleation. Scratching pretreatments, which leave residual nanocrystalline diamond seeds on the substrate surface, produced enhanced nucleation densities to  $\sim 10^8 \text{ cm}^{-2}$ . However, since diamond grows homoepitaxially on these diamond seeds, such pretreatments did not provide insights for the heterogeneous nucleation process of diamond and were not pursued in detail.

Diamond nucleation enhancement to densities greater than  $10^9 \text{ cm}^{-2}$  was obtained by applying a negative bias on the substrate during MPCVD. The critical role of the energetic ion flux was confirmed for the nucleation process by comparing nucleation on Si substrate regions which had essentially identical conditions except for the flux of energetic ions at the surface. Nucleation densities for substrate regions exposed to an energetic ion flux were at least 5 orders of magnitude greater than for unbiased substrate regions. The term *ion-assisted nucleation* was adopted instead of the conventional term, *bias-enhanced nucleation* (BEN), since it more clearly identifies the nucleation mechanism.

Consistent with the control of nucleation by energetic ion bombardment, a critical voltage of approximately -200 V was required for nucleation enhancement in excess of  $10^9$  nuclei/cm<sup>2</sup>. This observation indicated that an ionic mechanism controlled the process; ions with energies greater than the critical value can surmount the nucleation barrier(s). The temperature dependence of the ion-assisted nucleation process was also studied and nucleation enhancement was independent of temperature from 450°C to 800°C. This result supports the energetic ion nucleation mechanism since the ion energies in this process were significantly higher than thermal energies in the temperature range under consideration. A decrease in the nucleation density at higher temperatures is not fully understood, but was attributed to an increased removal of surface carbon by desorption and/or hydrogen abstraction. The bias current was not a strong function of the substrate temperature indicating that thermionic emission of electrons does not play a major role in this ion-assisted nucleation process. Nucleation densities were relatively independent of carbon concentration over the range from 1% - 3% CH<sub>4</sub>/H<sub>2</sub>, but dropped significantly at lower concentrations. Measurements of the bias current indicate that the ion flux is dominated by hydrogenic ions rather than carbonaceous ions since only small increases in bias current were observed upon addition of CH<sub>4</sub> to the system.

Experiments using sequential deposition techniques investigated the roles of specific chemical species under bias conditions. Nucleation enhancement was observed for processes where the substrate was bombarded by energetic carbon ions, but no enhancement resulted when energetic hydrogen, argon, or helium ions were incident on the substrate. This indicated that the carbon ions, although a small fraction of the total ion flux to the surface, control the nucleation of diamond in this ion-assisted process. However, the growth of the nuclei increased approximately linearly with total pretreatment time rather than ion flux. Therefore, growth is controlled by the neutral flux to the surface rather than by the ion flux which causes nucleation. A comparison of the neutral and ion fluxes is consistent with this model since the ion flux was estimated to be several orders of magnitude less than the neutral flux.

The role of secondary electron emission in ion-assisted pretreatments was found to be complicated and is not completely understood. Bias current measurements suggest that the increased electron emission results from ion bombardment. Increases in the measured bias current with time result from the a higher 2nd Townsend coefficient (ion-induced electron yield per ion) for the nucleating carbon with respect to the Si substrate. The measured bias current can be used as a means of process control since the ion flux to the substrate controls the ion-assisted nucleation process.

The characterization of the bias-deposited carbon proved difficult due to the complexity of this form of carbon. A complete understanding of the nature of these carbon films was only possible through the combined use and evaluation of a number of analytical techniques. Analysis of the bias-deposited material by raman spectroscopy, x-ray diffraction (XRD), transmission electron microscopy/diffraction (TEM/SAD), and scanning electron microscopy (SEM) suggests a mixture of diamond and non-diamond carbon in the nucleating clusters. SEM and raman spectroscopy analyses did not confirm the presence of diamond in bias-deposited carbon samples; without other information, these techniques led to the conclusion that the bias-deposited material had poor crystallinity and was diamond-like in character. However, x-ray and electron diffraction were able to confirm the presence of nanocrystalline diamond-phase nuclei. The small grain size (25 - 150 Å) of these diamond crystals, as determined from TEM, and the presence of a non-diamond carbon matrix resulted in the inaccurate picture painted by the SEM and raman analyses. Therefore, the characterization results of this thesis indicate that multiple characterization techniques should be used to confirm the presence/absence of diamond in a sample. The presence of diamond in the bias-deposited carbon films confirms the earlier postulate that diamond is required for significant nucleation enhancement. This explains why polycrystalline diamond films of good quality can be grown on the initial nucleation material by subsequent unbiased MPCVD; nanocrystalline diamond nuclei are present at high densities in the bias-deposited films.

A retarding field probe was used to experimentally measure the ion energy distribution at the substrate. This measurement was difficult and imprecise for several reasons. First, electron current was also collected and had to be subtracted to obtain the proper ion current from the measurement. Second, the measured current was actually a convolution of the ion energy distribution and the collection efficiency of the probe. Deconvolution of these contributions was difficult. Moreover, the experimental complexity of the probe measurement prevented its use for the wide range of experimental conditions studied in this thesis. However, an ion energy distribution was measured for a given set of ion-assisted nucleation parameters and a broad gaussian-

shaped distribution centered around 45 eV was obtained. This value is considerably lower than the applied bias voltage due to ion-neutral collisions in the sheath region.

## 6.2 Modeling Conclusions

The experimental results allowed the ion-assisted deposition process to be modeled to explain mechanism(s) leading to the formation of the diamond nuclei. Several models and calculations were considered to add insight to the experimental results for this thesis. A Monte Carlo simulation, *IONTRANS*, was used to predict the ion energy distribution and, despite some uncertainties in the input parameters due to the complexity of the plasma, good agreement was found between the experimental and simulated ion energy distributions. The simulation allowed investigation of the ion energy distribution as a function of various experimental parameters, thereby avoiding difficult and time-consuming retarding probe measurements.

Ion and neutral species fluxes were estimated based upon experimental data as well as data from the literature. The neutral flux was estimated to be several orders of magnitude larger than the ion flux which was predicted to be primarily hydrogenic rather than carbonaceous ions. Estimates using electron-neutral cross-sections, neutral-ion reaction rates, and measured species concentrations in the plasma led to the conclusion that  $\text{H}_3^+$  and  $\text{CH}_4^+$  are the main hydrogen and carbon ions in the MPCVD system.

A number of plausible nucleation mechanisms based on bombardment of the substrate with energetic ions were considered. The concept of a critical nucleus from standard nucleation theory is useful, however, this model does not account for many of the processes occurring during ion-assisted nucleation. It is likely that preferential sputtering (both physical and chemical) of diamond and non-diamond carbon does occur in this process, albeit on a limited basis due to the relatively small sputtering yields. This modification of the growing film may influence the morphology and structure of the material deposited. However, preferential sputtering was ruled out as a viable nucleation mechanism since it provides no means to form the initial diamond nuclei.

Thermal spikes result from the energy transfer to the substrate due to the bombardment with energetic ions. Accompanying pressure spikes and/or hydrogen stabilization may move this system into the diamond stability regime in the carbon phase diagram, very briefly, and may lead to the metastable formation of diamond. This mechanism requires kinetic processes which may, or may not, occur on the short time



scales involved. However, biased sequential deposition experiments found that energetic carbon atoms were necessary for nucleation enhancement. This rules out the thermal spike mechanism which is purely energetic in nature, and therefore, would be independent of chemical species. Thermal spikes may still contribute to the formation of diamond by other mechanisms, though, since the transfer of energy and corresponding excitation of a small localized region may assist in the formation or stabilization of the metastable diamond structure.

The carbon subplantation mechanism involves the near-surface implantation of the impinging energetic carbon species. The ion energies involved in the ion-assisted nucleation process allow carbon to be implanted in the near-surface region. The subplanted carbon is postulated to reside in interstitial lattice sites and produce large compressive stresses in the growing film. Calculations and experimental evidence indicate that these ion-induced stresses are sufficient to move the system into the diamond stability region. This mechanism differs from the thermal spike since the film continually exists in the diamond stability region and is not dependent on the kinetic limitations of the thermal spike. Carbon subplantation was concluded to be the most likely mechanism to account for all of the experimental evidence for diamond nucleation by an ion-assisted process.

### 6.3 Directions for Future Work

Although a much better understanding of the nucleation of diamond and ion-assisted nucleation has been gained through the research of this thesis, there is clearly more research necessary to fully understand the mechanism(s) for ion-assisted nucleation. Various aspects of this thesis can be investigated with more detail to provide further information, and new avenues of study are suggested in this section based on the work done for this thesis.

As discussed briefly in Chapter 3, the statistical aspects concerning the nucleation densities were not studied in detail. Additional measurements and image analysis programs which analyze nuclei densities and sizes would provide more information from experiments similar to those done in this thesis. Although nucleation densities were not treated quantitatively for many experiments, the nucleation data in this thesis indicate a relatively broad nucleation size distribution. A closer and more quantitative investigation of the distribution of nuclei sizes as a function of time under various conditions may help elucidate the dynamic aspects of this process. Surface diffusion was not considered in

detail in this work due to the lack of data available for this phenomenon. Modeling of both the spatial and size distributions for nuclei may provide estimates of surface diffusion of carbon under both biased and unbiased conditions.

To obtain more accurate nucleation size and density data, higher resolution techniques such as Atomic Force Microscopy (AFM) and TEM would provide much more information than the SEM analysis used in this work. It is important to remember that, due to resolution limitations, the techniques used in this thesis probed the nuclei well after the actual nucleation event occurred. Fundamental nucleation studies, including determination of the critical diamond nucleus size, are critical for the future of diamond thin film technology. AFM is a powerful technique for analyzing the surface topography of materials down to atomic scales and may provide the means for such basic research. In addition to improved resolution, this characterization method requires minimal sample preparation. Although AFM may be applicable for diamond nucleation research, there are problems to be considered when using this technique. Since the image obtained with an AFM is the convolution of the AFM tip and the surface being analyzed, issues regarding the shape and size of the tip are critical. This is especially important for nucleation studies given the potential atomic scale nuclei sizes. For this reason, AFM should always be complemented by another technique such as SEM to confirm the features observed. Although TEM was used in this thesis to provide important information on the structure of the bias-deposited films, detailed TEM research would provide even more insight. High-resolution cross-section TEM would allow investigation of the orientation and structure of the interfacial region. Furthermore, plan-view TEM may be appropriate for more accurate nucleation density measurements. However, the high costs and difficult sample preparation for TEM samples may be a limiting factor.

As alluded to throughout this thesis, nucleation research was limited by the lack of *in-situ* diagnostic and *in-vacuo* characterization techniques. Several examples of potential research areas if additional diagnostic and characterization tools were available for the MPCVD system include the following: the estimates of ion and neutral species concentrations could be verified by optical spectroscopy techniques and/or molecular beam mass spectrometry; *in-vacuo* XPS could provide better characterization of the substrate surface as a function of pretreatment times without the complicating issues of contamination during transfer to *ex-situ* systems; and *in-vacuo* raman spectroscopy or x-ray diffraction could determine the structure characteristics of the nuclei as they evolved in time. Although the addition of such capabilities to a MPCVD system has clear research benefits, the high equipment costs and maintenance issues are problematic.

The effects of alternate chemistries on nucleation and the ion-assisted pretreatment process were not investigated and remain unknown. In standard diamond deposition, oxygen has been shown to enhance growth and may have an interesting effect on nucleation [1-4]. On the one hand, atomic oxygen formed in the plasma may have detrimental effects on nucleation due to its high reactivity. However, the ability of atomic oxygen to etch non-diamond carbon more efficiently than atomic hydrogen may provide unexpected advantages for nucleation. Alternate chemistries can be studied both through addition of gases to the MPCVD plasma environment or with additional chemical emitters in the sequential deposition scheme. The sequential reactor provides a means to probe the biased nucleation processes which is not accessible by other standard diamond deposition techniques. A relatively small number of sequential experiments were done in this thesis, and this unique system offers the opportunity for more detailed experiments in which chemical species and deposition parameters can be uncoupled.

Secondary electron emission was shown to play an important, yet poorly understood, role for ion-assisted nucleation in this thesis. Since electron emission is extremely surface sensitive, this phenomenon may explain the differing results obtained for nucleation under applied bias with different substrate materials. Although not discussed in this thesis due to the limited nature of the experiments, the substrate material was observed to have a large effect on the nucleation process for ion-assisted pretreatments. Research at NC State has focused on the effects of different substrate materials in more detail [5]. Given the desire to deposit diamond films on a variety of materials, a more detailed investigation of the effects of the substrate and electron emission may prove both interesting and useful. Furthermore, such research may also provide insight into the role of carbide formation in ion-assisted nucleation. This phenomena has been investigated and appears to play some role since the tendency of the substrate to form a carbide has been correlated with the diamond nucleation density under bias conditions [5].

The controlling role of carbon ions in the ion-assisted nucleation process was confirmed in the sequential biased deposition experiments of this thesis. A subtle, but important, point is that the experiments should ideally be done with constant carbon ion flux to the surface. The constant integrated bias current used in the experiments of this thesis includes the hydrogenic ions which were postulated to dominate this current. Use of well-controlled carbon ion beams may lead to more understanding of the dependences in this process. The ion-assisted nucleation process is a specific example of a much larger class of research in the area of Ion-Beam Assisted Deposition (IBAD). These processes provide independent control of ion bombardment flux, energy and direction - parameters

which cannot be independently controlled in plasma processes [6]. Accurate control of the fluxes and energies of the species discussed in this work may allow ion-assisted processes to be optimized for diamond nucleation.

Finally, ion-assisted diamond nucleation pretreatments have received a lot of attention currently in the diamond research community since limited heteroepitaxial nucleation has been obtained on Si and SiC substrates using this process [7-10]. Careful control of the bias pretreatment and subsequent diamond growth parameters has produced highly textured polycrystalline diamond films with low-angle grain boundaries and close in- and out-of-plane registry with the underlying substrate. The deposition of heteroepitaxial and aligned diamond films was not investigated in this thesis. However, with the better understanding of the ion-assisted process obtained from this research, attempts at producing and understanding heteroepitaxial diamond films are possible. Since truly heteroepitaxial diamond films are the holy grail of diamond research, opening up a wide range of applications, this is a logical extension of the work done in this thesis.

#### 6.4 References

1. S. Kapoor, M. A. Kelly, and S. B. Hagstrom, *J. Appl. Phys.*, **77**, 6267 (1995).
2. S. Kapoor, Ph. D. Thesis - *Growth of Diamond Films by Cyclic Exposure to Different Chemistries*, Stanford University (1994).
3. Y. Liou, A. Inspektor, R. Weimer, D. Knight, and R. Messier, *J. Mater. Res.*, **5**, 2305 (1990).
4. C. Chen, Y. Huang, S. Hosomi, and I. Yoshida, *Materials Research Bulletin*, **24**, 87 (1989).
5. S. D. Wolter, J. T. Glass, and B. R. Stoner, *J. Appl. Phys.*, **77**, 5119 (1995).
6. J. E. Harper and J. J. Cuomo, *J. Vac. Sci. Technol. A*, **21**, (1982).
7. B. R. Stoner and J. T. Glass, *Appl. Phys. Lett.*, **60**, 698 (1992).
8. B. Stoner, S. Sahaida, J. Bade, P. Southworth, and P. Ellis, *J. Mater. Res.*, **8**, 1334 (1993).
9. B. R. Stoner, *et al.*, *Diamond Rel. Mater.*, **2**, 142 (1993).
10. D. K. Milne, *et al.*, *Diamond Rel. Mater.*, **4**, 394 (1995).

## APPENDIX A

### A.1 Related Publications by the Author

S. P. McGinnis, M. A. Kelly, S. B. Hagström, and R. L. Alvis  
"Observation of Diamond Nanocrystals in Carbon Films Deposited During Ion-Assisted Microwave Plasma Nucleation Pretreatments"  
*Journal of Applied Physics*, submitted September, 1995.

S. P. McGinnis, M. A. Kelly, and S. B. Hagström  
"Mechanisms for the Ion-Assisted Nucleation of Diamond"  
*Proceedings of the 4th International Symposium on Diamond Materials*  
The Electrochemical Society, 1995.

S. P. McGinnis, M. A. Kelly, and S. B. Hagström  
"Evidence of an Energetic Bombardment Mechanism for Bias-Enhanced Nucleation of Diamond"  
*Applied Physics Letters*, 66(23), p. 3117, 1995.

S. S. Perry, G. A. Somorjai, and S. P. McGinnis  
"Adhesion at Diamond-Metal Interfaces: A Chemical Composition Perspective"  
*Journal of Adhesion Science and Technology*, 9(6), p. 711, 1995.

S. P. McGinnis, M. A. Kelly, T. M. Gur, and S. B. Hagström  
"The Role of Surface Carbon in the Heterogeneous Nucleation of Diamond"  
*Proceedings of the 3rd International Symposium on Diamond Materials*,  
The Electrochemical Society, J.P. Dismukes and K.V. Ravi (editors), p. 153, 1993.

K. Nakajima, S. P. McGinnis, and M. A. Kelly  
"Silicon by XPS"  
*Surface Science Spectra*, 2(1), p. 61, 1993.

**A.2 Chemical Bond Strengths**

BOND	BOND STRENGTH		
	kJ/mol	kcal/mol	eV/molecule
<i>H - H</i>	436	104	4.5
<i>C - H</i>	415	99.2	4.3
<i>C - C</i>	344	82.2	3.6
<i>C = C</i>	615	147	6.4
<i>C ≡ C</i>	812	194	8.4
<i>C - O</i>	350	84	3.6
<i>C = O</i>	725	173	7.5
<i>C - N</i>	292	70	3.0
<i>C = N</i>	615	147	6.4
<i>C ≡ N</i>	890	213	9.2
<i>C - Si</i>	290	69.3	3.0
<i>C - F</i>	441	105	4.6
<i>H - F</i>	563	135	4.8
<i>H - Cl</i>	432	103	4.5
<i>Si - F</i>	590	141	6.1
<i>Si - Cl</i>	396	95	4.1

Table A.1 - Chemical bond strengths (L. Pauling, *General Chemistry*, Dover Publications, 1970, pp. 913).

### A.3 X-Ray Photoelectron Spectroscopy Quantification

The full expression for the intensity of a signal in XPS is given by equation A.1 where  $I_j$  is the measured intensity for species  $j$ ,  $I_0$  is the x-ray photon flux,  $G$  is the area sampled by the analysis,  $\sigma_j$  is the photoionization cross-section of species  $j$ ,  $K$  is the sample "condition" term,  $C_j(z)$  is the concentration of species  $j$  in atoms/cm<sup>3</sup>,  $z$  is the depth measured from the surface down into the sample,  $\lambda_j$  is the mean free path of the electron from species  $j$ ,  $\theta$  is the take-off angle of the detector,  $f$  is the spectrometer retardation factor,  $T$  is the spectrometer transmission factor, and  $D$  is the detector efficiency.

$$I_j = I_0 G \sigma_j K \int_0^{\infty} C_j(z) \exp\left[-z/\lambda_j \cos \theta\right] dz \cdot fTD \quad \text{A.1}$$

The signal for a thin overlayer on a substrate can be determined by considering the following the schematic in Figure A.1

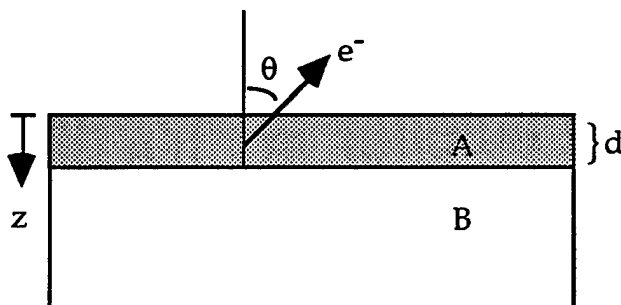


Figure A.1 - Schematic for XPS overlayer calculations.

The peak area which is measured by the XPS system is given by:

$$A_j = \int_0^t I_j dt \quad \text{A.2}$$

If the ratio of peak areas from regions A and B is used, a number of terms from equation A.1 will cancel since they are equal for the two regions being analyzed:

$$\frac{A_A}{A_B} = \frac{\int I_A dt}{\int I_B dt} = \frac{\sigma_A \int_0^d C_A(z) \exp\left[-z/\lambda_A \cos \theta\right] dz}{\sigma_B \int_0^\infty C_B(z) \exp\left[-z/\lambda_B \cos \theta\right] dz} \quad \text{A.3}$$

For a perfectly uniform layer and substrate, the concentrations are constant with depth,  $z$ , and can be removed from the integral. Non-uniform concentration profiles make this analysis significantly more difficult. Evaluating the result and simplifying yields:

$$\frac{A_A}{A_B} = \frac{\sigma_A C_A (-\lambda_A \cos \theta) \exp\left[-z/\lambda_A \cos \theta\right]_0^d}{\sigma_B C_B (-\lambda_B \cos \theta) \exp\left[-z/\lambda_B \cos \theta\right]_d^\infty} \quad \text{A.4}$$

$$\frac{A_A}{A_B} = \frac{\sigma_A C_A \lambda_A \left[ \frac{1 - \exp\left(-d/\lambda_A \cos \theta\right)}{\exp\left(-d/\lambda_B \cos \theta\right)} \right]}{\sigma_B C_B \lambda_B} \quad \text{A.5}$$

If it is assumed that the mean free paths are equal so  $l = l_A = l_B$ , a good assumption for peaks which are near each other due to the shape of the electron mean free path as a function of energy [3], the expression becomes even simpler:

$$\frac{A_A}{A_B} = \frac{\sigma_A C_A}{\sigma_B C_B} \left[ \exp\left(d/\lambda \cos \theta\right) - 1 \right] \quad \text{A.6}$$

Note that some XPS systems automatically correct for the photoionization cross-sections in the software analysis and therefore the cross-section ratio should be dropped from equation A.6.



#### A.4 Structure Factor Calculations for Diamond

The x-ray structure factor,  $F_{hkl}$ , is given by equation A.7 where the sum is over the  $N$  atoms in the unit cell,  $f_n$  is the atomic structure factor for species  $n$ ,  $(h, k, l)$  are the Miller plane indices, and  $(x_N, y_N, z_N)$  are the coordinate positions of the atoms in the unit cell [1].

$$F_{hkl} = \sum_1^N f_n e^{2\pi i(hx_N + ky_N + lz_N)} \quad \text{A.7}$$

Consider first the structure factor for an FCC lattice with 4 atoms/unit cell at the positions  $(0, 0, 0)$ ,  $(1/2, 1/2, 0)$ ,  $(1/2, 0, 1/2)$ , and  $(0, 1/2, 1/2)$ . Substituting these into equation A.7 gives:

$$F_{hkl} = f_c \left[ e^{2\pi i(0)} + e^{\pi i(h+k)} + e^{\pi i(h+l)} + e^{\pi i(k+l)} \right] \quad \text{A.8}$$

$$F_{hkl} = f_c \left[ 1 + e^{\pi i(h+k)} + e^{\pi i(h+l)} + e^{\pi i(k+l)} \right] \quad \text{A.9}$$

If  $(h, k, l)$  are unmixed (all even or all odd), the sums in the exponential terms are also even multiples of  $\pi i$  and therefore:

$$F_{hkl} = f_c [1 + 1 + 1 + 1] = 4f_c \quad \text{since } e^{n\pi i} = (-1)^n \quad \text{A.10}$$

If  $(h, k, l)$  are mixed (even and odd), the sums in the exponential terms give two odd and one even multiple of  $\pi i$  and therefore :

$$F_{hkl} = f_c [1 - 1 - 1 + 1] = 0 \quad \text{since } e^{n\pi i} = (-1)^n \quad \text{A.11}$$

This gives the structure factor for the FCC lattice. However, the diamond structure has a 2-atom basis with atoms at  $(0, 0, 0)$  and  $(1/4, 1/4, 1/4)$  which modifies the structure factor from the single-atom basis. Whenever a lattice contains a common translation, the corresponding terms in the structure factor can be factored out to simplify the expression:

$$F_{hkl} = 4 \left[ f_c + f_c e^{2\pi i \left( \frac{h}{4} + \frac{k}{4} + \frac{l}{4} \right)} \right] = 4f_c \left[ 1 + e^{\frac{\pi i}{2}(h+k+l)} \right] \quad \text{A.12}$$

For mixed indices, the structure factor is still zero even with the two-atom basis. However, the addition of another basis atom will cause more reflections to be missing. Planes will be missing if their intensity, which is given by the structure factor multiplied by its complex conjugate, is zero:

$$|F_{hkl}|^2 = 16f_c^2 \left[ 1 + e^{\frac{\pi i}{2}(h+k+l)} \right] \left[ 1 + e^{-\frac{\pi i}{2}(h+k+l)} \right] = 0 \quad \text{A.13}$$

Solving for  $(h + k + l)$ :

$$16f_c^2 \left[ 1 + e^{\frac{\pi i}{2}(h+k+l)} + e^{-\frac{\pi i}{2}(h+k+l)} + 1 \right] = 0 \quad \text{A.14}$$

$$16f_c^2 \left[ 2 + 2 \cos \frac{\pi}{2}(h+k+l) \right] = 0 \quad \text{since } e^{\pm i\phi} = \cos \phi \pm i \sin \phi \quad \text{A.15}$$

Therefore, additional missing reflections occur at:

$$\cos \frac{\pi}{2}(h+k+l) = -1 \quad \text{A.16}$$

$$(h+k+l) = 2n \quad \text{where } n \text{ is an odd integer} \quad \text{A.17}$$

Diamond will have missing reflections for all planes where:

$$(hkl) = \text{mixed and } (h+k+l) = 2n \text{ where } n \text{ is an odd integer}$$

## A.5 Sample Preparation Method for Cross-Sectional Transmission Electron Microscopy (TEM)\*

The following procedure outlines the modified metallographic method for the preparation of samples for cross-sectional transmission electron microscopy (XTEM). This technique, essentially the Bravman-Sinclair method, allows a thin, electron transparent foil to be prepared from any material such that the true microstructure of the material may be studied.

The method used to prepare the carbon films in this thesis for cross-sectional TEM was as follows:

- 1) Two 4 mm x 5 mm dice were extracted from the substrate (wafer) containing the film of interest using the Gatan model 610 ultrasonic cutting tool.
- 2) Four additional dice were cut from a spare silicon wafer.
- 3) After thorough mixing of the G-1 epoxy, the two dice containing the film were glued face-face with an ultra-thin layer of epoxy. Dummy dice were glued to the back of the first two dice to build up a stack of 6, with the middle interface containing the film of interest.
- 4) Using the Buehler diamond cut-off wheel, a 0.5 mm slice was removed from the center of the stack.
- 5) The samples were mounted on a platen with the cross-sections of all six dice and five glue layers facing up. This is referred to as "side 1."
- 6) Side 1 was prepared by successively grinding away material with the 305  $\mu\text{m}$ , 65  $\mu\text{m}$ , and 35  $\mu\text{m}$  Buehler diamond wheels, taking care to remove all the damage from the previous polishing step, and a little more. Final polish to a mirror finish was accomplished with 35  $\mu\text{m}$ , 15  $\mu\text{m}$ , and finally 0.055  $\mu\text{m}$  diamond slurry in a mixture with Buehler Mastermet.

- 7) With the Gatan model 610 ultrasonic cutter, a 3 mm core was extracted from the slice and polished stack. The specimen was cleaned and its thickness was determined with the vernier scale on an optical microscope.
- 8) Side 2, the opposite of side 1, was prepared on the VCR Group D500i dimpler by initially grinding (20 grams, 300 rpm) to a thickness of less than 755  $\mu\text{m}$  with a wide padded dimpling tool and 35  $\mu\text{m}$  diamond slurry.
- 9) Final dimpling was completed by thinning the center of the disc to less than 15  $\mu\text{m}$  by sequential polishing with a thin padded tool and 35  $\mu\text{m}$  and 15  $\mu\text{m}$  diamond slurry and finally a 0.055  $\mu\text{m}$  diamond slurry/Mastermet mixture.
- 10) Thinning to electron transparency was accomplished with a 4 keV argon ion beam (Gatan Precision Ion Polisher) at 40° incidence on side 2 for 1 - 2 minutes. The specimen was then turned over to mill the flat polished side 1 until perforation was achieved. The specimen was then placed in the TEM for examination.

Since a TEM analysis is only as good as the sample being examined, special care was taken to avoid artifacts from sample preparation. In the case of a thin diamond/DLC coating on a silicon substrate, a special considerations apply because of the relative hardnesses of the diamond film and the diamond polishing slurry. The way a large thin area was obtained for the film was to use as large a diamond particle as possible at each stage of the preparation and as low an angle as possible during ion-milling. This approach allowed the film to be "chipped" away as the substrate was polished, such that a high "bridge" of diamond film at the interface was avoided. By slightly modifying the standard approach of "short grinding time and long polishing time" (short time on big diamond particles), TEM samples revealing the microstructure of a thin diamond film were obtained on the first try.

\* R. A. Alvis, Advanced Micro Devices, Sunnyvale, CA 94088